

# **Recovering materials from batteries for electrocatalytic applications**

**Arshdeep Kaur**

**BEng(ChemEng), MTech(ChemEng)**

Submitted in fulfilment of the requirements for the degree of

**Doctor of Philosophy**

Centre for Material Science

School of Chemistry and Physics

Faculty of Science

Queensland University of Technology

**2025**

## **Keywords**

Electrocatalysts, green hydrogen, water splitting, oxygen evolution reaction, hydrogen evolution reaction, circular economy, repurpose, recycle, reuse, electronic waste, battery waste, electrolysis, Li-ion batteries, electrochemical analysis.

# Abstract

---

The rapid increase in global population and economic growth has led to a sharp rise in energy demand. At present, the world's economy remains heavily reliant on fossil fuels such as coal, oil, and natural gas, which are major contributors to greenhouse gas emissions, particularly carbon dioxide, causing severe environmental issues. As a result, extensive research is being conducted on renewable energy sources as potential alternatives to fossil fuels. Hydrogen-based energy is considered one of the most efficient solutions to reduce dependence on fossil fuels. In this context, hydrogen production through electrochemical water splitting has gained significant attention, as it is a zero-emission technology when powered by renewable energy. Thus, electrocatalysis plays a crucial role in this process by reducing the kinetic energy barriers associated with water splitting process.

Water splitting reactions are generally classified into two half-cell reactions: the oxygen evolution reaction (OER) and the hydrogen evolution reaction (HER). The HER takes place at the cathode, leading to hydrogen generation, while the OER occurs at the anode, resulting in oxygen formation. One of the primary challenges of this technology is the sluggish reaction kinetics, particularly for the OER. This necessitates the development of highly efficient electrocatalysts capable of overcoming kinetic limitations and enhancing the production of hydrogen and oxygen.

Noble metal-based electrocatalysts, particularly platinum group metals and their oxides (Pt, Pd, Ir, Ru, and Rh), are highly efficient for electrochemical water splitting. However, their high cost, scarcity, and extensive use in various industries have placed them on the endangered elements list, limiting the large-scale adoption of electrolyzers that rely on these catalysts. As a result, increasing research efforts have been directed toward alternative electrocatalysts, including transition metal oxides and hydroxides (Ni, Mn, Co, and Fe) for the oxygen evolution reaction (OER), as well as metal-based carbides, transition metal phosphides, and transition metal chalcogenides (sulphides and selenides) for the hydrogen evolution reaction (HER).

On the other hand, the growing accumulation of battery waste is a significant environmental concern. Approximately 8,000 tonnes of batteries are discarded into landfills annually, leading to severe land pollution due to the leaching of hazardous

chemicals, posing risks to both human health and the environment in Australia. Furthermore, according to IUPAC, several elements, including Co, As and Zn, etc. are at risk of complete depletion within the next 100 years due to excessive consumption in electronic applications. Additionally, elements such as Ni, Mn, Li, and Mg have been categorized as having limited availability. As a result, there has been a growing interest in exploring recycled battery waste for electrocatalytic applications.

Therefore, the studies conducted in this research is based on an opportunity to recycle spent batteries and recover valuable materials for water splitting reactions (OER and HER) and observe their electrocatalytic performance.

First and foremost, a study was conducted to investigate the potential of repurposing the current collector from a Toyota Prius battery module as a bifunctional electrocatalyst for overall electrochemical water splitting under alkaline conditions (Chapter 4). The Ni-coated iron electrode exhibited remarkable properties for both the oxygen evolution reaction (OER) and hydrogen evolution reaction (HER), displaying bifunctional behaviour upon repetitive cycling. Additionally, the repurposed material outperformed a Ni electrode of similar surface area in both reactions. The electrode demonstrated low overpotentials of 250 mV (OER) and 260 mV (HER), along with favourable Tafel slope values of 83 mV dec<sup>-1</sup> (OER) and 101 mV dec<sup>-1</sup> (HER), comparable to chemically synthesized catalysts. The key factor enabling this enhanced performance was the emergence of iron into the nickel layer, forming a stable mixed Fe/Ni oxide layer during potential cycling. This study highlights the importance of considering not only active materials but also current collectors as valuable components for recycling in rechargeable battery systems.

Further studies were performed on commonly used cathode materials, such as nickel manganese cobalt (NMC) oxide from Li-ion batteries, as electrocatalysts for water splitting reactions. NMC materials with varying metal ratios (NMC 622 and NMC 811) as electrocatalysts for the oxygen evolution reaction (OER) and hydrogen evolution reaction (HER) under alkaline conditions. While both materials exhibit excellent OER activity both showed poor performance for the HER. Additionally, among them NMC 622 demonstrates superior OER performance, achieving an overpotential of just 280 mV to reach 100 mA cm<sup>-2</sup> and a low Tafel slope of 42 mV dec<sup>-1</sup>. Moreover, it sustains high current densities of 150 mA cm<sup>-2</sup> for 24 h and remains stable under extensive potential

cycling, making it suitable for direct integration with renewable energy sources. These findings suggest that NMC cathode materials recovered from spent lithium-ion batteries hold promise as efficient OER electrocatalysts.

The recycling of electrode materials from lithium-ion batteries (LIBs) has attracted considerable interest due to environmental concerns, and energy-related challenges. To reduce recycling costs and optimize the use of transition metals in LIB cathode materials, extensive efforts have been made to develop a simple and effective method for converting recycled materials, from spent LIBs, into a highly efficient electrocatalyst for the oxygen evolution reaction (OER). Therefore, studies are conducted to investigate NMC 622 from spent Li-ion batteries. The material is subjected to cycling for example 50 lifetime cycles, 150 lifetime cycles and 200 lifetime cycles as well as blank NMC 622 (uncycled), and unprocessed NMC 622 are compared for OER performance. However, it was observed that the battery's usage history influenced the material's effectiveness as an electrocatalyst. An increase in the number of battery cycles led to a decline in OER performance. This study presented crucial points related to application of more efficient recovery methods of cathode materials from spent Li ion batteries, to ensure the particles retain the catalytic activity to be used as electrocatalysts.

On similar terms, this next part of the research study also explores the recovery of Lithium Iron Phosphate (LFP) from spent LFP-based Li-ion batteries and its potential application as an electrocatalyst for the oxygen evolution reaction (OER), a key process in electrochemical water splitting and green hydrogen production. Due, to the rapid growth of lithium-ion batteries to meet increasing energy demands is expected to create a significant waste management challenge at their end of life. Among these, lithium iron phosphate (LFP)-based batteries are gaining a larger market share, leading to a projected rise in LFP battery waste. Therefore, the findings in this study demonstrates that when recovered LFP is immobilized onto a Ni substrate, it undergoes reconstruction into a mixed Fe/Ni oxide surface layer, which exhibits high OER activity. Particularly, LFP recovered from cycled batteries retained excellent electrocatalytic performance, yielding a low Tafel slope of  $58 \text{ mV dec}^{-1}$ , overpotential values of 250 mV and 310 mV at 10 and 100  $\text{mA cm}^{-2}$ , respectively, and stable operation for 24 h at currents exceeding 200  $\text{mA cm}^{-2}$ . These results highlight the potential for recyclers to extract LFP from spent Li-ion batteries for use in water electrolysis, contributing to sustainable energy solutions.

Thus, the current study is framed within the concept of a circular economy, emphasizing reuse, recycling, and repurposing. As the research presented aims to explore the potential of transition metals from battery waste and repurpose them into electrocatalysts for water splitting reactions. Waste from various lithium-ion batteries, such as Nickel Metal Hydride (NiMH), Lithium Iron Phosphate (LFP), and Nickel Manganese Cobalt (NMC) that contains key elements like Ni, Fe, Co, Mn, and P, which are often regarded as harmful as heavy metals leach that pollute soil and water. Therefore, instead of battery ending up in the landfills, can be repurposed and thus promoting electronic waste management and environment protection. It also signifies resource recovery and converts waste into materials for green hydrogen production and supporting decarbonisation.

<b>Table of Contents</b>	
<b>Keywords</b>	II
<b>Abstract</b>	III
<b>Table of contents</b>	VII
<b>Table of figures</b>	IX
<b>List of Tables</b>	XIV
<b>List of publications</b>	XV
<b>Acknowledgements</b>	XVI
<b>Chapter 1</b>	1
1. Introduction	1
1.1 Background	1
1.2 Batteries	3
1.3 Battery waste	4
1.4 Components of battery waste	8
1.5 Context	10
1.6 Purpose	11
1.7 Significance	11
1.8 Thesis outline	11
References	14
<b>Chapter 2</b>	15
2. Literature Review	16
Background	16
2.1 Electrocatalysts	18
2.1.1 Hydrogen Evolution Reaction	18
2.1.2 Oxygen Evolution Reaction	19
2.1.3. Electrocatalysts based on transition metals	20
2.1.4 Bifunctional electrocatalysts	22
2.2 Electrocatalysts performance parameters	24
2.3. Electrocatalytic measurements	29
2.4 Stability	30
2.5 Efficiency	31
2.6 Electronic wastes from batteries	32
2.6.1 NMC (Nickel Manganese and cobalt)	33
2.6.2 LFP (Lithium iron phosphate)	35
2.6.3 Recovery from NiMH batteries waste	36
2.6.4 Recovering spent battery materials as electrocatalysts	38
2.7 Conclusion	39
References	40
<b>Chapter 3</b>	46
3. Research Design	47
3.1 Electrochemical method	47
3.2 Ink Preparation Method	49
3.3 Characterisation Techniques	50
3.3.1 Scanning Electron Microscopy (SEM)	50
3.3.2 Transmission Electron Microscopy (TEM)	51
3.3.3 Energy Dispersive X-ray Spectroscopy (EDS or EDX)	52
3.3.4 X-ray Photoelectron Spectroscopy	53
3.3.5 X-ray Diffraction (XRD)	54
3.4 Electrochemical Techniques	54
3.4.1 Cyclic voltammetry (CV)	54
3.4.2 Linear Sweep Voltammetry	57
3.4.3 Chronoamperometric Techniques	57

3.4.4	Tafel slope	58
3.4.5	Electrochemical Surface Area (ECSA)	58
	References	60
<b>Chapter 4</b>		<b>61</b>
4.	Repurposing the current collector of a car battery module into a bifunctional electrode for overall electrochemical water splitting.	62
4.1	Abstract	63
4.2	Introduction	63
4.3	Results and discussion	65
4.4	Experimental	75
4.5	Conclusions	76
4.6	Acknowledgements	77
	References	78
<b>Chapter 5</b>		<b>82</b>
5.	Investigating the potential use of Ni-Mn-Co (NMC) battery materials as electrocatalysts for electrochemical water splitting.	82
	Background	84
5.1	Abstract	84
5.2	Introduction	84
5.3	Results and Discussion	87
5.4	Conclusions	97
5.5	Experimental	97
5.6	Acknowledgements	99
	References	100
<b>Chapter 6</b>		<b>105</b>
6.	Recovering spent NMC battery materials for use as electrocatalysts	105
	Background	107
6.1	Abstract	107
6.2	Methodology of cell preparation	107
6.3	Results and Discussion	108
6.4	Characterisation	110
6.5	Conclusions	115
	References	115
<b>Chapter 7</b>		<b>118</b>
7.	Using Recovered Lithium Iron Phosphate Battery Material as an Electrocatalyst for the Oxygen Evolution Reaction	118
	Background	120
7.1	Abstract	120
7.2	Introduction	120
7.3	Results and Discussion	123
7.4	Conclusions	133
7.4	Experimental	134
	References	135
<b>8. Conclusions and Future Scope of work</b>		<b>142</b>
<b>Appendix 1: Peer reviewed Journal Articles and Conference Proceedings</b>		<b>148</b>
<b>Appendix 2: Supplementary information (Chapter 4)</b>		<b>149</b>
<b>Appendix 3: Supplementary information (Chapter 5)</b>		<b>152</b>
<b>Appendix 4: Supplementary information (Chapter 7)</b>		<b>154</b>

## Table of Figures

### Chapter 1

Figure 1.1	A Hydrogen Electrolyser project	1
Figure 1.2	Various future hydrogen development goals in Australia	2
Figure 1.3	Global Battery Market	3
Figure 1.4	Global Battery Demand by Application	4
Figure 1.5	Representation of the arrangement of small cylindrical lithium-ion battery (LIB) cells within a large car battery pack and high-capacity cells required for EVs.	5
Figure 1.6	Periodic table of endangered elements released by IUPAC	6
Figure 1.7	(a) Periodic Table produced by the European Chemical Society (EuChemS) to highlight element availability and vulnerability, (b) Modification of the (EuChemS) Periodic Table to include the extent to which element is recycled.	6, 7
Figure 1.8	Bar chart of the ranking of endangered elements blue-electrocatalytic performance and red-amount of elements in electronic devices.	8
Figure 1.9	Typical material composition for LIBs.	9
Figure 1.10	Aster plot of endangered element species and their possible water splitting electrocatalyst applications.	10

### Chapter 2

Figure 2.1	Hydrogen to carbon ratio in various fuels.	16
Figure 2.2	Volcano plot a) Exchange current density Vs M-H bond energy for metal surface (acidic media) <sup>17 2</sup> , b) exchange current density on monometallic surface Vs hydrogen binding energy calculated (alkaline media).	19
Figure 2.3	Synthesis of CoNiMn/NC	20
Figure 2.4	a) Linear Sweep Voltammetry curves, (b) Tafel plots (Co/NC, CoNi/NC, CoNiMn/NC) in 1.0 M KOH for HER.	21
Figure 2.5	Cyclic Voltammograms recorded in 1 M KOH for 1000 cycles at 100 mV sec <sup>-1</sup> for sample S-4, b) enlarged region showing the Ni oxidation process.	22
Figure 2.6	(a) Tafel plots of CuCo <sub>2</sub> O <sub>4</sub> @CuCo <sub>2</sub> S <sub>4</sub> , CuCo <sub>2</sub> O <sub>4</sub> , CuCo <sub>2</sub> S <sub>4</sub> , RuO <sub>2</sub> (Pt/C), and Ni foam for OER activity, (b) Tafel plots of CuCo <sub>2</sub> O <sub>4</sub> @CuCo <sub>2</sub> S <sub>4</sub> , CuCo <sub>2</sub> O <sub>4</sub> , CuCo <sub>2</sub> S <sub>4</sub> , RuO <sub>2</sub> (Pt/C), and Ni foam for HER activity.	23
Figure 2.7	The LCV curves of OER that are measured at 0.5 mV s <sup>-1</sup> in 1 M KOH for Ni-Co-Mn oxides heated at various temperatures for 150 min.	23
Figure 2.8	Evaluation parameters that decide the efficiency of electrocatalysts.	24
Figure 2.9	(a) Capture of H <sup>+</sup> from hydronium ions to form the protonated amine groups on PANI-CoP HNWs, (b) Polarisation curves of various electrocatalysts for HER in waters splitting reaction	25
Figure 2.10	(a) Procedure of synthesis of CoP/NCNHP hybrid (b) Polarisation curve of overall water splitting based CoP/NCNHP//CoPNCNHP	25, 26
Figure 2.11	TEM and HRTEM images of CoP	26, 27
Figure 2.12	The top and side view of Mn-Co-P with two Mn atoms substituting the subsurface Co atoms, HER free energy diagrams of Pt, Mn-Co-Co, and CoP.	27
Figure 2.13	The morphology structure for the defective carbon/CoP nanoparticles.	28

Figure 2.14	Polarisation curves of Ni-CoP@C, CoP@C, Ni2P@C, Ni-CoP NPs, PDA derived C, commercial RuO <sub>2</sub> , and bare CFP at scan rate of 10 mVsec <sup>-1</sup> in 1M.	29
Figure 2.15	The Tafel Plot value for NiFe –NiCoO <sub>2</sub> , NiCo –NiFe(CN) <sub>6</sub> , NiCo – LDH and NiCo alloy derived for OER <sup>3</sup> , (b) The Tafel Plot value for NiFe –NiCoO <sub>2</sub> , NiCo –NiFe(CN) <sub>6</sub> , NiCo –LDH and NiCo alloy for HER.	30
Figure 2.16	Stability measurements	31
Figure 2.17	CV of single layer nickel hydroxide (SL-Ni (OH) <sub>2</sub> ) on highly oriented pyrolytic graphite (HOPG) 1M KOH at scan rate of 50mV sec <sup>-1</sup> and in below figure electrode at different amount of Fe and at scan rate of 10 mV sec <sup>-1</sup> .	31

### Chapter 3

Figure 3.1	Three electrode setup	47
Figure 3.2	Three electrode electrochemical cell	47
Figure 3.3	Fe-Ni mesh sheet used for experimentation	48
Figure 3.4	Ni foam used for experimentation	48
Figure 3.5	Ink preparation method	49
Figure 3.6	Electrode preparation	50
Figure 3.7	JEOL 7001F electron microscope for understanding surface morphology of samples.	51
Figure 3.8	JEOL 2100 HR-TEM Transmission Electron Microscope, used for used for imaging of samples.	52
Figure 3.9	Kratos Supra Xray Photoelectron Spectroscope used for analysing the Oxidation states of samples.	53
Figure 3.10	General cyclic voltammetry profile.	55
Figure 3.11	Voltammogram of the reversible reduction for species Fc.	55
Figure 3.12	CVs recorded at 100 mV s <sup>-1</sup> for 2000 cycles in 1 M KOH in the OER region, HER region for the FNC electrode.	56
Figure 3.13	LSVs recorded at Fe/Ni current collector and nickel foam electrodes before and after 2000 potential cycles for OER and HER regions.	57
Figure 3.14	Tafel plots of Fe/Ni mesh and Ni foil electrodes before and after 2000 CV cycles (a) OER, (b) HER.	58
Figure 3.15	Current density V sweep rate from data obtained from cyclic voltammetric experiments recorded at different sweep rates for NMC 622-NF and NMC 811-NF electrodes in 1 M KOH after repetitive cucling for 2000 cycles.	59

### Chapter 4

Figure 4.1	Cross sectional SEM image and EDS map showing the distribution of Fe and Ni in the FNC electrode.	65
Figure 4.2	Cyclic voltammograms recorded at 100 mV sec <sup>-1</sup> for 20 cycles at (a) FNC and (b) NF electrodes in 1 M KOH.	66
Figure 4.3	(a) CVs recoded at 100 mV s <sup>-1</sup> for 2000 cycles in 1 M KOH in the OER region for the FNC electrode and (b) LSVs recorded at FNC and NF electrodes before and after 2000 potential cycles, (c) Tafel plots of FNC and NF electrodes before and after 2000 CV cycles and (d) Chronoamperometric curves recorded for 24 hr period at 1.75V in the OER region.	67
Figure 4.4	(a) CVs recoded at 100 mV s <sup>-1</sup> for 2000 cycles in 1 M KOH in the HER region for the FNC electrode and (b) LSVs recorded at FNC and NF electrodes before and after 2000 potential cycles, (c) Tafel	68

	plots of FNC and NF electrodes before and after 2000 CV cycles and (d) Chronoamperometric curves recorded for 24 hr period at -0.40 V in the HER region.	
Figure 4.5	SEM image and EDS mapping of the as received FNC.	70
Figure 4.6	SEM images and EDS mapping of the FNC electrode after 2000 cycles in the OER potential region (1.05 to 1.9 V, in 1 M KOH).	70
Figure 4.7	SEM images and EDS mapping of the FNC electrode after 2000 cycles in the HER potential region (1.05 to -0.50 V, in 1 M KOH).	71
Figure 4.8	XPS spectra of Ni 2p, Fe 2p and O 1s where the spectrum (lower) is recovered FNC and spectrum (upper) is the FNC electrode after 2000 cycles in the OER region.	72
Figure 4.9	Dynamic stability test for a two-electrode system using a FNC anode and cathode, operated at 1.9 V for 2 h followed by shutdown for 10 min which was repeated for a 24 h period.	73
Figure 4 S1	Digital image of recovered FNC electrode from battery module.	149
Figure S2	EDX spectra of NFC electrode (a) recovered from battery, (b) after 2000 cycles of OER and (c) after 2000 cycles of HER.	149
<b>Chapter 5</b>		
Figure 5.1	Cyclic voltammograms recorded at 100 mV sec <sup>-1</sup> for 20 cycles at (a) (a) NMC 622-NF, (b) NMC 811-NF and (c) NF electrodes in 1 M KOH.	88
Figure 5.2	LSVs recorded at 0.1 mV s <sup>-1</sup> at NMC 811-NF, NMC 622-NF and commercial NF electrodes in 1 M KOH.	89
Figure 5.3	LSVs recorded at 0.1 mV s <sup>-1</sup> at NMC 622-NF and NMC 811-NF before and after potential cycling (2000 cycles, 1.0 to 1.9 V) in 1 M KOH. Tafel plots obtained for NMC 622 and NMC 811 from the respective LSV data.	90
Figure 5.4	Chronoamperometric experiments conducted at 1.7 V for 24 h in 1 M KOH for NF substrate, NMC 622-NF and NMC 811-NF electrodes both before (blue) and after (red) repetitive potential cycling.	91
Figure 5.5	SEM image and EDS mapping (Ni, Mn, Co and O elements) of NMC 622-NF after repetitive potential cycling (2000 cycles, 1.0 to 1.9 V in 1 M KOH).	93
Figure 5.6	SEM image and EDS mapping (Ni, Mn, Co and O elements) of NMC 811-NF after repetitive potential cycling (2000 cycles, 1.0 to 1.9 V in 1 M KOH).	93
Figure 5.7	EDS mapping of NMC 811 before (upper) and after (lower) potential cycling.	94
Figure 5.8	EDS mapping of NMC 622 before (upper) and after (lower) potential cycling.	94
Figure 5.9	XPS spectra for Ni 2p, Mn 2p, Co 2p and O 1s for NMC 622-NF and NMC 811-NF electrodes before (a) and after (b) 2000 potential cycles (1.0 to 1.9 V at 100 mV s <sup>-1</sup> in 1 M KOH).	96
Figure 5 S1	SEM image and EDS mapping (Ni, Mn, Co and O elements) of NMC 622.	153
Figure 5 S2	EDS mapping (Ni, Mn, Co and O elements) of NMC 811 before cycling	154
Figure 5 S3	TEM images, SAED pattern and XRD pattern of NMC 622	155
Figure 5 S4	TEM images, SAED pattern and XRD pattern of NMC 811	155
Figure 5 S5	Cyclic voltammograms recorded for NMC 622-NF and NMC 811- NF at 100 mVsec <sup>-1</sup> for 2000 cycles.	155

Figure 5 S6	Current density V sweep rate from data obtained from cyclic voltammetric experiments recorded at different sweep rates for NMC 622-NF and NMC 811-NF electrodes in 1 M KOH after repetitive cycling for 2000 cycles.	156
Figure 5 S7	TEM images of NMC 622 after cycling	156
Figure 5 S8	TEM images of NMC 811 after cycling	156
<b>Chapter 6</b>		
Figure 6.1	LSVs recorded at 0.1 mV s <sup>-1</sup> for all the battery cycled electrodes between 1.0 to 1.9 V in 1 M KOH.	108
Figure 6.2	Cyclic voltammograms recorded for various cycled electrodes at 100 mVsec <sup>-1</sup> for 2000 cycles.	109
Figure 6.3	Chronoamperometric experiments conducted at 1.7 V for 24 h in 1 M KOH various electrodes before repetitive potential cycling.	110
Figure 6.4	SEM images of pristine unprocessed UP (NMC-622) sample.	111
Figure 6.5	SEM images of pristine SP23-2 (NMC 622) and after 150x lifetime cycles.	111
Figure 6.6	XPS spectra for Ni 2p and Co 2p for UP (NMC-622)) before and after 2000 OER cycles (1.0 to 1.9 V at 100 mV s <sup>-1</sup> in 1 M KOH) and SP23-2 (NMC 622) electrodes before 2000 OER cycles.	112
Figure 6.7	XPS spectra for Mn 2p and O1s for UP (NMC-622)) before and after 2000 OER cycles (1.0 to 1.9 V at 100 mV s <sup>-1</sup> in 1 M KOH) and SP23-2 (NMC 622) electrodes before 2000 OER cycles.	113
<b>Chapter 7</b>		
Figure 7.1	LSVs recorded at 0.1 mV s <sup>-1</sup> at (a, b) NF substrate, NF-FP, NF-LFP (Powder), NF-LFP, NF-LFP(CV5), NF-LFP(CV100) and (c) Tafel plots obtained for NF-LFP(CV5), NF-LFP(CV100), NF-LFP electrodes before cycling d) Chronoamperometric experiments conducted at 1.7 V for 24 h in 1 M KOH for NF substrate, NF-LFP(CV5), NF-LFP(CV100).	124
Figure 7.2	(a) Cyclic voltammograms recorded at 100 mV sec <sup>-1</sup> for NF, NF-LFP(CV5), NF-LFP(CV100), NF-LFP electrodes in 1 M KOH for 2000 cycle at 1.0 to 1.9 V, (b) Tafel plots obtained for NF-LFP(CV5), NF-LFP(CV100), NF-LFP electrodes after cycling and (c) Chronoamperometric experiments conducted at 1.7 V for 24 h in 1 M KOH for NF substrate, NF-LFP(CV5), NF-LFP(CV100), NF-LFP electrodes after repetitive OER potential cycling.	125
Figure 7.3	(a) SEM images of pristine LFP, LFP(CV5) and LFP(CV100) electrodes, and (b) EDS map of NF-LFP(CV100).	127
Figure 7.4	TEM images of (a, c) NF-LFP(CV5) and (b, d) NF-LFP(CV100) after 2000 OER cycles.	128
Figure 7.5	TEM-EDS mapping of (a) LFP(CV5) particles before the OER and (b) after 2000 OER cycles.	130
Figure 7.6	Ni 2p core level spectra for NF-LFP, LFP(CV5) and LFP(CV100) samples removed from the NF support after the OER.	130
Figure 7.7	Fe 2p core level spectra for NF-LFP, LFP(CV5) and LFP(CV100) samples removed from the NF support both before and after the OER.	131
Figure 7.8	P 1s core level spectra for NF-LFP, LFP(CV5) and LFP(CV100) samples removed from the NF support both before and after the OER.	132

Figure 7.9	O 1s core level spectra for NF-LFP, LFP(CV5) and LFP(CV100) samples removed from the NF support both before and after the OER.	133
Figure 7 S1	Current density Vs sweep rate from data obtained from cyclic voltammetric experiments recorded at different sweep rates for NF-LFP(CV5), NF-LFP(CV100), NF-LFP in 1 M KOH before after repetitive cycling	158
Figure 7 S2	Cyclic voltammograms recorded at 100 mV sec <sup>-1</sup> for NF and NF-LFP for 2000 cycles, 1.0 to 1.9 V) in 1 M KOH.	159
Figure 7 S3	TEM images of pristine LFP particles	159
Figure 7 S4	TEM images of LFP CV5 particles	160
Figure 7 S5	TEM images of LFP CV100 particles	160
Figure 7 S6	Li 1s core level spectra for LFP, LFP(CV5) and LFP(CV100) samples removed from the NF support both before and after the OER.	161

---

## List of Tables

<b>Chapter 2</b>		
Table 2.1	Various NMC type catalyst materials used for the OER identifying the catalyst substrate, overpotential required to pass $10 \text{ mA cm}^{-2}$ ( $\eta_{10}$ ) and onset values.	34
Table 2.2	Properties of various electrocatalysts .	37
<b>Chapter 3</b>		
Table 3.1	Preparation of the INK.	49
<b>Chapter 4</b>		
Table 4 S1	Properties of various electrocatalysts.	149
<b>Chapter 5</b>		
Table 5 S1	Various NMC type catalyst materials used for the OER identifying the catalyst substrate, overpotential required to pass $10 \text{ mA cm}^{-2}$ ( $\eta_{10}$ ) and onset values.	152
<b>Chapter 6</b>		
Table 6.1	Cell components and performance summary.	109
<b>Chapter 7</b>		
Table 7.1	Electrochemical data for LFP materials used in this study.	126

## List of Publications

### Peer reviewed articles included in this thesis

---

#### **Chapter 4:**

Arshdeep Kaur, Monireh Khosravi and Anthony P. O'Mullane, "Repurposing the current collector of a car battery module into a bifunctional electrode for overall electrochemical water splitting", Sustainable Energy & Fuels, 2486-2494, 2023.  
<https://doi.org/10.1039/D3SE00232B>.

#### **Chapter 5:**

Arshdeep Kaur, Jose Alarco and Anthony P. O'Mullane, "Investigating the potential use of Ni-Mn-Co (NMC) battery materials as electrocatalysts for electrochemical water splitting", ChemPhyChem, 1-8, 2024.

<https://doi.org/10.1002/cphc.202400124>.

#### **Chapter 6:**

Arshdeep Kaur, Jessica Crawford, Michael Horn, Anthony O'Mullane, "Recovering spent Lithium Nickel Manganese Cobalt (NMC) oxide cathodes from Li ion batteries for use as oxygen evolution reaction electrocatalysts", Electrochemistry Communications. (Submitted)

#### **Chapter 7:**

Arshdeep Kaur, Hongxia Wang, Umair Gulzar, Colm O'Dwyer and Anthony P. O'Mullane, "Using Recovered Lithium Iron Phosphate Battery Material as an Electrocatalyst for the Oxygen Evolution Reaction", CleanMat, 1-13, 2025.  
[doi.org/10.1002/clem.70005](https://doi.org/10.1002/clem.70005)

---

# Acknowledgements

First and foremost, praises and thanks to the Almighty, for endless blessings to complete the research successfully.

I would like to express my deepest gratitude to my principal supervisor, Professor Anthony O'Mullane, for giving me the opportunity to work in this research. I am thankful for his invaluable guidance, unwavering support, and insightful advice throughout this research. His deep expertise, critical feedback, and encouragement have played a crucial role in shaping this work. His leadership and vision in the field of electrochemistry have been a great source of inspiration, and it has been an absolute privilege to work under his supervision. I would like to thank Professor Jose Alarco and Professor Hongxia Wang as my associate supervisors to provide unconditional support during my research.

I am grateful for School of Chemistry and Physics, Faculty of Science, QUT for providing the resources and facilities that enabled me to pursue my Ph.D. degree. I sincerely appreciate the support of the Central Analytical Research Facility (CARF) at QUT, for training, facilities and technical help that played a crucial role in carrying out the experimental work. The research funding support from Australian Research Council (DP180102869 IH90100009) and scholarship support through QUT/Max Planck Institute of Colloids and Interfaces Joint Laboratory on Nanocatalysis for sustainable chemistry.

A special thanks to Monireh Khosravi for introducing me to the research topics and for assisting in setting up the initial experiments and setup. I am especially grateful to Sagar Dhananjay Jadhav for his unconditional help and constant support throughout the research journey. I would also like to extend my heartfelt thanks to my dear friends, Thi Hong Nga Ngo, Rusha Kamar, Hanisha Ponnuru, Maheshika Udunuwarage and Kinley Dorji for their encouragement, motivation, and unwavering belief in me, your support has been a source of strength during this research.

I am grateful my parents my father Dr. Darshan Singh, my mother Mrs. Ashadeep Kaur and my in-law parents Mr. Karmjeet Singh and Mrs. Rajinder Kaur for their endless love, patience, and encouragement. My brother Mr. Sandeep Singh and Bhabhi Dr. Harpreet Kaur, there love, and support have been my greatest blessing. A very special thanks to my husband, Sardar Ramanjeet Singh, for being there all the time, backing me up and believing in me. Words are less to express my gratitude for him. Thank you.

# Chapter 1

## Introduction

### 1.1 Background

Due to rapid growth in worldwide population and economic development, global energy demand has increased exponentially<sup>1, 2, 3</sup>. Currently, the World's economy is largely dependent on fossil fuels like coal, oil and gas which is responsible for generating greenhouse gas emissions like carbon dioxide causing environmental problems<sup>4, 6</sup> (Figure 1.1). Therefore, a significant amount of research is focused on renewable energy resources that could effectively replace fossil fuels. Hydrogen based energy is regarded as one of the most efficient sources that is capable of alleviating our fossil fuel dependency<sup>6</sup>. Consequently, hydrogen production from electrochemical water splitting has attracted a lot of attention as it is a zero-pollution technology if powered by renewables. Thus, this is one of the promising solutions to convert excess electrical energy (from renewable sources) into green hydrogen<sup>7, 8, 9</sup>. Among the various hydrogen production methods, electrochemical water splitting is expected to play a vital role<sup>10</sup>.

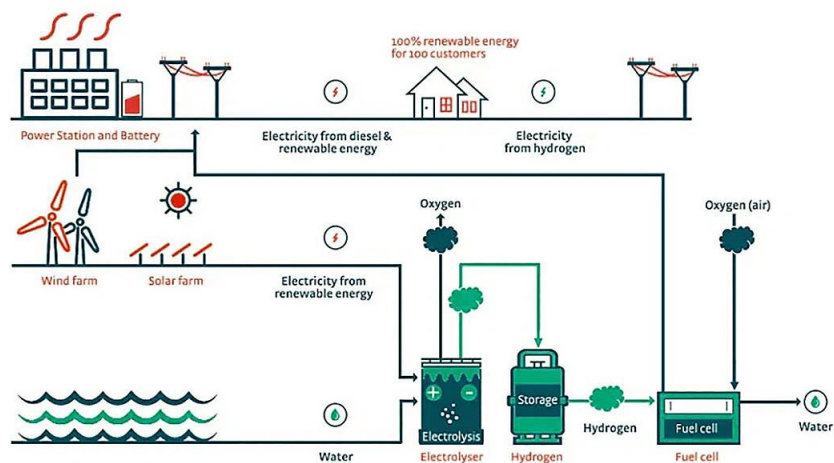


**Figure 1.1:** A Hydrogen Electrolyser project, Energy Industry Review, 2025<sup>8</sup>.

<https://energyindustryreview.com/wp-content/uploads/2021/05/Europe-at-the-Top-of-Hydrogen-Electrolyser-Projects.jpg>.

Figure 1 shows the concept of an electrolyser plant that consists of water as prime component feed and electricity generated by renewable energy sources like wind and solar to be used for water splitting process producing hydrogen. The hydrogen gas is further used by fuel cells in a power station for the generation of electricity<sup>11</sup>.

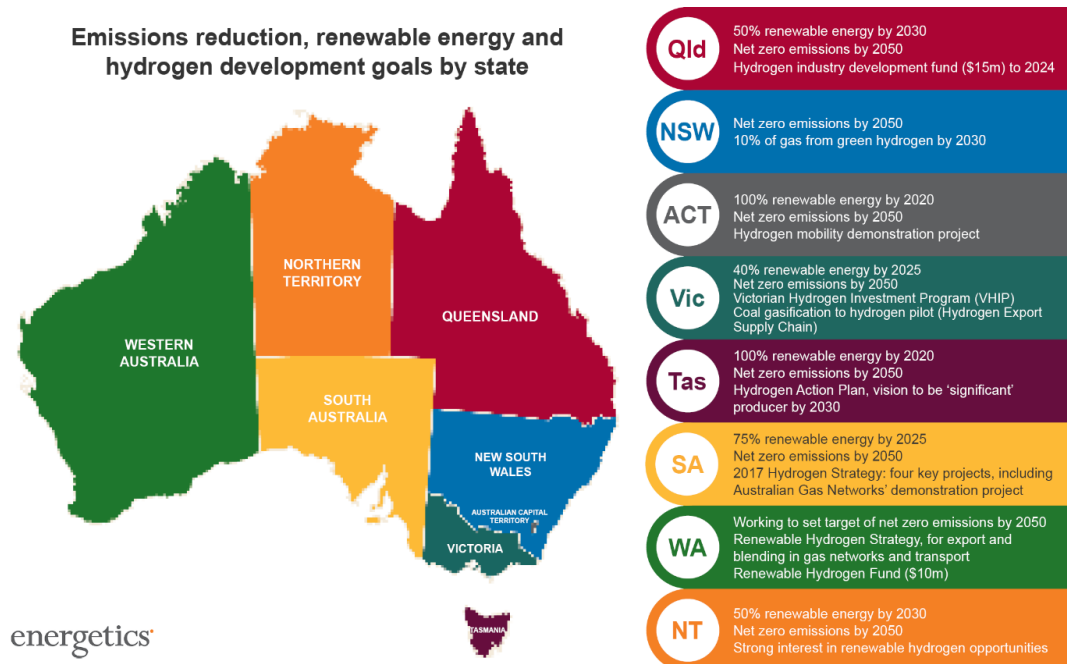


**Figure 1.2:** Various future hydrogen development goals in Australia<sup>9</sup>.

<https://www.energetics.com.au/media/2071/australia-climate-and-hydrogen-targets-by-state-v03.png>

Australia's National Hydrogen Strategy, launched in November 2019 gives clear pathway to position the country as a leader in the global hydrogen market by 2030 as described in Figure 1.2. The initial phase included Foundations and Demonstrations (up to 2025) and emphasizes building essential infrastructure, supporting pilot projects, advancing hydrogen technologies, and creating regulatory and market frameworks.

Then the focus shifts to scaling hydrogen production, improving supply chain efficiency, growing a domestic market, and establishing Australia as a leading hydrogen exporter. Through these stages, the government aims to leverage Australia's renewable energy resources to become a key player in the global hydrogen economy<sup>12</sup>. There are many methods to produce hydrogen like (A) Water gas shift reaction, (B) Thermochemical, (C) Electrochemical, and (D) Photochemical. However, considering the CO<sub>2</sub> gas emissions in the atmosphere,

electrochemical water splitting process stands out to be the best route to produce green hydrogen but requires the right catalyst for best performance <sup>13, 14, 15</sup>.

## 1.2 Batteries

Batteries are categorized into two main types:

1. Primary Batteries (single-use/disposable): Examples include AA, AAA and alkaline batteries as presented in Figure 1.3.
2. Secondary Batteries (rechargeable): Examples include lithium-ion batteries (LIBs), lead-acid batteries (LABs), and nickel-metal hydride (NiMH) batteries

Further classifications are based on application types like (a) Consumer batteries (used in portable electronics), (b) Stationary batteries (used in energy storage systems), (c) Industrial batteries (used in heavy-duty or specialized applications). Additionally, on a commercial basis batteries are also grouped by their chemical composition, like Alkaline batteries, Mercury batteries, Lead-acid batteries (LABs), Nickel-based batteries and Lithium-based batteries. In 2016, nickel-based, lithium-based, and lead-acid batteries collectively accounted for 94.8% of the global battery market <sup>16, 17</sup>.

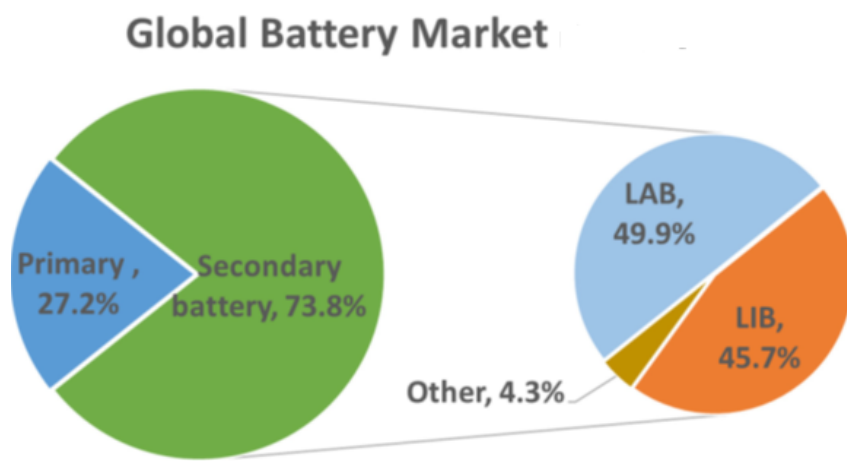


**Figure 1.3:** Global Battery Market, open access with licence CC-BY-NC-ND<sup>14</sup>.

The global battery market is projected to grow at an annual rate of 25%, reaching 2,600 GWh by 2030 as shown in Figure 1.4. This significant growth is primarily driven by the electrification of transportation and the integration of batteries into electricity grids <sup>17, 18</sup>.

As illustrated in Figure 1.4, the global battery market demand is broken down by application, showing the percentage contributions from 2018 to 2030. The most substantial growth is expected in electric mobility, with energy demand rising sharply from 142 GWh in 2018 to 2,333 GWh by 2030. This increase is largely attributed to electric vehicles (EVs), with passenger cars accounting for 60% of the total demand, while commercial vehicles make up the remaining 40%<sup>17,19</sup>.

### 1.3 Battery waste

Lithium-ion batteries (LIBs) used in electric vehicles (EVs) and energy storage systems generally have a lifespan of 5 to 15 years<sup>20</sup>. In 2020, most LIB waste in Australia originated from consumer electronics, such as mobile phones, tablets, and handheld power tools. Projections based on anticipated EV adoption rates indicate that Australia could generate between 137,000 and 180,000 tonnes of LIB waste annually by 2036<sup>21</sup>.

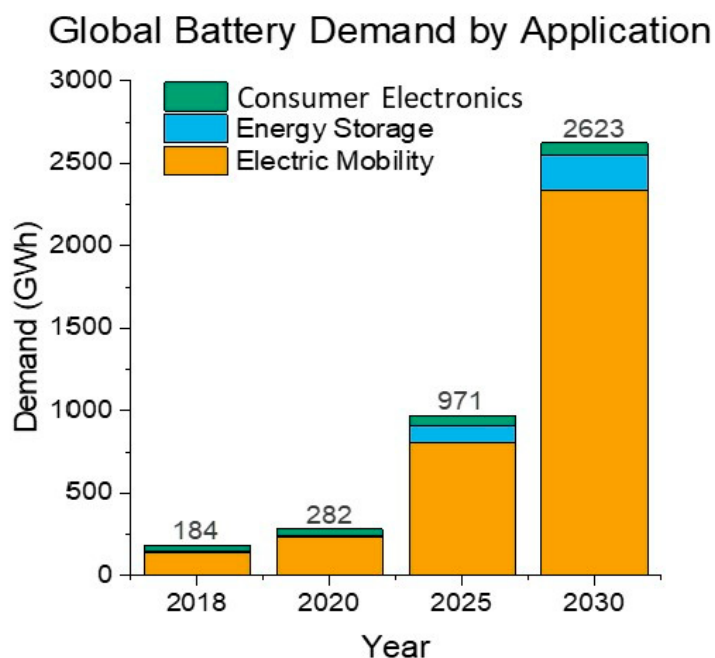


**Figure 1.4:** Global Battery Demand by Application, open access with licence CC-BY-NC-ND<sup>14</sup>.

In comparison, Europe has achieved a LIB collection rate of approximately 50%, highlighting the significant gap in Australia's recycling efforts. Additionally, offshore recycling of lithium-ion batteries (LIBs) in Australia results in a significant loss of valuable battery metals and materials. This lost value is estimated to range between AUD 4,400 and 17,200 per tonne of

batteries, amounting to a total economic loss of AUD 603 million to 3.1 billion. These losses are attributed to poor LIB collection rates, reliance on offshore recycling, and the landfilling of LIB waste<sup>22</sup>. Figure 1.5 provides a representation of large car battery pack and high-capacity cells required for EV's.

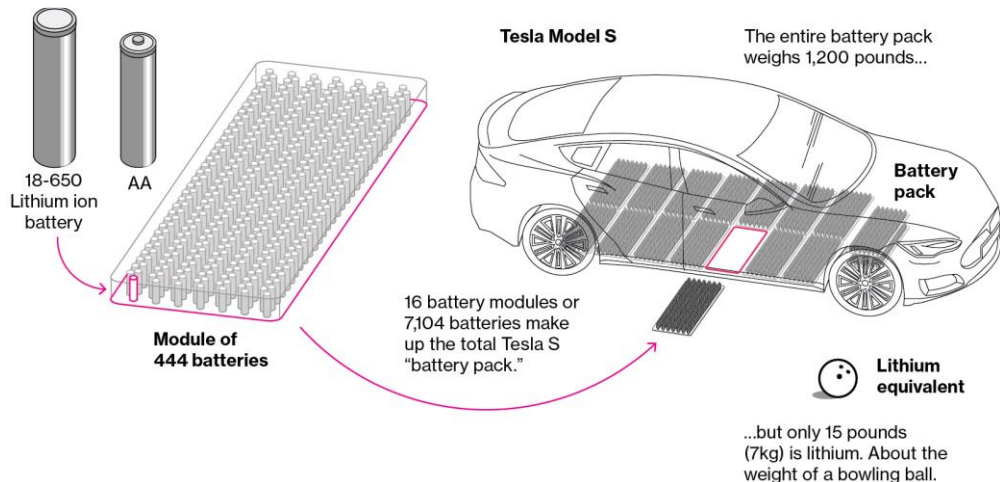


**Figure 1.5:** Representation of the arrangement of small cylindrical lithium-ion battery (LIB) cells within a large car battery pack and high-capacity cells required for EVs, open access with licence CC-BY-NC-ND<sup>20</sup>.

Developing onshore technology, capabilities, and infrastructure to process LIB waste aligns with Australia's shift towards circular economy principles and policies. Enhanced resource recovery not only minimizes waste but also provides an opportunity to establish domestic industries for battery material processing and system development, encouraging economic growth and sustainability<sup>23</sup>.

Electronic appliances contribute significantly to landfill waste, introducing toxic chemicals into the soil and water bodies, which indirectly contaminates plants and animals. Marine species are particularly vulnerable to pollution from e-waste, experiencing higher levels compared to other organisms (Freitas et al., 2020). For example, incidents such as methylmercury poisoning in Japan that caused Minamata disease, demonstrate the severe consequences of such contamination<sup>24, 25</sup>.

The toxic chemicals and elements from e-waste erosion not only pollute the environment but may also cause unfortunate health crises. The pathways of contamination and their effects on plant and animal physiology are increasingly studied by interdisciplinary researchers. Many

diseases caused by pollutants are linked to the generation of reactive oxygen and nitrogen species, as well as toxic elements that interact with biological entities such as DNA<sup>26</sup>, kidney tissue<sup>27</sup>, liver tissue<sup>28</sup>, and neurons<sup>29</sup>, leading to degeneration and dysfunction<sup>13</sup>.

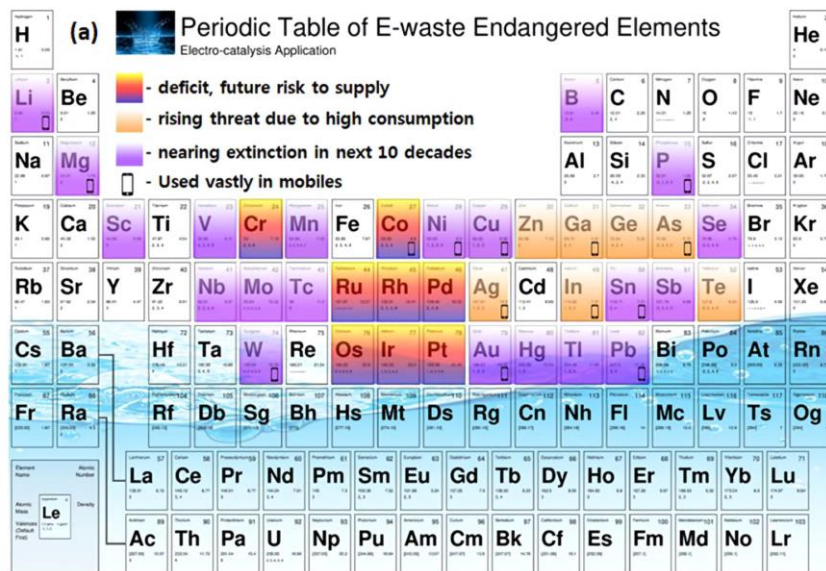


**Figure 1.6:** Periodic table of endangered elements released by IUPAC (Reused With Permission Copyright © 2021 Elsevier Inc)<sup>10</sup>.

Figure 1.6 presents the periodic table released by the International Union of Pure and Applied Chemistry (IUPAC) highlighting the elements that are either a rising threat due to high use or are near to depletion.

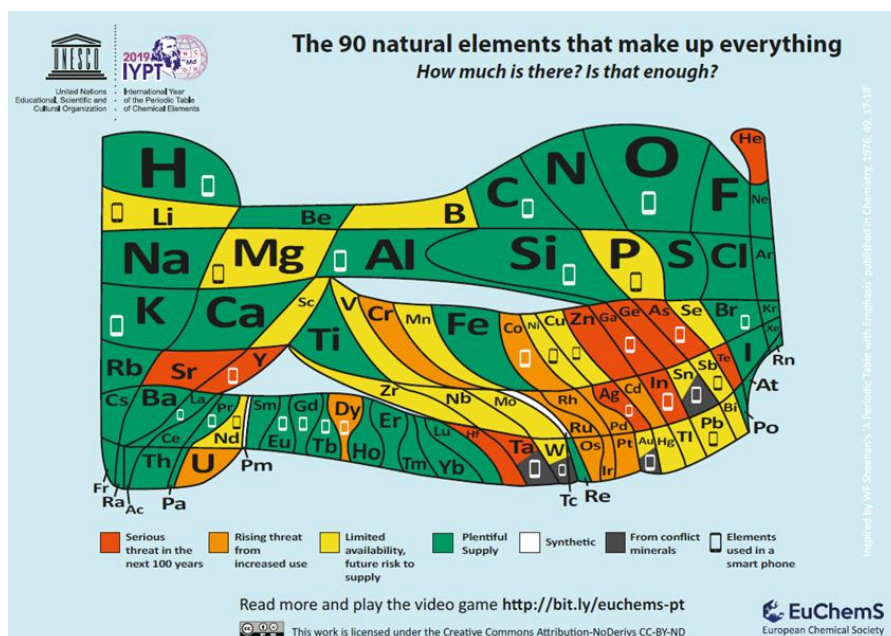


**Figure 1.7 (a):** Periodic Table produced by the European Chemical Society (EuChemS) to highlight element availability and vulnerability, open access with licence CC-BY-NC-ND<sup>28</sup>.

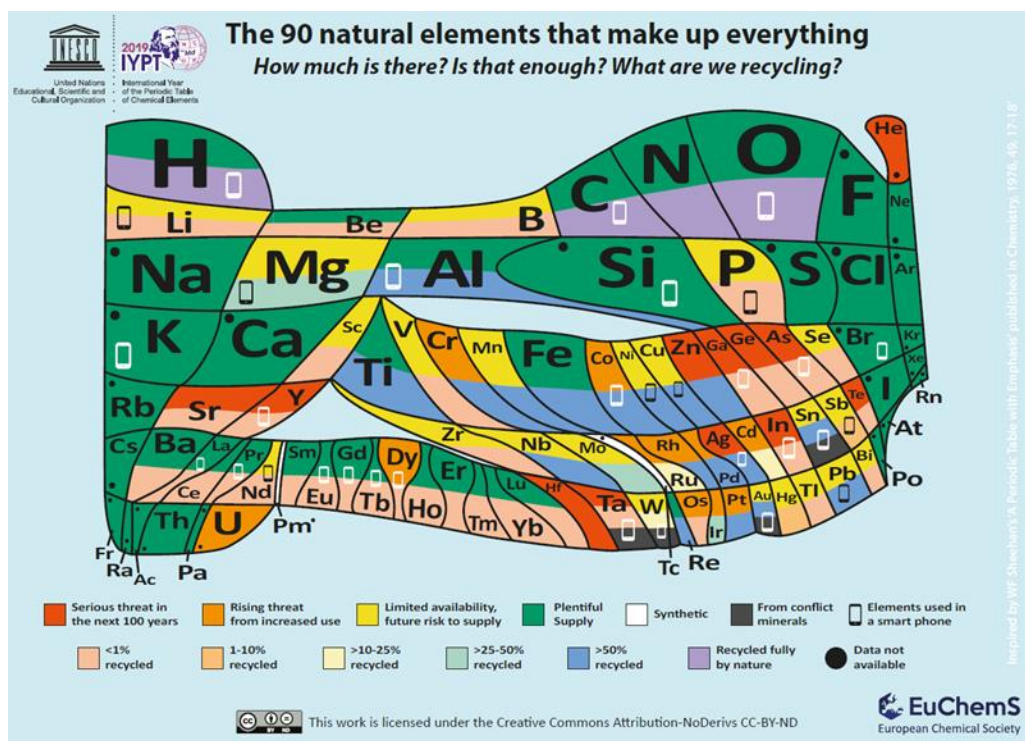


**Figure 17 (b):** Modification of the (EuChemS) Periodic Table to include the extent to which element is recycled, open access with licence CC-BY-NC-ND<sup>28</sup>.

Some elements like Fe and Mo are excessively used in electronic industry but also have excellent catalytic activity for water splitting reactions and are regarded as endangered elements by IUPAC. Elements like Ga, Zn, As, In, Ag, Co and Cr are considered for total extinction in 100 years. Also, elements like Li, Mn, Mg, Cu and Ni have limited availability and are close to extinction<sup>13</sup>.

A similar periodic table was shared by the European Chemical Society (Figure 1.7a) that presents elements of vulnerability with various colour codes. Elements in red are in serious threat in the coming 100 years while elements in green are plentiful. There are 31 elements with the symbol of mobile that represents the use of elements in mobile phones. There is another periodic table (Figure 1.7b), that represents the elements that are recovered from waste and directed to be reused<sup>30</sup>. These elements can be recovered from the electronic waste and can be reused and repurposed.

Therefore, certain elements are being heavily utilized by the electronics industry. To ensure sustainability, it is essential to recover and reuse these elements. The term "endangered

"element" in this context refers to the increasing disorder in our environment caused by the irreversible mixing of these elements with soil and water, rather than their extinction from the planet.

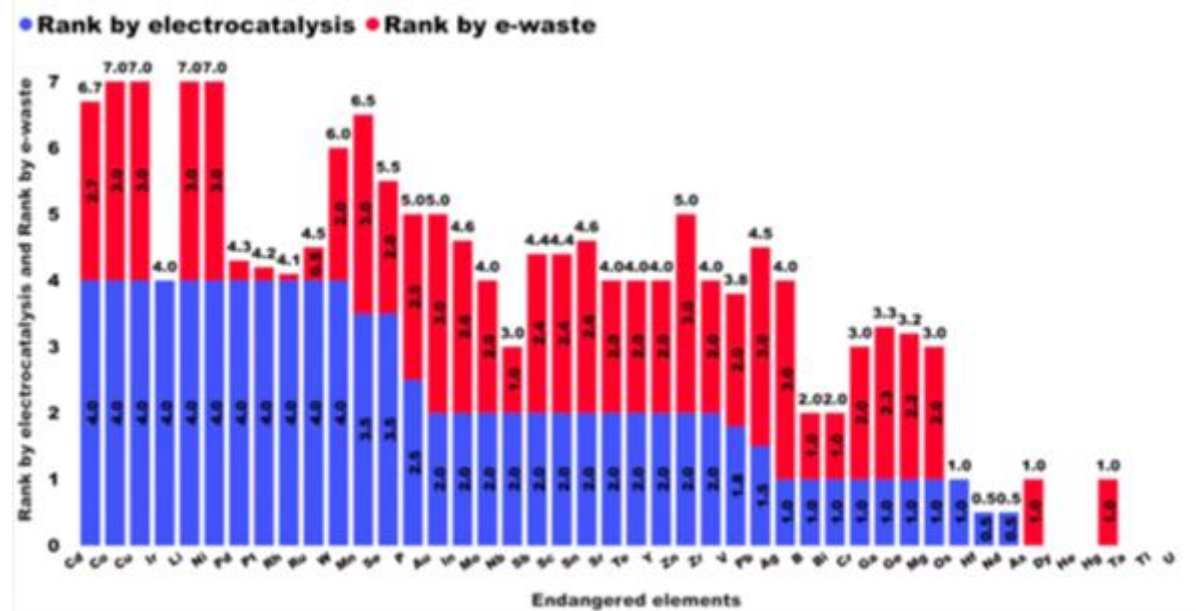


**Figure 1.8:** Bar chart of the ranking of endangered elements blue-electrocatalytic performance and red-amount of elements in electronic devices. (Reused With Permission Copyright © 2021 Elsevier Inc)<sup>10</sup>.

Additionally, Figure 1.8 shows the accumulation of e-waste and the electrocatalytic properties of these elements based on previous publications from the last five years (ranked from 1 to 4, with higher ranks indicates greater use as electrocatalysis or presence in electronic devices). These predictions highlight the urgent need to address the potential depletion of the elements. These elements have potential for the use of e-waste in energy conversion processes, particularly in water-splitting electrocatalysis for hydrogen generation<sup>13, 31</sup>.

#### 1.4 Components of battery waste

A typical battery consists of an anode, cathode, aluminium, carbon black and binder, separator plastics, electrolyte solution and copper as shown in Figure 1.9.

Accordingly, the component with the highest percentage of battery waste is the cathode (31%) and has the highest tendency to be used as water splitting catalysts. The popular lithium-ion battery technologies cathode materials mostly consist of Nickel manganese Cobalt (NMC), Nickel Cobalt Aluminium (NCA), Cobalt Oxide, Lithium Iron Phosphate (LFP) and Lithium Manganese Oxide (LMO)<sup>32</sup>.

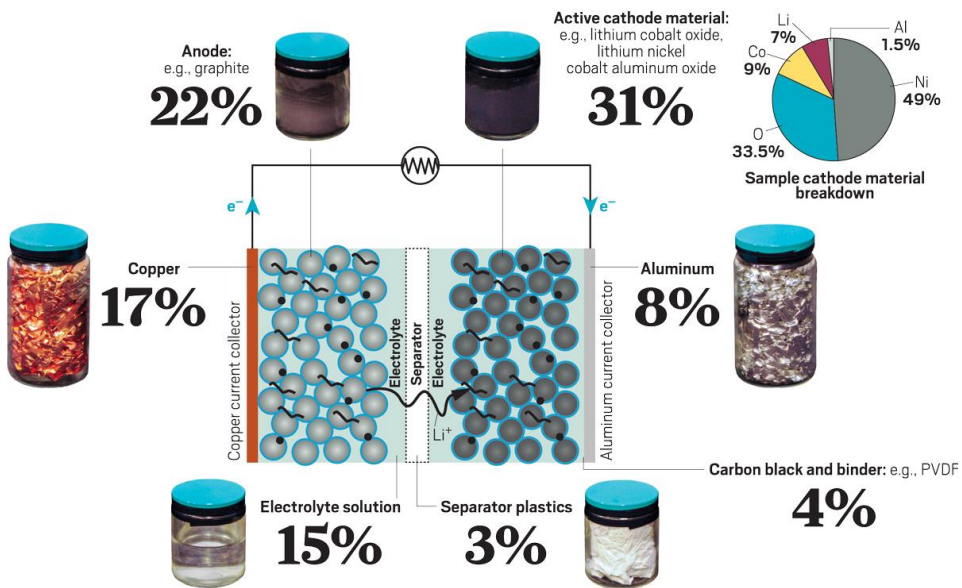


**Figure 1.9:** Typical material composition for LIBs, open access with licence CC-BY-NC-ND<sup>20</sup>.

In general water splitting reactions are divided into two half-cell reactions which are the oxygen evolution reaction (OER) and the hydrogen evolution reaction (HER). The HER occurs at the cathode and is responsible to release hydrogen and the OER occurs at anode, leading to the formation of oxygen. The major aspect that adds to the limitation of this technology is slow and poor kinetics of these two reactions, in particular for the OER. Thus, this generates the need for proficient electrocatalysts that are capable in reducing the kinetic barriers towards the production of hydrogen and oxygen<sup>33</sup>. The Aster plot in Figure 1.10, shows various endangered elements that are mentioned by IUPAC and the European Chemical Society that can repurposed for water splitting reactions.

The noble based metal electrocatalysts for the HER and OER are platinum group metals (Pt, Pd, Ir, Ru and Rh) and rank highest<sup>34, 35</sup> however, due to cost factors, other alternatives are considered. Therefore, various research groups have conducted studies on developing non-noble metal catalysts for the OER based on transition metals and their oxides/hydroxides and for the HER like metal-based carbides<sup>36</sup>, transition metal phosphides<sup>37</sup> and transition metals.

Additionally, in recent studies few non-noble metals are also being recognized as endangered elements by the International Union of Pure and Applied Chemistry (IUPAC). Furthermore, the Australian standard for electronic waste (AS/NSZ 5377:2013) recycling does not acknowledge disposal of waste batteries to landfill,<sup>38, 2</sup> thus, around 8000 tonnes of batteries end up in landfill in Australia each year, these batteries pollute land and environment as chemicals present in the batteries leach, threatening human health and the environment<sup>30, 39, 40</sup>.



**Figure 1.10:** Aster plot of endangered element species and their possible water splitting electrocatalyst applications, (Reused With Permission Copyright © 2021 Elsevier Inc)<sup>10</sup>.

Thus, it is becoming crucial to develop a sustainable solution to recover valuable materials from waste sources and transform them into value added materials. Rather than synthesizing the electrocatalyst, electronic waste from batteries like Lithium ion or Nickel Metal hydride (NiMH) can also be used as a source of electrocatalytic materials for water splitting reactions.

## 1.5 Context

The research presented in the thesis focuses on elucidating the potential of transition metals present in battery waste and repurposing it into water splitting electrocatalysts. Waste from various Lithium-ion batteries like Nickel Metal Hydride (NiMH), Lithium Iron Phosphate (LFP) and Nickel Manganese Cobalt (NMC) have essential elements like Ni, Fe, Co, Mn, and P that can be used as water splitting electrocatalysts. They are also termed as harmful heavy metals and pollute soil and water. Thus, apart from the fact that these elements have excellent electrochemical properties, the research would propose to reuse them to synthesise efficient

OER, HER or bifunctional electrocatalysts for water splitting reactions. Thus, the thesis is in the context of a circular economy of reuse, recycle and repurpose.

## **1.6 Purpose**

The major aim of this thesis is to perform electrochemical studies on potential wastes collected from Lithium-ion batteries in-particular cathode materials and evaluate their electrochemical properties.

The main objectives of this thesis are:

1. To carry out electrochemical studies on Ni-Fe mesh current collectors for the HER and OER from a NiMH battery waste as a prominent material for water splitting.
2. To carry out electrochemical studies on NMC from spent battery wastes for the OER in water splitting reactions. Varying the composite with respect to the ratio, for example NMC 811 & NMC 622 and performing comparative studies.
3. To carry electrochemical studies on recycled battery waste materials containing LFP electrodes.
4. Determine if battery history impacts on the subsequent electrocatalytic performance for water splitting reactions.

## **1.7 Significance**

It is being observed that electrocatalysts holds extensive potential to lower the kinetic barrier of water splitting reactions. A lot of work is being reported on various electrocatalysts for both the OER and HER in water splitting reactions. It is also envisaged that noble metal based electrocatalysts like Pt, Ru and Ir are not suitable to be used for long term commercial electrolyser applications, due to increasing costs and scarcity. Therefore, research is diverted either towards alloying noble metal based electrocatalyst or working on non-noble metal based electrocatalysts for a variety of applications such as alkaline water splitting for green hydrogen production.

## **1.8 Thesis Outline**

There are 7 chapter in this thesis.

### **Chapter 1: Introduction**

The chapter contains the background of the research, objectives and its significance.

## **Chapter 2: Literature Review**

The chapter presents basic knowledge about water electrolysis, electrocatalysts performance parameters, HER, OER and bifunctional electrocatalysts, electrocatalysts based on transition metals and electrocatalysts that have been derived from battery waste.

## **Chapter 3: Research Design**

The chapter consists of materials and methods to prepare the electrodes for testing, various electrochemical techniques to evaluate electrochemical behaviour of the electrodes, and all the characterisation techniques to analyse the chemical and structural properties of the electrodes.

## **Chapter 4: Repurposing the current collector of a car battery module into a bifunctional electrode for overall electrochemical water splitting.**

This chapter explores the possibility of repurposing the current collector from a Toyota Prius battery module as a bifunctional electrocatalyst that can be used for overall electrochemical water splitting under alkaline conditions. The Ni coated iron electrode was found to have ideal properties for both the oxygen evolution reaction (OER) and hydrogen evolution reaction (HER) while also demonstrating bifunctional behaviour for both reactions upon repetitive cycling. The repurposed material also outperformed a Ni electrode of comparable surface area for both the OER and HER. Overpotential values of 250 mV (OER) and 260 mV (HER) and low Tafel slope values of 83 mV dec<sup>-1</sup> (OER) and 101 mV dec<sup>-1</sup> (HER) indicated good electrochemical activity comparable to chemically synthesised catalysts. The key aspect for enabling this behaviour was found to be the emergence of iron into the nickel layer to create a stable mixed FeNi oxide layer upon potential cycling of the electrode. This work indicates that not only the active materials used in rechargeable batteries should be used for recycling but that the current collectors should also be considered as potentially highly valuable components.

## **Chapter 5**

## **Investigating the potential use of Ni-Mn-Co (NMC) battery materials as electrocatalysts for electrochemical water splitting.**

This chapter investigates the underexplored area of employing cathode materials such as nickel, manganese cobalt (NMC) oxide as an electrocatalyst for water splitting reactions. In this work I explore the possibility of using NMC materials of different metallic ratios (NMC 622 and 811) as oxygen evolution and hydrogen evolution catalysts under alkaline conditions. I show

that both materials are excellent oxygen evolution reaction (OER) electrocatalysts but perform poorly for the hydrogen evolution reaction. NMC 622 demonstrates the better OER activity with an overpotential of only 280 mV to pass 100 mA cm<sup>-2</sup> and a low Tafel slope of 42 mV dec<sup>-1</sup>. The material can also pass high current densities of 150 mA cm<sup>-2</sup> for 24 h while also being tolerant to extensive potential cycling indicating suitability for direct integration with renewable energy inputs. This work demonstrates that NMC cathode materials if recovered from Li ion batteries are suitable OER electrocatalysts.

Additionally, this work was also continued to observe the electrocatalytic performance of the materials obtained from actual Li-ion used batteries. Various samples with 50, 150 and 200 lifetime cycles were compared against the unprocessed sample. It was observed that as the cycling increased the OER performance decreased.

### **Chapter 6: Recovering spent NMC battery materials for use as electrocatalysts**

Here, in this chapter recovered NMC from used batteries is observed and how this would impact the performance and whether it would be comparable to the pristine NMC materials used in the previous chapter.

### **Chapter 7: Reusing LFP battery cathode materials for water splitting reactions.**

In the present chapter use of Lithium iron phosphate (LiFePO<sub>4</sub>) cathode materials from waste LIB's is conducted and explored as an oxygen evolution electrocatalysts with Nickel foam (NF) as substrate. Herein, various LFP based materials from waste Li-ion batteries such as LiFePO<sub>4</sub>-film, LiFePO<sub>4</sub>-powder, cycled batteries containing LiFePO<sub>4</sub>-cycled films are compared with respect to their electrochemical properties for water splitting. It was found that the effect of battery cycling impacted on the OER performance, and the materials recovered from Li based batteries possess promising electrochemical properties that can be utilized as electrocatalysts for water splitting reactions and is an effective approach to repurpose e-waste.

## **Chapter 8**

Conclusions and recommendations for future work.

## References

- 1 S. Chu and A. Majumdar, *Nature*, 2012, **488**, 294–303.
- 2 X. Huang, T. Shen, T. Zhang, H. Qiu, X. Gu, Z. Ali and Y. Hou, *Adv. Energy Mater.*, 2020, **10**, 1–21.
- 3 B. M. Hunter, H. B. Gray and A. M. Müller, *Chem. Rev.*, 2016, **116**, 14120–14136.
- 4 A. Vazhayil, L. Vazhayal, J. Thomas, S. Ashok C and N. Thomas, *Applied Surface Science Advances*, 2021, **6**, 100184.
- 5 M. A. Khan, H. Zhao, W. Zou, Z. Chen, W. Cao, J. Fang, J. Xu, L. Zhang and J. Zhang, *Recent Progresses in Electrocatalysts for Water Electrolysis*, Springer Singapore, Berlin, Germany, 2018, vol. 1.
- 6 A. Li, Y. Sun, T. Yao and H. Han, *Chemistry*, 2018, **24**, 18334–18355.
- 7 F. Dionigi, C. C. Weber, M. Primbs, M. Gocyla, A. M. Bonastre, C. Spöri, H. Schmies, E. Hornberger, S. Kühl, J. Drnec, M. Heggen, J. Sharman, R. E. Dunin-Borkowski and P. Strasser, *Nano Lett.*, 2019, **19**, 6876–6885.
- 8 Europe at the top of hydrogen electrolyser projects, <https://energyindustryreview.com/power/europe-at-the-top-of-hydrogen-electrolyser-projects>, (accessed January 2, 2025).
- 9 What does the decade hold for hydrogen in Australia?, <https://www.energetics.com.au/insights/thought-leadership/what-does-the-decade-hold-for-hydrogen-in-australia>, (accessed January 2, 2025).
- 10 P. E. Karthik, H. Rajan, V. R. Jothi, B. I. Sang and S. C. Yi, *Journal of Hazardous Materials*, 2022, 421.
- 11 H. Xiao, W. Dong, Q. Zhao, F. Wang and Y. Guo, *J. Hazard. Mater.*, 2021, **416**, 125808.
- 12 J. Xiao, R. Gao, B. Niu and Z. Xu, *J. Hazard. Mater.*, 2021, **407**, 124704.
- 13 Forecast 2023: Growth Renewable Energy Distributed Generation Drive Global Industrial Battery Market; Frost & Sullivan, San Antonio, TX, USA, 2018.
- 14 Y. Zhao, O. Pohl, A. I. Bhatt, G. E. Collis, P. J. Mahon, T. Rüther and A. F. Hollenkamp, *Sustain. Chem.*, 2021, **2**, 167–205.
- 15 World Economic Forum Global Battery Alliance. Vision Sustainable Battery Value Chain 2030: Unlocking Full Potential Power Sustainable Development Climate Change Mitigation, WeForum, Cologny, Switzerland, 2019.
- 16 A. D. Ballantyne, J. P. Hallett, D. J. Riley, N. Shah and D. J. Payne, *R. Soc. Open Sci.*, 2018, **5**, 171368.
- 17 R. Rapier, *The Lead-Acid Battery's Demise Has Been Greatly Exaggerated*, Forbes.
- 18 S. King and N. J. Boxall, *J. Clean. Prod.*, 2019, **215**, 1279–1287.
- 20 Y. Zhao, T. Ruether, A. I. Bhatt and J. Staines, *CSIRO, Australia*.
- 21 Global Secondary Battery Recycling Market 2019-2023, <https://www.businesswire.com/news/home/20181203005886/en/Global-Secondary-Battery-Recycling-Market-2019-2023-Rising-Stewardship-Collaboration-for-Battery-Recycling-to-Drive-Growth-Technavio>, (accessed January 14, 2025).
- 22 C. L. Campion, W. T. Li, B. L. Lucht Eshetu, J. P. Bertrand, S. Lecocq, S. Gruegeon, M. Laruelle and G. Armand, *Journal Electrochemical Society*, 2005, **152**, 804–811.

- 23 M. Zeeshan, A. Murugadas, S. Ghaskadbi, B. R. Ramaswamy and M. A. Akbarsha, *Environ. Pollut.*, 2017, **224**, 54–69.
- 24 Q. Liu, J. Cao, K. Q. Li, X. H. Miao, G. Li, F. Y. Fan and Y. C. Zhao, *Environ. Sci. Pollut. Res. Int.*, 2009, **16**, 329–338.
- 25 K.-L. Yan, J.-F. Qin, J.-H. Lin, B. Dong, J.-Q. Chi, Z.-Z. Liu, F.-N. Dai, Y.-M. Chai and C.-G. Liu, *J. Mater. Chem. A Mater. Energy Sustain.*, 2018, **6**, 5678–5686.
- 26 Y. Chen, X. Xu, Z. Zeng, X. Lin, Q. Qin and X. Huo, *Chemosphere*, 2019, **220**, 531–538.
- 27 A. Chen, K. N. Dietrich, X. Huo and S.-M. Ho, *Environ. Health Perspect.*, 2011, **119**, 431–438.
- 28 D. J. Cole-Hamilton, *Elements of Scarcity*.
- 29 A. A. Yaroshevsky, DOI:10.1134/S001670290601006X.
- 30 S. Liu, Z. Li, C. Wang, W. Tao, M. Huang, M. Zuo, Y. Yang, K. Yang, L. Zhang, S. Chen, P. Xu and Q. Chen, *Nat. Commun.*, DOI:10.1038/s41467-020-14565-w.
- 31 S. Wang, A. Lu and C. J. Zhong, *Nano Converg.*, DOI:10.1186/s40580-021-00254-x.
- 32 C. Hu, L. Zhang and J. Gong, *Energy Environ. Sci.*, 2019, **12**, 2620–2645.
- 33 D. Strmcnik, M. Uchimura, C. Wang, R. Subbaraman, N. Danilovic, D. Van Der Vliet, A. P. Paulikas, V. R. Stamenkovic and N. M. Markovic, *Nat. Chem.*, 2013, **5**, 300–306.
- 34 A. P. O'Mullane, *JPhys Energy*, 2020, 2.
- 35 S. Cobo, J. Heidkamp, P.-A. Jacques, J. Fize, V. Fourmond, L. Guetaz, B. Jousselme, V. Ivanova, H. Dau, S. Palacin, M. Fontecave and V. Artero, *Nat. Mater.*, 2012, **11**, 802–807.
- 36 T. R. Cook, D. K. Dogutan, S. Y. Reece, Y. Surendranath, T. S. Teets and D. G. Nocera, *Chem. Rev.*, 2010, **110**, 6474–6502.
- 37 N. T. Suen, S. F. Hung, Q. Quan, N. Zhang, Y. J. Xu and H. M. Chen, *Chem. Soc. Rev.*, 2017, **46**, 337–365.
- 38 J. K. Nørskov, J. Rossmeisl, A. Logadottir, L. Lindqvist, J. R. Kitchin, T. Bligaard and H. Jónsson, *J. Phys. Chem. B*, 2004, **108**, 17886–17892.

# CHAPTER 2

## LITERATURE REVIEW

### BACKGROUND

The rapid depletion of fossil fuels has led to increasingly severe energy and environmental challenges. Hydrogen gas has long been regarded as a clean and renewable energy carrier, offering a sustainable alternative to fossil fuels. However, the key obstacle to the widespread adoption of hydrogen energy is the ability to produce hydrogen efficiently and cost-effectively<sup>1</sup>. The hydrogen to carbon (H/C) ratio of various fuels is presented in Figure 2.1 and that illustrates that hydrogen is a clean energy source. Water is one of the most abundant substances on Earth, and its splitting presents a feasible and reliable approach for large-scale hydrogen production. In general water splitting reactions are divided into two half-cell reactions which are the oxygen evolution reaction (OER) and the hydrogen evolution reaction (HER). Among the various aspects, electrocatalysis plays a vital role and is responsible for lowering the kinetic energies of water splitting reactions as without catalyst water splitting would require much more energy<sup>2</sup>. The HER occurs at the cathode and is responsible to release hydrogen and the OER occurs at anode, leading to the formation of oxygen. The major aspect that adds to the limitation of this technology is slow kinetics of these two reactions, in particular for the OER. Thus, this generates the need for proficient electrocatalysts that are capable to reduce the kinetic barriers towards the production of hydrogen and oxygen<sup>3</sup>.

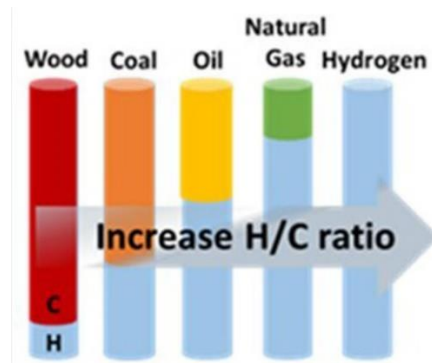
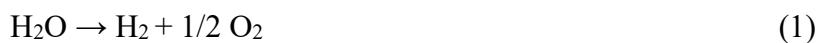


**Figure 2.1:** Hydrogen to carbon ratio in various fuels, open access with licence CC-BY-NC-ND<sup>4</sup>.

To design various kinds of electrocatalysts the operating conditions of water electrolysis needs to be considered as there are three major technologies for electrolysis a)

Proton exchange membrane electrolysis where water splitting reaction takes place in acidic conditions, b) high-temperature solid oxide water electrolysis that occurs at very high temperatures<sup>4</sup> and, c) alkaline electrolysis that uses an alkaline environment for water splitting reactions<sup>5</sup>. Therefore, electrocatalysts are designed according to high catalytic activities suitable to these operating conditions, which should be of optimum cost so that it is commonly used and holds good durability<sup>6</sup>.

Water electrolysis is splitting of water molecules in hydrogen and oxygen with the application of external energy (electric current or heat) resulting in a water splitting reaction, that is,



The process consists of two electrodes where direct current is applied through the power supply. The positive electrode is called the anode where oxygen evolution reaction occurs, and the negative electrode is called the cathode where hydrogen evolution reaction takes place. After the passing of electric current there is a transfer of ions and electrons at the anode and cathode<sup>7</sup>. Moreover, water electrolysis is an endothermic reaction where external energy is required<sup>8</sup>. The energy is given in the form of electricity or heat. After assuming the reaction to be reversible, the laws of thermodynamics can be used to quantify the energy necessary for the process of water splitting.



Here,  $\Delta H$  presents total energy necessary to split the water molecule. The energy can be thermally or electrically produced and presents the system to be irreversible, therefore, at STP (Standard Temperature and Pressure)  $\Delta H = 5285.88 \text{ kJ/moles}$ ,  $\Delta G = 5237.23 \text{ kJ/mol}$  and  $T \Delta S = 548.65 \text{ kJ/mol}$ <sup>9</sup>. This section focuses on the electrocatalysts that are highly efficient for the HER and OER reactions and lead to high catalytic performance. Many industrial materials like transformers, electric motors consist of copper which could be recovered and then reused for other electronic and energy applications. Likewise, e-waste, such as the cathode from recycled Li-ion batteries which consists of various transition metals like Ni, Co, Mn, Al could in principle be repurposed. These materials have enough potential to replace costly Ru and Pt based electrocatalysts in water splitting reactions. Thus, redirecting electronic waste would not only reduce the impact on the environment but it would ensure availability and sustainability for future generations. Therefore, this section highlights key materials recovered from spent electronic wastes that could be used as catalysts for water splitting.

## 2.1. Electrocatalysts

Electrocatalysts speed up the transfer of electrons through the electrode while providing appropriate active sites for optimal binding of reactants that enables the required electrochemical transformation such as the HER and the OER, where the latter is the main focus of this thesis<sup>3, 10, 11</sup>. There are two categories for HER and OER catalysts, i.e. noble and non-noble metal based electrocatalysts. Usually, noble based metal electrocatalysts for both the HER and OER are platinum group based (Pt, Pd, Ir, Ru and Rh) and rank highest in the volcano plot (Figure 2) as an electrocatalyst<sup>12, 13</sup>. Most non-noble metal catalysts for the OER are based on Ni, Fe, and Co and for the HER are metal based carbides<sup>14</sup>, transition metal phosphides<sup>15</sup> and transition metal chalcogenides (sulphides and selenides)<sup>16</sup>.

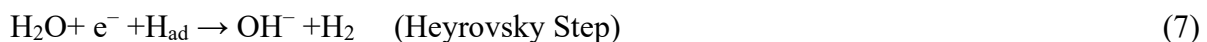
### 2.1.1. Hydrogen Evolution Reaction

The hydrogen evolution reaction (HER) is the significant half reaction that involves hydrogen production at the cathode involving a two-electron transfer process. Therefore, the mechanism of the HER reaction is highly reliant on the pH of the electrolyte in which the reaction proceeds.

Following are the reactions that occur in acidic media and Equation 3, 4 & 5 are the Volmer, Heyrovsky and Tafel step equations respectively<sup>8</sup>.



While, in alkaline media the reactions that occur are Volmer, Heyrovsky and Tafel equations as described below in Equation 6, 7 and 8 respectively<sup>20</sup>. Active sites H\* are formed that results in hydrogen production as in Equation 8. Also, hydroxyl ions are produced with hydrogen adsorption and water is dissociated.



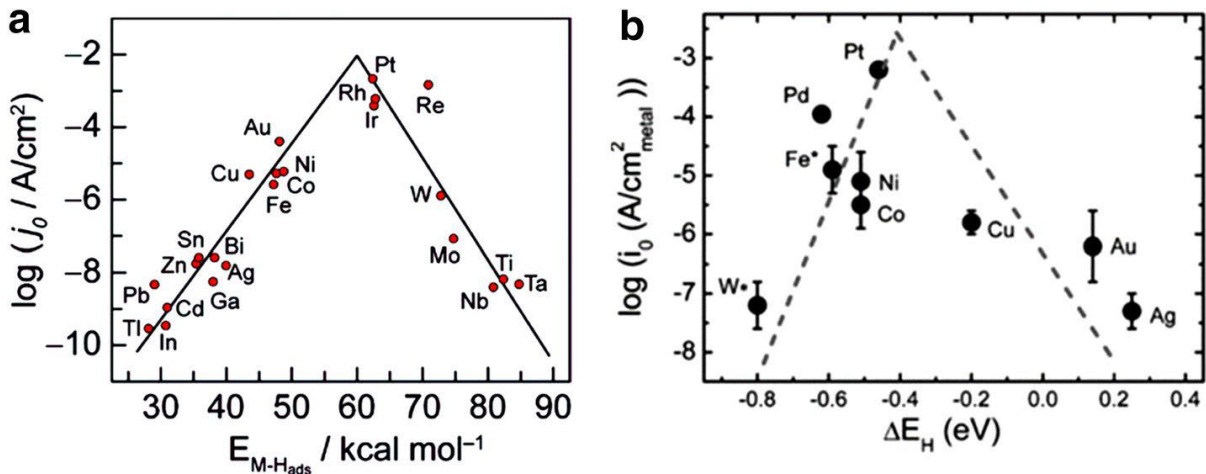


**Figure 2.2:** Volcano plot a) Exchange current density Vs M-H bond energy for metal surface (acidic media), b) exchange current density on monometallic surface Vs hydrogen binding energy calculated (alkaline media) open access with licence CC-BY-NC-ND<sup>4</sup>.

Usually, for predicting the efficiency of the hydrogen evolution reaction, the Gibbs free energy of hydrogen adsorption is a good descriptor thus, a small value of hydrogen binding energy would promote the HER in both acidic and alkaline media. The volcano plot in Figure 2.2 provides the activities of various metals in alkaline and acidic media. It is observed that Pt is the best fit for both media with optimum hydrogen adsorption energy and high current density<sup>4</sup>.

### 2.1.2. Oxygen evolution reaction (OER)

As mentioned before, the OER is the other half reaction that involves oxygen production at the anode and requires the transfer of four electrons. This requires more overpotential as compared to the HER. The reaction is found to proceed via two different mechanisms: (a) adsorbate evolution mechanism (AEM) and (b) the lattice oxygen mediated mechanisms<sup>21</sup>.

(a) Adsorbate Evolution Mechanism (AEM): Here the reaction involves four proton and electron transfer reactions from the metal centres as the active sites (M) producing  $\text{O}_2$  molecules in acidic as well as alkaline media.



The reaction pathway for alkaline media involves the processes described in equations 8 to 12. As observed, on the active site of the metal the hydroxide anions are adsorbed and forms M–OH. Thereafter, M–OH further forms M–O after deprotonation occurs. For the formation of O<sub>2</sub> there are two ways, first is that M–O reacts with OH<sup>−</sup> and forms M–OOH intermediate and produces O<sub>2</sub> by deprotonation of M–OOH. The other way is M–O species are converted to O<sub>2</sub> with the generation of the M active site. This way is observed to have a kinetic barrier. In acidic media oxygen is evolved by M–OH, M–O, and M–OOH as in alkaline media <sup>22, 23, 24</sup>. Therefore, to enhance the electrocatalytic performance of OER electrocatalysts, a detailed knowledge of the binding energies of all intermediates are important as the reaction overpotential is highly reliant on the binding strengths of the intermediates.

(b) Lattice Oxygen mediated mechanism: Here, the lattice oxygen on the catalyst directly contributes to the oxygen evolution reaction (OER). On similar terms this method is applied on gas phase catalytic oxidation reaction demonstrated on alloy catalyst <sup>25, 26, 27, 28</sup>.

### 2.1.3. Electrocatalysts based on transition metals

This section presents the work done by various research groups on the OER, HER and bifunctional transition metal based electrocatalysts which can perform both the OER and HER processes. For example, Jiang et al., <sup>28</sup> presented the synthesis of CoNiMn/NC and observed that Ni and Mn provides active sites to the hollow structure of CoNiMn/NC. Thus, the presence of Co, Mn, Ni with N enriched carbon shows a synergistic effect. The synthesis of CoNiMn/NC is shown in Figure 2.3. The Tafel slope of Co/NC and CoNi/NC is 127.36 mV/dec and 81.24 mV/dec, respectively CoNiMn/NC exhibits the lowest Tafel slope value of 64.38 mV/ dec as presented in Figure 4.3 (a) and (b).

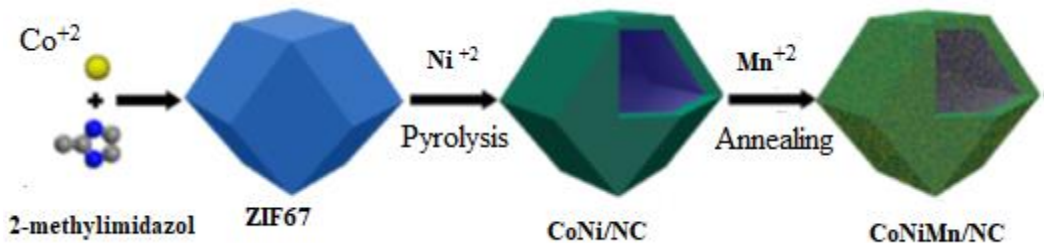


**Figure 2.3:** Synthesis of CoNiMn/NC (Reused with permission. Copyright © 2020 Elsevier Inc) <sup>28</sup>.

Li et al.,<sup>29</sup> presented transition metal phosphides like cobalt phosphides with great potential for future applications in electrochemical water splitting reaction. With resemblance to hydrogenase, cobalt phosphides demonstrate proficient electrocatalytic HER performance. Chen et al.,<sup>30</sup> presented work to convert LiCoO<sub>2</sub> from spent lithium-ion batteries into efficient electrocatalysts for the OER. After cycling for 500 cycles the spent LIBs can deliver a current density of 9.68 mA/cm<sup>2</sup> at 1.65 V with a Tafel slope value of 72.58 mV/dec. Sultana et al.,<sup>31</sup> studied low-cost stainless steel (AISI 316) and this research also presents that OER efficiency is further accelerated by the existence of Fe/Ni oxides & metallic gold.

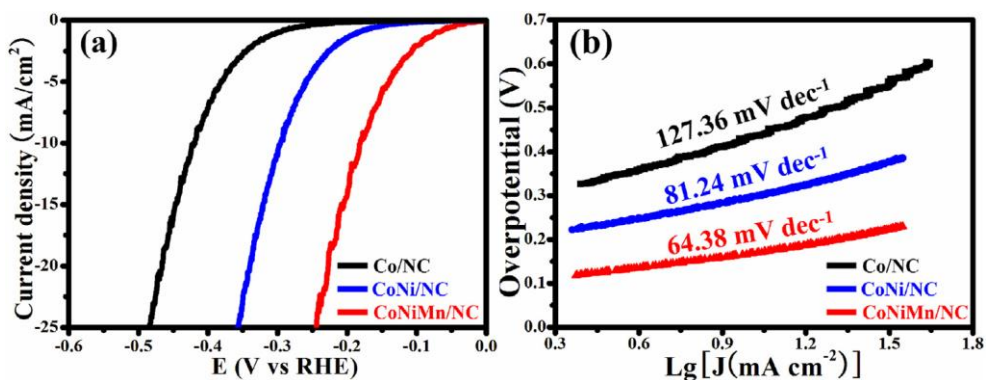


**Figure 2.4:** a) Linear Sweep Voltammetry curves, (b) Tafel plots (Co/NC, CoNi/NC, CoNiMn/NC) in 1.0 M KOH for HER (Reused With Permission Copyright © 2020 Elsevier Inc)<sup>28</sup>.

This electrocatalyst shows a low Tafel slope value of 29 mV/dec and excellent performance for high current densities of 100 mA/cm<sup>2</sup>. Babar et al.,<sup>32</sup> developed a pathway to utilize e-waste from waste copper wires. Copper hydroxide nanowires were grown via chemical oxidation on waste Cu wires followed by an electrodeposition process to deposit nickel iron hydroxide nanosheets. Due to efficient electron transport, high mass activity as well as high surface area, the electrocatalyst showed an excellent OER performance with low overpotential values of 275 mV and 390 mV at 20 and 100 mA cm<sup>2</sup> respectively, with a Tafel slope of 83 mV/dec. Farzana et al.,<sup>33</sup> worked on a spent Zn-C battery to recover Mn<sub>3</sub>O<sub>4</sub>, where a low overpotential of 360 mV was required to reach 10 mA/cm<sup>2</sup> with a Tafel slope of 64 mV/dec thus, indicating excellent activity under alkaline conditions for the OER. Natarajan et al.,<sup>34</sup> presented spent lithium-ion batteries that are rich in Mn and Co based elements and used recovered spinal MnCo<sub>2</sub>O<sub>4</sub> spheres for catalysing the OER in alkaline conditions with an overpotential of 400 mV @ 10mA cm<sup>-2</sup> and Tafel slope of 80 mV dec<sup>-1</sup>. This study signifies

the efficiency of the recovered spinal  $\text{MnCo}_2\text{O}_4$  microspheres to be used as water splitting OER electrocatalyst.

#### 2.1.4 Bifunctional electrocatalysts

Additionally, bifunctional metal catalysts are defined as active catalysts that could switch activity between the OER and HER without undergoing degradation<sup>35, 36</sup>. This is important as electrolyzers when shut down pass a reverse current which degrades the cathode<sup>37</sup>. Developing a catalyst that can tolerate this would allow for an electrolyzer that can track the input from intermittent renewable energy sources. Abu Sayeed<sup>38</sup> demonstrated bi-functional electrode that switches between the HER and OER. The synthesis method includes platinum electrode being highly activated and then further immersed in nickel nitrate solution. After electrochemical cycling of the electrode, it forms an active Pt/Ni alloy at the Pt surface. This electrocatalyst instantly switches between the HER and OER without losing activity which is shown in Figure 2.5. It can be seen clearly in Figure (2.5a) that the electrode is active for both the HER and OER for up to 1000 cycles. Figure 2.5b shows that the Ni oxidation response gradually shifts to higher potential with cycling which was attributed to alloy formation.

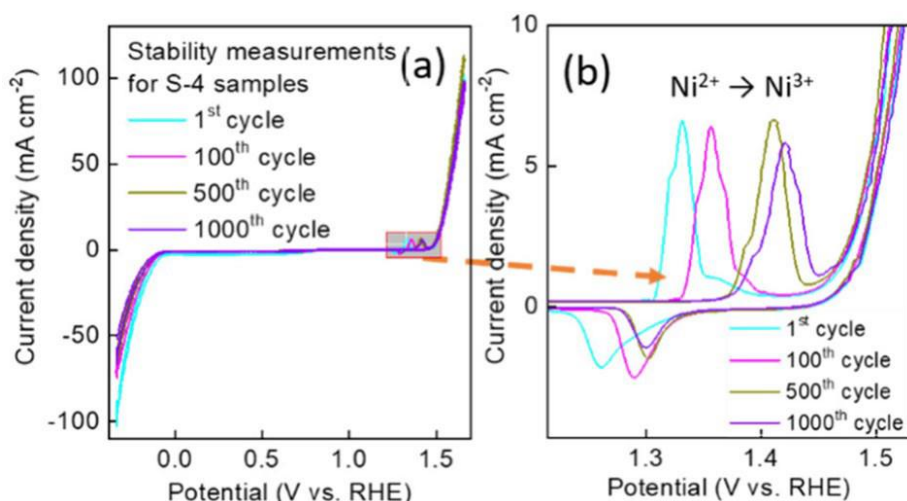


**Figure 2.5:** Cyclic Voltammograms recorded in 1 M KOH for 1000 cycles at  $100 \text{ mV s}^{-1}$  for sample S-4, b) enlarged region showing the Ni oxidation process (Reused With Permission Copyright © 2020 Wiley)<sup>38</sup>.

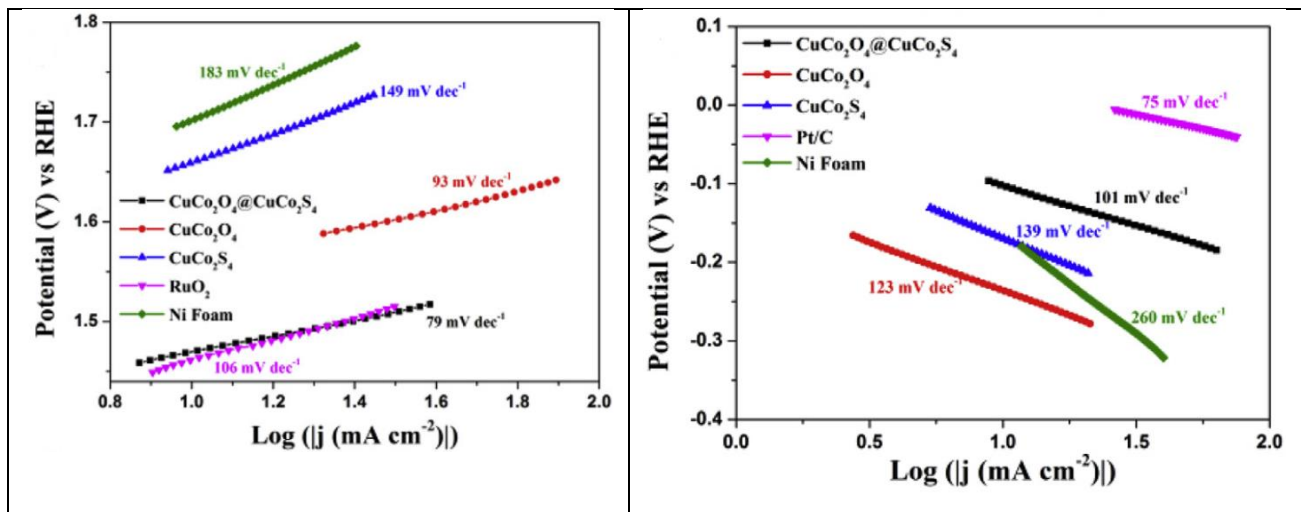


**Figure 2.6:** (a) Tafel plots of  $\text{CuCo}_2\text{O}_4@\text{CuCo}_2\text{S}_4$ ,  $\text{CuCo}_2\text{O}_4$ ,  $\text{CuCo}_2\text{S}_4$ ,  $\text{RuO}_2$  (Pt/C), and Ni foam for OER activity<sup>40</sup>, (b) Tafel plots of  $\text{CuCo}_2\text{O}_4@\text{CuCo}_2\text{S}_4$ ,  $\text{CuCo}_2\text{O}_4$ ,  $\text{CuCo}_2\text{S}_4$ ,  $\text{RuO}_2$  (Pt/C), and Ni foam for HER activity, Reused with permission © 2020 Elsevier Ltd<sup>40</sup>.

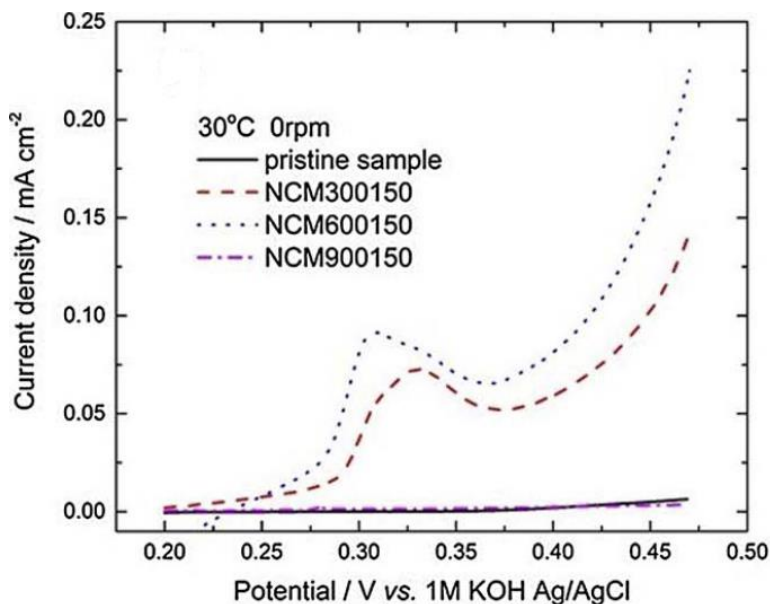


**Figure 2.7:** The LCV curves of OER that are measured at  $0.5 \text{ mV s}^{-1}$  in 1 M KOH for Ni-Co-Mn oxides heated at various temperatures for 150 min. Reused with permission © 2021 Elsevier Ltd<sup>52</sup>.

Xux et al.,<sup>40</sup> reported 3D hierarchical  $\text{CuCo}_2\text{O}_4@\text{CuCo}_2\text{S}_4$  heterostructure catalysts. With the synergistic effects exhibiting superior electrochemical stability, overpotential value of 240 and 101 mV for OER and HER respectively, and a current density of  $10 \text{ mA cm}^{-2}$ . The Tafel slope of 79 mV/dec for OER and 101 mV/dec for HER are presented in Figure 2.6 (a) and (b).

Wei *et. al.*,<sup>39</sup> worked on spent lithium-ion batteries to prepare bifunctional air electrodes by using nickel manganese cobalt (NMC) oxides. The composite of Ni-Co-Mn obtained contain significant catalytic properties for oxygen reduction reactions and oxygen evolution reactions.

The OER properties are shown in Figure 2.7, and it is observed that NCM600150 shows better OER performance as compared with other samples heated at different temperatures for 150 min. Also, an onset potential of 235 mV and more negative than other samples. Sultana and O' Mullane<sup>36</sup> studied Ni-P, Ni-S, Ni-Se electrocatalysts and found that there is a variation in surface composition after the OER due to the depletion of anion component owing to oxidation. These results are also confirmed by electrochemical experiments. Thus, it is being questioned that the materials with varying composition before the onset of OER should be termed as bifunctional or not as it would be helpful in resolving the issue of oxidation of the cathode in alkaline electrolyzers. It also emphasises the importance of characterising electrode materials after the OER.

## 2.2 Electrocatalyst performance parameters

An efficient catalyst is capable of lowering the kinetic energy barrier for the water splitting reaction, therefore, some evaluation parameters<sup>3</sup> are discussed in this section as mentioned in Figure 2.8 . The main goal is to improve activity, stability and efficiency of the process.

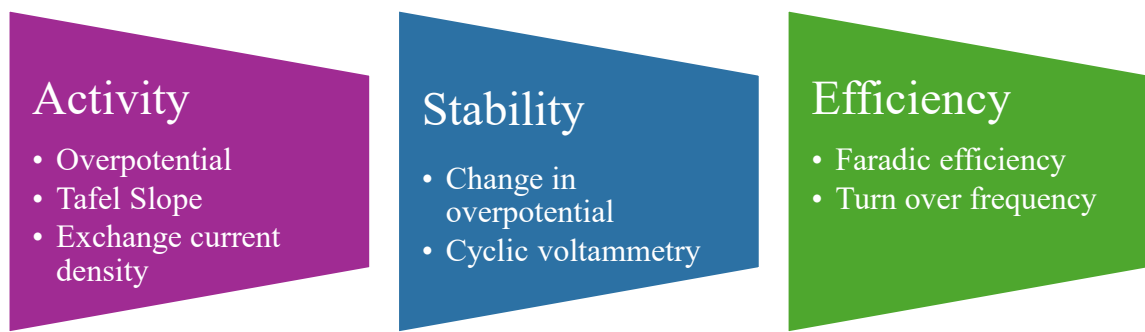


**Figure 2.8:** Evaluation parameters that decides the efficiency of electrocatalysts<sup>8, 57, 42</sup>.

There are various strategies as described below could be used to enhance the electrocatalytic activity of recovered catalyst materials, for example, (A) improving electrical conductivity. This property has a significant effect on electron transfer in an electrochemical reaction<sup>17</sup>. It is stated by Jin *et al.*,<sup>43</sup> that phosphides rich in metal content has less ionic character and more metallic character which have high electrocatalytic performance than phosphorus rich phosphides. Also, they compared two types of cobalt phosphides CoP and Co<sub>2</sub>P with similar

structure and electrochemical properties, in which Co<sub>2</sub>P nanowire exhibit a higher electrochemical performance for overall water splitting. Similarly, Feng et al.<sup>44</sup>, for example, used polyaniline (PANI) nanodots (NDs) and carbon fibres (CFs) as support and used to form Carbon Fibre CN supported polyaniline-CoP hybrid nano wires PANI-CoP HNW-CFs, thus increasing the electrocatalytic performances by accelerating electron transfer<sup>44</sup> for boosting HER reactions in water splitting given in Figure 2.9. (a) and Figure 2.9 (b) shows polarisations curves of different electrocatalysts for HER.

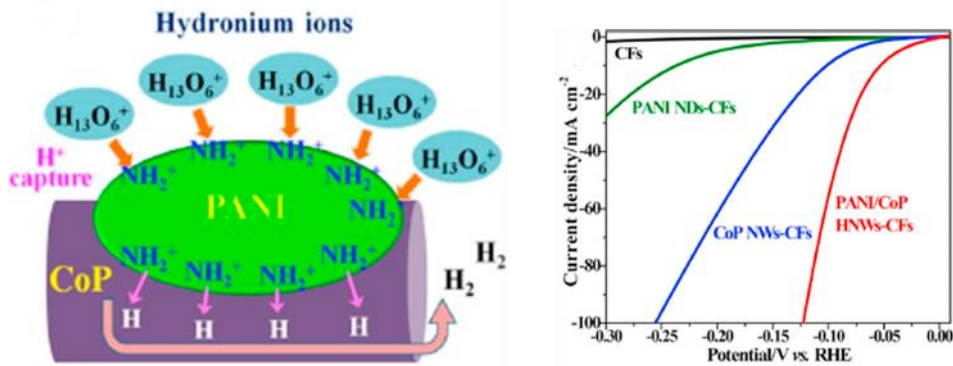


**Figure 2.9:** (a) Capture of H<sup>+</sup> from hydronium ions to form the protonated amine groups on PANI-CoP HNWs, (b) Polarisation curves of various electrocatalysts for HER in waters splitting reaction (Reused with permissions © 2021 Elsevier Ltd)<sup>43</sup>.

(B) Surface area of the catalyst that is construction of the novel hybrid nanostructure with CoP NPs which are embedded in N-doped carbon nanotube hollow polyhedron (NCNHP) are described in (Figure 2.10 (a)).

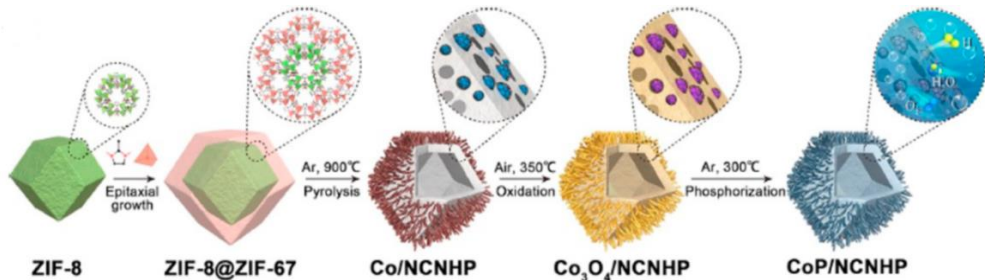


**Figure 2.10 (a):** Procedure of synthesis of CoP/NCNHP hybrid<sup>43</sup> (Reused with permissions © 2021 Elsevier Ltd).

The hollow polyhedron nanostructure has enlarged the specific surface area of the catalyst benefitting charge and mass transport in electrocatalysis<sup>45</sup> which was used for water splitting. Figure 2.10 (b) shows the polarisation curve demonstrating overall water splitting with CoP/NCNHP//CoPNCNHP electrode configuration.

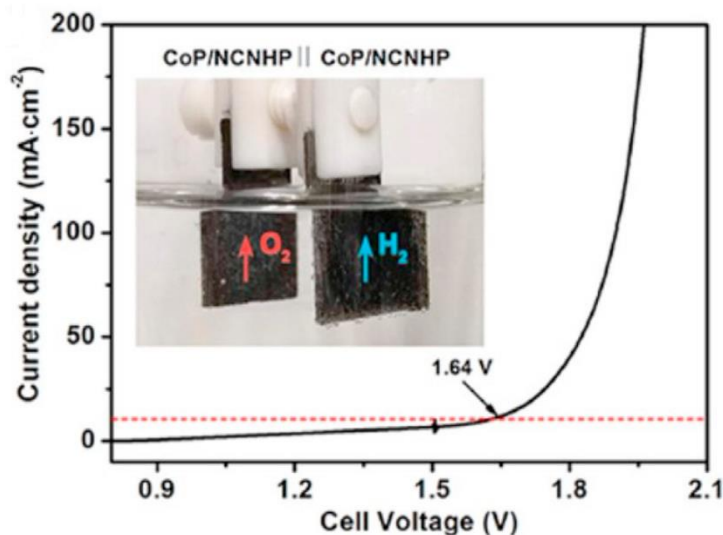


**Figure 2.10 (b):** Polarisation curve of overall water splitting based CoP/NCNHP//CoPNCNHP (Reused with permissions © 2021 Elsevier Ltd)<sup>43</sup>.

(C) Intrinsic activity; with the available active sites the intrinsic activity of each site also plays a vital role to improve the catalytic performance of the catalyst by exposing high- index facets or active sites. For example, Cao et al, presented work on preparation of 3D flower-like CoP micro balls (MBs) showed considerably improved intrinsic activity of active sites and enabled the promotion of electrocatalytic activity<sup>46, 47, 48</sup> (Figure 2.11a) towards the HER and OER as compared with disordered CoP NWs (nanowires).

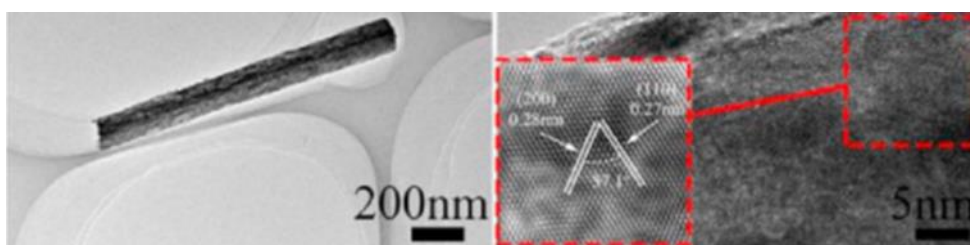


**Figure 2.11(a):** TEM and HRTEM images of CoP (Reused with permissions © 2021 Elsevier Ltd)<sup>43</sup>.

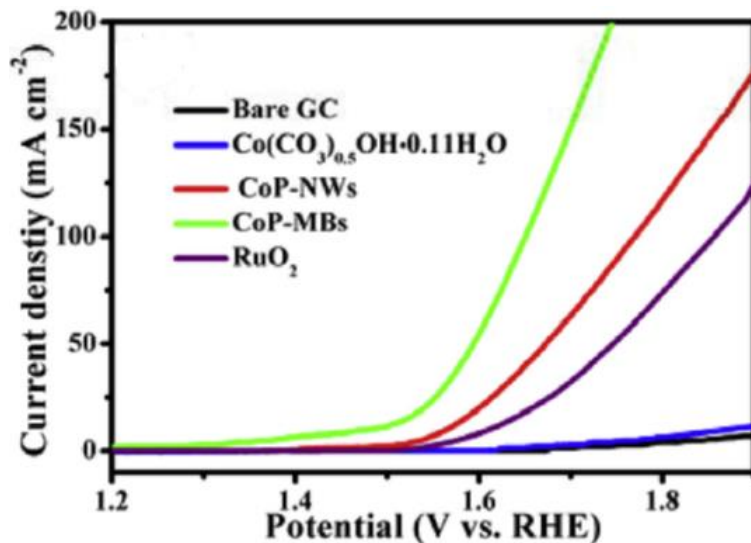


**Figure 2.11 (b):** Polarization curves of different catalysts towards OER (Reused with permissions © 2021 Elsevier Ltd) <sup>43</sup>.

The OER activity of the CoP nanostructures in the alkaline electrolyte was evaluated. The reference electrocatalyst RuO<sub>2</sub> displayed a OER activity with an overpotential of 377.7 mV to reach the current density of 10 mA cm<sup>-2</sup>. CoP MBs generated a current density of 10.0 mA cm<sup>-2</sup> at an overpotential of 289.4 mV, that is lower than CoP NWs (341.2 mV) (Figure 2.11(b)). (D) Modulation of Electronic structure which is incorporation of heteroatoms with different atomic radii and electronegativities into the lattice of transition metal phosphides TMPs could facilitate induction of subtle lattice distortion. This causes redistribution of electron density and effectively regulates the electronic structure at the atomic level. For example, incorporation of a metal element into CoP is efficient strategy for enhancing the electrocatalytic performance. For example, synthesis of the Mn-doped CoP nanosheet array on Ti mesh (Mn-Co-P/Ti), this functions as highly capable electrocatalysts for the HER <sup>49</sup> as modulates the adsorption energy of H on the surface as shown in Figure 2.12.

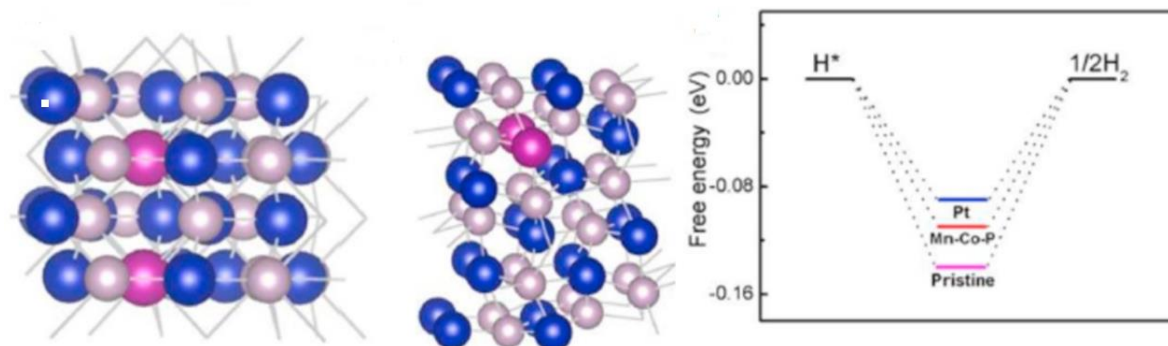


**Figure 2.12:** The top and side view of Mn-Co-P with two Mn atoms substituting the subsurface

Co atoms, HER free energy diagrams of Pt, Mn-Co-Co, and CoP<sup>43</sup> (Reused with permissions © 2021 Elsevier Ltd).

(E) Interface modulation is selectively constructing heterostructures with highest quality interfaces to influence catalytic activity. There was a drastic increase observed for HER performance when Lin et al.,<sup>50</sup> used the difference in the surface energies between the active sites of CoP and NiCoP to construct a novel CoP/NiCoP heterojunction with a nanotadpole NT-like morphology (Figure 2.13).

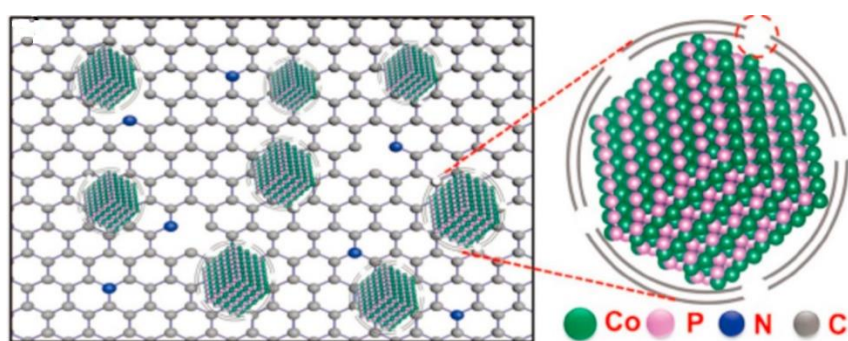


**Figure 2.13:** The morphology structure for the defective carbon/CoP nanoparticles (Reused with permissions © 2021 Elsevier Ltd)<sup>43</sup>.

(F) Phase engineering is construction of nanomaterials with two or more phases induces strong electronic and synergistic effects. This improves the catalytic performance of the materials. For instance, a novel *in situ* isomorphous substitution method is used for the fabrication of carbon-encapsulated Ni<sup>2+</sup> post-modified CoP nanowire (NiCoP@C) with a single orthorhombic CoP phase structure<sup>51</sup>. NiCoP@C, which exhibits an orthorhombic CoP phase, demonstrated exceptional electrocatalytic performance and stability for the oxygen evolution reaction (OER), with low overpotential of 279 mV at a current density of 10 mA/cm<sup>2</sup>. This highlights the crucial impact of phase engineering in improving the OER performance of cobalt phosphides. The polarisation curves in Figure 2.14 shows comparison between Ni-CoP@C, CoP@C, Ni2P@C, Ni-CoP NPs, polydopamine (PDA)-derived C, commercial RuO<sub>2</sub>, and bare CFP (carbon fibre paper) at scan rate of 10 mVs<sup>-1</sup> in 1M.

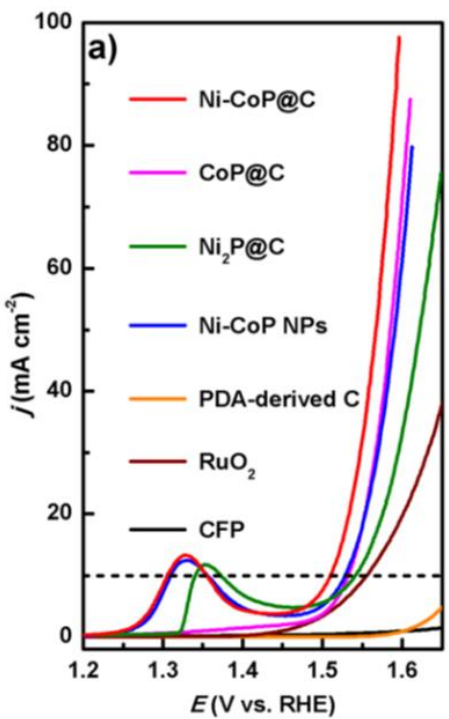


**Figure 2.14:** Polarisation curves of Ni-CoP@C, CoP@C, Ni<sub>2</sub>P@C, Ni-CoP NPs, PDA derived C, commercial RuO<sub>2</sub>, and bare CFP at scan rate of 10 mVsec<sup>-1</sup> in 1M, Reused with permissions © 2019 Elsevier Ltd <sup>43</sup>.

(G) Synergistic effect is a strong synergistic effect among different elements could also help to promote electrocatalytic activity. Li et al.<sup>30</sup> reported the synthesis of dodecahedral CoP/CN@MoS<sub>2</sub> derived from ZIF-67, where CoP nanoparticles were integrated into nitrogen-doped carbon matrices. As a result, the resulting dodecahedral CoP/CN@MoS<sub>2</sub> exhibited exceptional HER performance in both alkaline and acidic environments, along with impressive OER performance. Mechanistic studies revealed that the highly conductive CoP and porous CN worked together to enhance conductivity and facilitate faster electron transfer during electrochemical reactions.

### 2.3. Electrocatalytic measurements

The sample obtained would be measured for various electrochemical parameters as discussed below <sup>83</sup>. The activity of electrocatalyst is measured by (A) Overpotential that is Thermodynamic potential for the electrochemical water splitting reaction is 1.23V at 25°C. However, the reaction requires a higher potential than the normal thermodynamic potential due to kinetic limitations. The excess potential is known as the overpotential ( $\eta$ ). This parameter is usually measured with the corresponding value of a current density of 10mA cm<sup>-2</sup> that

compares the activity of the catalyst to others<sup>53</sup>. (B) Tafel Slope which is measured by  $\eta = b \log j + a$ , where  $\eta$  is overpotential,  $b$  is Tafel slope,  $j$  is the current density and  $a$  is the charge transfer coefficient. The Tafel slope ( $b$ ) is related to electron transfer kinetics based on catalytic reaction and small Tafel slope value corresponds to faster reaction kinetics<sup>44, 54, 55, 56</sup> shown in Figure 2.15 (a, b) for various Ni, Co, Fe based electrocatalysts. (C) Exchange current density that is the exchange current density explains the charge transfer under equilibrium conditions and high value of current density signifies greater charge transfer leading to faster kinetics<sup>11, 57, 3</sup>.

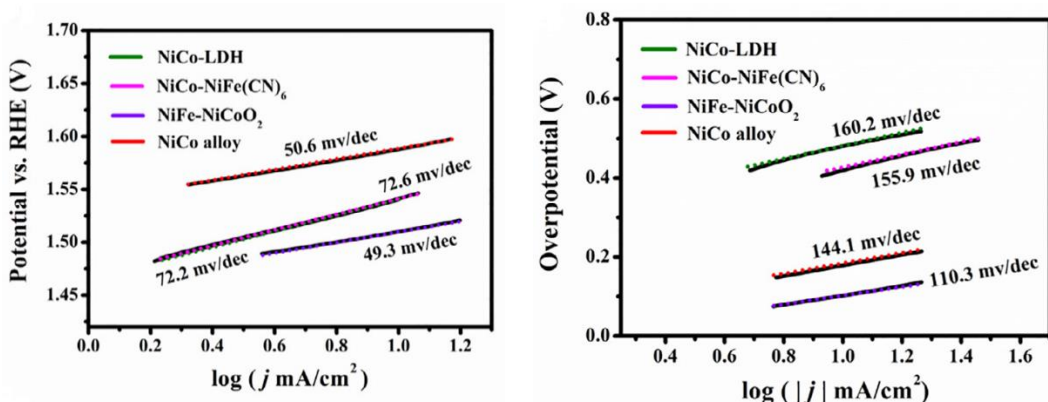


**Figure 2.15:** (a) The Tafel Plot value for NiFe –NiCoO<sub>2</sub>, NiCo –NiFe(CN)<sub>6</sub>, NiCo –LDH and NiCo alloy derived for OER, (b) The Tafel Plot value for NiFe –NiCoO<sub>2</sub>, NiCo –NiFe(CN), NiCo –LDH and NiCo alloy for HER. Reused with permission © 2021 Elsevier and Science Press<sup>58</sup>.

Therefore, the designed catalyst should have higher value of exchange current density and lower value of Tafel Slope shown in Figure 2.15 (a, b).

## 2.4. Stability

The stability of the electrocatalyst is generally observed by two methods<sup>85, 88</sup> (A) I-t curve (Chronoamperometry)/ E-t curve (chronopotentiometry), this method determines the variation in current with respect to time under constant potential. The longer the current and potential remains constant better is the catalyst stability. The I-t curve of NiCoP electrode reproduced from NiCoP scrapped wires from electronic waste was evaluated for HER reaction in alkaline medium demonstrates super stability of 36 hr at constant overpotential of 203mV<sup>58</sup> as shown in Figure 2.16<sup>56</sup>.

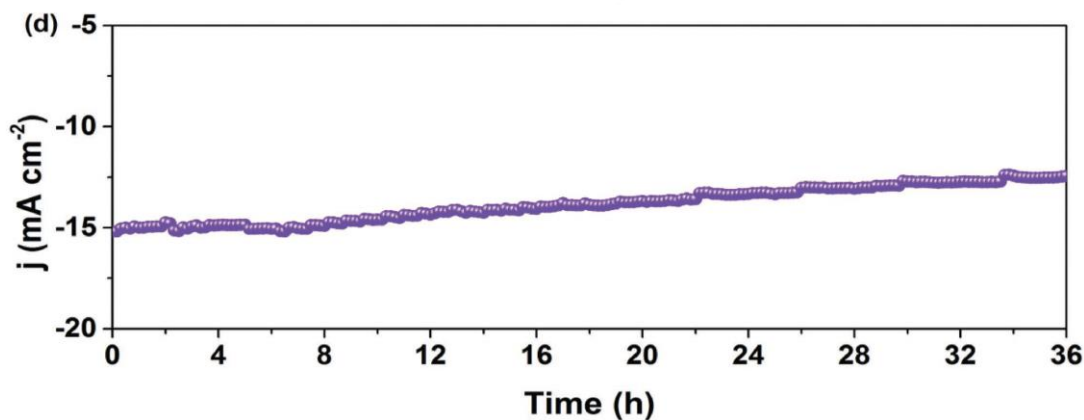


**Figure 2.16:** Stability measurements <sup>55</sup> (Reused with permission © 2021 Elsevier and Science Press).

(B) Cyclic voltammetry is method measures the current by cycling the potential normally with cycles at the decided scan rate is presented in Figure 2.17 <sup>38</sup>. Also, to measure the overpotential shift linear sweep voltammetry method is applied before and after CV cycling at value of current density <sup>60,66</sup> as presented in Figure 2.17.

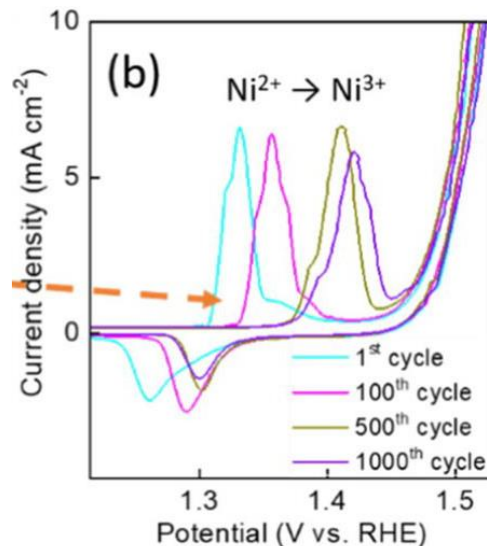


**Figure 2.17:** Cyclic voltammograms recorded in 1 M KOH for 1000 cycles at 100 mV s<sup>-1</sup> for sample related to Pt-Ni electrode<sup>38</sup>.

## 2.5. Efficiency

Efficiency is measured by, (A) Faradaic efficiency which is defined as the ratio of experimentally calculated quantity of H<sub>2</sub> and O<sub>2</sub> to the theoretically calculated quality of H<sub>2</sub> and O<sub>2</sub>. Experimental value is calculated by chronoamperometric or chrono potentiometric and experimental value is calculated by water gas displacement or gas chromatography. (B) Turn

over frequency as this parameter describes the conversion of reactants into products per catalytic site per unit.

## 2.6. Electronic wastes from batteries

The electronics market has increased exponentially due to the prominence of the worldwide production of LIB (lithium-Ion Batteries) which is estimated to increase, due to its applicability in various electronic goods like mobile phones, batteries and hybrid electronic vehicles<sup>61</sup>. Furthermore, it is predicted that batteries have an expected life of 3 years for consumer-based products and 10 years for electric vehicles. Most electronic waste contains valuable metals that could be recovered. Therefore, reusability of metals after recovering them from waste batteries in particular is currently considered as an emerging research area<sup>62, 63</sup>. For instance, in Australia, the most common electronic device is the mobile phone that contains 25% of metals that are recoverable like gold, silver, copper and many platinum group-based metals<sup>64</sup>. The most common battery that is used in various electronic devices such as smartphones, electric vehicles and laptops is the Li-ion battery. Usually, traditional Li-ion battery consists of an anode, cathode, electrolyte, separator, copper, and aluminium foils as current collector, sealing parts and a container. Therefore, on dismantling consists of positive electrodes containing metal oxides powders on aluminium foil<sup>41</sup>. The battery consists of 35% cathode, 26% sealing and 18% anode. The Li ion battery consists of inserted Li compounds like LiCoO<sub>2</sub> (LCO), LiFePO<sub>4</sub> (LFP) and LiNi/Mn/Co/O<sub>2</sub>, LiNi/Co/Al/O<sub>2</sub> (NCA)<sup>65</sup>. The positive electrode metal oxides consist of LiCoO<sub>2</sub>, LiMn<sub>2</sub>O<sub>4</sub> and LiFePO<sub>4</sub>, etc., that depends on the type of lithium-ion batteries. Negative electrodes consist of carbon powders on copper foil. Additionally, separators, polymers binders and electrolytes are other materials that can also be recovered<sup>66, 67, 68, 52</sup>.

To further portray the seriousness to recycle the precious elements the “International Union of Pure and Applied Chemistry (IUPAC)<sup>69</sup> and “European Chemical Society” shared a periodic table that indicates elements according to their use in the electronic industry as mentioned in Chapter 1. IUPAC declared complete depletion of few elements in next 100 years like Cr, Ln, Co, As, Zn, Ga, Ge and Te due to their excessive use in electronic industry with few elements like Ni, Mn, Li and Mg being categorised with limited availability. The periodic table presented by the European Chemical Society also details the extinction of many elements with their use. The origin and traceability of the elements is given importance as most of them fall in the category of extinction or becoming susceptible to extinction with time<sup>19</sup>.

### 2.6.1. NMC (Nickel Manganese and cobalt)

Transition metal based electrocatalysts have gained attention as they acquire more than one oxidation state. This makes them more stable during continuous oxidation and reduction occurring during an electrocatalytic reaction<sup>70, 71, 72</sup>. Furthermore, being cheaper than precious metals they are easily available and more suited towards industrial use. One of the other major advantages of transition-based metal oxides is their ability to mix by uniformly distributing them in oxide structures. These electrocatalysts are binary or even ternary and mixing offers distinct benefits of possessing the advantages of each component to improve performance<sup>73</sup>. Moreover, altering the electronic structure of active sites promotes water splitting reactions<sup>74, 75, 76</sup>.

Sivakumar et al., 2019<sup>77</sup> worked on different compositions of Ni, Mn Co oxides and studied various composites for their OER performance and reported an OER current density for  $\text{Ni}_{1.5}\text{Co}_{0.5}\text{Mn}_{0.75}\text{O}_4$  of  $10\text{ mA cm}^{-2}$  at  $1.80\text{ V}$  and Tafel slope of  $68\text{ mV dec}^{-1}$  which is comparable to similar  $\text{NiCo}_2\text{O}_4$  catalysts. Additionally, Priamushko et al., 2020<sup>78</sup> reported on  $\text{Ni}_x\text{Co}_y\text{Mn}_z\text{O}_4$  for the OER and found that  $\text{Ni}_x\text{Co}_y\text{Mn}_z\text{O}_4$  calcined at  $300^\circ\text{C}$  exhibited high current density and a low onset potential when loaded onto Ni foam that required an overpotential of  $400\text{ mV}$  at  $10\text{mA cm}^{-2}$ . Also, Salem et al., 2023<sup>79</sup> reported an equimolar trimetallic  $\text{Mn}_1\text{Ni}_1\text{Co}_1\text{-P/NF}$  as a proven highly active bifunctional electrocatalyst for water splitting reactions and with an ultra-low overpotential of  $14\text{ mV}$  to pass a current density of  $10\text{ mA cm}^{-2}$  for the HER. Recent work has also been reported on mixed transition metal oxides in their ternary form like nanocast mixed Ni–Co–Mn Oxides for the OER<sup>78</sup>,  $\text{NiCoMnO}_4$  nanoparticles on N-doped graphene for the OER and ORR<sup>80</sup>. Other examples include nickel cobalt manganese spinel oxide nanoparticles as electrocatalyst for the OER and ORR<sup>81</sup> Plasma-Modulated Trimetallic Mn-Ni-Co Phosphides<sup>79</sup> and  $\text{MnNiCoO}_4/\text{N-MWCNT}$  nanocomposite catalyst for overall water splitting reactions<sup>82</sup>.

Table 2.1. Various NMC type catalyst materials used for the OER identifying the catalyst substrate, overpotential required to pass  $10\text{ mA cm}^{-2}$  ( $\eta_{10}$ ) and onset values.

Catalyst material	Substrate used	Overpotential ( $\eta_{10}$ ) mV	Tafel slope (mV dec <sup>-1</sup> )	Reference
NiCo <sub>2</sub> S <sub>4</sub> nanowire arrays	Ni Foam	260	40.1	1
NiCo <sub>2</sub> O <sub>4</sub> /NF	No Foam	330	66.9	1
Ni <sub>3</sub> S <sub>2</sub> /NF	Ni Foam	300	51	1
NiCoP/NF	Ni Foam	280	87	1
NiCo-OH/NF	Ni Foam	201	91	2
Ni <sub>2</sub> P/NF	Ni Foam	93	85	2
MNC-P/NF	Ni Foam	350	85	3
MNC-OH/NF	Ni Foam	-	114	3
Ni <sub>x</sub> Co <sub>y</sub> Mn <sub>z</sub> O <sub>4</sub>	Ni Foam		79-97 (before cycling)	3
Ni <sub>x</sub> Co <sub>y</sub> Mn <sub>z</sub> O <sub>4</sub> from KIT-6 silica calcined at 300°C	Ni Foam	400	79-84 (after cycling)	3
NiCoMnO <sub>4</sub> nanoparticles	Nitrogen-doped graphene	392	128	4
NiCoMnO <sub>4</sub>	Nitrogen-MWCNT	-	-	4,5
Ni <sub>x</sub> Co <sub>y</sub> Mn <sub>z</sub> O <sub>4</sub> from KIT-6 silica calcined at 300°C	Ni Foam	400	-	3
Nickel-cobalt-manganese spinel oxide nanoparticles	Glassy carbon	180	68 (before cycling)	6
Co-doped Ni-Mn LDH nanoplates	Glassy carbon	310	59	7
Mn <sub>1</sub> -Ni <sub>1</sub> -Co <sub>1</sub> -P-(O)	Nickel foam	289	85	8
Ni-Co-Mn oxalates (ball milled to oxides)	Glassy carbon	367	43.8	9
Mn-NiCoP nanopins arrays	Ni foam	266 (100 mA cm <sup>-2</sup> )	53	10
1.5Mn-NiCo hydroxide nanosheets with carbon nanotubes	Ni foam	239	92.1	11

To optimise the catalytic activity of the electrocatalyst in the water splitting process few approaches are applied like mounting the catalyst on the substrates with large surface areas like nickel foam (NF). Greater surface area increases surface roughness as well as enables movement of electrolyte, thus promoting availability of active sites and electrical conductivity<sup>82</sup>. Table 2. 1 shows various NMC type catalyst materials used for OER.

As reported by Sivanantham et al., 2016<sup>83</sup> NiCo<sub>2</sub>S<sub>4</sub> nanowire arrays were grown on 3D Ni foams that form efficient bifunctional electrocatalysts in a highly alkaline environment. Moreover, Xu *et. al.*, 2020<sup>84</sup> developed Mn doped Ni<sub>2</sub>P supported on Nickel foam that proved to be a competent bifunctional electrocatalyst. Also, work done by Liang et al., 2016<sup>85</sup> used NF to support NiCoP porous nanostructures and were able to achieve superior bifunctional performance. Work performed by Liu *et. al.*, 2020<sup>86</sup> reported Cr-doped NiCo<sub>2</sub>O<sub>4</sub> (Cr-NiCo<sub>2</sub>O<sub>4</sub>) nanoneedles (NNs) on nickel foam (NF) as high performance bifunctional electrocatalysts. Therefore, proving NF as a proficient substrate that enhances the electrocatalytic activity of catalyst materials.

### 2.6.2. LFP (Lithium iron phosphate)

As discussed above, in recent years, significant interest is developed to explore various cost effective non-noble metal catalysts for OER reactions. Like oxides and metal oxides of first row transition metals, this is due to their abundant availability, durability and high catalytic performance. For instance, Co based oxides,<sup>87, 88, 89</sup> metal cations tuned in layer double hydroxides (LDH) (Ni, Fe, Co, Mn LDH)<sup>90</sup>, Fe-doped nickel-based (oxy)- hydroxides (NiFe-OxHy) shows faster kinetics towards the OER<sup>91</sup>. Additionally, enormous attention is attracted by phosphate-based groups due to its prominent structure like studies have shown that the 3D structure of nickel–borate–phosphate (Ni–Bi–Pi) and iron-doped nickel phosphate (Ni:Pi–Fe/NF) enabled greater utilization of active sites, improved electrolyte diffusion, and facilitated oxygen desorption. Additionally, Ni:Pi significantly contributed to water adsorption due to the presence of amorphous regions created by phosphate groups, ultimately enhancing OER activity and their high catalytic activity<sup>92</sup>. Furthermore, the phosphate groups assist in oxidation on metal atoms as they are classic proton acceptors<sup>89</sup>. For example, Co based phosphates are termed as highly active electrocatalyst for OER reactions<sup>93, 94, 95</sup>. Phosphate-based electrocatalysts like Ni-based phosphate (Ni : Pi Fe) shows lower overpotentials than Ni based electrocatalysts<sup>92</sup>. Lui *et. al.*, 2012, worked with electrochemical tuning on olivine-type lithium transition-metal phosphates LiMPO<sub>4</sub> (M= Fe, Mn, Co, Ni) showing promising OER

performance<sup>96</sup>. Similarly, Wu *et. al.*, 2020 worked to synthesized Fe dopped LiCoPO<sub>4</sub> for enhanced OER activity<sup>87</sup>. In recent studies, earth abundant iron phosphate demonstrated favourable results as OER catalysts. Additionally, Cui et al., 2021 demonstrated, Ni incorporated LiFePO<sub>4</sub> that shows promising OER activity<sup>97</sup>.

Anantharaj *et. al.*, 2021<sup>98</sup>, discussed prominent role in Ni-Fe electrocatalysts for OER reactions and stated that nickel-alkaline batteries with Ni(OH)<sub>2</sub> anodes exhibited a decrease in cell voltage when operated with unpurified KOH containing up to 1 ppm of Fe, while no such effect was observed with purified KOH. Additionally, this study revealed that Fe incorporation from the electrolyte into the Ni(OH)<sub>2</sub> electrode not only reduced the cell voltage but also lowered the onset overpotential for the oxygen evolution reaction (OER) in an alkaline medium<sup>99</sup>. This marked the first instance where researchers identified the role of Fe in enhancing the OER activity of Ni(OH)<sub>2</sub>. Subsequent studies explored the mechanisms behind Fe influence on the OER performance of Ni- and Co-based oxygen evolution catalysts leading to multiple conclusions. The few important predictions are, Fe<sup>3+</sup> facilitates the generation of OER-active Ni<sup>4+</sup> by serving as the strongest Lewis acid among 3d transition metals<sup>100</sup>; Fe<sup>3+</sup> primarily stabilizes the active Ni<sup>2+</sup> ions, preventing their further oxidation. This is evidenced by the anodic shift of the Ni(OH)<sub>2</sub> → NiOOH oxidation peak<sup>101</sup>, Fe<sup>3+</sup> ions that substitute Ni<sup>3+</sup> ions at the edges, corners, and defect sites within the NiOOH matrix serve as the primary active sites<sup>102</sup>. The studies led by Anantharaj *et. al.*,<sup>98</sup> finally concluded that Fe<sup>3+</sup> ions enhance the conductivity of the catalytic film, thereby improving OER activity, The incorporation of Fe<sup>3+</sup> enhances OER by inhibiting the metal oxidation step while promoting the metal reduction step involved in oxygen evolution and the strong Lewis acidity of Fe<sup>3+</sup> facilitates the oxidation of Ni<sup>3+</sup>, leading to the formation of highly active Ni<sup>4+</sup> ions within the NiOOH matrix. Therefore, all these points state that Fe enhances the OER activity in water splitting reaction.

Therefore, in the present research the use of Lithium iron phosphate (LiFePO<sub>4</sub>) cathode materials from waste LIB's is investigated for potential use as oxygen evolution electrocatalysts with Ni foam as the substrate.

### 2.6.3 Recovery from NiMH batteries waste

NiMH batteries contain transition metals Ni, (36-42%,) Co (3-4%,), Mn and Fe, and are rich in rare earth elements such as (La, Ce, Pr and Nd) (8-10%)<sup>103</sup>. Dismantling of NiMH batteries provides an external case that consists of positive, negative electrodes and separators. The positive electrode is Ni foam covered by dark paste consisting of hydroxides and oxides

Table 2.2: Properties of various electrocatalysts

Electrocatalyst	Overpotential (mV) to reach 10 mAcm <sup>-2</sup>	Tafel slope (mVdec <sup>-1</sup> )	Electrolyte	Reference
Ni Foam	217	130 (HER)	1M KOH	1
Ni Foam	337	97 (OER)	1M KOH	1
Stainless steel	420	233 (HER)	1M KOH	1
Stainless steel	277	51 (OER)	1M KOH	1
Stainless steel foil	361	57 (OER)	1M KOH	2
Ni-Fe LDH	260	274 (HER)	1M KOH	3
Ni-Fe LDH	330	51.44 (OER)	1M KOH	3
Ni-Fe-O	209	161 (HER)	1M KOH	3
Ni-Fe-O	360	61.59 (OER)	1M KOH	3
Ni-Fe-OP	209	161 (HER)	1M KOH	3
Ni-Fe-OP	310	43.10 (OER)	1M KOH	3
NiFeLDH/Cu(OH) <sub>2</sub> /Cu	275 to reach (20 mAcm <sup>-2</sup> )	83 (OER)	1 M KOH	4
In situ growth of Fe (Ni)OOH on Stainless Steel	300	34 (OER)	I M KOH	5
316L Stainless Steel	370	30 (OER)	I M KOH	6
Cathodised Stainless Steel Mesh	275	70 (OER)	I M KOH	7
Stainless Steel Mesh with interacted Ni(Fe)O <sub>x</sub> H <sub>4</sub> nanosheets	310 to reach (20 mAcm <sup>-2</sup> )	37 (OER)	I M KOH	8
304 Stainless Steel	323	51 (OER)	I M KOH	9
Pentlandites: Fe <sub>8</sub> Ni S <sub>8</sub>	493	75 (OER)	I M KOH	10
Ni-Fe-P/SSAT Ni-Fe-P coating on anodically treated stainless steel.	323	43, 88 (OER)	I M KOH	11
Ni-FeP/SS (Ni-FeP on polished stainless steel.)	341	48, 184 (OER)	I M KOH	11
Ni-FeP/SSAT Ni-Fe-P coating on anodically treated stainless steel.	327	93 (HER)	I M KOH	11
Ni-FeP/SS (Ni-FeP on polished stainless steel)	363	119 (HER)	I M KOH	11

of Ni, Co, Mn, K, Fe and Zn (31, 28, 28, 2, 10, 1.5, 16 weight % respectively), and traces of other metals. While negative electrode consists of rare earth elements (REE) with more than 50 wt% concentration like most commonly found REE are neodymium, praseodymium, lanthanum and cerium (10, 2, 27, 24 weightt % respectively) and other metals found in negative electrode are of Co, Mn, K, Fe, Zn (18, 9, 4, 1.5 and 0.8 weight % respectively), and traces of few other elements <sup>104, 105</sup>. Few synthesised materials from spent batteries are mentioned in Table 2.2 that also provides information about their electrocatalytic activities.

Ni-Fe alloys with varying compositions are known to exhibit electrochemical properties for both the OER and HER and are highly useful for electrolyzers for water splitting<sup>106</sup>. As mentioned by Yatish *et. al.*,<sup>107</sup> experimental analysis reported that coating of Ni-Fe shows excellent electrocatalytic activity for water splitting. Additionally, when Ni is alloyed with various metals for example Fe, there is variation in the properties of pure nickel that affects kinetics, electronic configuration and H<sub>2</sub>O and H<sub>2</sub> adsorption as well as desorption<sup>108</sup>. Ni-Fe based electrocatalysts generally show reduced overpotential for the OER and increased stability compared to NiO<sup>109</sup>. A low overpotential value of 310 mV for the OER at 10 mA cm<sup>-2</sup> and 209 mV for the HER with a 43.10 mV dec<sup>-1</sup> Tafel slope was reported for a NiFeOP catalyst for water splitting owing to the electrocatalytic activity of Ni the Fe combination<sup>47</sup>.

#### 2.6.4 Recovering spent battery materials as electrocatalysts

Lithium cobalt oxide (LCO) is a widely used cathode material in lithium-ion batteries (LIBs). However, the recycling of electrode materials has gained significant attention due to environmental concerns and energy demands. To lower recycling costs and maximize the utilization of transition metals in used LIB cathodes, Chen *et al.*, 2016<sup>31</sup> developed a method to transform recycled LCO from spent LIBs into an efficient electrocatalyst for the oxygen evolution reaction (OER). Firstly, the LCO based LIB's were cycled for different cycles from 100 to 500C and then were tested for their electrocatalytic performance. It was observed that the activity of the LCO catalyst improved as the number of cycles in the LIBs increased. The improvement in OER activity was attributed to the formation of a new phase of Li<sub>1-x</sub>CoO<sub>2</sub> and the surface corrosion of LCO during the Li<sup>+</sup> insertion and extraction process. These results suggest that spent LIBs cathode material can serve as an efficient, durable, economical, and earth-abundant electrocatalyst for OER, with promising potential for practical applications. However, there is also reduced oxygen evolution reaction (OER) performance observed in nickel-manganese-cobalt (NMC) battery materials after extensive cycling which can be

attributed to several interrelated factors like, (A) Structural Degradation and Oxygen Loss: Prolonged cycling of NMC cathodes leads to structural deterioration, often accompanied by the release of lattice oxygen<sup>110</sup>. (B) Electrolyte Oxidation and Surface Reactions: At elevated voltages, especially above 4.4 V, NMC cathodes can release reactive lattice oxygen, which interacts with the electrolyte, leading to its oxidation and decomposition. This process results in the formation of surface films and the depletion of active sites essential for OER, thereby reducing catalytic efficiency<sup>111</sup>.

## 2.7. Conclusion

From the literature review a lot of work is being reported on various electrocatalysts for both the OER and HER. It is also envisaged that noble metal based electrocatalysts like Pt, Ru and Ir are not suitable for large scale rollout of commercial electrolyzers. Therefore, research is diverted either towards alloying noble metal based electrocatalyst or working on non-noble metal based electrocatalysts. However, there are several areas that could be investigated and discovered. Therefore, the major objectives of the present research work are recovery of electrocatalytic materials from spent NiMH battery and Lithium-ion batteries and to observe the electrocatalytic properties of transition metals like Ni-Fe from NiMH batteries, Ni, Mn and Co (NMC) and LFP from spent Li-ion batteries. Thus, apart from the fact that these elements have excellent electrochemical properties, this research proposes an approach to recover them from spent batteries and reuse them to synthesise an efficient OER, HER or bifunctional electrocatalyst for overall water splitting. Thus, to synthesise an efficient electrocatalysts for a variety of applications such as water splitting for green hydrogen production and potentially CO<sub>2</sub> conversion to useful products. For example, very little work in direct repurposing of cathode into electrocatalyst is carried and secondly, it can help in reducing the cost and complexity of recycling.

## References

- 1 D. Guo, J. Qi, W. Zhang and R. Cao, *ChemSusChem*, 2017, **10**, 394–400.
- 2 S. Liu, Z. Li, C. Wang, W. Tao, M. Huang, M. Zuo, Y. Yang, K. Yang, L. Zhang, S. Chen, P. Xu and Q. Chen, *Nat. Commun.*, , DOI:10.1038/s41467-020-14565-w.
- 3 S. Wang, A. Lu and C. J. Zhong, *Nano Converg.*, , DOI:10.1186/s40580-021-00254-x.
- 4 C. Hu, L. Zhang and J. Gong, *Energy Environ. Sci.*, 2019, **12**, 2620–2645.
- 5 D. Strmcnik, M. Uchimura, C. Wang, R. Subbaraman, N. Danilovic, D. Van Der Vliet, A. P. Paulikas, V. R. Stamenkovic and N. M. Markovic, *Nat. Chem.*, 2013, **5**, 300–306.
- 6 A. P. O'Mullane, 2020.
- 7 J. Lin, Y. Yan, C. Li, X. Si, H. Wang, J. Qi, J. Cao, Z. Zhong, W. Fei and J. Feng, *Nanomicro Lett.*, 2019, **11**, 1–11.
- 8 E. Skúlason, G. S. Karlberg, J. Rossmeisl, T. Bligaard, J. Greeley, H. Jónsson and J. K. Nørskov, *Phys. Chem. Chem. Phys.*, 2007, **9**, 3241–3250.
- 9 N. A. Kelly, *Hydrogen production by water electrolysis*, 2014.
- 10 J. Zhang, Q. Zhang and X. Feng, 2019.
- 11 X. Cao, T. Wang and L. Jiao, *Advanced Fiber Materials*, 2021, **3**, 210–228.
- 12 L. Xie, Q. Liu, X. Shi, A. M. Asiri, Y. Luo and X. Sun, *Inorg. Chem. Front.*, 2018, **5**, 1365–1369.
- 13 R. B. Levy and M. Boudart, *Science*, 1973, **181**, 547–549.
- 14 P. Liu and J. A. Rodriguez, *J. Am. Chem. Soc.*, 2005, **127**, 14871–14878.
- 15 B. Hinnemann, P. G. Moses, J. Bonde, K. P. Jørgensen, J. H. Nielsen, S. Horch, I. Chorkendorff and J. K. Nørskov, *J. Am. Chem. Soc.*, 2005, **127**, 5308–5309.
- 16 N. M. Marković, S. T. Sarraf, H. A. Gasteiger and P. N. Ross, *Journal of the Chemical Society, Faraday Transactions*, 1996, **92**, 3719–3725.
- 17 S. Trasatti, *J. Electroanal. Chem. Interfacial Electrochem.*, 1972, **39**, 163–184.
- 18 T. R. Cook, D. K. Dogutan, S. Y. Reece, Y. Surendranath, T. S. Teets and D. G. Nocera, *Chem. Rev.*, 2010, **110**, 6474–6502.

- 19 D. J. Cole-Hamilton, *Elements of Scarcity*, .
- 20 N. T. Suen, S. F. Hung, Q. Quan, N. Zhang, Y. J. Xu and H. M. Chen, *Chem. Soc. Rev.*, 2017, **46**, 337–365.
- 21 J. K. Nørskov, J. Rossmeisl, A. Logadottir, L. Lindqvist, J. R. Kitchin, T. Bligaard and H. Jónsson, *J. Phys. Chem. B*, 2004, **108**, 17886–17892.
- 22 I. C. Man, H. Y. Su, F. Calle-Vallejo, H. A. Hansen, J. I. Martínez, N. G. Inoglu, J. Kitchin, T. F. Jaramillo, J. K. Nørskov and J. Rossmeisl, *ChemCatChem*, 2011, **3**, 1159–1165.
- 23 H. Li, C. Tsai, A. L. Koh, L. Cai, A. W. Contryman, A. H. Fragapane, J. Zhao, H. S. Han, H. C. Manoharan, F. Abild-Pedersen, J. K. Nørskov and X. Zheng, *Nat. Mater.*, 2016, **15**, 364.
- 24 A. Grimaud, O. Diaz-Morales, B. Han, W. T. Hong, Y. L. Lee, L. Giordano, K. A. Stoerzinger, M. T. M. Koper and Y. Shao-Horn, *Nat. Chem.*, 2017, **9**, 457–465.
- 25 Y. Zhu, H. A. Tahini, Z. Hu, Z. G. Chen, W. Zhou, A. C. Komarek, Q. Lin, H. J. Lin, C. T. Chen, Y. Zhong, M. T. Fernández-Díaz, S. C. Smith, H. Wang, M. Liu and Z. Shao, *Adv. Mater.*, 2020, **32**, 1–8.
- 26 D. Zhong, T. Li, D. Wang, L. Li, J. Wang, G. Hao, G. Liu, Q. Zhao and J. Li, *Nano Res.*, 2022, **15**, 162–169.
- 27 J. S. Yoo, X. Rong, Y. Liu and A. M. Kolpak, *ACS Catal.*, 2018, **8**, 4628–4636.
- 28 B. Jiang and Z. Li, *J. Solid State Chem.*, , DOI:10.1016/j.jssc.2020.121912.
- 29 Z. Li, H. Feng, M. Song, C. He, W. Zhuang and L. Tian, 2021.
- 30 N. Chen, J. Qi, X. Du, Y. Wang, W. Zhang, Y. Wang, Y. Lu and S. Wang, *RSC Adv.*, 2016, **6**, 103541–103545.
- 31 U. K. Sultana, J. F. S. Fernando and A. P. O'Mullane, *Sustain. Mater. Technol.*, , DOI:10.1016/j.susmat.2020.e00177.
- 32 P. Babar, A. Lokhande, V. Karade, B. Pawar, M. G. Gang, S. Pawar and J. H. Kim, *Journal of Colloid and Interface Science*, 2019, **537**, 43–49.

- 33 R. Farzana, M. A. Sayeed, J. Joseph, K. Ostrikov, A. P. O'Mullane and V. Sahajwalla, *ChemElectroChem*, 2020, **7**, 2073–2080.
- 34 S. Natarajan, S. Anantharaj, R. J. Tayade, H. C. Bajaj and S. Kundu, *Dalton Trans.*, 2017, **46**, 14382–14392.
- 35 U. K. Sultana, J. D. Riches and A. P. O'Mullane, *Adv. Funct. Mater.*, 2018, **28**, 1–8.
- 36 U. K. Sultana and A. P. O'Mullane, *ChemElectroChem*, 2019, 2630–2637.
- 37 Y. Uchino, T. Kobayashi, S. Hasegawa, I. Nagashima, Y. Sunada, A. Manabe, Y. Nishiki and S. Mitsushima, *Electrocatalysis*, 2018, **9**, 67–74.
- 38 M. Abu Sayeed, C. Woods, J. Love and A. P. O'Mullane, *ChemElectroChem*, 2020, **7**, 4369–4377.
- 39 J. Wei, S. Zhao, L. Ji, T. Zhou, Y. Miao, K. Scott, D. Li, J. Yang and X. Wu, *Resour. Conserv. Recycl.*, 2018, **129**, 135–142.
- 40 X. Xu, Z. Huang, C. Zhao, X. Ding, X. Liu, D. Wang, Z. Hui, R. Jia and Y. Liu, *Ceramics International*, 2020, **46**, 13125–13132.
- 41 Y. Li, X. Bao, D. Chen, Z. Wang, N. Dewangan, M. Li, Z. Xu, J. Wang, S. Kawi and Q. Zhong, 2019.
- 43 Z. Jin, P. Li and D. Xiao, *Green Chem.*, 2016, **18**, 1459–1464.
- 44 J. X. Feng, S. Y. Tong, Y. X. Tong and G. R. Li, *J. Am. Chem. Soc.*, 2018, **140**, 5118–5126.
- 45 Y. Pan, K. Sun, S. Liu, X. Cao, K. Wu, W. C. Cheong, Z. Chen, Y. Wang, Y. Li, Y. Liu, D. Wang, Q. Peng, C. Chen and Y. Li, *J. Am. Chem. Soc.*, 2018, **140**, 2610–2618.
- 46 H. Cao, Y. Xie, H. Wang, F. Xiao, A. Wu, L. Li, Z. Xu, N. Xiong and K. Pan, *Electrochim. Acta*, 2018, **259**, 830–840.
- 47 J. Chen, Z. Guo, Y. Luo, M. Cai, Y. Gong, S. Sun, Z. Li and C. J. Mao, *ACS Sustain. Chem. Eng.*, 2021, **9**, 9436–9443.
- 48 X. Xu, Z. Xia, X. Zhang, R. Sun, X. Sun, H. Li, C. Wu, J. Wang, S. Wang and G. Sun, *Appl. Catal. B*, 2019, **259**, 118042.
- 49 T. Liu, Y. Zou and D. Liu, *Int. J. Veh. Des.*, 2016, **70**, 98–112.

- 50 Y. Lin, K. Sun, S. Liu, X. Chen, Y. Cheng, W. C. Cheong, Z. Chen, L. Zheng, J. Zhang,  
X. Li, Y. Pan and C. Chen, *Adv. Energy Mater.*, 2019, **9**, 1–12.
- 51 X. Han, C. Yu, H. Huang, W. Guo, C. Zhao, H. Huang, S. Li, Z. Liu, X. Tan, Z. Gao,  
J. Yu and J. Qiu, *Nano Energy*, 2019, **62**, 136–143.
- 52 J. B. Goodenough and K. S. Park, *J. Am. Chem. Soc.*, 2013, **135**, 1167–1176.
- 53 S. Fang, D. Bresser and S. Passerini, *Adv. Energy Mater.*, ,  
DOI:10.1002/aenm.201902485.
- 54 D. Liu, H. Ai, M. Chen, P. Zhou, B. Li, D. Liu, X. Du, K. H. Lo, K. W. Ng, S. P. Wang,  
S. Chen, G. Xing, J. Hu and H. Pan, *Small*, 2021, **2007557**, 1–10.
- 55 V. R. Jothi, R. Bose, H. Rajan, C. Jung and S. C. Yi, *Advanced Energy Materials*, 2018,  
**8**, 1–11.
- 56 J. Maya-Cornejo, A. Garcia-Bernabé and V. Compañ, *Int. J. Hydrogen Energy*, 2018,  
**43**, 872–884.
- 57 B. M. Hunter, H. B. Gray and A. M. Müller, *Chem. Rev.*, 2016, **116**, 14120–14136.
- 58 R. Shi, J. Wang, Z. Wang, T. Li and Y. F. Song, *J. Energy Chem.*, 2019, 74–80.
- 59 J. Lin, P. Wang, H. Wang, C. Li, X. Si, J. Qi, J. Cao, Z. Zhong, W. Fei and J. Feng,  
*Advanced Science*, , DOI:10.1002/advs.201900246.
- 60 A. Li, Y. Sun, T. Yao and H. Han, *Chemistry*, 2018, **24**, 18334–18355.
- 61 W. Lv, Z. Wang, H. Cao, Y. Sun, Y. Zhang and Z. Sun, *ACS Sustainable Chemistry  
and Engineering*, 2018, **6**, 1504–1521.
- 62 X. Wang, G. Gaustad, C. W. Babbitt and K. Richa, *Resour. Conserv. Recycl.*, 2014, **83**,  
53–62.
- 63 X. Zeng and J. Li, *Front. Environ. Sci. Eng.*, 2014, **8**, 792–796.
- 64 R. Geyer and V. Doctori Blass, *Int. J. Adv. Manuf. Technol.*, 2010, **47**, 515–525.
- 65 A. U. N. Izzati, H. T. B. M. Petrus and A. Prasetya, *IOP Conf. Ser. Earth Environ. Sci.*, ,  
DOI:10.1088/1755-1315/882/1/012002.
- 66 K. Edström, T. Gustafsson and J. O. Thomas, *Electrochim. Acta*, 2004, **50**, 397–403.

- 67 B. L. Ellis, K. T. Lee and L. F. Nazar, *Chem. Mater.*, 2010, **22**, 691–714.
- 68 V. Etacheri, R. Marom, R. Elazari, G. Salitra and D. Aurbach, *Energy Environ. Sci.*, 2011, **4**, 3243–3262.
- 69 P. E. Karthik, H. Rajan, V. R. Jothi, B. I. Sang and S. C. Yi, *Journal of Hazardous Materials*, 2022, 421.
- 70 J. O. Bockris and T. Otagawa, *J. Electrochem. Soc.*, 1984, **131**, 290–302.
- 71 *Journal Applied Electrochemistry*, 1983, **15**, 29–38.
- 72 H. Willems, A. G. C. Kobussen, I. C. Vinke, J. H. W. De Wit and G. H. J. Broers, *J. Electroanal. Chem. Interfacial Electrochem.*, 1985, **194**, 287–303.
- 73 M. Li and Y. Xiong Xiaotian Liu Xiangjie Bo Yufan Zhang Ce Hana Guo, *Facile synthesis electro spun MFe<sub>2</sub>O<sub>4</sub> (M = Co,Ni, Cu, Mn) spinel nanofibers excellent electrocatalytic properties oxygen evolution hydrogen peroxide reduction*, .
- 74 S.-Y. Zhang, H.-L. Zhu and Y.-Q. Zheng, *Electrochim. Acta*, 2019, **299**, 281–288.
- 75 *Construction Fe<sub>2</sub>O<sub>3</sub>@CuO Heterojunction Nanotubes Enhanced Oxygen Evolution Reaction*, .
- 76 X. Xiong, C. You, Z. Liu, A. M. Asiri and X. Sun, *ACS Sustain. Chem. Eng.*, 2018, **6**, 2883–2887.
- 77 P. Sivakumar, P. Subramanian, T. Maiyalagan, A. Gedanken and A. Schechter, *Mater. Chem. Phys.*, 2019, **229**, 190–196.
- 78 T. Priamushko, R. Guillet-Nicolas, M. Yu, M. Doyle, C. Weidenthaler, H. Tuysuz and F. Kleitz, *ACS Appl. Energy Mater.*, 2020, **3**, 5597–5609.
- 79 K. E. Salem, A. A. Saleh, G. E. Khedr, B. S. Shaheen and N. K. Allam, *Energy Environ. Mater.*, 2022, 1–13.
- 80 A. Pendashteh, J. Palma, M. Anderson and R. Marcilla, *Appl. Catal. B*, 2017, **201**, 241–252.
- 81 Y. Wang, D. Y. C. Leung, J. Xuan and H. Wang, *Renew. Sustain. Energy Rev.*, 2016, **65**, 961–977.
- 82 X. Yu and A. Manthiram, *Catal. Sci. Technol.*, 2015, **5**, 2072–2075.

- 83 A. Sivanantham, P. Ganesan and S. Shanmugam, *Adv. Funct. Mater.*, 2016, **26**, 4661–4672.
- 84 P. Xu, L. Qiu, L. Wei, Y. Liu, D. Yuan, Y. Wang and P. Tsakaras, *Catal. Today*, 2020, **355**, 815–821.
- 85 H. Liang, A. N. Gandi, D. H. Anjum, X. Wang, U. Schwingenschlögl and H. N. Alshareef, *Nano Lett.*, 2016, **16**, 7718–7725.
- 86 T. Liu and P. Diao, *Nano Res.*, 2020, **13**, 3299–3309.
- 87 X. Wu, Y. Lin, Y. Ji, D. Zhou, Z. Liu and X. Sun, *ACS Applied Energy Materials*, 2020, **3**, 2959–2965.
- 88 T. Wu, S. Sun, J. Song, S. Xi, Y. Du, B. Chen, W. A. Sasangka, H. Liao, C. L. Gan, G. G. Scherer, L. Zeng, H. Wang, H. Li, A. Grimaud and Z. J. Xu, *Nature Catalysis*, 2019, **2**, 763–772.
- 89 J. Huang, Y. Sun, Y. Zhang, G. Zou, C. Yan, S. Cong, T. Lei, X. Dai, J. Guo, R. Lu, Y. Li and J. Xiong, *Advanced Materials*, , DOI:10.1002/adma.201705045.
- 90 M. Luo, Z. Cai, C. Wang, Y. Bi, L. Qian, Y. Hao, L. Li, Y. Kuang, Y. Li, X. Lei, Z. Huo, W. Liu, H. Wang, X. Sun and X. Duan, *Nano Research*, 2017, **10**, 1732–1739.
- 91 X. Meng, J. Han, L. Lu, G. Qiu, Z. L. Wang and C. Sun, *Small*, 2019, **15**, 1–10.
- 92 R. Guo, X. Lai, J. Huang, X. Du, Y. Yan, Y. Sun, G. Zou and J. Xiong, *ChemElectroChem*, 2018, **5**, 3822–3834.
- 93 G. M. Carroll, D. K. Zhong and D. R. Gamelin, *Energy Environ. Sci.*, 2015, **8**, 577–584.
- 94 M. W. Kanan and D. G. Nocera, *Science*, 2008, **321**, 1072–1075.
- 95 S. Cobo, J. Heidkamp, P.-A. Jacques, J. Fize, V. Fourmond, L. Guetaz, B. Jousselme, V. Ivanova, H. Dau, S. Palacin, M. Fontecave and V. Artero, *Nat. Mater.*, 2012, **11**, 802–807.
- 96 Y. Liu, H. Wang, D. Lin, C. Liu, P. C. Hsu, W. Liu, W. Chen and Y. Cui, *Energy and Environmental Science*, 2015, **8**, 1719–1724.

- 97 B. Cui, C. Liu, J. Zhang, J. Lu, S. Liu, F. Chen, W. Zhou, G. Qian, Z. Wang, Y. Deng, Y. Chen and W. Hu, *Science China Materials*, 2021, **64**, 2710–2718.
- 98 S. Anantharaj, S. Kundu and S. Noda, *Nano Energy*, 2021, **80**, 105514.
- 99 A. Hickling and S. Hill, *Discuss. Faraday Soc.*, 1947, **1**, 236.
- 100 N. Li, D. K. Bediako, R. G. Hadt, D. Hayes, T. J. Kempa, F. von Cube, D. C. Bell, L. X. Chen and D. G. Nocera, *Proc. Natl. Acad. Sci. U. S. A.*, 2017, **114**, 1486–1491.
- 101 M. Görlin, J. Ferreira de Araújo, H. Schmies, D. Bernsmeier, S. Dresp, M. Gliech, Z. Jusys, P. Chernev, R. Krahnert, H. Dau and P. Strasser, *J. Am. Chem. Soc.*, 2017, **139**, 2070–2082.
- 102 M. B. Stevens, C. D. M. Trang, L. J. Enman, J. Deng and S. W. Boettcher, *J. Am. Chem. Soc.*, 2017, **139**, 11361–11364.
- 103 T. Müller and B. Friedrich, *J. Power Sources*, 2006, **158**, 1498–1509.
- 104 V. Innocenzi, N. M. Ippolito, I. De Michelis, M. Prisciandaro, F. Medici and F. Vegliò, *J. Power Sources*, 2017, **362**, 202–218.
- 105 V. Innocenzi and F. Vegliò, *J. Power Sources*, 2012, **211**, 184–191.
- 106 C. C. Hu and Y. R. Wu, *Mater. Chem. Phys.*, 2003, **82**, 588–596.
- 107 Y. Ullal and A. C. Hegde, *International Journal of Hydrogen Energy*, 2014, **39**, 10485–10492.
- 108 M. Durovi, J. Hn and K. Bouzek, , DOI:10.1016/j.jpowsour.2021.229708.
- 109 M. A. Sayeed, J. F. S. Fernando and A. P. O'Mullane, *Adv. Sustain. Syst.*, 2018, **2**, 1–7.
- 110 Y. Chu, Y. Mu, L. Zou, F. Wu, L. Yang, Y. Feng and L. Zeng, *ChemElectroChem*, , DOI:10.1002/celc.202300653.
- 111 W. M. Dose, W. Li, I. Temprano, C. A. O'Keefe, B. L. Mehdi, M. F. L. De Volder and C. P. Grey, *ACS Energy Lett.*, 2022, **7**, 3524–3530.

# Chapter 3

## Research Design

This chapter elaborates on the research methodology used for this thesis that includes experimental and characterisation techniques.

### 3.1 Electrochemical method

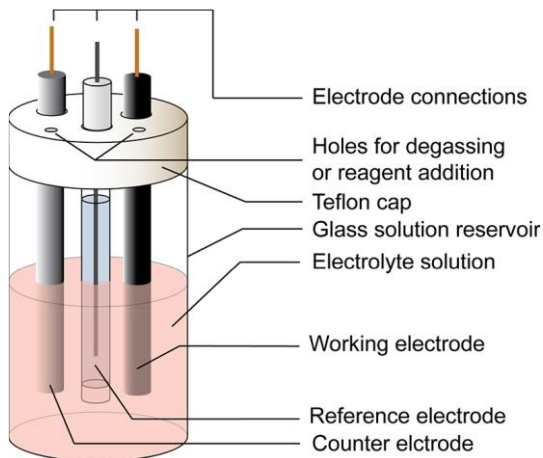


**Figure: 3.1** Three electrode setup <sup>1</sup>

A conventional three-electrode setup was employed for all electrochemical experiments at room temperature ( $22 \pm 3^\circ\text{C}$ ) using a Biologic VSP workstation controlled by EC-Lab software (version 11.34). A high-purity graphite carbon rod (1 mm diameter, Johnson Matthey Ultra “F” purity grade) and a leakless Ag/AgCl (3M KCl) electrode (eDAQ Pty Ltd) was used as the counter and reference electrodes, respectively.

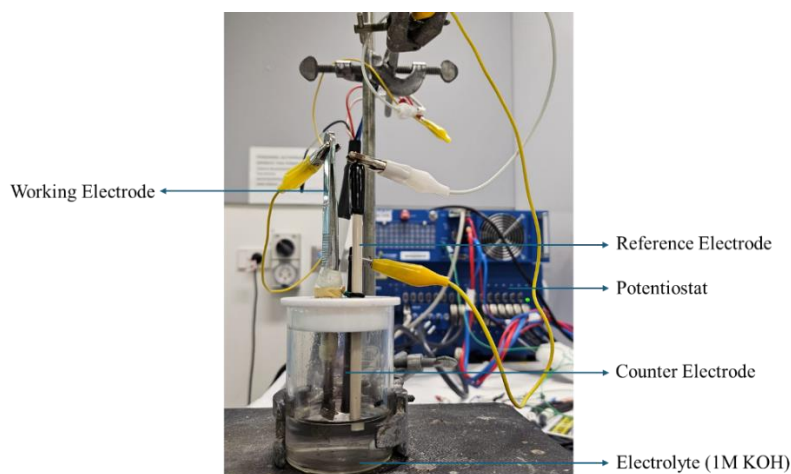


**Figure 3.2:** Three electrode electrochemical cell

The working electrodes were individually prepared for each sample, for example to carry out experiments related to repurposing the current collector from a Toyota Prius battery module, working electrodes were prepared from NF (Nickel Foam) and the FNC (Fe/Ni current collector). Electrodes were ultrasonically cleaned for 30 min after cutting them for appropriate dimensions and then dried for 1 h in air (also described in Chapter 4). The current density was normalised to the geometric surface area of the electrode, taking the perforated (mesh) form of the FNC electrode into account.



**Figure 3.3:** Fe-Ni mesh sheet used for experimentation.

For the work related to NMC and LFP materials, Nickel Foam (NF)( $1 \times 1.5 \text{ cm}^2$ ) was cleaned with 3 M HCl to remove surface oxides and then sonicated in acetone, ethanol and deionised water for 30 min each followed by drying overnight at 60 degrees.



**Figure 3.4:** Ni foam used for experimentation

The electrochemical cell was oxygen-saturated, and all experiments were conducted on a standard laboratory bench. After testing, the working electrodes were rinsed with Milli-Q water (resistance 18.2 MΩ cm) to remove residual electrolyte and dried at room temperature for further characterization. All measurements were performed in a 1 M KOH electrolyte solution.

The recorded potentials were converted to the RHE scale using the equation:

$$E_{\text{RHE}} = E_{\text{Ag}/\text{AgCl}} + (0.059 \times pH) + 0.197 \text{ V} \quad (1)$$

The overpotential ( $\eta$ ) for the oxygen evolution reaction (OER) was determined using:

$$\eta = E_{\text{RHE}} - 1.23 \text{ V} \quad (2)$$

### 3.2 Ink Preparation Method

1 mg of NMC/LFP catalyst was dissolved in Nafion (100 μL) (purchased from Sigma Aldrich) and ethanol/water solvent in a 1:1. The mixture was stirred followed by 60 min sonication to disperse it. Around 300 μL of ink was then used for immersing the NMC or LFP material on the nickel foam.



**Figure 3.5:** Ink preparation method, Reused with permission Copyright © 2021 Elsevier Inc)<sup>2</sup>

The prepared electrode was dried at 60° overnight and then in an oven at room temperature (also described in Chapter 5 & 6). The current density was normalised to the geometric surface area of the electrode (1×1 cm<sup>2</sup>).

Table: 3.1 Preparation of the INK

<b>Sample</b>	<b>Nafion</b>	<b>Catalyst (mg)</b>	<b>Ethanol/Water (1:1)</b>
1.	5% (50 µL)	1	950 µL
2.	10% (100 µL)	1	900 µL
3.	5% (50 µL)	5	950 µL
4.	10% (100 µL)	5	900 µL
5.	5% (50 µL)	10	950 µL
6.	10% (100 µL)	10	900 µL

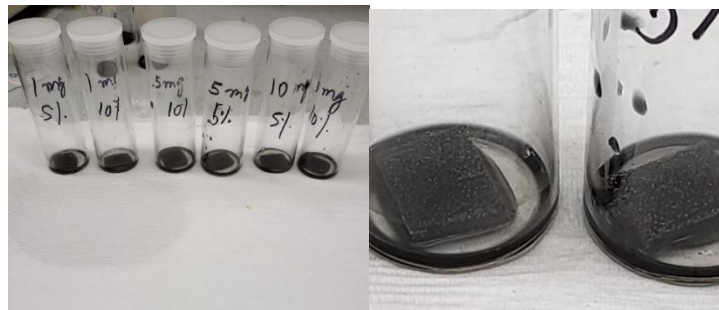


**Figure 3.6:** Electrode preparation

### 3.3 Characterisation Techniques

Samples were analysed with various characterisation techniques like Scanning Electron Microscopy (SEM), Transmission Electron Microscopy (TEM), Energy Dispersive X-ray Spectroscopy (EDS or EDX), X-ray Photoelectron Spectroscopy and X-ray Diffraction (XRD).

#### 3.3.1 Scanning Electron Microscopy (SEM)

Scanning Electron Microscopy (SEM) is a powerful imaging technique used to obtain high-resolution images of the surface morphology and composition of materials. It operates by focusing a beam of high-energy electrons onto a specimen, which interacts with the material surface, producing various signals such as secondary electrons, backscattered electrons, and characteristic X-rays. These signals provide detailed information about the sample topography, texture, and elemental composition. In the present research work the morphology of the samples was analysed by scanning electron microscopy (SEM) using a JEOL 7001F electron microscope at an operating voltage of 5 kV <sup>3</sup>.



**Figure 3.7:** JEOL 7001F electron microscope for understanding surface morphology of samples.

### 3.3.2 Transmission Electron Microscopy (TEM)

Transmission Electron Microscopy (TEM) is a high-resolution imaging technique used to study the internal structure, morphology, and composition of materials at the nanometer and atomic scale. Unlike Scanning Electron Microscopy (SEM), which provides surface images, TEM operates by transmitting a high-energy electron beam through an ultrathin sample. As the electrons pass through the sample, they interact with the material, producing contrast based on variations in thickness, density, and composition. The transmitted electrons are then focused by electromagnetic lenses to form a highly magnified image on a detector or screen. TEM is widely used in materials science, nanotechnology, biology, and semiconductor research for analysing crystallographic structures, defects, interfaces, and nanoparticles.

Advanced TEM techniques, such as High-Resolution TEM (HRTEM), Selected Area Electron Diffraction (SAED), and Energy Dispersive X-ray Spectroscopy (EDS), further enhance its capabilities by providing atomic-level imaging, crystallographic information, and elemental composition analysis. Despite its exceptional resolution, TEM requires extensive sample preparation and operates under high vacuum conditions. For the current research work HRTEM, SAED, and STEM-EDS measurements were performed using a JEOL 2100 TEM instrument operating at an accelerating voltage of 200 kV. The JEOL 2100 machine was

equipped with a high-sensitivity OXFORD 80 mm<sup>2</sup> silicon drift X-ray detector for accurate elemental analysis and JEOL BF/DF detectors for STEM imaging <sup>4</sup>.



**Figure 3.8:** JEOL 2100 HR-TEM Transmission Electron Microscope, used for used for imaging of samples.

### 3.3.3 Energy Dispersive X-ray Spectroscopy (EDS or EDX)

Energy Dispersive X-ray Spectroscopy (EDS or EDX) is an analytical technique used for elemental composition analysis in conjunction with Scanning Electron Microscopy (SEM) or Transmission Electron Microscopy (TEM). EDS operates by detecting characteristic X-rays emitted from a sample when it is bombarded with high-energy electrons. Each element in the sample produces a unique X-ray emission spectrum, allowing for qualitative and quantitative identification of the elements present. The technique provides rapid and localized elemental analysis, making it widely applicable in materials science, nanotechnology, metallurgy, forensics, and biological research. While EDS is highly effective for elemental mapping and composition analysis and for the experiments related to current research energy dispersive spectroscopy (EDS) was performed for elemental analysis using a JEOL 7001F electron microscope at an operating voltage 15 kV, respectively <sup>3</sup>.

### 3.3.4 X-ray Photoelectron Spectroscopy

X-ray Photoelectron Spectroscopy (XPS) is a surface-sensitive analytical technique used to determine the elemental composition, chemical state, and electronic structure of materials. It operates by irradiating a sample with X-rays, typically from an aluminum (Al K $\alpha$ ) or magnesium (Mg K $\alpha$ ) source, causing core electrons to be ejected from the atoms in the material. The kinetic energy of these emitted electrons is measured, and based on the binding energy calculations, the specific elements and their oxidation states can be identified. XPS is widely used in materials science, nanotechnology, catalysis, corrosion studies, and thin-film analysis due to its ability to provide detailed chemical state information and depth profiling. However, it is limited to analysing the top few nanometers of a sample and requires an ultra-high vacuum environment for operation<sup>5</sup>.



**Figure 3.9:** Kratos Supra Xray Photoelectron Spectroscope used for analysing the Oxidation states of samples.

In the present research, X-ray photoelectron spectroscopy (XPS) data was collected using an Omicron Multiclan Lab Ultra-High Vacuum Scanning Tunnelling Microscope (UHV-STM) where a 125 mm hemispherical electron energy analyser was incorporated. XPS measurements were performed using non-monochromatic Mg K $\alpha$  (1253.6 eV) X-ray source (DAR 400, Omicron Nanotechnology), and the incident angle was 65° to the sample surface. The analyser pass energy of 50 eV with steps of 0.5 eV and the dwell time was 200ms. High-resolution scans with a narrow region for Ni 2p, Mn 2p, Co 2p, C 1 s and O 1 s were taken at 20 eV pass energy, 0.2 eV steps and with a 200ms dwell time. Besides a wide scan of low

binding energy region was performed from 250 eV to 0 eV swept at high resolution. The base pressure in the analysis chamber was  $1.0 \times 10^{-9}$  Torr and the pressure was  $1.0 \times 10^{-8}$  Torr during the measurement.

### 3.3.5 X-ray Diffraction (XRD)

X-ray Diffraction (XRD) is described as a powerful and widely used technique for determining the crystallographic structure, phase composition, and other characteristics of materials. The key principle behind XRD is the diffraction of X-rays by the regularly spaced planes of atoms in a crystalline material. When X-rays are directed onto a crystalline sample, they are scattered by the planes of atoms in the crystal lattice. The diffraction pattern that results from this scattering provides valuable information about the material's internal structure. The diffraction pattern is analysed by applying Bragg's Law:

$$n\lambda = 2d\sin\theta \quad (3)$$

Where  $n$  is an integer (typically 1),  $\lambda$  is the wavelength of the X-rays,  $d$  is the distance between planes of atoms (interplanar spacing), and  $\theta$  is the angle of diffraction. The diffraction pattern reveals the spacing between these planes and, in turn, the arrangement of atoms in the crystal. For the present research powder XRD patterns were collected and analysed using a Rigaku Smart Lab diffractometer<sup>6</sup>.

## 3.4 Electrochemical Techniques

Electrochemistry serves as an effective method for investigating reactions that involve electron transfer, as it connects the movement of electrons to resulting chemical transformations.

### 3.4.1 Cyclic voltammetry (CV)

Cyclic voltammetry (CV) is a widely used and highly effective electrochemical technique for analysing the oxidation and reduction processes of molecular species. The outlines in Figure 3.10 are known as voltammograms or cyclic voltammograms. The x-axis represents the applied potential ( $E$ ), while the y-axis denotes current ( $I$ ) flow. Figure 3.10 includes an arrow that indicates the direction of the potential scan used to collect the data. A key parameter is introduced and is known as the scan rate ( $v$ ), represents the rate at which the potential was varied linearly during the experiment, at a speed of  $100 \text{ mV s}^{-1}$  per second.

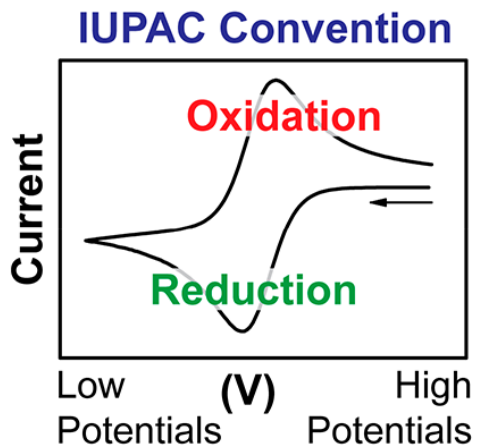


**Figure 3.10:** General cyclic voltammetry profile open access with licence CC BY-NC-ND<sup>7</sup>

The Nernst equation establishes a relationship between the potential of an electrochemical cell ( $E$ ), the standard potential of a species ( $E^\circ$ ), and the relative activities of the oxidized (Ox) and reduced (Red) forms of the analyte at equilibrium. In this equation,  $F$  represents Faraday's constant,  $R$  is the universal gas constant,  $n$  denotes the number of electrons involved, and  $T$  is the temperature

$$E = E^\circ + \frac{RT}{nF} \ln \frac{(Ox)}{Red} = E^\circ + 2.3026 \frac{RT}{nF} \log_{10} \frac{(Ox)}{(Red)} \quad (4)$$

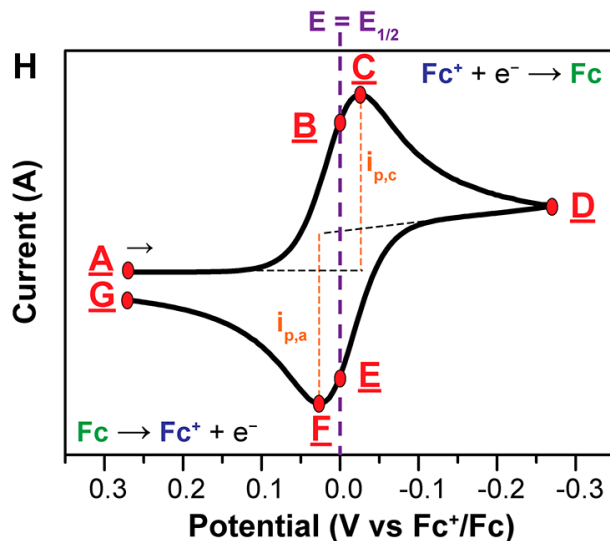


**Figure 3.11:** Voltammogram of the reversible reduction for species Fc open access with licence CC BY-NC-ND<sup>7</sup>.

For example, reduction of ferrocene ( $Fc$ ) species is presented in Figure 3.11 and explained as follows. As the potential is scanned negatively (cathodically) from point A to point D (Figure 3), the concentration of  $[Fc^+]$  near the electrode gradually decreases as it

undergoes reduction to Fc. At point C, where the peak cathodic current ( $I_{p,c}$ ) is observed, the current is primarily controlled by the diffusion-driven replenishment of  $\text{Fc}^+$  from the bulk solution. The diffusion layer, which is the region near the electrode containing the reduced Fc, continues to expand during the scan. This expansion slows the mass transport of  $\text{Fc}^+$  to the electrode surface, leading to a decline in current as the scan progresses further in the negative direction ( $C \rightarrow D$ ). Upon reaching the switching potential at point D, the scan direction is reversed, and the potential is swept in the positive (anodic) direction. As a result of the prior reduction process, the concentration of  $\text{Fc}^+$  at the electrode surface is depleted, while Fc accumulates, maintaining equilibrium as described by the Nernst equation. During the anodic scan, Fc at the electrode surface undergoes oxidation back to  $\text{Fc}^+$  as the potential becomes more positive. At points B and E, the concentrations of  $\text{Fc}^+$  and Fc at the electrode surface are equal, satisfying the Nernst equation, where  $E = E_{1/2}$ . This corresponds to the midpoint potential between the two peaks (C and F), providing a simple method to estimate the formal reduction potential ( $E_{o'}$ ) for a reversible electron transfer<sup>7</sup>. The separation of the two peaks arises due to the diffusion of the analyte to and from the electrode.

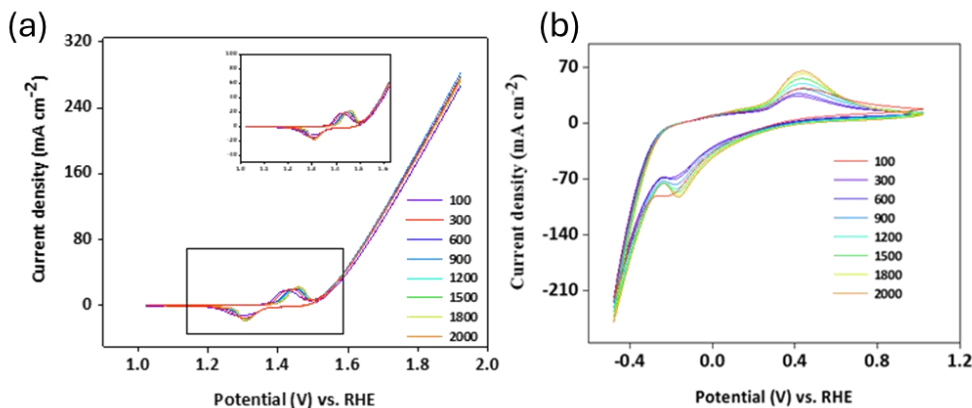


**Figure 3.12 (a, b):** CVs recorded at  $100 \text{ mV s}^{-1}$  for 2000 cycles in  $1 \text{ M KOH}$  in the OER region, HER region for the FNC electrode (Reused With Permission Copyright © 2023 Royal Society of Chemistry<sup>8</sup>).

In the present work (Figure 3.12), CV is used to obtain a comprehensive knowledge of electrochemical reactions and electron transfer reactions. Thus, it deals with the location of potentials of various species and how the catalyst behaves in the redox reaction process. And 2000 CV cycles are observed from 0 to -1.5 V for Hydrogen evolution reaction with the sweep rate of 100mV/sec. Similarly, for oxygen evolution reaction the potential is between 0 to 0.9V with the sweep rate of 100mV/sec for 2000 CV cycles.

### 3.4.2. Linear Sweep Voltammetry

It is an electrochemical technique used to study redox reactions by applying a linearly varying potential to an electrode while measuring the resulting current. It provides insight into the kinetics and thermodynamics of electron transfer processes. In LSV, the electrode potential is swept at a constant rate in one direction, typically starting from a region where no reaction occurs and moving toward a potential where redox reactions take place. The measured current is plotted against the applied potential to generate a voltammogram.

As the potential reaches the redox potential of the analyte, an increase in current is observed due to oxidation or reduction. The current initially rises due to an increase in the reaction rate, but as the analyte near the electrode surface is depleted, the current eventually reaches a peak and then declines, primarily due to diffusion limitations. Unlike cyclic voltammetry (CV), where the potential is scanned forward and then reversed, LSV only applies a potential sweep in a single direction<sup>9</sup>. Here in this work for HER the potential is between -1 to -1.5V with sweep rate of 0.1mV/sec and for OER the potential applied is between 0.3-0.9 V with sweep rate of 0.1mV/s<sup>8</sup> (Figure 3.13).

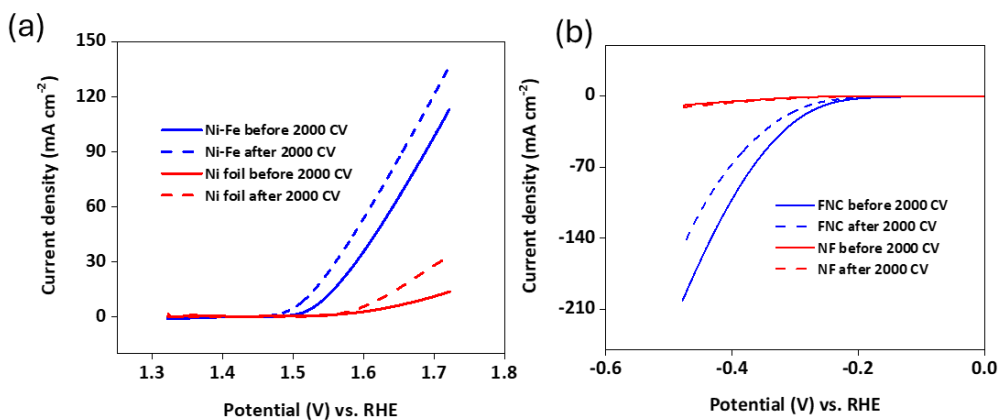


**Figure 3.13 (a, b):** LSVs recorded at Fe/Ni current collector and nickel foam electrodes before and after 2000 potential cycles for OER and HER regions at  $0.1\text{mV s}^{-1}$  (Reused With Permission Copyright © 2023 Royal Society of Chemistry)<sup>8</sup>.

### 3.4.3. Chronoamperometric Techniques

Chronoamperometry is an electrochemical technique that examines the variation of current over time under potentiostat control. In a simple redox system,



where only the oxidized species (O) or the reduced species (R) is initially present, the resulting current is the Faradaic current  $I_f$ , which arises solely from the electron transfer process. In current research, this technique is used to measure the stability of the electrocatalyst. A potential is applied to the working electrode and the current of the electrode is measured as a function of time and also referred in Figure 15 (Chapter 2) presenting stability measurements of the electrode.

### 3.4.4. Tafel slope

The Tafel slope is a parameter used in electrochemistry to describe the relationship between the overpotential and the current density during an electrochemical reaction, typically in the context of a redox process. It is obtained from the Tafel equation, which relates the rate of an electrochemical reaction to the applied overpotential. The Tafel slope provides insight into the kinetics of the reaction, specifically the rate at which the reaction rate increases with an increase in overpotential. The Tafel equation is expressed as:

$$\eta = a + b \log (j) \quad (6)$$

Where  $\eta$  is the overpotential (the difference between the applied potential and the equilibrium potential),  $a$  is a constant related to the exchange current density and the reaction mechanism.,  $b$  is the Tafel slope,  $j$  the current density. The Tafel slope ( $b$ ) is a critical parameter for understanding the kinetics of an electrochemical reaction. It is typically determined from the linear region of a plot of  $\eta$  versus  $\log(j)$ , known as a Tafel plot <sup>9</sup>. Figure 3.14 presents Tafel plots of Fe/Ni mesh and Ni foil electrodes before and after 2000 CV cycles (a) OER, (b) HER<sup>8</sup>.

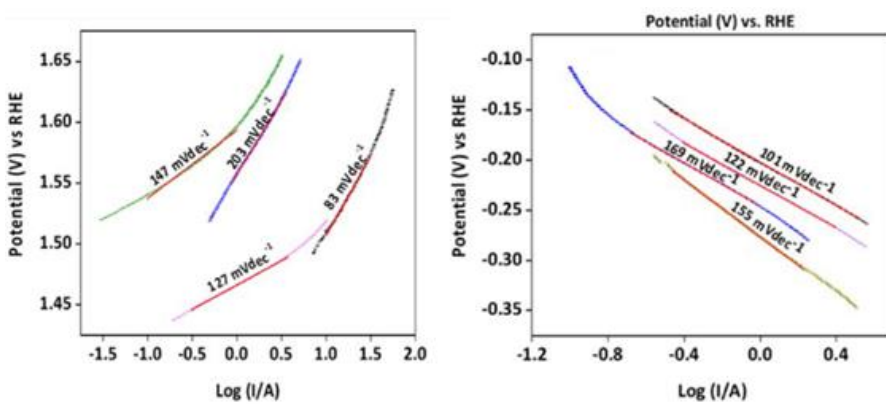


**Figure 3.14:** Tafel plots of Fe/Ni mesh and Ni foil electrodes before and after 2000 CV cycles (a) OER, (b) HER<sup>8</sup>.

### 3.4.5. Electrochemical Surface Area (ECSA)

The electrochemically active surface area (ECSA) of each system was estimated based on the electrochemical double-layer capacitance of the catalytic surface. This capacitance was determined using two approaches: (1) by analysing the non-Faradaic capacitive current linked to double-layer charging as a function of scan rate in cyclic voltammograms and (2) by evaluating the frequency-dependent impedance of the system through electrochemical impedance spectroscopy (EIS) as presented in Figure 3.16<sup>10</sup>. In this case, the measurement of double-layer charging using cyclic voltammetry (CV) is involved identifying a potential range where no significant Faradaic processes take place. The ECSA of the catalyst is calculated from the double layer capacitance according to the equation <sup>11</sup>.

$$\text{ECSA} = \frac{C_{DL}}{C_s} \quad (7)$$

Where  $C_{DL}$  is double layer capacitance (Ni Foam in present studies) ( $\mu\text{F}$ ) and  $C_s$  is the specific capacitance of the smooth surface ( $\mu\text{F cm}^{-2}$ ). Using the estimated specific capacitance of  $40 \text{ mF cm}^{-2}$  for NiFe oxides in alkaline solutions the ECSA of the studied electrode <sup>41,149</sup>. The double-layer capacitance ( $C_{DL}$ ) of the electrode surface was calculated from the slope of the anodic charging currents plotted against the scan rates. Normally, the scan rates were obtained between  $10-100 \text{ mV s}^{-1}$  at  $25^\circ\text{C}$ . From the CVs, the average capacitive current,  $I_{dl}$  is calculated. The linear slope of  $I_{dl}$  as a function of scan rates makes it possible to determine  $C_{DL}$  foam <sup>14</sup> as per equation; Here,  $I_c$  and  $I_a$  are cathodic and anodic currents. For obtaining the ECSA data cyclic voltammetric experiments recorded at different sweep rates for electrodes in  $1 \text{ M KOH}$  after repetitive cycling for 2000 cycles are presented in Figure 3.15.

$$I_{dl} = \frac{|I_c| + |I_a|}{2} \quad (8)$$

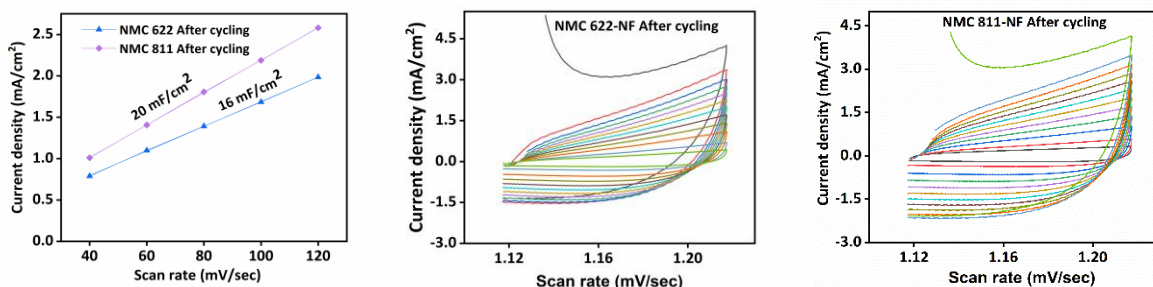


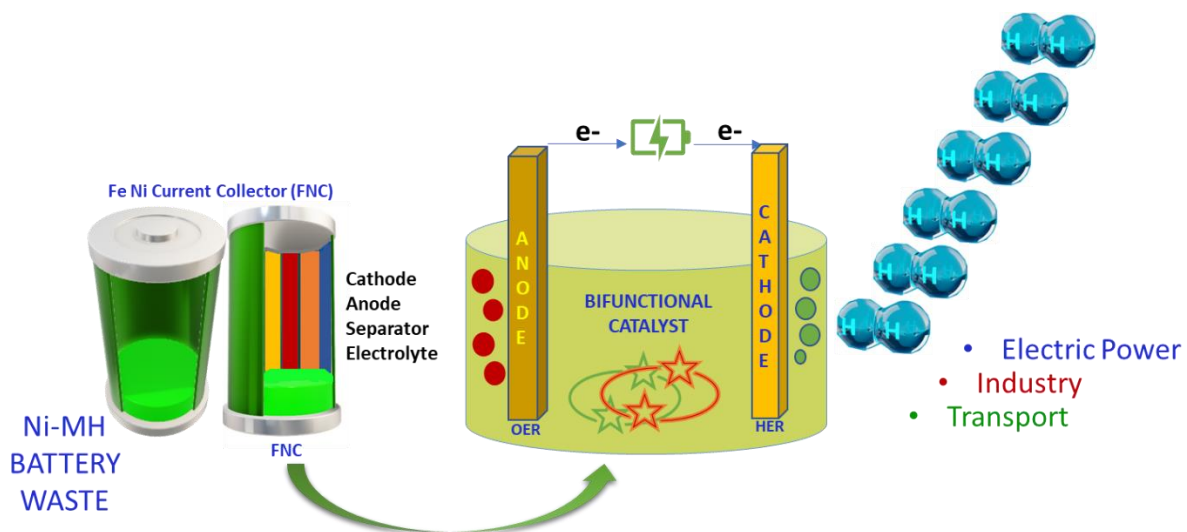
**Figure 3.15:** Current density V sweep rate from data obtained from cyclic voltammetric experiments recorded at different sweep rates for NMC 622-NF and NMC 811-NF electrodes in  $1 \text{ M KOH}$  after repetitive cycling for 2000 cycles CC BY-NC 4.0<sup>10</sup>.

## References

- (1) Zhang, T.; Xue, Z.; Xie, Y.; Huang, G.; Peng, G. Fabrication of a Boron-Doped Nanocrystalline Diamond Grown on an WC-Co Electrode for Degradation of Phenol. *RSC Adv.* **2022**, *12* (41), 26580–26587.
- (2) Vazhayil, A.; Vazhayal, L.; Thomas, J.; Ashok C, S.; Thomas, N. A Comprehensive Review on the Recent Developments in Transition Metal-Based Electrocatalysts for Oxygen Evolution Reaction. *Applied Surface Science Advances* **2021**, *6*, 100184.
- (3) Oldstein, J.; Newbury, D. E.; Joy, D. C.; Lyman, C. E.; Echlin, P.; Lifshin, E.; Sawyer. *Scanning Electron Microscopy X-Ray Microanalysis*; Springer, 2017.
- (4) Williams, D. B.; Carter, C. B. *Transmission Electron Microscopy: Textbook Materials Science*; Springer, 2009.
- (5) Briggs, D.; Grant, J. T. *Surface Analysis Auger X-Ray Photoelectron Spectroscopy*; IM Publications, 2003.
- (6) Klug, H. P.; Alexander, L. E. *X-Ray Diffraction Procedures Polycrystalline Amorphous Materials*; Wiley-Interscience, 1974.
- (7) Elgrishi, N.; Rountree, K. J.; McCarthy, B. D.; Rountree, E. S.; Eisenhart, T. T.; Dempsey, J. L. A Practical Beginner’s Guide to Cyclic Voltammetry. *J. Chem. Educ.* **2018**, *95* (2), 197–206.
- (8) Kaur, A.; Khosravi, M.; O’Mullane, A. P. Repurposing the Current Collector of a Car Battery Module into a Bifunctional Electrode for Overall Electrochemical Water Splitting. *Sustain. Energy Fuels* **2023**, *7* (10), 2486–2494.
- (9) Brett, C.; Oliveira Brett, A. M. *Electrochemistry: Principles, Methods, and Applications*; Oxford University Press: London, England, 1993.
- (10) Kaur, A.; Alarco, J.; Mullane, A. P. O. Investigating the Potential Use of Ni-Mn-Co (NMC) Battery Materials as Electrocatalysts for Electrochemical Water Splitting. *Chemphyschem* **2024**, *25* (14), e202400124.
- (11) McCrory, C. C. L.; Jung, S.; Peters, J. C.; Jaramillo, T. F. Benchmarking Heterogeneous Electrocatalysts for the Oxygen Evolution Reaction. *Journal of the American Chemical Society* **2013**, *135* (45), 16977–16987.
- (12) Guo, D.; Qi, J.; Zhang, W.; Cao, R. Surface Electrochemical Modification of a Nickel Substrate to Prepare a NiFe-Based Electrode for Water Oxidation. *ChemSusChem* **2017**, *10* (2), 394–400.
- (13) Lu, X.; Zhao, C. Electrodeposition of Hierarchically Structured Three-Dimensional Nickel-Iron Electrodes for Efficient Oxygen Evolution at High Current Densities. *Nat. Commun.* **2015**, *6* (1), 6616.
- (14) Santos, A. L.; Cebola, M. J.; Antunes, J.; Santos, D. M. F. Insights on the Performance of Nickel Foam and Stainless Steel Foam Electrodes for Alkaline Water Electrolysis. *Sustain. Sci. Pract. Policy* **2023**, *15* (14), 11011.

# Chapter 4

## Repurposing the current collector of a car battery module into a bifunctional electrode for overall electrochemical water splitting.



The following paper has been published in a peer reviewed journal based in this chapter.

Arshdeep Kaur, Monireh Khosravi and Anthony P. O'Mullane, “Repurposing the current collector of a car battery module into a bifunctional electrode for overall electrochemical water splitting”, **Sustainable Energy & Fuels**, 7, 2486-2494, 2023. DOI:

<https://doi.org/10.1039/D3SE00232B>

The authors listed below have certified that:

1. They meet the criteria for authorship and that they have participated in the conception, execution, or interpretation, of at least that part of the publication in their field of expertise.
2. They take public responsibility for their part of the publication, except for the responsible author who accepts overall responsibility for the publication.
3. There are no other authors of the publication according to these criteria.
4. Potential conflicts of interest have been disclosed to (a) granting bodies, (b) the editor or publisher of journals or other publications, and (c) the head of the responsible academic unit, and
5. They agree to the use of the publication in the student's thesis and its publication on the QUT's ePrints site consistent with any limitations set by publisher requirements.

<b>Contribution</b>	<b>Statement of Contribution</b>
<i>Arshdeep Kaur</i>	Methodology, investigation, data curation, writing – original draft
<i>Monireh Khosravi:</i>	Conceptualisation, investigation, data curation, supervision, writing – review & editing
<i>Anthony O'Mullane</i>	Conceptualisation, methodology, resources, supervision, funding acquisition, writing – review & editing

#### **4.1 Abstract**

Renewable power-driven electrochemical water splitting is rapidly emerging as a viable approach for producing large scale green hydrogen which is free from greenhouse emissions. However, there is a continuous need to develop electrocatalysts that are abundant and can be generated with minimal impact on the environment. Here, we explore the possibility of repurposing the current collector from a Toyota Prius battery module as a bifunctional electrocatalyst that can be used for overall electrochemical water splitting under alkaline conditions. The Ni coated iron electrode was found to have ideal properties for both the oxygen evolution reaction (OER) and hydrogen evolution reaction (HER) while also demonstrating bifunctional behaviour for both reactions upon repetitive cycling. The repurposed material also outperformed a Ni electrode of comparable surface area for both the OER and HER. Overpotential values of 250 mV (OER) and 260 mV (HER) and low Tafel slope values of  $83 \text{ mV dec}^{-1}$  (OER) and  $101 \text{ mV dec}^{-1}$  (HER) indicated good electrochemical activity comparable to chemically synthesised catalysts. The key aspect for enabling this behaviour was found to be the emergence of iron into the nickel layer to create a stable mixed FeNi oxide layer upon potential cycling of the electrode. This work indicates that not only the active materials used in rechargeable batteries should be used for recycling but that the current collectors should also be considered as potentially highly valuable components

#### **4.2 Introduction**

Global energy demand has increased dramatically in recent decades due to population growth and the extraordinary increase in industrial development. Governments in developed countries have failed to act which is largely due to the resistance mounted by the fossil fuel industry.<sup>1</sup> The ubiquitous use of coal, oil and gas has therefore resulted in the generation of extremely harmful levels of greenhouse gases. This is now at point where global warming is manifesting as highly frequent extreme weather events.<sup>2</sup> Indeed, a recent study has indicated that staying below  $1.5^\circ\text{C}$  would require governments and companies to cease developing new fields and mines while also prematurely decommissioning a large number of existing assets.<sup>3</sup> Therefore, there is a significant research effort being carried out on developing renewable energy driven approaches to significantly reduce fossil fuel use. Hydrogen as an energy carrier has been identified as a promising alternative to alleviate fossil fuel dependency.<sup>4</sup> Consequently, green hydrogen production from electrochemical water splitting has attracted a lot of attention as it is a zero-emission technology if powered by renewable energy sources.<sup>5-7</sup>

Electrochemical water splitting can be divided into two half-cell reactions which are the oxygen evolution reaction (OER) and the hydrogen evolution reaction (HER).<sup>8,9</sup> To facilitate these reactions, electrocatalysts are used to reduce the overpotential while increasing the kinetics of electron transfer associated with each half reaction. One major limitation is the sluggish electron transfer kinetics of the OER and therefore there is a need to develop electrocatalysts that minimises this effect.<sup>8</sup>

Noble metal based electrocatalysts, in particular platinum group metals and their oxides (Pt, Pd, Ir, Ru and Rh) are excellent catalysts for electrochemical water splitting reactions.<sup>10, 11</sup> However, their cost, scarcity and use in many other applications has put them on the endangered elements list,<sup>12</sup> and will therefore slow the widespread deployment of electrolyzers that wish to use these catalysts. Therefore, studies on transition metal oxides/hydroxides like Ni, Mn, Co and Fe for the OER<sup>4, 13-18</sup> and metal-based carbides,<sup>19</sup> transition metal phosphides<sup>20</sup> and transition metal chalcogenides (sulphides and selenides)<sup>21, 22</sup> for the HER as alternative electrocatalysts have gained significant attention. A more recent development is the synthesis of bifunctional materials that can act as both HER and OER electrocatalysts<sup>23-27</sup> which can help simplify the catalyst manufacturing process for electrolyzers. It is of particular benefit if the material produced can be switched between the HER and OER without losing activity for both reactions.<sup>23, 28</sup> This would be appropriate for electrolyzers directly connected to intermittent renewable energy sources that suffer from rapid shut down and turn on processes that can severely impact electrolyser performance due to reverse current processes that occur during these periods.<sup>29, 30</sup> This scenario is of particular interest for remote communities that are typically powered by gas turbines or diesel and would offer a way of reducing emissions while also offering more energy security, long term economic return and community empowerment.<sup>31</sup>

A significant environmental issue that is emerging and will continue to increase is the extensive generation of battery waste.<sup>32</sup> This will become particularly important with the rapid uptake of electric vehicles, grid level storage of renewable energy as well as domestic energy storage. Furthermore for countries like Australia, the Australian standard for electronic waste recycling (AS/NSZ 5377:2013) does not acknowledge the disposal of waste batteries to landfill,<sup>33, 34</sup> thus, around 8000 tonnes of batteries end up in landfill in Australia each year. This results in significant land pollution due to chemical leaching from the batteries, threatening human health and the environment.<sup>32, 35-37</sup> However, this also offers an opportunity to recycle spent batteries and recover valuable materials. Promisingly, new recycling methods and future battery recycling infrastructure are being developed.<sup>32, 36-38</sup> One particular opportunity in this area is to use recovered materials for electrocatalytic applications, in particular electrochemical water splitting as many battery chemistries possess compositions that are amenable to these reactions.<sup>39, 40</sup> For example, Chen et al.,<sup>41</sup> converted LiCoO<sub>2</sub> from spent lithium-ion batteries into efficient electrocatalysts for the OER. Babar et al.,<sup>42</sup> developed a pathway to utilise e-waste from waste copper wires with efficient OER performance while Farzana et al.,<sup>15</sup> synthesised Mn<sub>3</sub>O<sub>4</sub> from a spent Zn-C battery, with high electrochemical performance for the OER in an alkaline electrolyte.

In this work, we examine a Ni metal hydride battery taken from a Toyota Prius battery module and investigate whether the current collector used in this battery, with minimal treatment, can be used as a water splitting electrocatalyst. The motivation for investigating this material is that it comprises of both Fe and Ni which has been shown to be a highly active OER electrocatalysts in alkaline conditions when used as a mixed Fe/Ni oxide/oxyhydroxide material.<sup>14, 43-52</sup>

### 4.3 Results and discussion

As mentioned in the Experimental section the Fe/Ni current collector (FNC) from the battery module is in the form of a mesh as shown in Figure S1. To identify the composition of the electrode material SEM/EDX analysis was initially undertaken as shown in Figure 4.1. A cross section image shows that the current collector electrode which has a thickness of 52 µm is in fact an iron support coated with a thin layer of Ni (ca. 4 µm thick) on both sides of the electrode. ICP-OES (Inductively Coupled Plasma – Optical Emission Spectroscopy) analysis showed that the the nickel content was 5% of the sample. Given that the Fe/Ni combination has been found to be highly active for the OER in alkaline electrolyte, in particular, the material was investigated for this reaction and benchmarked against a Ni electrode.

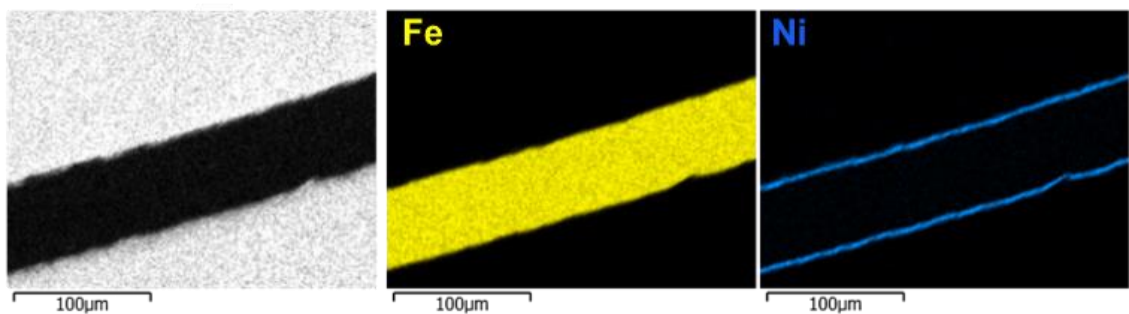


**Figure 4.1:** Cross sectional SEM image and EDS map showing the distribution of Fe and Ni in the FNC electrode.

Initially, repetitive cyclic voltammetric experiments (20 cycles) were performed on FNC (Figure 4.2a) and NF electrodes (Figure 4.2b). These experiments indicate that the FNC electrode passes higher current density for both the OER and HER when compared to a NF electrode when normalised to geometric area. Both electrodes show typical redox behaviour for Ni with an oxidation peak at ca. 1.40 V and a corresponding reduction peak at ca. 1.30 V which is attributed to the  $\text{Ni}^{2+/\text{3}+}$  redox couple. It can be seen for the FNC electrode (Figure 4.2a) that there is a second redox process with an oxidation peak at ca. 0.36 V and a cathodic counterpart at ca. -0.08 V, which is attributed to the  $\text{Fe}^{2+/0}$  redox couple. This is an interesting observation for the FNC electrode as it indicates that the electrolyte can immediately access the underlying Fe in the electrode as the response was observed in the first potential cycle (Figure 4.2a).

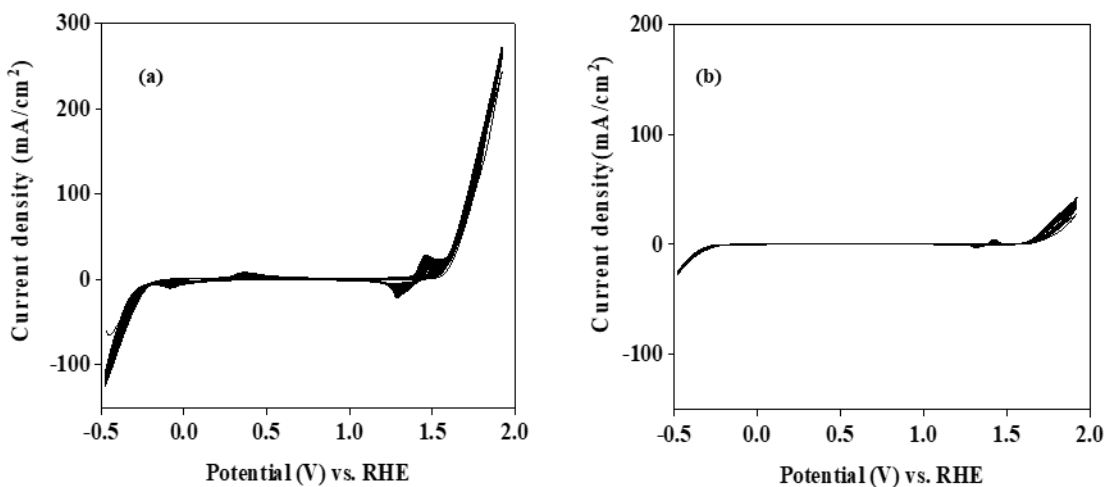


**Figure 4.2:** Cyclic voltammograms recorded at  $100 \text{ mV sec}^{-1}$  for 20 cycles at (a) FNC and (b) NF electrodes in 1 M KOH.

The OER was then studied for both the NF and FNC electrodes without initiating the HER and therefore the potential window was limited to 1.05 to 1.90 V vs RHE (Figure 4.3a). Prior to repetitive potential cycling, a linear sweep voltammogram (LSV) was recorded (at  $0.1 \text{ mV s}^{-1}$ ) (Figure 4.3b) to characterise the performance of the recycled material. This resulted in an onset potential value of 1.52 V and an overpotential value at  $10 \text{ mA cm}^{-2}$  ( $\eta_{10}$ ) of 290 mV. The FNC electrode was then subjected to repetitive potential cycling for 2000 cycles at  $100 \text{ mV s}^{-1}$  to check for stability. At this higher sweep rate, the  $\text{Ni}^{2+/\text{3}^+}$  redox process is apparent and gradually shifts to more positive potentials as the number of cycles increases. This is an indication that the surface chemistry is gradually changing upon repetitive cycling and may be due to the presence of the underlying Fe. Previous reports have demonstrated that the incorporation of Fe into Ni oxide/hydroxide materials results in a shift in potential for the Ni redox process as mentioned in the work presented by Deng et al.<sup>53</sup> However, the stability of the FNC electrode is good with little decrease in the current density being passed even when high values of  $275 \text{ mA cm}^{-2}$  are being reached.

After the cyclic voltammetric stability tests, a LSV was repeated to monitor any change in the onset and over potential values (a reduced potential window with an upper limit of 1.75 V was used to minimise bubble formation at the slow sweep rate). After 2000 cycles a decrease in the onset potential and  $\eta_{10}$  values to 1.48 V and 250 mV, respectively (Figure 3b) were observed for the FNC electrode indicating a marked increase in performance due to the potential cycling process. The NF electrode was subjected to the same electrochemical testing where it can be seen from the LSV data (Figure 4.3b) that the current density values (normalised to the geometric area) for the NF electrode are substantially lower than that for the FNC electrode. As is the case with the FNC electrode, the repetitive potential cycling process also resulted in a marginal increase in OER performance for the NF electrode. The Tafel slope

for FNC after 2000 cycles is  $127 \text{ mV dec}^{-1}$  which is significantly less than the Tafel slope value of NF of  $208 \text{ mV dec}^{-1}$ . From the Tafel slope data the FNC electrode both before and after potential cycling has a lower value than the NF electrode indicating improved electrode transfer kinetics or a difference in the rate determining step.

Chronoamperometry experiments were then performed for the FNC and NF electrodes (Figure 4.3d). A reasonably stable current density recorded at  $1.75 \text{ V}$  for the FNC electrode is obtained which is significantly greater than the current density passed at a NF electrode. The results are consistent with a previous study on a layered type system where an iron ore based catalyst was covered with a layer of  $\text{Ni(OH)}_2$ . It was found that the activity increased and the Tafel slope value gradually decreased from  $127 \text{ mV dec}^{-1}$  to  $72 \text{ mV dec}^{-1}$  upon increasing the  $\text{Ni(OH)}_2$  percentage on the iron ore.<sup>54</sup> Previous work has also demonstrated that amorphous NiFe(oxy)hydroxide mesoporous nanosheets deposited on nickel foam showed excellent activity and stability.<sup>55</sup> It has been suggested that the presence of Fe suppress the higher oxidation states of Ni when it is oxidised prior to the OER which enhances OER activity.<sup>48</sup> This may also explain the gradual shift to more positive potentials in the Ni oxidation process (Figure 4.3a) prior to the OER and indicates that Fe is present in the surface layer of the oxidised FNC electrode.

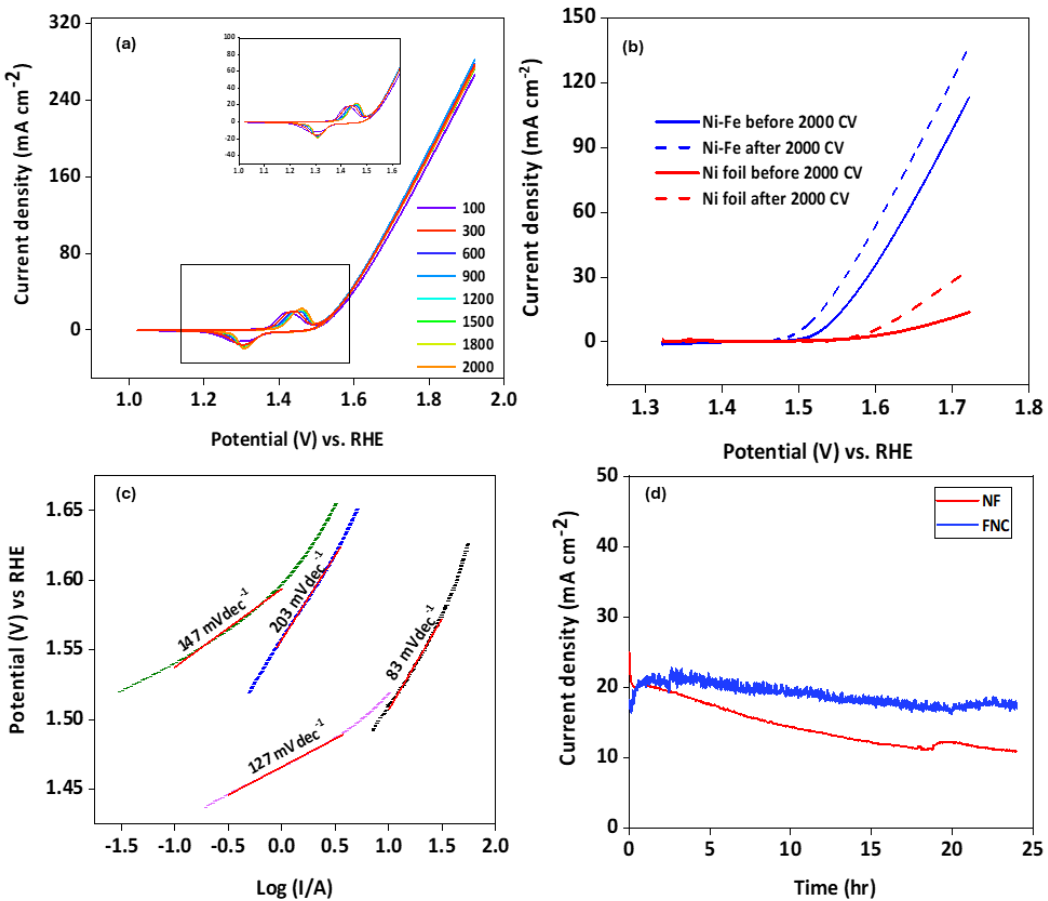


**Figure 4.3:** (a) CVs recorded at 100 mV s<sup>-1</sup> for 2000 cycles in 1 M KOH in the OER region for the FNC electrode and (b) LSVs recorded at FNC and NF electrodes before and after 2000 potential cycles, (c) Tafel plots of FNC and NF electrodes before and after 2000 CV cycles and (d) Chronoamperometric curves recorded for 24 hr period at 1.75V in the OER region.

In an analogous manner to the OER study, the FNC and NF electrodes were initially characterised by a slow sweep rate LSV (Figure 4.4b) followed by repetitive potential cycling for 2000 cycles (1.0 to -0.5 V) at 100 mV s<sup>-1</sup> (Figure 4.4a). The effect of cycling was then determined by analysis of a LSV after the cycling process (Figure 4.4b). For the FNC electrode the Fe<sup>2+/0</sup> redox couple prior to the large increase in current due to the HER is clearly evident and increases in magnitude as the number of cycles increases. This indicates that either the area of the electrode is increasing or more iron becomes exposed at the surface of the electrode upon cycling. It was found that after 2000 cycles that the activity of the FNC electrode decreased slightly as indicated by the lower current density and slightly more negative onset potential (Figure 4.4b). For the NF electrode the cycling process resulted in a marginal increase in HER activity. However, the FNC electrode significantly outperformed the NF electrode in terms of current density and less negative onset potential.

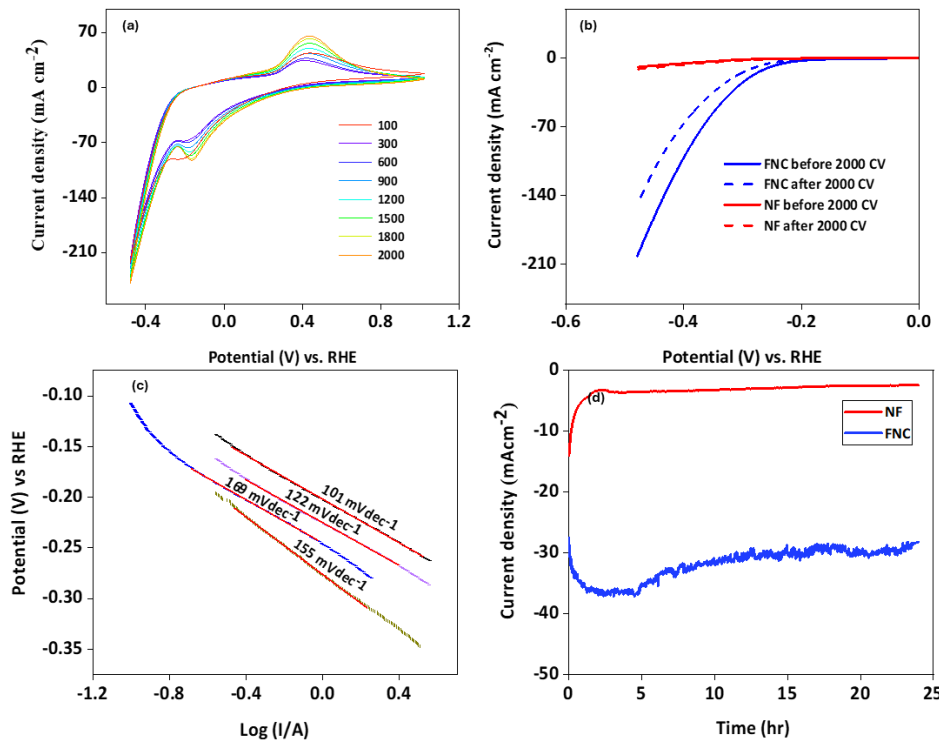


**Figure 4.4:** (a) CVs recorded at 100 mV s<sup>-1</sup> for 2000 cycles in 1 M KOH in the HER region for the FNC electrode and (b) LSVs recorded at FNC and NF electrodes before and after 2000 potential cycles, (c) Tafel plots of FNC and NF electrodes before and after 2000 CV cycles and (d) Chronoamperometric curves recorded for 24 hr period at -0.40 V in the HER region.

The Tafel slope value for FNC ( $101 \text{ mV dec}^{-1}$ ) was found to be lower than NF ( $155 \text{ mV dec}^{-1}$ ) before potential cycling while a similar trend was detected after potential cycling with a lower Tafel slope value for FNC ( $122 \text{ mV dec}^{-1}$ ) than NF ( $169 \text{ mV dec}^{-1}$ ). In both cases there is a slight increase in Tafel slope after potential cycling indicating that this electrochemical treatment impacts performance. The Tafel slope values obtained for all electrodes is consistent with the Volmer-Heyrovsky mechanism where the Volmer step is the rate determining step ( $\text{H}_2\text{O} + \text{e}^- \rightarrow \text{OH}^- + \text{H}_{\text{ad}}$ ).

The consistently lower Tafel slope values for FNC compared to NF can be attributed to the fact that the adsorption of  $\text{H}_2\text{O}$  on Fe sites is more favourable than Ni,<sup>56</sup> which ultimately lowers the energy barrier for the Volmer step on FNC compared to the NF electrode. The Tafel slope values of FNC is comparable with previous studies on Fe/Ni based electrodes such as Chen et al.,<sup>57</sup> where they reported Tafel slopes values of  $161 \text{ mV dec}^{-1}$  and  $274 \text{ mV dec}^{-1}$  for a nickel iron oxyphosphide (NiFeOP) and NiFe layered double hydroxide electrode, respectively, while Messaoudi et al.<sup>58</sup> reported a Tafel slope of  $179 \text{ mV dec}^{-1}$  for a NiFe (3:1) alloy electrocatalyst. Chronoamperometric data in Figure 4.4(d) shows stable current density for FNC with a much higher value than the NF electrode. The performance of this material was then benchmarked in Table S1 against various types of Fe/Ni materials that have been investigated for the OER and HER which shows that the performance of this recycled material is comparable to many electrocatalysts that have been chemically synthesised. To understand the influence of the electrode composition and why the FNC electrode shows such improved performance compared to NF, the material was then extensively characterised.

To observe the surface morphology of FNC, SEM imaging and EDS mapping was performed as shown in Figure 4.5. The surface has a rough texture, however the distribution of Ni and Fe is homogeneous across the sample (the Fe is visible due to the penetration depth of EDX). There is evidence of some pinholes in the Ni layer as seen from the EDS mapping images showing a depletion of Ni and increased Fe content. There is also oxygen present due to some surface oxidation from exposure to the atmosphere, but the content is low (4.4 wt % as seen in Figure S2a). However it can also be seen that the oxygen is localised at the pinholes which is expected as Fe will more readily oxidise than Ni. This data explains why the  $\text{Fe}^{2+/0}$  redox couple (Figure 1a) is immediately apparent from the first cycle in the CV.

After the FNC electrode was subjected to 2000 potential cycles, the morphology of the electrode changed significantly (Figure 4.6). The surface became quite rough and the higher magnification image shows distinct flake like materials formed on the electrode surface which are typical of metal hydroxides such as  $\text{Ni(OH)}_2$ <sup>59</sup> and FeNi layered double hydroxides.<sup>60</sup> It was also noticed that large clusters had formed on the surface of the electrode after cycling. The EDS maps indicate that these clusters are Fe rich and co-located with oxygen, suggesting the formation of iron oxide clusters on the surface of the FNC electrode. The large increase in oxygen content (33.3 wt %, Figure S2b) across the sample is

expected after the electrode had been subjected to 2000 cycles into the OER region. Therefore, this suggests that a Fe/Ni oxidised layer has been formed upon which some iron oxide clusters have formed which results in improved OER activity (Figure 4.2b).

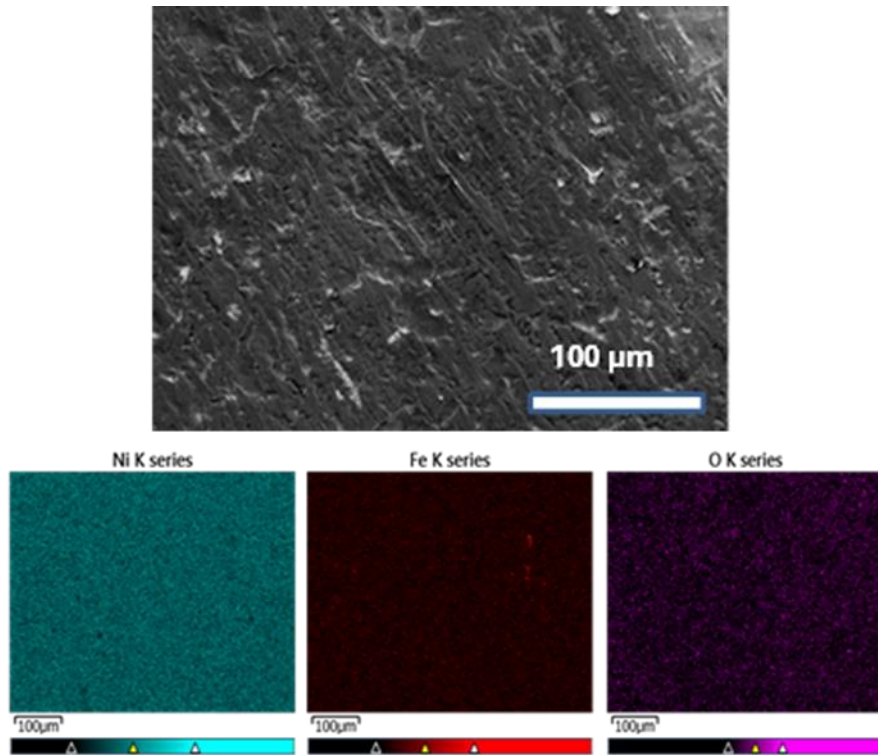


**Figure 4.5.** SEM image and EDS mapping of the as received FNC.

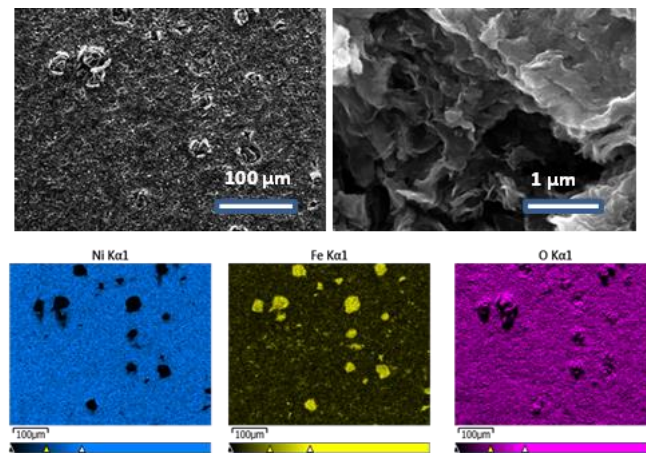


**Figure 4.6:** SEM images and EDS mapping of the FNC electrode after 2000 cycles in the OER potential region (1.05 to 1.9 V, in 1 M KOH).

The FNC electrode after 2000 cycles into the HER region was also investigated by SEM and EDS mapping (Figure 4.7). After this treatment the electrode surface has roughened and interestingly the surface is decorated with iron oxide clusters as seen from the EDS mapping images. The extent of iron oxide cluster formation is less than that seen after 2000 cycles into the OER region (Figure 6),

nevertheless the restructuring of the surface is considerable. This corrosion of the surface under hydrogen evolution conditions was not expected. However previous studies have demonstrated that cathodic corrosion of metal surfaces is possible in alkaline solutions,<sup>61</sup> due to the formation of anionic Zintl-type clusters.<sup>62</sup>

It has also been reported that this cathodic corrosion process can result in the formation of metal oxide nanoparticles.<sup>63</sup> In this case corrosion of the FNC electrode results in precipitation of iron oxide clusters on the surface which is also reflected in the increase of the oxygen content (Figure S2c). This would explain the slight decrease in HER activity after cycling (Figure 4b) as iron oxide is not an active electrocatalyst for the HER.

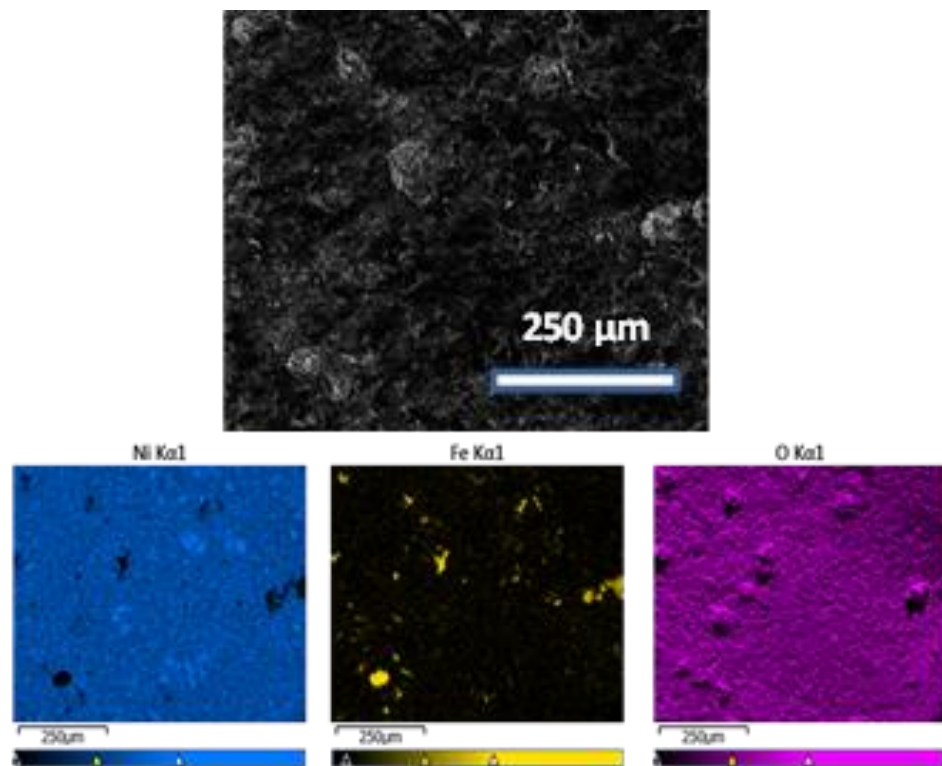


**Figure 4.7:** SEM images and EDS mapping of the FNC electrode after 2000 cycles in the HER potential region (1.05 to -0.50 V, in 1 M KOH).

Given the significant increase in performance of the FNC electrode for the OER compared to NF (Figure 4.3a) and the increase in activity after repetitive potential cycling (Figure 4.3b) the FNC electrode was characterised using XPS for the recovered FNC electrode and the cycled electrode. An XPS survey spectrum confirmed the presence of Ni, Fe and O elements at the surface of the recovered and cycled electrodes. The high-resolution XPS spectrum of Ni 2p shown in Figure 4.8 (a) shows two main peaks that are attributed to Ni 2p<sub>1/2</sub> and Ni 2p<sub>3/2</sub> due to spin-orbit splitting. For the recovered electrode the surface oxidation state is predominantly in the 2+ oxidation state where the Ni 2p<sub>3/2</sub> peak

at 854.5 eV, Ni 2p<sub>1/2</sub> peak at 872.8 eV and two satellite peaks at 860.6 eV and 878.9 eV are consistent with NiO or Ni(OH)<sub>2</sub><sup>64, 65</sup>.

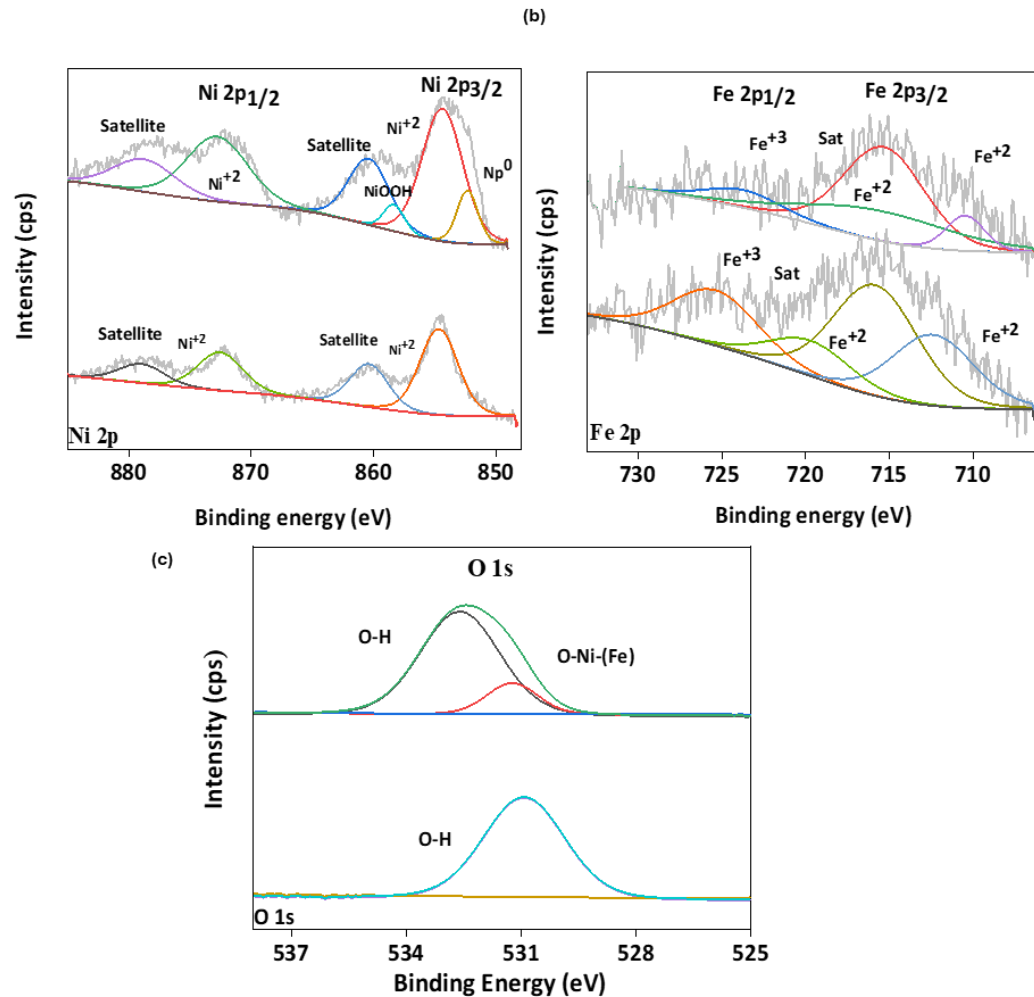


**Figure 4.8:** XPS spectra of Ni 2p, Fe 2p and O 1s where the spectrum (lower) is recovered FNC and spectrum (upper) is the FNC electrode after 2000 cycles in the OER region.

After the OER cycling experiment new peaks were observed at 852.3 eV and 858.4 eV, which could be attributed to metallic Ni<sup>17</sup> and NiOOH<sup>55</sup>, respectively. The high-resolution spectrum of Fe 2p is shown in Figure 4.8 (b). Characteristic peaks of Fe in the +2 and +3 oxidation state<sup>46, 55, 66</sup> are seen for the recovered FNC indicating some surface oxide formation before electrochemical treatment which is expected for any Fe species at the surface of the electrode which would oxidise when exposed to ambient conditions. Similar peaks are observed for the FNC electrode after potential cycling in the OER region, however the intensity is diminished slightly, possibly due to the extensive oxide formation on the electrode surface. High resolution O 1s spectra are shown in Figure 4.8c. For the recovered FNC electrode there is one peak at 530.9 eV which is attributed to M-O (here, M= Fe or Ni) species on the electrode surface. After potential cycling in the OER region, two major peaks are observed at 531.2 eV

and 532.6 eV corresponding to M-O and M-OH species, which is consistent with the formation of NiOOH<sup>67</sup> seen in the Ni 2p spectrum.

The cyclic voltammetric responses for the FNC electrode for the OER (Figure 4.3a) and HER (Figure 4.4a) over 2000 cycles indicate that the electrode could potentially be used as the anode and cathode for overall water splitting. The data shown in Figure 4.2 (a) which covers a potential range incorporating both the HER and OER also indicates that this electrode is tolerant to significant changes in the applied potential without dramatic decreases in activity for both reactions.

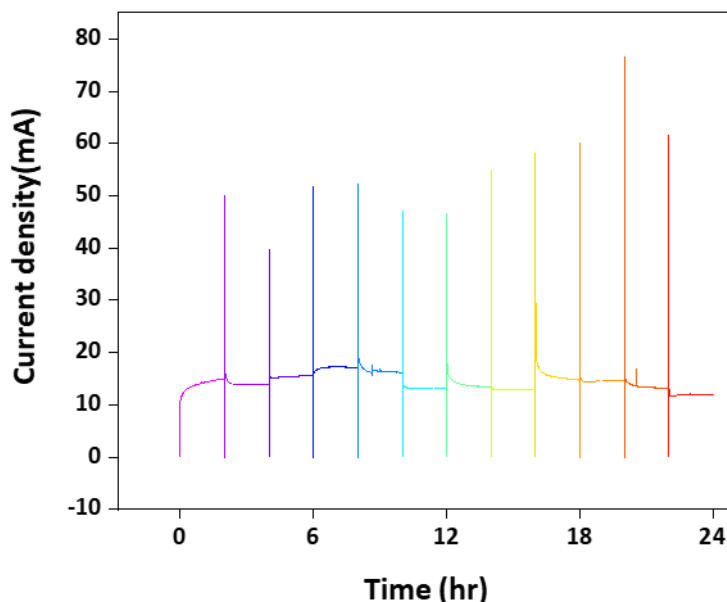


**Figure 4.9:** Dynamic stability test for a two electrode system using a FNC anode and cathode, operated at 1.9 V for 2 h followed by shutdown for 10 min which was repeated for a 24 h period.

This bifunctional behaviour indicates that a two-electrode system for overall water splitting is feasible using this FNC electrode. Commercial alkaline electrolyzers are continuously run at lower capacity when hydrogen production is not required. This is to minimise changes in the potential across the two electrodes upon rapid start up or shut down conditions<sup>29, 30, 68</sup> that impact the composition of the electrodes, in particular the cathode. For systems that may require direct integration with intermittent renewable energy sources, such as in remote areas there may not be sufficient battery backup capacity to facilitate this standby mode of operation, developing an electrolyser with cheap electrodes that can tolerate significant voltage changes could be advantageous in this scenario.

The stability of the FNC electrodes in a two electrode electrolysis system was then subjected to rapid shutdown and start-up conditions that could be faced by commercial electrolyzers directly integrated with a solar or wind energy input<sup>69</sup>. A 2 h period of electrolysis was undertaken followed by rapid shutdown for 10 min after which a further 2 h period of electrolysis was undertaken and this

process was repeated for 24 h (Figure 4.9). A large spike in current is seen upon shutdown and start up for each period which is expected. However, the current passed during electrolysis remained steady over the entire 24 h period, indicating that the FNC electrode is quite tolerant to these harsh operating parameters and may be applicable for a remote system where electrolyzers are integrated directly with intermittent sources of energy. It can be seen from this data that the presence of Fe in the FNC electrode is highly beneficial to the activity of the electrode when compared to the Ni only NF electrode, in particular for the OER.

This enhanced performance has been reported previously for other Fe/Ni systems and is attributed to the formation of a mixed metal oxide layer on the surface of the electrode, containing NiOOH which has been identified by many groups as the active site for the OER. The presence of Fe is believed to suppress the extensive oxidation of Ni species during the OER which results in improved activity. Indeed, it has been reported that  $\beta$ -NiOOH is a more effective OER catalyst than  $\gamma$ -NiOOH as Ni exists as  $\text{Ni}^{3+}$  in the former compared to  $\text{Ni}^{3+}$  in the latter. However, there is still some contention regarding the OER mechanism as it has also been demonstrated that Fe in the 3+ oxidation state is the active site within a mixed  $\text{Ni}_{1-x}\text{Fe}_x\text{OOH}$  oxyhydroxide system.<sup>70</sup> For the FNC electrode the presence of  $\text{Fe}^{3+}$  species was also detected at the electrode surface (Figure 4.8b) and may also contribute to the increased OER activity. Finally in our system the presence of some  $\text{Ni}^0$  under the surface layer of the catalyst as seen in the XPS Ni 2p spectrum (Figure 4.8a) would increase the conductivity of the electrode and enhance electron transfer. For the HER the restructuring of the electrode surface after some cathodic corrosion did impact on the electrode performance, however the enhancement in activity over the NF was still significant. Nevertheless, the electrode performed reasonably well as a HER electrocatalyst and facilitated the use of this electrode as a cathode during overall water splitting without a loss in performance over a 24 h period. It should however also be noted that this work indicates that electrodes of this type, i.e. Ni based electrodes should be carefully examined after HER studies to determine if cathodic corrosion processes have occurred.

It can be seen from this data that the presence of Fe in the FNC electrode is highly beneficial to the activity of the electrode when compared to the Ni only NF electrode, in particular for the OER. This enhanced performance has been reported previously for other Fe/Ni systems and is attributed to the formation of a mixed metal oxide layer on the surface of the electrode, containing NiOOH which has been identified by many groups as the active site for the OER. The presence of Fe is believed to suppress the extensive oxidation of Ni species during the OER which results in improved activity. Indeed, it has been reported that  $\beta$ -NiOOH is a more effective OER catalyst than  $\gamma$ -NiOOH as Ni exists as  $\text{Ni}^{3+}$  in the former compared to  $\text{Ni}^{3.7+}$  in the latter. However, there is still some contention regarding the OER mechanism as it has also been demonstrated that Fe in the 3+ oxidation state is the active site within a mixed  $\text{Ni}_{1-x}\text{Fe}_x\text{OOH}$  oxyhydroxide system.<sup>70</sup> For the FNC electrode the presence of  $\text{Fe}^{3+}$  species was also detected at the electrode surface (Figure 4.8b) and may also contribute to the increased OER

activity. Finally in our system the presence of some Ni<sup>0</sup> under the surface layer of the catalyst as seen in the XPS Ni 2p spectrum (Figure 4.8a) would increase the conductivity of the electrode and enhance electron transfer. For the HER the restructuring of the electrode surface after some cathodic corrosion did impact on the electrode performance, however the enhancement in activity over the NF was still significant. Nevertheless, the electrode performed reasonably well as a HER electrocatalyst and facilitated the use of this electrode as a cathode during overall water splitting without a loss in performance over a 24 h period. It should however also be noted that this work indicates that electrodes of this type, i.e. Ni based electrodes should be carefully examined after HER studies to determine if cathodic corrosion processes have occurred.

#### 4.4 Experimental

##### *Materials and methods*

The Ni-MH battery cell of a Toyota Prius battery module was dismantled manually to separate the Fe/Ni current collector (FNC) from the cathode, separator, and other battery components. The nickel foil (NF) sheet (>99.9% purity) with 0.125 mm thickness was purchased from Sigma Aldrich. Potassium hydroxide (Sigma Aldrich KOH 99.99% purity) and absolute ethanol (Sigma Aldrich) were used without further purification. The Milli-Q water with resistivity of 18.2 MΩ.cm, Milli pack) was used for preparing electrolyte solutions and all washing purposes. Before all electrochemical and characterisation experiments the FNC and NF were ultrasonically cleaned in ethanol for 30 min to remove metal oxides from their surfaces.

##### *Characterisation*

The morphology, micro/nanostructure and qualitative chemical composition of the samples were analysed by scanning electron microscopy (SEM) and energy dispersive spectroscopy (EDS) using a JEOL 7001F electron microscope. X-ray photoelectron spectroscopy (XPS) data were collected using an Omicron Multiclan Lab Ultra-High Vacuum Scanning Tunnelling Microscope (UHV-STM) where a 125 mm hemispherical electron energy analyser was incorporated. Non-monochromatic Mg K $\alpha$  (1253.6 eV) X-ray source (DAR 400, Omicron Nanotechnology) was used for XPS experiments, and the incident angle was 65° to the surface of the sample. The analyser passed energy of 50 eV with steps of 0.5 eV and the dwell time was 200 ms. High-resolution scans with a narrow region for Fe 2p, Ni 2p, Mn 2p, C 1 s and O 1 s were taken at 20 eV pass energy, 0.1 eV steps and with a 200 ms dwell time. Besides a wide scan of low binding energy region was performed from 250 eV to 0 eV swept at high resolution. The base pressure in the analysis chamber was  $1.0 \times 10^{-9}$  Torr and the pressure was  $1.0 \times 10^{-8}$  Torr during the measurement. Atomic compositions of the surface were calculated using the CasaXPS version 2.3.15 software and a linear baseline with Kratos library Relative Sensitivity Factors (RSFs).

### *Electrochemical Measurements*

All electrochemical measurements were conducted in a conventional three electrode cell at room temperature ( $22 \pm 2^\circ\text{C}$ ) using a BioLogic VSP workstation operated by EC-lab software (version 11.34). A graphite carbon rod with high purity (1 mm diameter, Johnson Matthey Ultra “F” purity grade) and a leakless Ag/AgCl (eDAQ Pty Ltd) were used as counter and reference electrodes, respectively. Working electrodes were prepared from NF and the FNC. For each analysis the NF and FNC electrodes were cut in appropriate dimension and then ultrasonically cleaned for 30 min in absolute ethanol and drying for 1 hr in air. The working electrodes were washed with Milli-Q water after electrochemical tests to remove any electrolyte solution from the surface and dried at room temperature for further characterisation. All measurements were conducted in 1 M KOH electrolyte solution. The following equation was used to convert the recorded potential to the RHE scale for all electrochemical measurements:

$$E_{RHE} = E_{Ag/AgCl} + (0.059 \times pH) + 0.197 \text{ V}$$

while the overpotential ( $\eta$ ) for the OER was calculated using the following formula:

$$\eta = E_{RHE} - 1.23 \text{ V}$$

The current density was normalised to the geometric surface area of the electrode, taking the perforated (mesh) form of the FNC electrode into account. Cyclic voltammetry (CV) and linear sweep voltammetry (LSV) techniques were undertaken at  $20 \text{ mV s}^{-1}$  and  $0.1 \text{ mV s}^{-1}$ , respectively.

### **4.5 Conclusions**

The recovery of the current collector from a Toyota Prius battery module was investigated as an electrocatalyst for electrochemical water splitting. It was found that the material was active for both OER and HER reactions due to the composition of the electrode that consisted of an Fe substrate covered by a thin Ni layer. The morphology of the electrode and its surface chemistry was found to change after repetitive cycling in potential regions associated with the OER and HER, which was more pronounced in the latter case. The formation of Fe at the surface of the Ni layer resulted in a mixed Fe/Ni oxide system which was significantly more active for water splitting reactions than a Ni electrode when normalised to the geometric area of the electrodes. The recovered electrode was stable to OER currents of up to  $300 \text{ mA cm}^{-2}$  and HER currents as high as  $150 \text{ mA cm}^{-2}$ . A two electrode system consisting of the recovered electrode as the anode and cathode for performing overall water splitting was also stable to harsh start up and shut down conditions over a 24 period of intermittent electrolysis. Therefore, the recovered current collector from a waste of Ni-MH battery is a potential candidate for use in alkali water electrolysis that is integrated directly with intermittent energy supplies.

#### **4.6 Acknowledgements**

AOM acknowledges funding from the Australian Research Council (DP180102869). The authors acknowledge the instrumentation and technical support of the QUT Central Analytical Research Facility (CARF) and scholarship support through the QUT/Max Planck Institute of Colloids and Interfaces Joint Laboratory on Nanocatalysis for Sustainable Chemistry.

## References

1. T. A. Hansen, *Renewable and Sustainable Energy Reviews*, 2022, **158**, 112144.
2. F. Song, G. J. Zhang, V. Ramanathan and L. R. Leung, *Proc. Natl. Acad. Sci. U. S. A.* , 2022, **119**, e2117832119.
3. K. Trout, G. Muttitt, D. Lafleur, T. Van de Graaf, R. Mendelevitch, L. Mei and M. Meinshausen, *Environmental Research Letters*, 2022, **17**, 064010.
4. A. Vazhayil, L. Vazhayal, J. Thomas, S. Ashok C and N. Thomas, *Applied Surface Science Advances*, 2021, **6**, 100184-100184.
5. S. M. Ibn Shamsah, *Journal*, 2021, **11**.
6. A. Li, Y. Sun, T. Yao and H. Han, *Chemistry - A European Journal*, 2018, **24**, 18334-18355.
7. F. Dionigi, C. C. Weber, M. Primbs, M. Gocyla, A. M. Bonastre, C. Spöri, H. Schmies, E. Hornberger, S. Kühl, J. Drnec, M. Heggen, J. Sharman, R. E. Dunin-Borkowski and P. Strasser, *Nano Letters*, 2019, **19**, 6876-6885.
8. M. Xiao, J. Zhu, G. Li, N. Li, S. Li, Z. P. Cano, L. Ma, P. Cui, P. Xu, G. Jiang, H. Jin, S. Wang, T. Wu, J. Lu, A. Yu, D. Su and Z. Chen, *Angewandte Chemie - International Edition*, 2019, **58**, 9640-9645.
9. S. Liu, Z. Li, C. Wang, W. Tao, M. Huang, M. Zuo, Y. Yang, K. Yang, L. Zhang, S. Chen, P. Xu and Q. Chen, *Nature Communications*, 2020, **11**.
10. L. Xie, Q. Liu, X. Shi, A. M. Asiri, Y. Luo and X. Sun, *Inorganic Chemistry Frontiers*, 2018, **5**, 1365-1369.
11. K. S. Exner, *Journal*, 2021, **26**.
12. A. Brunning, The Periodic table's endangered elements,  
<https://www.acs.org/content/acs/en/greenchemistry/research-innovation/endangered-elements.html>).
13. Y. Tang, S. Zheng, S. Cao, H. Xue and H. Pang, *Journal of Materials Chemistry A*, 2020, **8**, 18492-18514.
14. C. Feng, M. B. Faheem, J. Fu, Y. Xiao, C. Li and Y. Li, *ACS Catalysis*, 2020, DOI: 10.1021/acscatal.9b05445.
15. R. Farzana, M. A. Sayeed, J. Joseph, K. Ostrikov, A. P. O'Mullane and V. Sahajwalla, *ChemElectroChem*, 2020, **7**, 2073-2080.
16. J. M. Barforoush, T. E. Seuferling, D. T. Jantz, K. R. Song and K. C. Leonard, *ACS Applied Energy Materials*, 2018, **1**, 1415-1423.

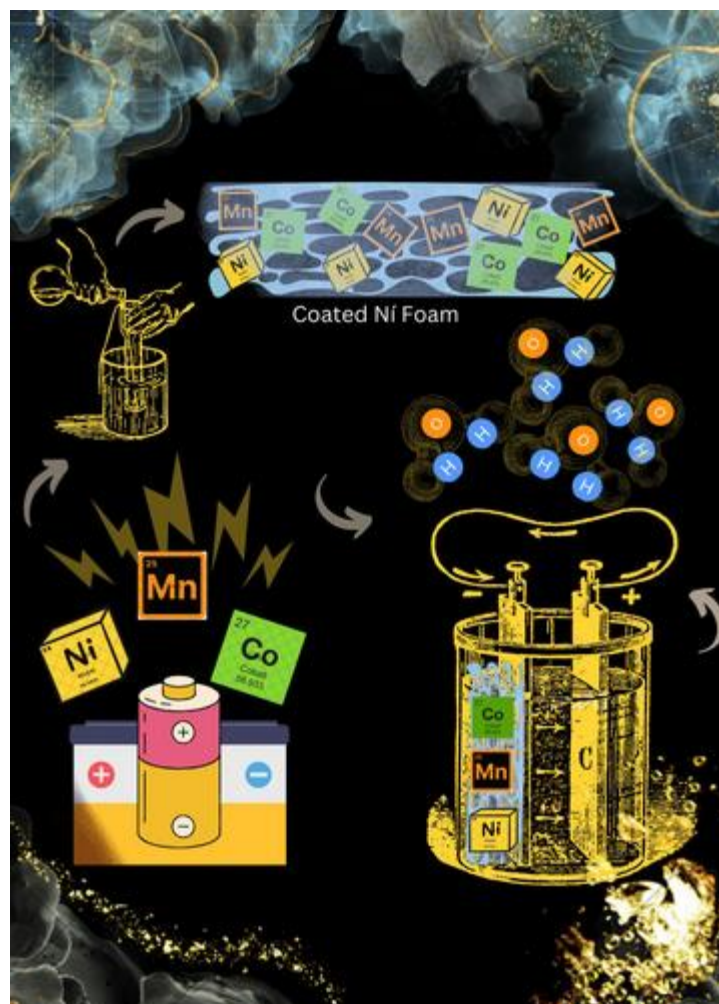
17. U. K. Sultana, J. D. Riches and A. P. O'Mullane, *Advanced Functional Materials*, 2018, **28**, 1-8.
18. P. Swarnkar, D. K. Sarfo, A. S. Pannu, T. Rainey, T. Sundararajan and A. P. O'Mullane, 2022, **7**, 2100705.
19. R. B. Levy and M. Boudart, *Science*, 1973, **181**, 547-549.
20. P. Liu and J. A. Rodriguez, *J. Am. Chem. Soc.*, 2005, **127**, 14871-14878.
21. B. Hinnemann, P. G. Moses, J. Bonde, K. P. Jørgensen, J. H. Nielsen, S. Horch, I. Chorkendorff and J. K. Nørskov, *J. Am. Chem. Soc.*, 2005, **127**, 5308-5309.
22. U. K. Sultana and A. P. O'Mullane, *ChemElectroChem*, 2019, DOI: 10.1002/celc.201801731, DOI:10.1002/celc.201801731.
23. U. K. Sultana, J. F. S. Fernando and A. P. O'Mullane, *Sustainable Materials and Technologies*, 2020, **25**.
24. Y. Zhao, C. Chang, F. Teng, Y. Zhao, G. Chen, R. Shi, G. I. Waterhouse, W. Huang and T. Zhang, *Advanced Energy Materials*, 2017, **7**, 1700005.
25. P. Kanagavalli, R. Sudha, S. Boopathi and S. S. Kumar, *Electrochim. Commun.*, 2017, **82**, 61-65.
26. H. A. Bandal, A. R. Jadhav, A. H. Tamboli and H. Kim, *Electrochim. Acta*, 2017, **249**, 253-262.
27. C. Xiao, Y. Li, X. Lu and C. Zhao, *Adv. Funct. Mater.*, 2016, **26**, 3515-3523.
28. M. Abu Sayeed, C. Woods, J. Love and A. P. O'Mullane, *ChemElectroChem*, 2020, **7**, 4369-4377.
29. Y. Uchino, T. Kobayashi, S. Hasegawa, I. Nagashima, Y. Sunada, A. Manabe, Y. Nishiki and S. Mitsushima, *Electrochemistry*, 2018, **86**, 138-144.
30. Y. Uchino, T. Kobayashi, S. Hasegawa, I. Nagashima, Y. Sunada, A. Manabe, Y. Nishiki and S. Mitsushima, *Electrocatalysis*, 2018, **9**, 67-74.
31. T. Thai, A. Rajabipour, C. Fairfield and S. Thennadil, *Australian Journal of Multi-Disciplinary Engineering*, 2022, **18**, 15-25.
32. J. J. Roy, S. Rarotra, V. Krikstolaityte, K. W. Zhuoran, Y. D.-I. Cindy, X. Y. Tan, M. Carboni, D. Meyer, Q. Yan and M. Srinivasan, *Adv. Mater.*, 2021, DOI: <https://doi.org/10.1002/adma.202103346>, 2103346.
33. R. Farzana, K. Hassan and V. Sahajwalla, 2019, DOI: 10.1038/s41598-019-44778-z, 1-12.
34. K. Hassan, R. Farzana and V. Sahajwalla, *SN Applied Sciences*, 2019, **1**, 1-13.

35. R. Farzana, R. Rajarao, P. R. Behera, K. Hassan and V. Sahajwalla, 2019, DOI: 10.3390/nano8090717.
36. R. Ahirwar and A. K. Tripathi, *Environmental Nanotechnology, Monitoring & Management*, 2021, **15**, 100409.
37. M. Kaya, *Waste Management*, 2016, **57**, 64-90.
38. J. Neumann, M. Petranikova, M. Meeus, J. D. Gamarra, R. Younesi, M. Winter and S. Nowak, *Adv. Energy Mater.*, 2022, **12**, 2102917.
39. P. E. Karthik, H. Rajan, V. R. Jothi, B.-I. Sang and S. C. Yi, *J. Haz. Mater.*, 2022, **421**, 126687.
40. H. Saleem, M. Khosravi, S. Maroufi, V. Sahajwalla and A. P. O'Mullane, *Sustainable Energy & Fuels*, 2022, **6**, 4829-4844.
41. N. Chen, J. Qi, X. Du, Y. Wang, W. Zhang, Y. Wang, Y. Lu and S. Wang, *RSC Advances*, 2016, **6**, 103541-103545.
42. P. Babar, A. Lokhande, V. Karade, B. Pawar, M. G. Gang, S. Pawar and J. H. Kim, *Journal of Colloid and Interface Science*, 2019, **537**, 43-49.
43. C. Liang, P. Zou, A. Nairan, Y. Zhang, J. Liu, K. Liu, S. Hu, F. Kang, H. J. Fan and C. Yang, *Energy & Environmental Science*, 2019, DOI: 10.1039/C9EE02388G, 10.1039/C1039EE02388G.
44. Q. Zhang, H. Zhong, F. Meng, D. Bao, X. Zhang and X. Wei, *Nano Research*, 2018, **11**, 1294-1300.
45. W. Zhang, Y. Wu, J. Qi, M. Chen and R. Cao, *Advanced Energy Materials*, 2017, **7**, 1602547-n/a.
46. M. A. Sayeed and A. P. O'Mullane, *RSC Adv.*, 2017, **7**, 43083-43089.
47. Y. Li and C. Zhao, *ACS Catalysis*, 2017, **7**, 2535-2541.
48. D. Guo, J. Qi, W. Zhang and R. Cao, *ChemSusChem*, 2017, **10**, 394-400.
49. Q. Luo, M. Peng, X. Sun, Y. Luo and A. M. Asiri, *Int. J. Hydrogen Energy*, 2016, **41**, 8785-8792.
50. F. Dionigi and P. Strasser, *Advanced Energy Materials*, 2016, **6**, 1600621-n/a.
51. H. S. Ahn and A. J. Bard, *J. Am. Chem. Soc.*, 2016, **138**, 313-318.
52. S. Zou, M. S. Burke, M. G. Kast, J. Fan, N. Danilovic and S. W. Boettcher, *Chem. Mater.*, 2015, **27**, 8011-8020.
53. J. Deng, M. R. Nellist, M. B. Stevens, C. Dette, Y. Wang and S. W. Boettcher, *Nano Letters*, 2017, **17**, 6922-6926.

54. M. A. Sayeed, J. F. S. Fernando and A. P. O'Mullane, *Advanced Sustainable Systems*, 2018, **2**, 1-7.
55. M. Abu Sayeed, G. J. Millar and A. P. O'Mullane, *ChemElectroChem*, 2019, **6**, 3667-3673.
56. M. A. Sayeed and A. P. O'Mullane, *ChemPhysChem*, 2019, **20**, 3112-3119.
57. J. Chen, Z. Guo, Y. Luo, M. Cai, Y. Gong, S. Sun, Z. Li and C. J. Mao, *ACS Sustainable Chemistry and Engineering*, 2021, **9**, 9436-9443.
58. Y. Messaoudi, H. Belhadj, M. R. Khelladi and A. Azizi, *RSC Adv.*, 2022, **12**, 29143-29150.
59. T. Nguyen, M. Boudard, M. J. Carmezim and M. F. Montemor, *Scientific Reports*, 2017, **7**, 39980.
60. M. Su, S. Zhu, Z. Cui, Z. Li, S. Wu, M. Guo, H. Jiang and Y. Liang, *Sustainable Energy & Fuels*, 2021, **5**, 3205-3212.
61. A. I. Yanson, P. Rodriguez, N. Garcia-Araez, R. V. Mom, F. D. Tichelaar and M. T. M. Koper, *Angew. Chem. Int. Ed.*, 2011, **50**, 6346-6350.
62. T. Wirtanen, T. Prenzel, J.-P. Tessonnier and S. R. Waldvogel, *Chem Rev.*, 2021, **121**, 10241-10270.
63. M. L. Kromer, J. Monzó, M. J. Lawrence, A. Kolodziej, Z. T. Gossage, B. H. Simpson, S. Morandi, A. Yanson, J. Rodríguez-López and P. Rodríguez, *Langmuir*, 2017, **33**, 13295-13302.
64. A. Y. Faid, A. O. Barnett, F. Seland and S. Sunde, *Electrochimica Acta*, 2020, **361**, 137040-137040.
65. Y. Wu, Y. Gao, H. He and P. Zhang, *Electrochimica Acta*, 2019, **301**, 39-46.
66. S. Chen, Z. Kang, X. Zhang, J. Xie, H. Wang, W. Shao, X. Zheng, W. Yan, B. Pan and Y. Xie, *ACS Central Science*, 2017, **3**, 1221-1227.
67. B. P. Payne, M. C. Biesinger and N. S. McIntyre, *Journal of Electron Spectroscopy and Related Phenomena*, 2009, **175**, 55-65.
68. M. Little, M. Thomson and D. Infield, *Int. J. Hydrogen Energy*, 2007, **32**, 1582-1588.
69. S. Pascuzzi, A. S. Anifantis, I. Blanco and G. Scarascia Mugnozza, 2016, **8**, 629.
70. D. Friebel, M. W. Louie, M. Bajdich, K. E. Sanwald, Y. Cai, A. M. Wise, M.-J. Cheng, D. Sokaras, T.-C. Weng, R. Alonso-Mori, R. C. Davis, J. R. Bargar, J. K. Nørskov, A. Nilsson and A. T. Bell, *J. Am. Chem. Soc.*, 2015, **137**, 1305-1313.

## Chapter 5

# Investigating the potential use of Ni-Mn-Co (NMC) battery materials as electrocatalysts for electrochemical water splitting.



The following paper has been published in a peer reviewed journal based in this chapter.

**Arshdeep Kaur, Jose Alarco and Anthony P. O'Mullane, "Investigating the potential use of Ni-Mn-Co (NMC) battery materials as electrocatalysts for electrochemical water splitting", ChemPhyChem, 2024. <https://doi.org/10.1002/cphc.202400124>**

The authors listed below have certified that:

1. They meet the criteria for authorship and that they have participated in the conception, execution, or interpretation, of at least that part of the publication in their field of expertise.
2. They take public responsibility for their part of the publication, except for the responsible author who accepts overall responsibility for the publication.
3. There are no other authors of the publication according to these criteria.
4. Potential conflicts of interest have been disclosed to (a) granting bodies, (b) the editor or publisher of journals or other publications, and (c) the head of the responsible academic unit, and
5. They agree to the use of the publication in the student's thesis and its publication on the QUT's ePrints site consistent with any limitations set by publisher requirements.

<b>Contribution</b>	<b>Statement of Contribution</b>
Arshdeep Kaur	Methodology, investigation, data curation, writing – original draft.
Jose Alarco	Conceptualisation, methodology, resources, supervision.
Anthony O'Mullane	Conceptualisation, methodology, resources, supervision, funding acquisition, writing – review & editing.

**Background:** To explore the potential of waste materials from lithium-ion batteries, electrochemical studies were conducted, focusing primarily on cathode materials and previous chapter investigated, Fe/Ni mesh current collectors recovered from a Toyota Prius NiMH battery module were examined for their electrocatalytic activity. The results revealed that the recovered material effectively enabled both the Hydrogen Evolution Reaction (HER) and the Oxygen Evolution Reaction (OER), demonstrating its potential as a bifunctional electrocatalyst for water splitting. In this Chapter, cathode materials such as Nickel, Manganese, and Cobalt (NMC) oxides are examined as potential electrocatalysts. Due to the varying compositions of NMC used in batteries, the electrochemical analysis is conducted to compare the performance of the commonly used NMC 622 and NMC 811 battery materials against a nickel foam (NF).

## 5.1 Abstract

The imminent generation of significant amounts of Li ion battery waste is of concern due to potential detrimental environmental impacts. However, this also poses an opportunity to recycle valuable battery materials for later use. One underexplored area is using commonly employed cathode materials such as nickel, manganese cobalt (NMC) oxide as an electrocatalyst for water splitting reactions. In this work we explore the possibility of using NMC materials of different metallic ratios (NMC 622 and 811) as oxygen evolution and hydrogen evolution catalysts under alkaline conditions. We show that both materials are excellent oxygen evolution reaction (OER) electrocatalysts but perform poorly for the hydrogen evolution reaction. NMC 622 demonstrates the better OER activity with an overpotential of only 280 mV to pass 100 mA cm<sup>-2</sup> and a low tafel slope of 42 mV dec<sup>-1</sup>. The material can also pass high current densities of 150 mA cm<sup>-2</sup> for 24 h while also being tolerant to extensive potential cycling indicating suitability for direct integration with renewable energy inputs. This work demonstrates that NMC cathode materials if recovered from Li ion batteries are suitable OER electrocatalysts.

## 5.2 Introduction

The requirement to reduce fossil fuel use due to environmental concerns has raised a major challenge to develop highly efficient renewable energy driven systems at scale. The replacement of fossil fuels with green intermittent renewable sources such as wind and solar requires the development of technologies that use electricity in real time as well as ensuring reasonable storage capacity when renewable electricity supply is low or interrupted. There are two approaches in this area, the development of rechargeable batteries for storage in the short

term and the generation of hydrogen via electrolysis as a fuel to be utilised when required in the longer term. Li ion batteries dominate the battery market given their ubiquitous use in electronics and electric vehicle markets while it is also an emerging technology for home and grid level storage of electricity.<sup>[1-2]</sup> The rapid emergence and adoption of Li ion batteries however poses an upcoming challenge when end of life is reached, which is often only 5-6 years for electric vehicle batteries.<sup>[3]</sup> With significant calls to electrify industry as well as the agricultural and transport sectors,<sup>[4-6]</sup> the continued deployment of Li ion batteries is expected to grow substantially which will result in a significant waste issue in years to come.

The disposal of waste batteries into landfill and incineration still occurs in many territories.<sup>[7]</sup> This is highly detrimental to the environment as significant land pollution can occur due to metal leaching while incineration produces toxic emissions which also threatens human health.<sup>[8-11]</sup> Therefore, recycling strategies need to be adopted to recover the various components of the battery. Fortunately, new recycling methods are being investigated and future battery recycling infrastructure is currently being developed.<sup>[9-12]</sup>

In terms of battery materials the cathode often contains highly desirable metals such as the popular lithium nickel manganese cobalt (NMC) oxide cathode material which has dominated the battery electric vehicle (BEV) market during this decade.<sup>[13]</sup> There are many formulations dependent on the battery manufacturer and typically encompass NMC at different ratios such as NMC111, NMC532, NMC622 and NMC811 where the main aim is to reduce the amount of cobalt. High Ni content not only increases the energy density and rate capability of the battery but also lowers the cost due to the increasing scarcity of cobalt and associated supply chain issues.<sup>[13]</sup> Given the recent dominance of this battery chemistry means there will be a significant waste issue when BEVs in particular come to end of life.

Although global reserves of lithium, nickel, cobalt, and platinum group metals may meet their cumulative demand in the short-term (2020–2030) and medium-term (2020–2050) it has been determined that these reserves are insufficient for the long-term (2020–2100)<sup>[6]</sup> if the electrification of industry and transport is adopted. However, this also presents an opportunity to recycle battery waste and use these materials in a completely different application such as electrochemical water splitting to produce green hydrogen which possesses the highest energy density per unit mass ( $140\text{ MJ kg}^{-1}$ ) and therefore can be utilised to promote a green and carbon free economy.<sup>[14],[15],[16]</sup> Indeed, electrochemical water splitting has been identified as a viable and sustainable method to produce one of the purest forms of hydrogen

gas.<sup>[17]</sup> However, one of the most significant drawbacks is that the reaction kinetics of the oxygen evolution reaction (OER) are slow which restricts the industrial application of electrolyzers at a very large scale.<sup>[18]</sup> Therefore, research is focused on the development of OER electrocatalysts that can reduce the OER overpotential and increase the kinetics of the reaction.<sup>[16]</sup> A large constraint is cost and there is significant research into using cheap and sustainable materials for electrochemical water splitting. To date a variety of single, bimetallic and trimetallic transition metal oxides based on Fe, Co, Ni and Mn have been investigated for the OER as well as in their reduced form as hydrogen evolution reaction (HER) electrocatalysts,<sup>[19-25]</sup> for alkaline electrolysis. In many instances bifunctional materials are being studied that are active for both the OER and HER which can facilitate overall water splitting.<sup>[26-33]</sup> This is particularly relevant for electrolyzers that need to be designed for dynamic operation to avoid unintended impacts on stability and efficiency.<sup>[5]</sup>

To further emphasise the need to recycle battery/electronic waste the International Union of Pure and Applied Chemistry (IUPAC)<sup>[34]</sup> and European Chemical Society released a periodic table that indicates the elements according to their use in the electronic industry. The IUPAC declared the complete extinction of a few elements in next 100 years such as Cr, Ln, Co, As, Zn, Ga, Ge and Te due to their excessive use in the electronic industry and elements such as Ni, Mn, Li and Mg being categorised as having limited availability.<sup>[35]</sup> Therefore there has been an emergence of studies on recycled battery waste for electrocatalytic applications such as water splitting and fuel cell relevant reactions.<sup>[36-43]</sup> The NMC formulation of Li ion battery cathodes is of interest given previous work on studying these types of materials for water splitting. Sivakumar et al.,<sup>[44]</sup> worked on different compositions of Ni, Mn and Co oxides for their OER performance. Additionally, Priamushko et al.,<sup>[45]</sup> reported on  $\text{Ni}_x\text{Co}_y\text{Mn}_z\text{O}_4$  for its OER activity and found that  $\text{Ni}_x\text{Co}_y\text{Mn}_z\text{O}_4$  demonstrated high current density and a low onset potential when loaded onto Ni foam (NF) while Salem et al.,<sup>[46]</sup> reported that trimetallic  $\text{Mn}_1\text{Ni}_1\text{Co}_1\text{-P/NF}$  is bifunctional water splitting catalyst. Recent work has also been reported on mixed transition metal oxides in their ternary form like nanocast mixed Ni–Co–Mn oxides for the OER,<sup>[45]</sup>  $\text{NiCoMnO}_4$  nanoparticles on N-doped graphene for both the OER and oxygen reduction reaction (ORR).<sup>[47]</sup> In addition, nickel, cobalt manganese spinel oxide nanoparticles are active for the OER and ORR, while plasma- modulated trimetallic Mn-Ni-Co phosphides<sup>[46]</sup> and  $\text{MnNiCoO}_4/\text{N-MWCNT}$  nanocomposite catalysts<sup>[48], [48]</sup> have been reported for overall water splitting. Sivanantham et al<sup>[49]</sup>, reported that  $\text{NiCo}_2\text{S}_4$  nanowire arrays grown on 3D NFs form efficient bifunctional electrocatalysts in a highly alkaline environment. Moreover, Xu *et.*

*al.*,<sup>[50]</sup> developed Mn doped Ni<sub>2</sub>P supported on nickel foam as a bifunctional electrocatalyst. Liang et al.,<sup>[51]</sup> used NF to support NiCoP porous nanostructures to achieve stable bifunctional performance while Liu *et. al.*,<sup>[52]</sup> reported that Cr-doped NiCo<sub>2</sub>O<sub>4</sub> (Cr-NiCo<sub>2</sub>O<sub>4</sub>) nanoneedles on nickel foam demonstrate high performance as a bifunctional electrocatalyst. These studies indicate the potential suitability of NMC battery materials for these types of reactions.

Herein, we report on the potential use of two commonly used cathode materials in Li ion batteries, NMC 811 and NMC 622 to probe their effectiveness as electrocatalysts for water splitting activity and determine if the NMC 811 material with lower Co content outperformed NMC 622 while also investigating any compositional changes that may occur after the OER.

### 5.3 Results and Discussion

The NMC 622 and NMC 811 materials synthesised in this study consist of micron sized particles where the latter material shows a slightly smaller particle size as seen in the scanning electron microscopy (SEM) images in Figures S1 and S2. In both cases an even distribution of Ni, Mn and Co can be seen throughout the particles as shown in the SEM/EDS mapping experiments (Figure S1-2). Transmission electron microscopy (TEM) images were also taken and it shows that both materials are crystalline (Figure S3, S4). XRD patterns for both materials are also shown in Figure S3 and S4 and are consistent with Li-NMC oxide materials in the correct elemental ratios which was also confirmed with inductively coupled plasma optical emission spectroscopy.

The electrochemical activity of NMC 811 and NMC 622 materials supported on a NF electrode was then assessed in a 1 M KOH solution. Initially the materials were screened using cyclic voltammetry at 100 mV s<sup>-1</sup> for 20 cycles (Figure 5.1) and compared with commercial nickel foam (NF). The NMC 622-NF electrode exhibits a higher current density in the OER region from 1.50 to the end of the positive sweep (Figure 5.1a) compared to NMC 811-NF (Figure 5.1b). The commercial NF electrode initially exhibited comparable current density in the OER potential region, however the performance rapidly decayed upon cycling (Figure 5.1c). For both NMC electrodes the current density remained stable with cycling. In all cases the distinctive redox process at ca. 1.4 V associated with the oxidation of Ni<sup>2+</sup> oxide is evident before the onset of the OER.<sup>[53-56]</sup> This redox process is associated with the oxidation of Ni<sup>2+</sup> species into Ni<sup>3+</sup> species such as NiOOH prior to the onset of the OER.

On the reverse sweep a reduction response is observed due to the reduction of these higher oxidation state oxides formed on the electrode. In the case of the unmodified NF electrode (Figure 5.1c) there is a clear distinction between the redox process and onset of the OER, however this is not evident for the NMC electrodes and indicates that the process is perturbed by the presence of Co and Mn elements within the electrode material. The presence of secondary metals is known to affect the redox behaviour of Ni oxides which results in a much broader oxidation response.<sup>[57]</sup> From Figure 5.1 it can be seen that the potential range also encompasses the HER region which can be seen by the increase in current below ca. -0.20 V. In all cases the current magnitude is comparable indicating that these materials are not particularly active for the HER and therefore were not explored in any more detail for this particular reaction. However, one observation is that cycling into the HER region does not impact on the OER performance of the NMC electrodes and indicates that these materials would be suitable for electrolyzers directly integrated with intermittent renewable sources that are susceptible to reverse current flow which often damages the anode electrocatalysts.<sup>[58-59]</sup> This data indicates that these materials are potentially tolerant to such input voltage profiles intermittent renewable sources that are susceptible to reverse current flow which often damages the anode electrocatalysts.<sup>[58-59]</sup> This data indicates that these materials are potentially tolerant to such input voltage profiles.

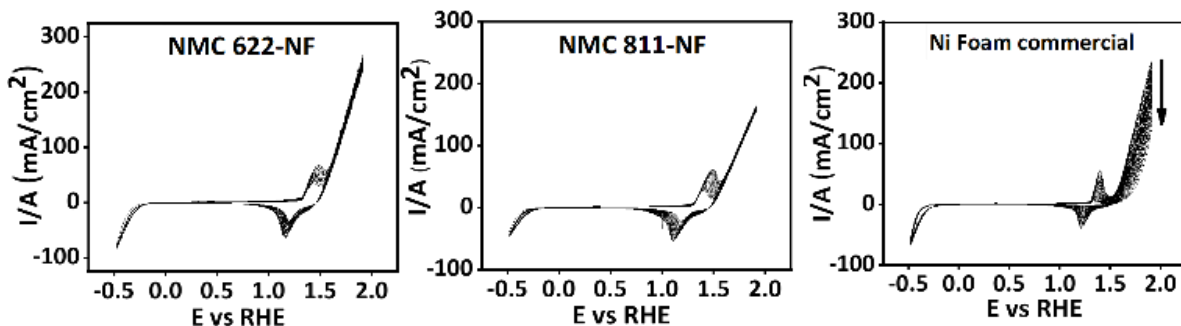


**Figure 5.1:** Cyclic voltammograms recorded at  $100 \text{ mV s}^{-1}$  for 20 cycles at (a) (a) NMC 622-NF, (b) NMC 811-NF and (c) NF electrodes in 1 M KOH.

The OER behaviour of these electrodes was then investigated in more detail with slow scan rate ( $0.1 \text{ mV s}^{-1}$ ) linear sweep voltammetry (LSV) which was also iR-corrected (Figure 5.2). This data indicates that the NMC 622-NF electrode outperforms NMC 811 and NF in terms of current density and is able to pass quite significant current densities of up to  $450 \text{ mA cm}^{-2}$ . The potential that was required to pass  $100 \text{ mA cm}^{-2}$  was 1.57, 1.63 and 1.67 V for NMC

622-NF, NMC 811-NF and NF electrodes, respectively. The reproducibility of the electrodes was also tested an additional LSV responses for both NMC electrodes is shown in Figure S5 indicating comparable behaviour between electrode batches. In terms of benchmarking, the overpotential value required to reach a current density of  $10 \text{ mA cm}^{-2}$  ( $\eta_{10}$ ) is often used. In this work  $\eta_{10}$  for NMC 622-NF was 280 mV which is comparable to many previous reports on multimetallic oxides. It was reported that Mn, Ni Co phosphides/NF had an overpotential of 289 mV,<sup>[46]</sup> while  $\text{Ni}_x\text{Co}_y\text{Mn}_z\text{O}_4$  on NF gave an overpotential of 400 mV.<sup>[45]</sup> Sivanantham et al., reported on  $\text{NiCo}_2\text{S}_4$  nanowire arrays on NF with a value of 260 mV,<sup>[49]</sup> while Liang et al., reported an overpotential of 300 mV at NiCoP on NF.<sup>[51]</sup> The values obtained at NMC 622 – NF are comparable to previous studies and also outperform recently reported trimetallic and bimetallic electrocatalysts using NF as a substrate and is highlighted in Table S1

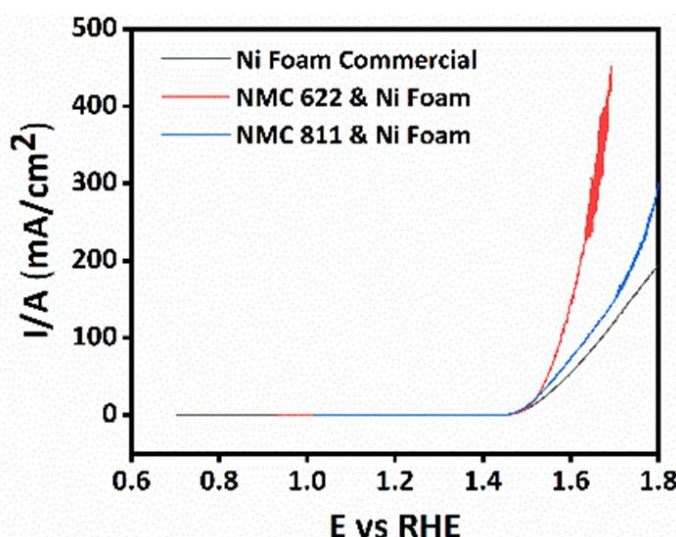


**Figure 5.2.** LSVs recorded at  $0.1 \text{ mV s}^{-1}$  at NMC 811-NF, NMC 622-NF and commercial NF electrodes in 1 M KOH.

Tafel plots were also plotted which gave tafel slopes of  $42$  and  $40 \text{ mV dec}^{-1}$  for NMC 622-NF (Figure 5.3c) and NMC 811-NF (Figure 5.3d) electrodes, respectively indicating similar kinetics and rate determining step for the OER. These low Tafel slope values highlights the effects of active centres at a ternary compound (Ni-Mn-Co) that enhances the electrocatalytic activity.<sup>[46], [60]</sup>

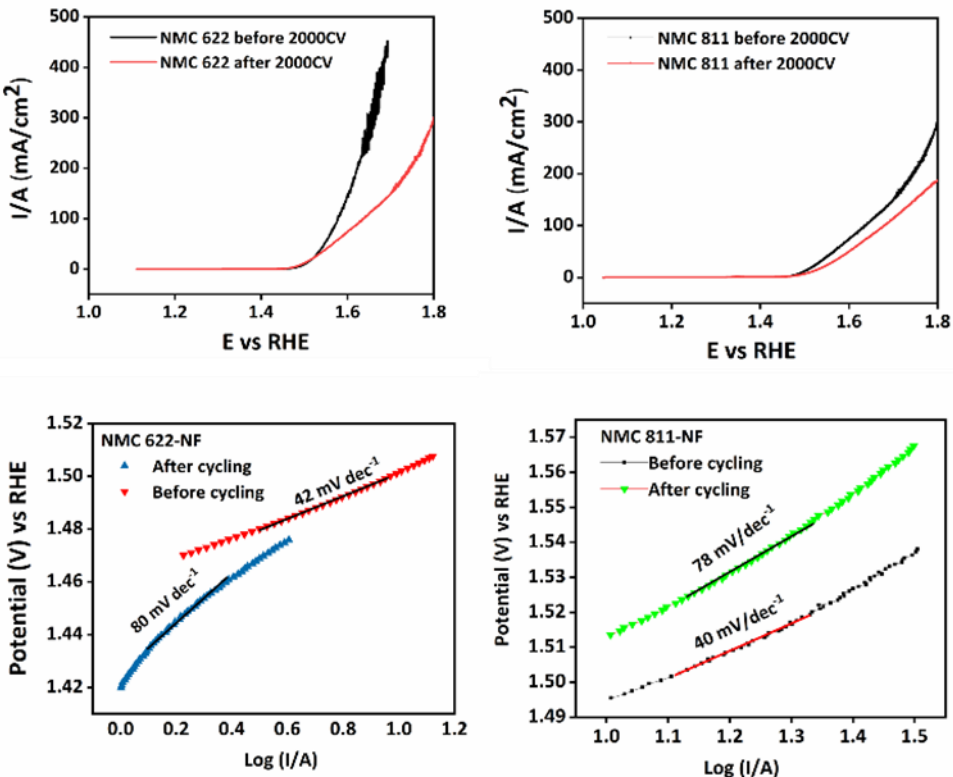


**Figure 5.3:** LSVs recorded at 0.1 mV s<sup>-1</sup> at NMC 622-NF and NMC 811-NF before and after potential cycling (2000 cycles, 1.0 to 1.9 V) in 1 M KOH. Tafel plots obtained for NMC 622 and NMC 811 from the respective LSV data.

The values obtained in this study are lower than many previous studies such as at ternary nickel cobalt manganese spinel oxide ( $\text{Ni}_{1.5}\text{Co}_{0.75}\text{Mn}_{0.75}\text{O}_4$ ) with a Tafel slope of 68 mV dec<sup>-1</sup>,<sup>[44]</sup> NiCoMnO<sub>4</sub> nanoparticles on N-doped graphene with a Tafel slope of 128 mV dec<sup>-1</sup>,<sup>[60]</sup> an MNC-P/NF electrode with a Tafel slope of 84 mV dec<sup>-1</sup>,<sup>[46]</sup> and  $\text{Ni}_x\text{Co}_y\text{Mn}_z\text{O}_4$  with a tafel slope in the range of 79–97 mV dec<sup>-1</sup>.<sup>[45]</sup>

The electrodes were then assessed for their durability and stability by being subjected to 2000 potential cycles (1.0 to 1.9 V) at a sweep rate of 100 mV s<sup>-1</sup> as shown in Figure S6. During repetitive potential cycling the redox process prior to the OER increased in magnitude and the oxidation process shifted to more positive potentials indicating that a change in surface area of the electrode occurs and/or a change in the surface composition of the electrode. Previous studies indicated that  $\text{Ni}^{2+}$  can be converted to  $\text{Ni}^{3+}$ ,  $\text{Co}^{2+}$  to  $\text{Co}^{3+}$  and  $\text{Mn}^{2+}$  to  $\text{Mn}^{3+}$  to  $\text{Mn}^{4+}$  species prior to the OER and this process is expected to introduce surface sites in the form of various metal oxides phases that can lower the binding energy with the formation of M-OOH species (M is the transition metal).<sup>[44, 61-63]</sup>

After the repetitive cycling process, slow scan rate LSV curves were again recorded. It can be seen that for both NMC 622-NF (Figure 5.3a) and NMC 811-NF(Figure 5.3b) electrodes that there is a decrease in the current density passed compared to before cycling. The potential values to reach  $100 \text{ mA cm}^{-2}$  increased from 1.57 to 1.63 V and 1.63 to 1.67 V for NMC 622-NF and NMC 811-NF electrodes, respectively. This indicates that repetitive cycling impacts on the performance of these electrode materials and may be due to structural or compositional changes on the electrode surface as indicated by the cyclic voltammetric data in Figure S5. Tafel plots were then plotted before and after repetitive cycling for both NMC 622-NF (Figure 5.3c) and NMC 811-NF (Figure 3d) electrodes to determine any change in values. For the NMC 622-NF electrode the tafel slope increased from 42 to  $80 \text{ mV dec}^{-1}$  while for the NMC 811-NF electrode it increased from 40 to  $78 \text{ mV dec}^{-1}$  indicating that the potential cycling process affected the kinetics of the reaction for both electrodes in a very similar manner.

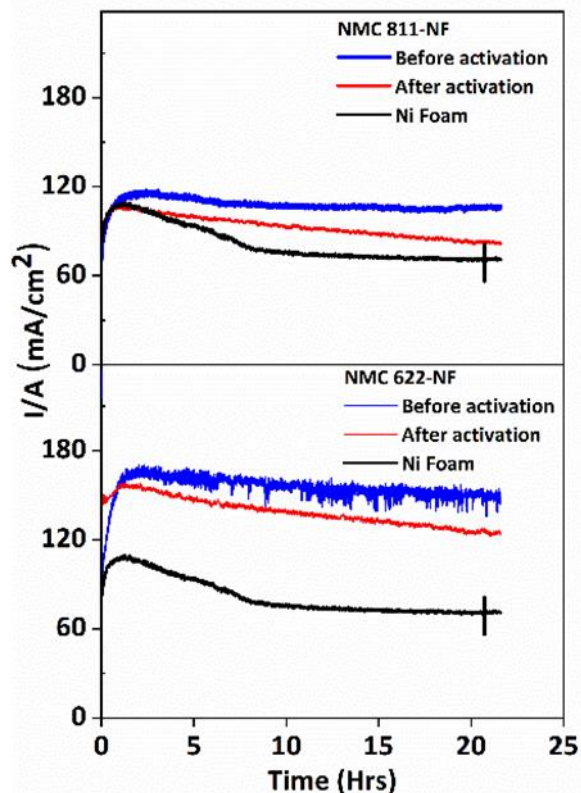


**Figure 5.4:** Chronoamperometric experiments conducted at 1.7 V for 24 h in 1 M KOH for NF substrate, NMC 622-NF and NMC 811-NF electrodes both before (blue) and after (red) repetitive potential cycling.

The electrodes were then tested under constant potential conditions at an applied voltage of 1.7 V using pristine electrodes and those that had previously been cycled (2000 cycles) (Figure 5.4). This potential was chosen to ensure that reasonable current densities were

passed during the stability test to represent more practical conditions. As shown in Figure 5.4 both electrodes show stable and high current density before cycling for 24 h. NMC 622-NF shows the better performance with a maximum current density of  $164 \text{ mA cm}^{-2}$  which only dropped to  $150 \text{ mA cm}^{-2}$  after 24 h.

Both electrodes significantly outperformed the commercial NF electrode which showed a much more dramatic decrease in current density over the electrolysis period. Whereas, NMC 811-NF (Figure 5.4) shows a maximum current density of  $117 \text{ mA cm}^{-2}$  which decreased to  $107 \text{ mA cm}^{-2}$  after 24 h. However, after potential cycling (2000 cycles) both electrodes showed a decrease in current density with again a slight decay in performance over the 24 h electrolysis period. The surface area of the electrodes was then determined after the repetitive cycling process using double layer capacitance measurements ( $C_{dl}$ ) (Figure S7). For NMC 622-NF a  $C_{dl}$  value of  $16 \text{ mF cm}^{-2}$  was measured whereas NMC 811-NF gave a higher value of  $20 \text{ mF cm}^{-2}$ .

Therefore, even though NMC 622-NF has a lower surface area it still exhibits a higher current during electrolysis (Figure 5.4) indicating that the intrinsic activity of the material is also significantly higher. The increased activity of the NMC 622-NF material may be due to the higher Co and Mn content within the material as Co oxide/hydroxide in particular is a highly active electrocatalyst for the OER and has been reported to outperform its Ni based counterpart.<sup>[64-66]</sup> In addition previous work on Mn incorporated into NiCo hydroxide nanosheets was found to optimise the reaction pathway and decrease the reaction kinetics energy barrier.<sup>[67]</sup> The catalysts were then analysed after repetitive potential cycling in the OER region to provide a more accurate representation of the active form of the catalyst rather than the initial pristine state. It is now well recognised that the majority of OER electrocatalysts undergo significant changes in either their morphology or composition when exposed to the harsh conditions of oxygen evolution<sup>[37, 68-73]</sup> and in particular when exposed to repetitive potential cycling.

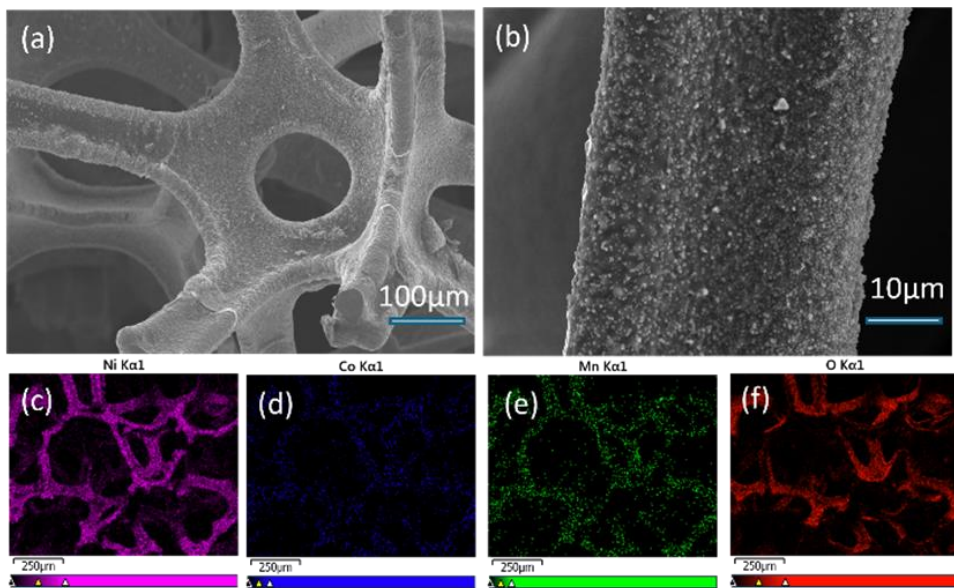


**Figure 5.5:** SEM image and EDS mapping (Ni, Mn, Co and O elements) of NMC 622-NF after repetitive potential cycling (2000 cycles, 1.0 to 1.9 V in 1 M KOH).

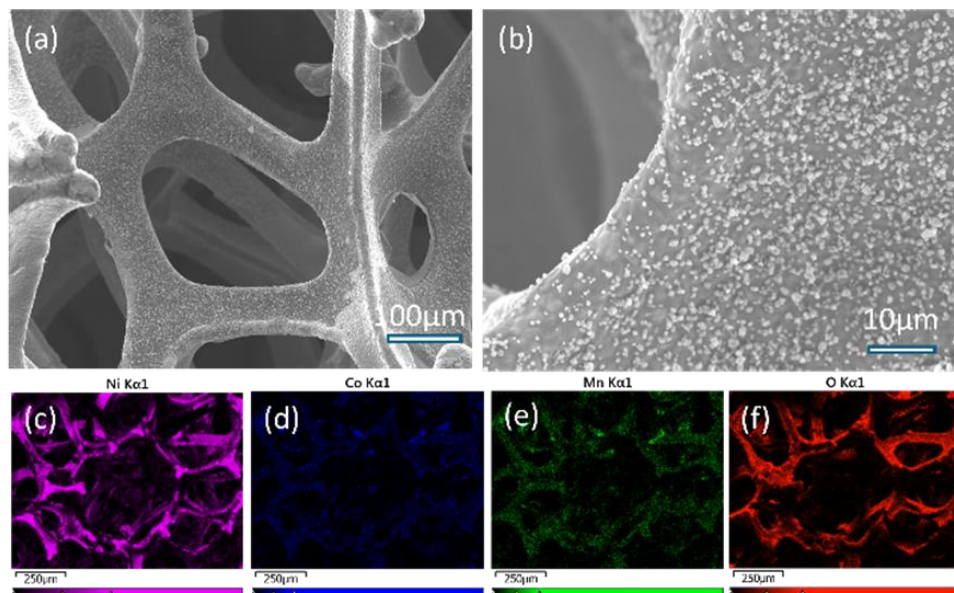


**Figure 5.6:** SEM image and EDS mapping (Ni, Mn, Co and O elements) of NMC 811-NF after repetitive potential cycling (2000 cycles, 1.0 to 1.9 V in 1 M KOH).

SEM analysis of NMC 622-NF (Figure 5a, b) shows that the even distribution of catalyst particles on the NF remains intact while EDS mapping (Figure 5.5 c-f) also shows an even distribution of Ni, Mn, Co and O elements. Similarly for NMC 811-NF (Figure 5.6) the catalyst particle distribution on the NF electrode is maintained with an even distribution of Ni, Mn, Co and O elements across the sample.

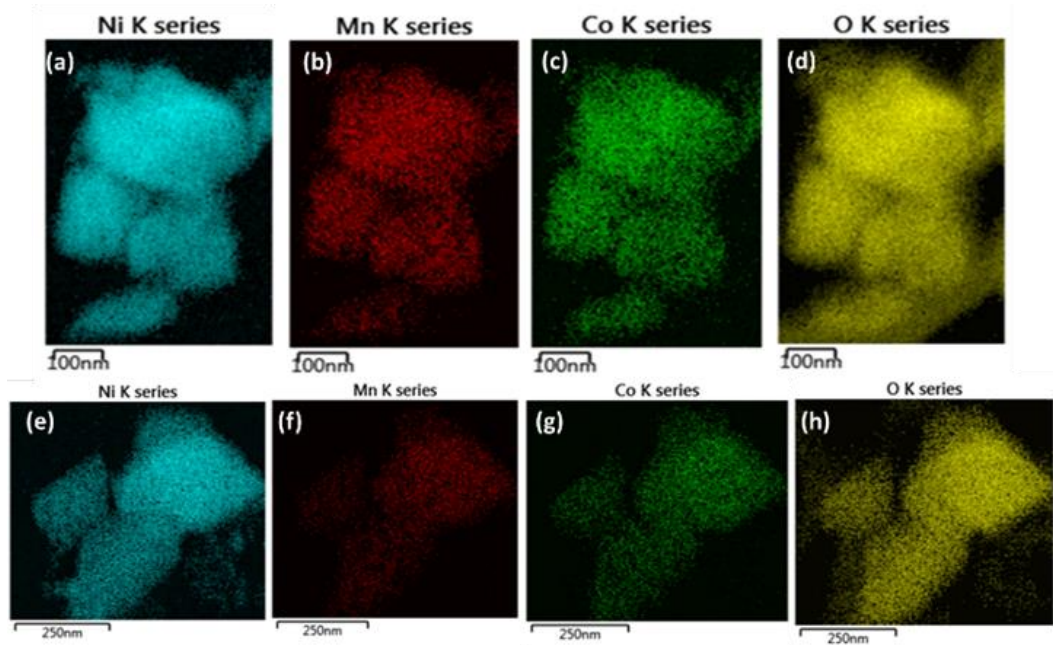


**Figure 5.7:** EDS mapping of NMC 811 before (upper) and after (lower) potential cycling.

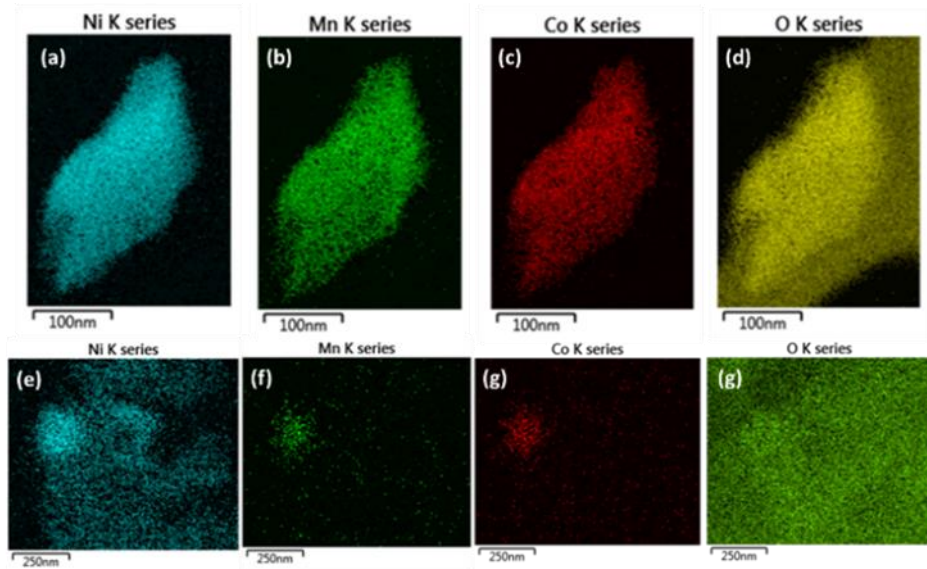


**Figure 5.8:** EDS mapping of NMC 622 before (upper) and after (lower) potential cycling.

However, when the catalyst particles were analysed with TEM/EDS after potential cycling there was a significant difference between the two materials. For NMC 811 the EDS mapping of the particles before cycling (Figure 5.7 a-d) shows an even distribution of Ni, Mn, Co and O, while after cycling (Figure 5.7 e-h) there is a slight decrease in the intensity of the Mn and Co signals compared to Ni. For NMC 622 the EDS mapping before cycling (Figure 5.8 a-d) also shows an even distribution of elements, however after cycling a significant change occurred whereby there is a significant loss of Co and Mn elements from the particle while the

Ni content remains high. This indicates that for the NMC 622 material there is some leaching of Mn and Co from the particles which results in a Ni enriched particle.

XPS analysis was also undertaken to identify the oxidation state of the catalyst particles before and after potential cycling (Figure 5.9). For both electrodes the loss of Mn and Co during repetitive cycling results in some loss in OER activity as seen from the data in Figure 5.3 (a, b) as well as the slight drop in long term performance over 24 h at high current density (Figure 5.4). Even though the ECSA of NMC 622 is lower than NMC 811 and the loss of Mn and Co from the particle is more significant, the performance is still significantly better than NMC 811.

The Ni 2p core level spectrum for NMC 622 (Figure 5.9 a) shows contributions at 854.2 and 860.4 eV for Ni 2p<sub>3/2</sub> and peaks at 872.8 and 878.7 eV corresponding to Ni 2p<sub>1/2</sub>. This is indicative of Ni in a 2<sup>+</sup> oxidation state<sup>[74], [75]</sup> and is composed of Ni(OH)<sub>2</sub> and NiO. After cycling there is an increase in the magnitude of the contribution at 860.4 eV, indicating an increase in the amount of NiO.<sup>[76]</sup> Previous work has shown that Ni(OH)<sub>2</sub> can also partially convert into NiO upon repetitive cycling in the OER region.<sup>[77]</sup> TEM characterisation of the electrode after cycling (Figure S8) demonstrated that the crystalline state was maintained with lattice spacings of 0.20 and 0.22 nm that corresponds to the (012) and (100) crystal planes of NiO<sup>[78], [79]</sup> and CoO,<sup>[80]</sup> respectively. For NMC 811 a similar trend was observed, however there are additional contributions after cycling, in particular at 855.6 eV which indicates the possible formation of some Ni<sup>3+</sup> species (NiOOH),<sup>[81]</sup> which is typically observed when Ni<sup>2+</sup> precursors are used as OER electrocatalysts.<sup>[82-83]</sup>

The high resolution XPS Mn 2p spectrum obtained before and after OER (Figure 5.9) have two main spin orbitals that belong to Mn 2p<sub>3/2</sub> and Mn 2p<sub>1/2</sub>. NMC 622 shows peaks at 640.9 and 644.4 eV before cycling (Figure 5.9a) indicating the presence of Mn<sup>2+</sup> and Mn<sup>4+</sup> oxides.<sup>[84]</sup> After cycling there are no obvious oxidation state changes, however the intensity of the signal is much lower which is consistent with the TEM results (Figure 8) which show a much lower Mn content. For NMC 811 the Mn 2p spectrum before cycling is very similar to NMC 622, however after cycling there is evidence of the formation of some Mn<sup>3+</sup> species from the contribution at 642.7 eV.<sup>[46, 84]</sup>

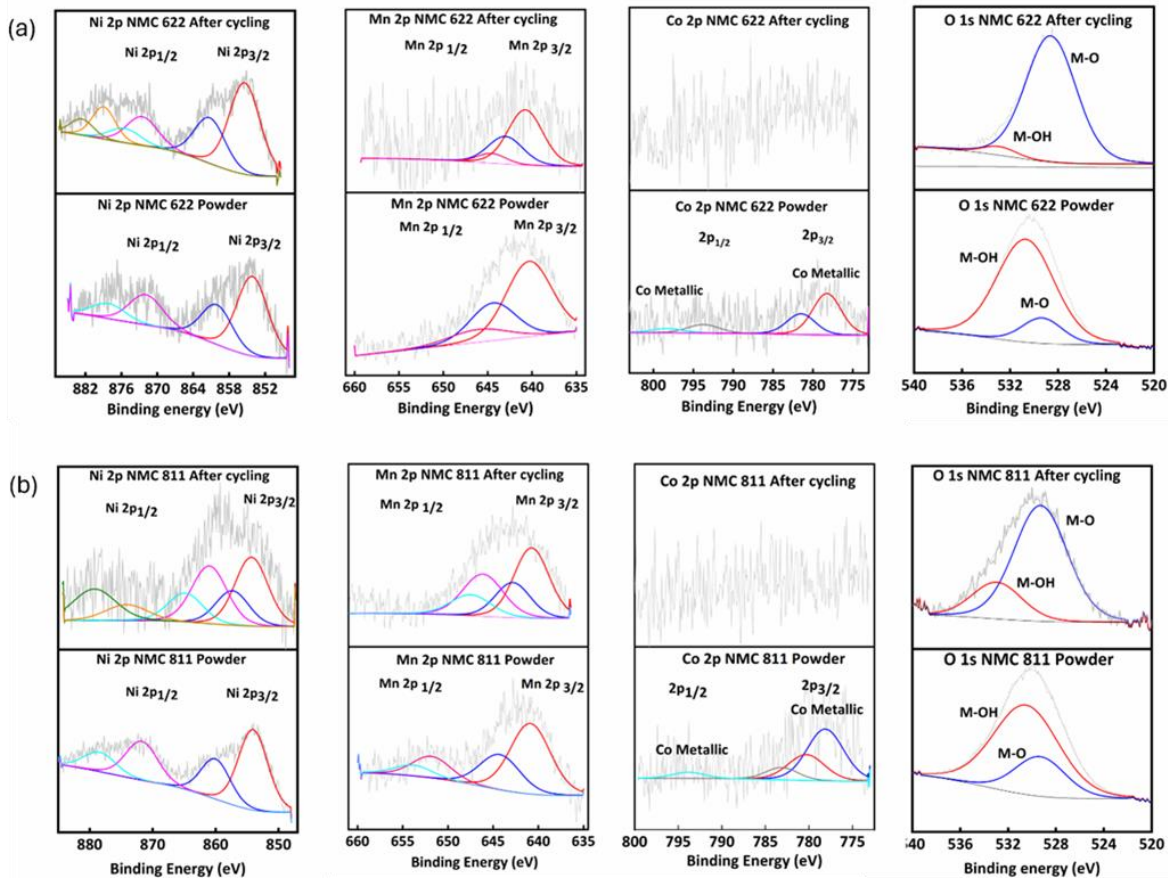


**Figure 5.9:** XPS spectra for Ni 2p, Mn 2p, Co 2p and O 1s for NMC 622-NF and NMC 811-NF electrodes before (a) and after (b) 2000 potential cycles (1.0 to 1.9 V at 100 mV s<sup>-1</sup> in 1 M KOH).

The high resolution Co 2p spectra for the pristine electrodes (Figure 5.9 a, b) is quite weak and for both electrodes demonstrates the presence of some metallic Co at 778.2 eV[85],[44] whereas the peak at the higher binding energy is indicative of Co<sup>2+</sup> species.[86-87] After potential cycling the Co signal for both electrodes is very weak (data was therefore not fitted) indicating the loss of Co from the surface of the catalyst which is also consistent with the decreased Co intensity in the EDS mapping experiments in Figures 5.8 and 5.9.

Finally, the O 1s spectra of the catalysts before and after cycling was studied. For both electrodes the presence of hydroxyl groups is the dominant form and M-OH contributions are highlighted in the figure at the higher binding energy where the M-OH content for NMC 622 and NMC 811 are 84.7 % and 74.5 %, respectively. The lattice oxygen content (M-O) for NMC 811 (25.5 %) is higher than NMC 622 (15.3 %), however after cycling the transformation from

M-OH species to M-O species is significant. In particular for, NMC 622 the M-O content (95.2%) dominates the surface and is consistent with the observation of NiO in the TEM images (Figure S8). For NMC 811 after cycling the M-O content is less (77.2 %), while in the TEM images (Figure S9) lattice spacings of 0.26 and 0.47 nm are observed which are consistent with the (111) planes of NiMnO<sub>2</sub>[88] and NiMnCoO<sub>2</sub>.[60] This data shows that both NMC materials are effective OER electrocatalysts that can maintain reasonably high current densities at low overpotentials. The NMC material with the higher Mn and Co content (NMC 622) is more active both before and after repetitive potential cycling, but interestingly leaches Mn and Co from the surface of the catalyst to a greater extent than NMC 811. This does impact on performance, however even after extensive potential cycling high current densities can still be maintained which demonstrates the potential of this material to be used for water splitting applications.

#### 5.4 Conclusion

NMC battery materials were investigated for their potential use as electrocatalysts for water splitting reactions. It was found that NMC electrodes are not suitable for the HER and exhibited similar current densities as commercial NF electrodes. However, both NMC 622 and NMC 811 materials demonstrated promising OER activity in 1 M KOH, however the material with the higher Mn and Co content exhibited better performance for both long term continuous electrolysis and after repetitive potential cycling. In both cases there is evidence of loss of some Mn and Co from the catalyst surface which is more evident for NMC 622. The tolerance of these electrodes to potential cycling (1.0 to 1.9 V for 2000 cycles) with only a slight decrease in performance shows promise for using these materials as anodes in electrolyzers that are directly integrated with intermittent renewable energy sources that are subject to fluctuations in the input voltage. This work indicates that recovering NMC from Li ion batteries could be worthwhile as it offers an alternative application for these recovered materials. Future work will focus on determining the relationship between battery history (cycling, discharge/charge rates) and OER performance of recovered NMC materials.

#### 5.5 Experimental

##### *NMC materials synthesis*

A transition metal hydroxide precursor was initially synthesised via controlled co-precipitation using a continuously stirred, sealed reaction vessel purged with N<sub>2</sub>. Initially, a 2M solution was prepared using a stock solution with determined concentrations of Ni, Mn, and

Co using the required amounts of  $\text{NiSO}_4 \cdot 6\text{H}_2\text{O}$ ,  $\text{MnSO}_4 \cdot \text{H}_2\text{O}$ , and  $\text{CoSO}_4 \cdot 7\text{H}_2\text{O}$  (99.99%, Sigma Aldrich) in water to obtain the required molar ratios for either NMC 622 or NMC 811. Then an aqueous solution of 4 M NaOH and a solution of 2 M  $\text{NH}_4\text{H}_2\text{O}$  were prepared and used as a buffer and complexation agent, respectively. Initially a volume of 1 M ammonium hydroxide was kept at 55 °C using a stirrer speed of 800 rpm for the total 12 h reaction time. The transition metal solution was dosed continuously for the first 4 h while the buffer/complexation agent were added using a built-in-house, programmed, three mini-dosing pump system, to maintain a TM/ $\text{NH}_4$  ratio around 0.9 and a pH of 11-12 (adjusted by NaOH additions with a feedback signal from a calibrated pH meter) for the duration of the reaction. The precipitate was then filtered and washed with deionized water until the filtrate had a neutral pH, before vacuum-drying at 100 °C overnight to produce the transition metal hydroxide precursor. This was then ground gently with  $\text{LiOH} \cdot \text{H}_2\text{O}$  at a Li/TM molar ratio of 1.05:1. The mixture was calcined in oxygen at 500°C for 5 h followed by heating to 850 °C for 12 h at a heating rate of 5°C min<sup>-1</sup> to obtain either NMC 622 or NMC 811.

### *Materials*

Potassium hydroxide purchased from Sigma Aldrich (KOH 99.99% purity) and absolute ethanol (Sigma Aldrich) were used. For the preparation of electrolyte solutions and washing purposes Milli-Q water with resistivity of 18.2 MΩ.cm was used. NF (1×1.5 cm<sup>2</sup>) (Sigma) was cleaned with 3 M HCl to remove surface oxides and then sonicated in acetone, ethanol and deionised water for 30 min each followed by drying overnight at 60 degrees. 1mg of NMC catalyst was dissolved in Nafion (100 μL) and ethanol/water solvent in a 1:1. The mixture was stirred followed by 60 min sonication to disperse it. Around 300 μL of ink was then used for immersing the NMC material on the nickel foam. The prepared electrode was dried at 60 degrees overnight and then in an oven at room temperature.

### *Electrochemical experiments*

A conventional three electrode cell was used for all electrochemical experiments at room temperature ( $22 \pm 3^\circ\text{C}$ ) using a Biologic VSP workstation operated by EC -lab software (version 11.34). A graphite carbon rod with high purity (1 mm diameter, Johnson Matthey Ultra “F” purity grade) and a leakless Ag/AgCl (eDAQ Pty Ltd) were used as counter and reference electrodes, respectively. Working electrodes were prepared from NF and NMC material as mentioned in the previously discussed method. The electrochemical cell was saturated with oxygen and the experiments were carried out on the bench in the laboratory.

The working electrodes were washed with Milli-Q water after electrochemical tests to remove any electrolyte solution from the surface and dried at room temperature for further characterisation. All measurements were conducted in 1 M KOH electrolyte solution. The following equation was used to convert the recorded potential to the RHE scale for all electrochemical measurements:

$$E_{RHE} = E_{Ag/AgCl} + (0.059 \times pH) + 0.197 V$$

while the overpotential ( $\eta$ ) for the OER was calculated using the formula  $\eta = E_{RHE} - 1.23$  V. The current density was normalised to the geometric surface area of the electrode.

### *Characterisation*

The morphology of the samples was analysed by scanning electron microscopy (SEM) and energy dispersive spectroscopy (EDS) using a JEOL 7001F electron microscope at an operating voltage of 5 kV and 15 kV, respectively. X-ray photoelectron spectroscopy (XPS) data was collected using an Omicron Multiclan Lab Ultra-High Vacuum Scanning Tunnelling Microscope (UHV-STM) where a 125 mm hemispherical electron energy analyser was incorporated. XPS measurements were performed using non-monochromatic Mg K $\alpha$  (1253.6 eV) X-ray source (DAR 400, Omicron Nanotechnology), and the incident angle was 65° to the sample surface. The analyser pass energy of 50 eV with steps of 0.5 eV and the dwell time was 200 ms. High-resolution scans with a narrow region for Ni 2p, Mn 2p, Co 2p, C 1 s and O 1 s were taken at 20 eV pass energy, 0.2 eV steps and with a 200 ms dwell time. Besides a wide scan of low binding energy region was performed from 250 eV to 0 eV swept at high resolution. The base pressure in the analysis chamber was  $1.0 \times 10^{-9}$  Torr and the pressure was  $1.0 \times 10^{-8}$  Torr during the measurement. Powder XRD patterns were collected using a Rigaku SmartLab diffractometer. HRTEM, SAED, and STEM-EDS measurements were performed using a JEOL 2100 TEM instrument operating at an accelerating voltage of 200 kV. The JEOL 2100 machine was equipped with a high-sensitivity OXFORD 80 mm<sup>2</sup> silicon drift X-ray detector for accurate elemental analysis and JEOL BF/DF detectors for STEM imaging.

## **5.6 Acknowledgements**

AOM acknowledges partial funding from the Australian Research Council (DP180102869, IH190100009). The authors acknowledge the instrumentation and technical support of the QUT Central Analytical Research Facility (CARF) and scholarship support

through the QUT/Max Planck Institute of Colloids and Interfaces Joint Laboratory on Nanocatalysis for Sustainable Chemistry.

## References

- [1] H. Sahebi, M. Khodoomi, M. Seif, M. Pishvae, T. Hanne, *J. Energy Storage*, **2023**, *63*, 106970.
- [2] N. Ntube, H. Li, *J. Energy Storage*, **2023**, *59*, 106403.
- [3] C. Zhan, X. Zhang, G. Tian, D. T. Pham, M. Ivanov, A. Aleksandrov, C. Fu, J. Zhang, Z. Wu, *Environ. Sci. Pollution Res.*, **2023**, *30*, 47956-47971.
- [4] S. Griffith, *The Big Switch*, Black Inc., Melbourne, 2022, 65-68.
- [5] D. S. Mallapragada, Y. Dvorkin, M. A. Modestino, D. V. Esposito, W. A. Smith, B.-M. Hodge, M. P. Harold, V. M. Donnelly, A. Nuz, C. J. J. Bloomquist, *Joule*, **2023**, *7*, 23-41.
- [6] C. Zhang, J. Yan, F. You, *Adv. Appl. Energy*, **2023**, *9*, 100116.
- [7] V. Srivastava, V. Rantala, P. Mehdipour, T. Kauppinen, S. Tuomikoski, A. Heponiemi, H. Runtti, P. Tynjälä, G. Simões Dos Reis, U. Lassi, *Chem. Eng. J.*, **2023**, *474*, 145822.
- [8] R. Farzana, R. Rajarao, P. R. Behera, K. Hassan, V. Sahajwalla, **2019**, 2073-2080.
- [9] J. J. Roy, S. Rarotra, V. Krikstolaityte, K. W. Zhuoran, Y. D.-I. Cindy, X. Y. Tan, M. Carboni, D. Meyer, Q. Yan, M. Srinivasan, *Adv. Mater.*, **2021**, *282*, 2103346.
- [10] R. Ahirwar, A. K. Tripathi, *Environ. Nanotechnol., Monitoring Manag.*, **2021**, *15*, 100409.
- [11] M. Kaya, *Waste Manag.*, **2016**, *57*, 64-90.
- [12] J. Neumann, M. Petranikova, M. Meeus, J. D. Gamarra, R. Younesi, M. Winter, S. Nowak, *Adv. Energy Mater.*, **2022**, *12*, 2102917.
- [13] L. Chen, X. Li, Y. Luo, W. Tan, Q. Ma, M. Wang, J. Yang, *J. Cleaner Prod.*, **2024**, *434*, 139917.
- [14] Y. Wu, *Mater. Lett.*, **2017**, *209*, 532-534.
- [15] T. Liu, *ChemElectroChem*, **2017**, *4*, 1840–1845.
- [16] N. K. Shrestha, S. A. Patil, S. Cho, Y. Jo, H. Kim, H. Im, *J. Mater. Chem. A*, **2020**, *8*, 24408-24418.
- [17] A. Vazhayil, L. Vazhayal, J. Thomas, S. Ashok C, N. Thomas, *Appl. Surf. Sci. Adv.*, **2021**, *6*, 100184-100184.
- [18] K. Ioannis, *Nanostructured Electrocatalysts*, **2014**, *53*, 102-121.
- [19] A. H. Al-Naggar, N. M. Shinde, J.-S. Kim, R. S. Mane, *Coord. Chem. Rev.*, **2023**, *474*, 214864.

- [20] Y. Zhang, F. Gao, D. Wang, Z. Li, X. Wang, C. Wang, K. Zhang, Y. Du, *Coord. Chem. Rev.*, **2023**, *475*, 214916.
- [21] S. M. Ibn Shamsah, *Catalysts*, **2021**, *11*, 429.
- [22] Z. Chen, W. Wei, B.-J. Ni, *Curr. Opinion Green Sustain. Chem.*, **2021**, *27*, 100398.
- [23] J. Chen, Z. Guo, Y. Luo, M. Cai, Y. Gong, S. Sun, Z. Li, C. J. Mao, *ACS Sustain. Chem. Eng.*, **2021**, *9*, 9436-9443.
- [24] F.-T. Tsai, Y.-T. Deng, C.-W. Pao, J.-L. Chen, J.-F. Lee, K.-T. Lai, W.-F. Liaw, *J. Mater. Chem. A*, **2020**, *8*, 9939-9950.
- [25] A. P. O'Mullane, *J. Phys. Energy*, **2020**, *2*, 041001.
- [26] U. K. Sultana, J. F. S. Fernando, A. P. O'Mullane, *Sustain. Mater. Technol.*, **2020**, *25*, e00177.
- [27] M. Abu Sayeed, G. J. Millar, A. P. O'Mullane, *ChemElectroChem*, **2019**, *6*, 3667-3673.
- [28] U. K. Sultana, J. D. Riches, A. P. O'Mullane, *Adv. Funct. Mater.*, **2018**, 1804361.
- [29] M. A. Sayeed, A. P. O'Mullane, *J. Mater. Chem. A*, **2017**, *5*, 23776-23784.
- [30] C. Xu, M. Zhang, X. Yin, Q. Gao, S. Jiang, J. Cheng, X. Kong, B. Liu, H.-Q. Peng, *J. Mater. Chem. A*, **2023**, *11*, 18502-18529.
- [31] N. Rahamathulla, A. P. Murthy, *J. Energy Storage*, **2023**, *73*, 109127.
- [32] B. Sun, G. Dong, J. Ye, D.-f. Chai, X. Yang, S. Fu, M. Zhao, W. Zhang, J. Li, *Chem. Eng. J.*, **2023**, *459*, 141610.
- [33] G. Ma, J. Ye, M. Qin, T. Sun, W. Tan, Z. Fan, L. Huang, X. Xin, *Nano Energy*, **2023**, *115*, 108679.
- [34] P. E. Karthik, H. Rajan, V. R. Jothi, B. I. Sang, S. C. Yi, *J. Haz. Mater.*, **2022**, *421*, 126687.
- [35] D. J. C. Hamilton, *Chemistry International*, **2019**, *41*, 23-28.
- [36] H. Saleem, M. Khosravi, S. Maroufi, V. Sahajwalla, A. P. O'Mullane, *Sustain. Energy Fuels*, **2022**, *6*, 4829-4844.
- [37] A. Kaur, M. Khosravi, A. P. O'Mullane, *Sustain. Energy Fuels*, **2023**, *7*, 2486-2494.
- [38] S. A. Mirshokraee, M. Muhyuddin, R. Morina, L. Poggini, E. Berretti, M. Bellini, A. Lavacchi, C. Ferrara, C. Santoro, *J. Power Sources*, **2023**, *557*, 232571.
- [39] K. S. Bejigo, S. Natarajan, K. Bhunia, V. Elumalai, S.-J. Kim, *J. Cleaner Production*, **2023**, *384*, 135520.
- [40] A. Kotkar, S. Dash, P. Bhanja, S. Sahu, A. Verma, A. Mukherjee, M. Mohapatra, S. Basu, *Electrochim. Acta*, **2023**, *442*, 141842.
- [41] H. Jungi, A. Karmakar, S. Kundu, J. Mitra, *J. Mater. Chem. A*, **2023**, *11*, 13687-13696.
- [42] P. E. Karthik, H. Rajan, V. R. Jothi, B.-I. Sang, S. C. Yi, *J. Haz. Mater.*, **2022**, *421*, 126687.

- [43] R. Farzana, M. A. Sayeed, J. Joseph, K. Ostrikov, A. P. O'Mullane, V. Sahajwalla, *ChemElectroChem*, **2020**, *7*, 2073-2080.
- [44] P. Sivakumar, P. Subramanian, T. Maiyalagan, A. Gedanken, A. Schechter, *Mater. Chem. Phys.*, **2019**, *229*, 190-196.
- [45] T. Priamushko, R. Guillet-Nicolas, M. Yu, M. Doyle, C. Weidenthaler, H. Tuysuz, F. Kleitz, *ACS Appl. Energy Mater.*, **2020**, *3*, 5597-5609.
- [46] K. E. Salem, A. A. Saleh, G. E. Khedr, B. S. Shaheen, N. K. Allam, *Energy Environ. Mater.*, **2023**, *6*, e12324.
- [47] Afshin Pendashteha, Jesus Palmaa, M. Anderson, R. Marcilla, *Appl. Cat. B*, **2017**, *201*, 241- 252.
- [48] X. Yu, A. Manthiram, *Catal. Sci. Technol.*, **2015**, *5*, 2072-2075.
- [49] A. Sivanantham, P. Ganesan, S. Shanmugam, *Adv. Funct. Mater.*, **2016**, *26*, 4661-4672.
- [50] P. Xu, L. Qiu, L. Wei, Y. Liu, D. Yuan, Y. Wang, P. Tsakaras, *Catal. Today*, **2020**, *355*, 815-821.
- [51] H. Liang, A. N. Gandi, D. H. Anjum, X. Wang, U. Schwingenschlögl, H. N. Alshareef, *Nano Lett.*, **2016**, *16*, 7718-7725.
- [52] T. Liu, P. Diao, *Nano Res.*, **2020**, *13*, 3299-3309.
- [53] M. Abu Sayeed, C. Woods, J. Love, A. P. O'Mullane, *ChemElectroChem*, **2020**, *7*, 4369-4377.
- [54] M. E. G. Lyons, L. Russell, M. O'Brien, R. L. Doyle, I. Godwin, M. P. Brandon, *Int. J. Electrochem. Sci.*, **2012**, *7*, 2710-2763.
- [55] M. E. G. Lyons, M. P. Brandon, *J. Electroanal. Chem.*, **2010**, *641*, 119-130.
- [56] L. D. Burke, T. A. M. Twomey, *J. Electroanal. Chem.*, **1984**, *167*, 285-290.
- [57] Q. Abbas, H. Khurshid, R. Yoosuf, J. Lawrence, B. A. Issa, M. A. Abdelkareem, A. G. Olabi, *Sci. Rep.*, **2023**, *13*, 15654.
- [58] Y. Uchino, T. Kobayashi, S. Hasegawa, I. Nagashima, Y. Sunada, A. Manabe, Y. Nishiki, S. Mitsushima, *Electrochemistry*, **2018**, *86*, 138-144.
- [59] Y. Uchino, T. Kobayashi, S. Hasegawa, I. Nagashima, Y. Sunada, A. Manabe, Y. Nishiki, S. Mitsushima, *Electrocatal*, **2018**, *9*, 67-74.
- [60] A. Pendashteh, J. Palma, M. Anderson, R. Marcilla, *Appl. Cat. B*, **2017**, *201*, 241-252.
- [61] J. Deng, M. R. Nellist, M. B. Stevens, C. Dette, Y. Wang, S. W. Boettcher, *Nano Lett.*, **2017**, *17*, 6922-6926.
- [62] W. H. Lee, M. H. Han, Y.-J. Ko, B. K. Min, K. H. Chae, H.-S. Oh, *Nat. Commun.*, **2022**, *13*, 605.

- [63] Y.-C. Liu, J. A. Koza, J. A. Switzer, *Electrochim. Acta*, **2014**, *140*, 359-365.
- [64] D. K. Sarfo, J. Crawford, J. D. Riches, A. P. O'Mullane, *Chem Catal.*, **2023**, *3*, 100750.
- [65] A. Roy, M. Z. Tariq, M. La, D. Choi, S. J. Park, *J. Electroanal. Chem.*, **2022**, *920*, 116633.
- [66] C. Xiaodong, L. Jianqiao, Y. Tiefeng, Z. Zhiyuan, S. Chunyu, Y. Shuai, G. Xin, W. Nannan, C. Lifeng, *Energy Mater.*, **2022**, *2*, 200028.
- [67] K. Wu, C. Cao, K. Li, C. Lyu, J. Cheng, H. Li, P. Hu, J. Wu, W.-M. Lau, X. Zhu, P. Qian, J. Zheng, *Chem. Eng. J.*, **2023**, *452*, 139527.
- [68] P. Swarnkar, D. K. Sarfo, A. S. Pannu, T. Rainey, T. Sundararajan, A. P. O'Mullane, *Adv. Mater. Technol.*, **2022**, *7*, 2100705.
- [69] T. H. Nga Ngo , J. Love, A. P. O'Mullane, *ChemElectroChem*, **2023**, *10*, e202300438.
- [70] J. Wang, S.-J. Kim, J. Liu, Y. Gao, S. Choi, J. Han, H. Shin, S. Jo, J. Kim, F. Ciucci, H. Kim, Q. Li, W. Yang, X. Long, S. Yang, S.-P. Cho, K. H. Chae, M. G. Kim, H. Kim, J. Lim, *Nat. Catal.*, **2021**, *4*, 212-222.
- [71] A. Malek, Y. Xue, X. Lu, *Angew Chem Int Ed*, **2023**, *62*, e202309854.
- [72] M. Görlin, M. Gliech, J. F. de Araújo, S. Dresp, A. Bergmann, P. Strasser, *Catal. Today*, **2016**, *262*, 65-73.
- [73] A. Bergmann, E. Martinez-Moreno, D. Teschner, P. Chernev, M. Gliech, J. F. de Araujo, T. Reier, H. Dau, P. Strasser, *Nat. Commun.*, **2015**, *6*, 8625.
- [74] B. Jiang, Z. Li, *J. Solid State Chem.*, **2021**, *295*, 121912.
- [75] J.F. Marco, J.R. Gancedo, M. Gracia, J.L. Gautier, E. Ríos, F.J. Berry, *J. Solid State Chem.*, **2000**, *153*, 74-81.
- [76] B. P. Payne, M. C. Biesinger, N. S. McIntyre, *J. Electron Spectroscopy Related Phenomena*, **2009**, *175*, 55-65.
- [77] R. Agoston, M. Abu Sayeed, M. W. M. Jones, M. D. de Jonge, A. P. O'Mullane, *Analyst*, **2019**, *144*, 7318-7325.
- [78] Y. Zhang, R. Xu, Z. Qin, S. Feng, W. Wang, C. Chen, A. Ju, *RSC Adv.*, **2020**, *10*, 22422-22431.
- [79] X. Liu, J. Cao, C. Huang, Z. Chen, X. Fan, K. Shi, Z. Yang, W. Zhang, *Mater. Res. Express*, **2020**, *7*, 065502.
- [80] C. L. Ke Wang, W. Wang, N. Mitsuzaki, Z. Chen., *J. Mater. Sci. Mater. Electronics*, **2019**, *30*, 4144-4151.
- [81] D. Xiong, W. Li, L. Liu, *Chem. Asian J.*, **2017**, *12*, 543-551.
- [82] S. Klaus, Y. Cai, M. W. Louie, L. Trottochaud, A. T. Bell, *J. Phys. Chem. C*, **2015**, *119*, 7243-7254.

- [83] Y.-H. Chung, I. Jang, J.-H. Jang, H. S. Park, H. C. Ham, J. H. Jang, Y.-K. Lee, S. J. Yoo, *Sci. Rep.*, **2017**, *7*, 8236.
- [84] J. Wang, D. Zhang, F. Nie, R. Zhang, X. Fang, Y. Wang, *Environ. Sci. Pollution Res.*, **2023**, *30*, 15377-15391.
- [85] R. Arian, A. M. Zardkhoshouei, S. S. Hosseiny Davarani, *ChemElectroChem*, **2020**, *7*, 2816-2825.
- [86] C. C. Wang, M. Liu, B. Y. Man, C. S. Chen, S. Z. Jiang, S. Y. Yang, X. G. Gao, S. C. Xu, B. Hu, Z. C. Sun, J. J. Guo, J. Hou, *AIP Advances*, **2012**, *2*, 012182.
- [87] B. Lu, J. Zang, W. Li, J. Li, Q. Zou, Y. Zhou, Y. Wang, *Chem. Eng. J.*, **2021**, *422*, 130062-130062.
- [88] M. Dinesh, Y. Haldorai, R. T. Rajendra Kumar, *Ceramics Int.*, **2020**, *46*, 28006-28012.

**Recovering spent Lithium Nickel Manganese Cobalt (NMC) Oxide  
Cathodes from Li Ion Batteries for Use as Oxygen Evolution Reaction  
Electrocatalysts**

*Arshdeep Kaur,<sup>1,2</sup> Hongxia Wang,<sup>1,2</sup> Michael R Horn<sup>1,3</sup> Jessica Crawford<sup>1,3</sup> and Anthony P.  
O'Mullane<sup>1,2\*</sup>*

<sup>1</sup> School of Chemistry and Physics, Queensland University of Technology (QUT), Brisbane, QLD 4001, Australia

<sup>2</sup> Centre for Materials Science, Queensland University of Technology (QUT), Brisbane, QLD 4001, Australia

<sup>3</sup> Future Battery Industry Cooperative Research Centre, Project 022: Electrochemical Testing, School of Chemistry and Physics, Queensland University of Technology (QUT), Brisbane, QLD 4001, Australia

\* [anthony.omullane@qut.edu.au](mailto:anthony.omullane@qut.edu.au)

The authors listed below have certified that:

1. They meet the criteria for authorship and that they have participated in the conception, execution, or interpretation, of at least that part of the publication in their field of expertise.
2. They take public responsibility for their part of the publication, except for the responsible author who accepts overall responsibility for the publication.
3. There are no other authors of the publication according to these criteria.
4. Potential conflicts of interest have been disclosed to (a) granting bodies, (b) the editor or publisher of journals or other publications, and (c) the head of the responsible academic unit, and
5. They agree to the use of the publication in the student's thesis and its publication on the QUT's ePrints site consistent with any limitations set by publisher requirements.

Contribution	Statement of Contribution
Arshdeep Kaur	Conceptualisation, methodology, investigation, data curation, writing – original draft
Hongxia Wang	Methodology, supervision, writing – review & editing
Michael Horne	Methodology, resources, writing – review & editing
Jessica Crawford	Methodology, resources, writing – review & editing
Anthony O'Mullane	Conceptualisation, methodology, resources, supervision, funding acquisition, writing – review & editing

**Background:** The previous chapter investigated the potential of NMC materials for use as electrocatalysts for the OER under alkaline conditions. It was demonstrated that NMC has promise for this reaction, however it is still not clear if NMC recovered from cycled batteries would impact of performance and if it would be comparable to the pristine NMC materials used in the previous chapter. As it was identified that NMC622 showed the better activity, this material was used in Li ion batteries and cycled for a different number of cycles and then recovered from the spent batteries and tested for their OER activity.

## 6.1 Abstract

Li ion battery (LIB) waste is an emerging environmental issue given the rapid electrification of the transport sector and industry more broadly. Promisingly, there is an increased focus on LIB recycling as a potential resource for sustaining future energy technologies. Here we investigate whether a typical LIB cathode material such as nickel manganese cobalt (NMC) oxide can be recovered and used directly as an electrocatalyst for the oxygen evolution reaction (OER). We show that the NMC 622 formulation is an effective electrocatalyst which shows good activity after recovery from a cycled battery. The impact of battery history, i.e. number of cycles performed at 1C, is investigated where it was found that cycling up to 200 times gradually decreases the performance of the material for the OER. However, this approach opens up an opportunity for salvaging batteries that are defective or rejected at quality control stages of battery production which is referred to in the industry as battery scrap and is a much lesser known component of battery production and recycling.

## 6.2 Introduction

Lithium-ion batteries (LIBs) are used in various applications such as electric vehicles, grid level storage, and portable electronics.<sup>1</sup> In most commercial LIBs, graphite serves as the standard material for the anode,<sup>2</sup> implying the cathode material is a key factor in determining the battery's energy density and operating voltage. Nickel-rich layered oxides, such as  $\text{LiNi}_x\text{Co}_y\text{Al}_z\text{O}_2$  and  $\text{Li Ni}_x\text{Co}_x\text{Mn}_z\text{O}_2$ , as well as nickel-rich cobalt-free oxides are prominent transition metal oxides that are often used in LIBs.<sup>3</sup> At any stage of their lifecycle, the presence of flammable and toxic substances in LIBs means that improper disposal can lead to significant environmental and safety concerns.

Therefore, recycling LIBs has gained significant attention not only because of environmental concerns but also resource limitations and our ever-increasing energy demands for storing renewable electricity and powering modern technologies. With increasing electrification of industry and transport there will be a significant level of battery waste to deal

with in the coming decades that can be viewed as a resource rather than a waste product. This concept of urban mining is gaining traction as a means of alleviating this upcoming problem. In fact the global recycled battery market is expected to reach \$23.72 billion by 2030,<sup>4</sup> and the number of recycling companies focused on LIBs is increasing in Europe, North America, and Asia.<sup>5</sup> However, of more immediate concern is the amount of battery scrap generated during the manufacturing process which consists of defective cells that do not meet quality assurance standards. The estimated global average scrap rate was 7.67 % for 2023<sup>6</sup> while it has also been predicted that production scrap will account for more than half of the total LIB recycling source until 2025.<sup>7</sup> The recycling of LIB materials typically involves either physical recovery techniques or costly chemical recycling methods.<sup>8,9</sup> To minimize cost and maximize the utilization of transition metals in LIB cathode materials, work is underway on developing straightforward methods to directly use recycled LIB components<sup>10</sup> such as LCO (Lithium Cobalt Oxide) cathodes from spent LIBs as electrocatalysts for the oxygen evolution reaction (OER).<sup>11</sup> The direct use of recovered cathode materials alleviates chemical leaching processes which also generate a waste stream and therefore offers an alternative use of spent batteries or battery scraps discarded during production.

We have previously shown that NMC oxides with compositions of NMC 622 and NMC 811 that are typically used as LIB cathodes have inherently good electrocatalytic activity for the OER where NMC 622 with the lower Ni content has better activity than NMC 811.<sup>12</sup> However, it is not clear what impact battery cycling has on the OER performance of this material. Therefore, in this work we recover NMC 622 from batteries cycled up to 200 times at 1 C and investigate the performance of the material for the OER in 1 M KOH electrolyte and determine the effect of battery history on direct recycling of NMC cathodes.

### 6.3 Experimental

#### Materials

Potassium hydroxide (99.99 %), absolute ethanol and nickel foam (NF) were purchased from Sigma Adrich. Milli-Q water with resistivity of 18.2 MΩ.cm was used for the preparation of electrolyte solutions. The battery cell material was NMC 622, manufactured by Targray.

#### Methodology of battery cell preparation

The slurry recipe for cathodes was 93% active material (AM), 4 % carbon black (CB) and 3 % PVDF. Graphite-based anodes were prepared in a similar way using commercially relevant binders. The cells constructed were of a small pouch cell design. The cells were tested on a

Biologic BCS-810 workstation, operated by BT-Lab software. Details of the cell components and battery performance of the constructed cells are presented in Table 6.1.

After the battery cells completed cycling, the electrode material was mechanically removed from the foil and placed in NMP (N-methyl-2-pyrrolidone) to remove the PVDF binder which in principle can be re-used. Then, sonication was performed for an hour in NMP. The material was then centrifuged after sonication to retrieve the powder and washed in ethanol and finally left to settle overnight. The top layer was decanted and then dried in a vacuum oven.

**Table 6.1:** Cell components and performance summary

Cell ID	Cathode ML NCM622 (mg/cm <sup>2</sup> )	Anode ML Graphite (mg/cm <sup>2</sup> )	Neg/ Pos ratio	Life Cycle count @1C	Theoretical Capacity (mAh)	Cycle 7: C/10 discharge capacity (mAh)
<b>Cell 1</b>	12.64	7.55	1.34	50	52.05	50.79
<b>Cell 2</b>	12.62	7.33	1.30	150	51.97	50.63
<b>Cell 3</b>	12.73	7.39	1.30	200	52.42	49.09

Electrolyte contained in all cells was LP40 in 1:1 EC/DMC (1.3g).

### Electrochemical experiments

A Biologic VSP workstation was used with a three-electrode cell configuration. A leakless Ag/AgCl (eDAQ Pty Ltd) and a high purity graphite rod (1 mm diameter, Johnson Matthey Ultra “F” purity grade) were used as the reference and counter electrodes, respectively. NF (1 × 1.5 cm<sup>2</sup>) was cleaned with 3 M HCl to remove any surface oxides and then washed with acetone, ethanol and deionised water for 30 min each, followed by overnight drying at 60 °C. 1 mg of NMC catalyst (pristine or recovered) was dispersed in Nafion (100 µL) and ethanol/water solvent in a 1:1 ratio followed by 60 min sonication. 300 µL of this ink was then used for immobilising the NMC material on the NF and dried at 60 °C overnight. For OER experiments the potential was converted to the RHE scale and the current density was normalised to the geometric surface area of the electrode. LSV curves were recorded with  $iR_u$  compensation at 85 %.

## Characterisation

The morphology of the samples was analysed by scanning electron microscopy (SEM) and energy dispersive spectroscopy (EDS) using a JEOL 7001F electron microscope. X-ray photoelectron spectroscopy (XPS) data was collected using an Omicron Multiclan Lab Ultra-High Vacuum Scanning Tunnelling Microscope (UHV-STM).

## 6.4 Results and Discussion

Previous comparative studies between different types of NMC battery cathode materials such as NMC 811 and NMC 622 indicated that NMC 622 was superior for the OER.<sup>12</sup> However, the impact of battery cycling was not explored and how that may influence the OER activity of the recovered material. Therefore, the OER behaviour of unused NMC 622 as well as cycled NMC 622 recovered from Li ion batteries, was examined in detail for their OER performance.

The batteries used to source the cycled NMC 622 were subjected to 8 formation cycles with discharge rates of  $3 \times C/10$  and  $5 \times C/5$ , combined with the same charge rates. The formation cycles were followed by a rate test ( $1 \times C/10$ ,  $C/5$ ,  $C/2$ ,  $1C$ ,  $2C$ ,  $3C$ ) to deliberately induce stress and accelerated ageing effects. Finally, an arbitrary number of cycles at  $1C$  were performed, with the number of cycles varied from 50 to 200 depending on the sample identifier (see below). All charging cycles after formation were completed with a  $C/2$  charge current.

The OER activity in Figure 6.1a is shown by slow scan rate ( $0.1 \text{ mV s}^{-1}$ ), linear sweep voltammetry (LSV) from 1.0 to 1.9 V vs RHE in 1 M KOH. The unprocessed sample (UP) was not assembled into a battery and shows the earliest onset potential (1.54 V) and highest current density in the potential region of study. The next sample of NMC 622 was assembled in a battery but not cycled (Cell 0). When the sample denoted Cell 0 was recovered from the battery and tested, it showed decreased performance. This is reflected by a later onset potential (1.58 V) and lower current density for Cell 0 (Figure 6.1a). Therefore, the process of pouch cell assembly and subsequent disassembly for the recovery of NMC 622 from the binder, impacts slightly on performance. Interestingly after 50 battery cycles (Cell 1) the material showed some recovery in its OER performance with an onset potential of 1.56 V and improved current density. Upon further battery cycling for 150 cycles (Cell 2) and 200 cycles (Cell 3) the onset potential remained constant, however the current density decreased indicating that battery cycling has an impact on OER activity. It should be noted that the same mass of active material is used for all electrodes.

Promisingly, all the electrodes achieve substantially high current densities of up to 400 mA cm<sup>-2</sup> in the potential window of study indicating practical applicability. The potential required to reach a current density of 100 mA cm<sup>-2</sup> was 1.62 V for UP, 1.64 V for Cell 1 and 1.67 V for Cell 2, Cell 3, and Cell 0. The Tafel slopes were then determined as shown in Figure 6.1b where values of 42, 55, 73, 89 and 96 mV dec<sup>-1</sup> were calculated for electrodes UP, Cell 1, Cell 0, Cell 2, and Cell 3, respectively.

This trend shows a gradual reduction in electron transfer kinetics with increased cycles of the material in a battery. The durability and stability of the electrodes were evaluated by subjecting them to 2000 potential cycles between 1.0 and 1.9 V at a sweep rate of 100 mV s<sup>-1</sup>, as illustrated in Figure 6.1(c). During repeated cycling, the magnitude of the oxidation process at ca. 1.5 V increased and shifted to higher potentials indicating potential changes in the electrode's surface area and modifications in its surface composition with possible formation of metal oxides phases and introduction of metal hydroxide species on the surface after cycling.

Even though the Ni<sup>2+</sup>/Ni<sup>3+</sup> redox process increased with cycling, the OER activity is observed to decrease in all cases. It was found that the final current density being passed after 2000 cycles is lowest for Cell 3 which indicates that battery cycling impacts long term durability under these accelerated ageing conditions.

The electrodes were then tested under continuous electrolysis conditions and held at 1.7 V for 21 h (Figure 6.1d). As expected, a similar trend is observed to the cyclic voltammetric data in Figure 6.1(a). After ca. 2 h of electrolysis there is a peak in performance of all electrodes and after 21 h of electrolysis the current densities were all within 10 % of each other except for Cell 3 which showed significantly reduced current density indicating that more extensive battery cycling is detrimental to OER performance.

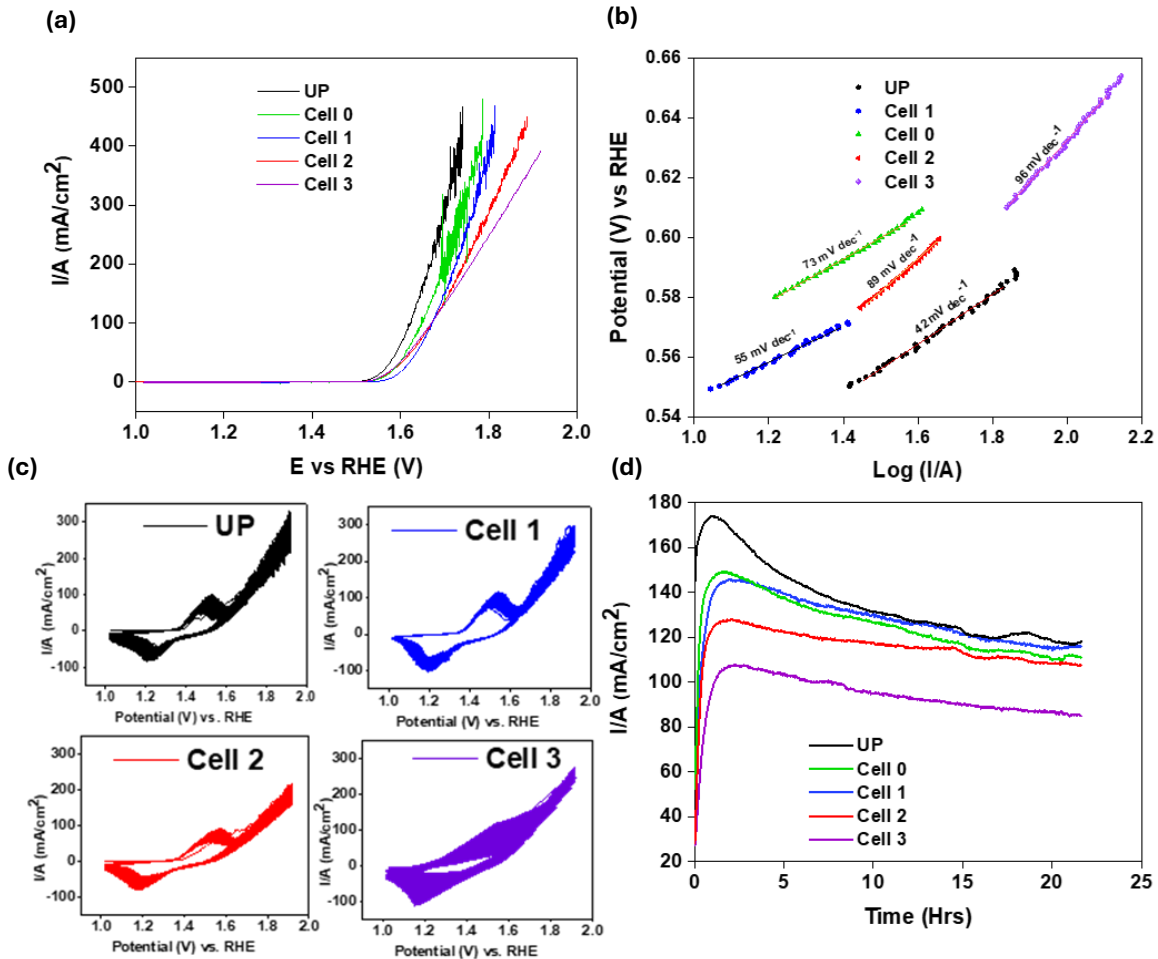


**Figure 6.1.** (a) LSVs recorded at  $0.1 \text{ mV.s}^{-1}$  between 1.0 to 1.9 V, (b) Tafel slopes, (c) cyclic voltammograms recorded at  $100 \text{ mV.s}^{-1}$  for 2000 cycles and (d) chronoamperometric experiments conducted at 1.7 V for 21 h for UP, Cell 0, Cell 1, Cell 2 and Cell 3 electrodes in 1 M KOH.

The electrochemical analysis of the NMC materials presents interesting observations that lead to the conclusion that more extensive battery cycling of up to 200 cycles leads to worse performance for the NMC 622 electrodes. It has been reported in a previous study that when LiCoO<sub>2</sub> is cycled more extensively in a battery, that more active sites become available and the OER improves.<sup>11</sup> To understand this outcome the NMC 622 pristine powder of sample UP and recovered from Cell 3 (200 cycles) were observed by SEM prior to any OER experiments to understand the surface morphology changes that may arise due to battery cycling. As shown in Figure 6.2a, SEM images of the UP sample show that the particles are well distributed with sizes in the order of microns (Figure 6.2b) that are in close proximity but not agglomerated. Upon closer inspection each larger particle consists of smaller particles that

are less than 1 micron in diameter (Figure 6.2c). However, the structures of NMC 622 recovered from Cell 3 shown in Figure 6.2d are distinctly different with much smaller particles that result in more film like formation on the substrate that contain large and deep cracks at the micro scale. After cycling in the battery the larger micron sized particles are reduced in size to the nanoscale that agglomerate across the electrode surface (Figure 6.2e, f). The electrochemical surface area (ECSA) was determined via double layer charging experiments (Figure 6.2g-i) where the ECSA for the UP cell was  $1.4 \text{ cm}^2$  and the Cell 3 sample was  $1.67 \text{ cm}^2$ . This indicates that the inherent specific activity of the recovered Cell 3 material is significantly lower due to battery cycling even though the surface area was higher due to particle pulverisation. After repetitive cycling in the OER region, the ECSA for the UP sample increased to  $1.85 \text{ cm}^2$  and  $1.83 \text{ cm}^2$  for the UP and Cell 3 samples, respectively indicating that the specific activity of the recovered battery material is still lower.

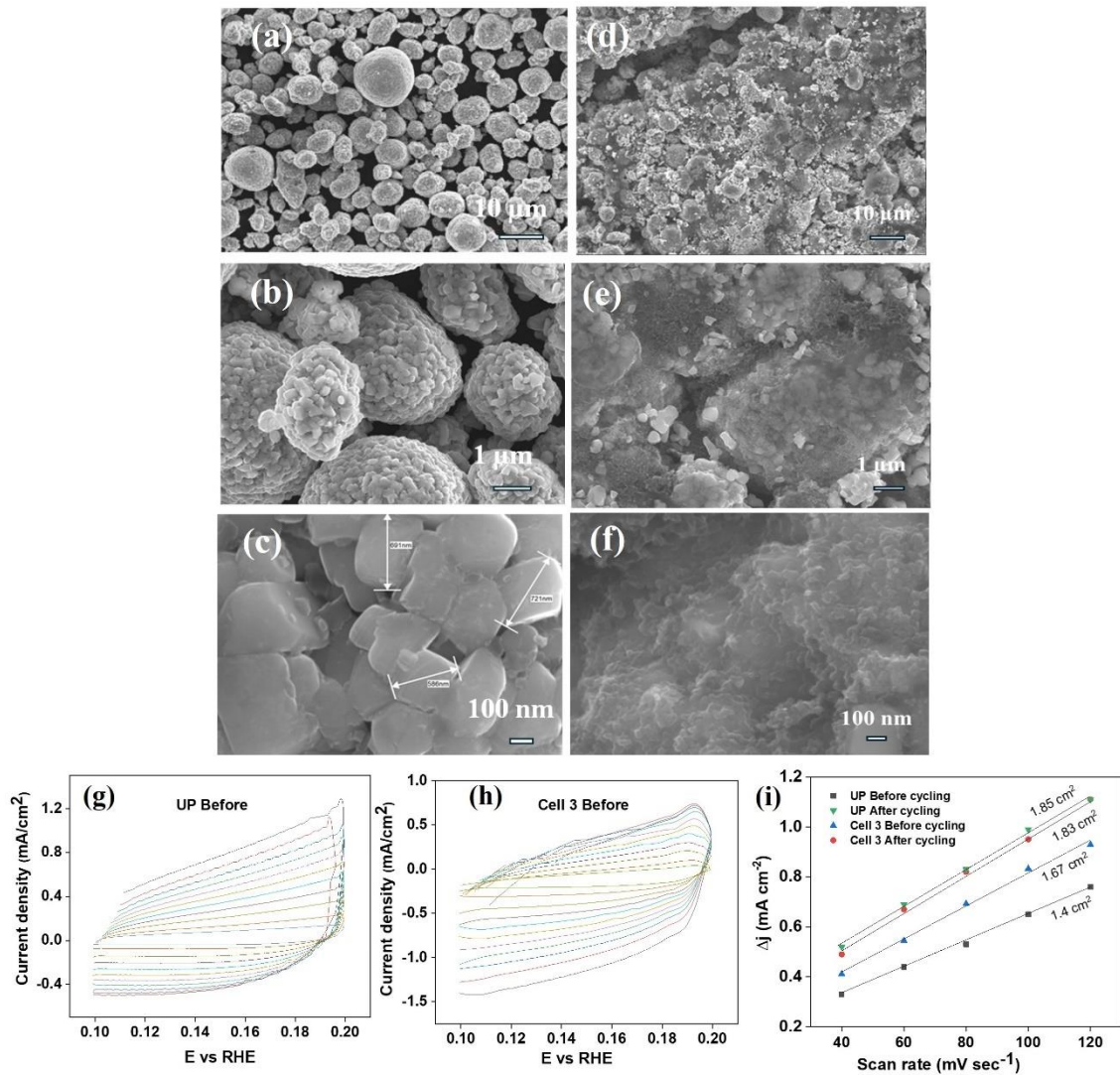


**Figure 6.2.** SEM images of (a-c) unprocessed UP (NMC-622) sample and (d-f) NMC 622 recovered from Cell 3. CVs recorded from 40 to 120 mV s<sup>-1</sup> in 1 M KOH at (g) UP (NMC-622) and (h) NMC 622 recovered from Cell 3. (i) Plots determining the ECSA for UP and Cell 3 before the OER and after being subjected to 2000 cycles in the OER region (1 to 1.9 V).

Further studies were conducted to observe the oxidation states of the unprocessed sample (UP (NMC 622)) compared with NMC 622 recovered from Cell 3. It is observed in Figure 4 that the Ni 2p core level spectrum shows peaks around 855.4 eV that belongs to Ni 2p<sub>3/2</sub> for the Ni<sup>+2</sup> oxidation state with a satellite peak around 860.4 eV.<sup>13</sup> Peaks at 872.4<sup>14</sup>, 874.1<sup>15</sup> and 878.4 eV belong to the Ni 2p<sub>1/2</sub> orbital for the Ni<sup>+2</sup> oxidation state<sup>16</sup> that is attributed to the formation of hydroxides. Similar peaks were observed for NMC 622 from Cell 3. The high resolution XPS Co 2p spectrum for the UP (NMC 622) sample shows peaks at 780.01 and 781.8 eV attributed to Co 2p<sub>3/2</sub><sup>17, 18</sup> while the peak at 793.1 and 798.3 eV belongs to Co 2p<sub>1/2</sub> representing the Co<sup>+2</sup> oxidation state.<sup>19</sup> For NMC 622 recovered from Cell 3 the XPS spectrum is mostly unchanged apart from a shift to a lower binding energy position from 780.0 eV to 779.6 eV indicating a more reduced Co surface species.

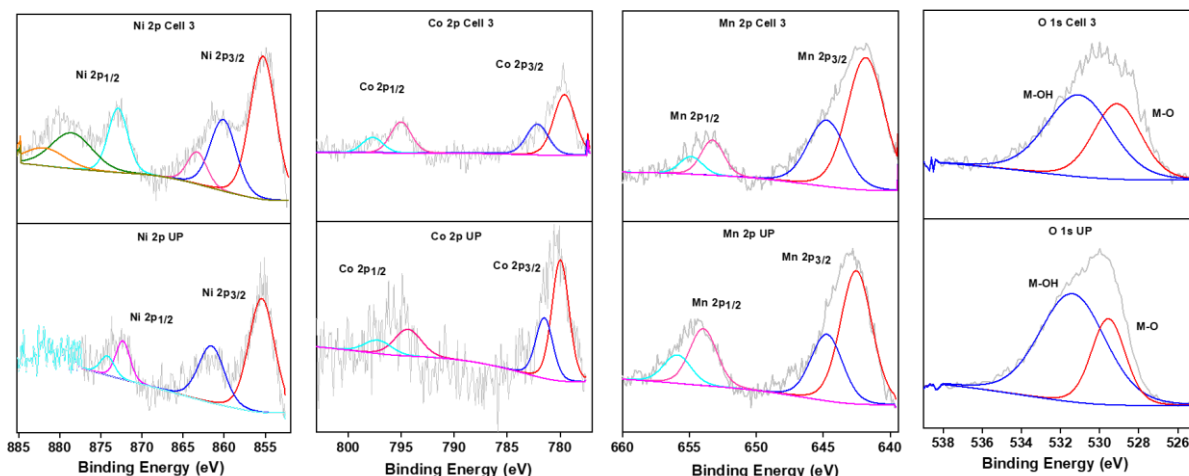


**Figure 6.3.** XPS spectra for Ni 2p, Co 2p, Mn 2p and O1s for UP (NMC 622) and Cell 3 recovered NMC 622.

The high-resolution Mn 2p spectrum of NMC 622 (UP) shows prominent peaks at 642.5 and 653.6 eV that refers to 2p<sub>3/2</sub> orbitals. Additionally, peaks at 644.7 eV and 656.1 eV belongs to Mn 2p<sub>1/2</sub> for the Mn<sup>+2</sup> oxidation state.<sup>16,22</sup> For NMC 622 from Cell 3 a similar set of peaks were observed, however there is also a slight decrease in binding energy for the main peak to 642.1 eV as seen for the case of Co 2p. Finally, the O 1s spectra for NMC 622 (UP) shows the

prominent presence of hydroxyl groups in the form of M-OH and metal oxides (M-O). However, for NMC 622 recovered from Cell 3 the extent of M-OH groups on the surface is diminished. The XPS data indicates that there are minor differences in the surface chemistry of the particles for the unprocessed NMC 622 and the material recovered from a battery that was cycled 200 times. The differences are the lower amount of M-OH species and less oxidised Co and Mn species on the surface of the NMC 622 material after 200 battery cycles which may impact on the activity and stability of the electrode. This result indicates that this proposed direct recycling approach is most suited to NMC 622 containing LIBs that fail quality assurance tests after their production. This may be a viable economic pathway to recover the cost incurred for failed cells that still undergo the formation and aging steps during their manufacture which account for approximately one-third of the manufacturing cost allocation.

## 6.5 Conclusions

This study contributes important missing information for the potential use of recovered NMC 622 battery materials as OER electrocatalysts. It was found that battery history impacted the electrocatalytic activity of the recovered material where increasing the number of battery cycles resulted in a gradual decrease in performance for the OER. The particles recovered from an NMC 622 battery that was cycled 200 times had a significantly changed morphology with higher surface area than the pristine NMC 622 with a slightly more reduced surface chemistry containing fewer M-OH species. This resulted in the inherent specific activity of the recovered material being lower for the OER. This outcome however opens a pathway for the often-overlooked problem of battery scrap that is produced during battery manufacturing consisting of cells that fail quality assurance tests. Recycling these NMC 622 cathodes may be a viable route to recover the costs associated with manufacturing such failed cells.

## 6.6 Acknowledgements

AOM acknowledges partial funding from the Australian Research Council (DP180102869, IH190100009). The authors acknowledge the instrumentation and technical support of the QUT Central Analytical Research Facility (CARF) and scholarship support through the QUT/Max Planck Institute of Colloids and Interfaces Joint Laboratory on Nanocatalysis for Sustainable Chemistry. MRH and JC acknowledge funding support from the Electrochemical Testing Project (Project 022) of the Future Battery Industries Cooperative Research Centre.

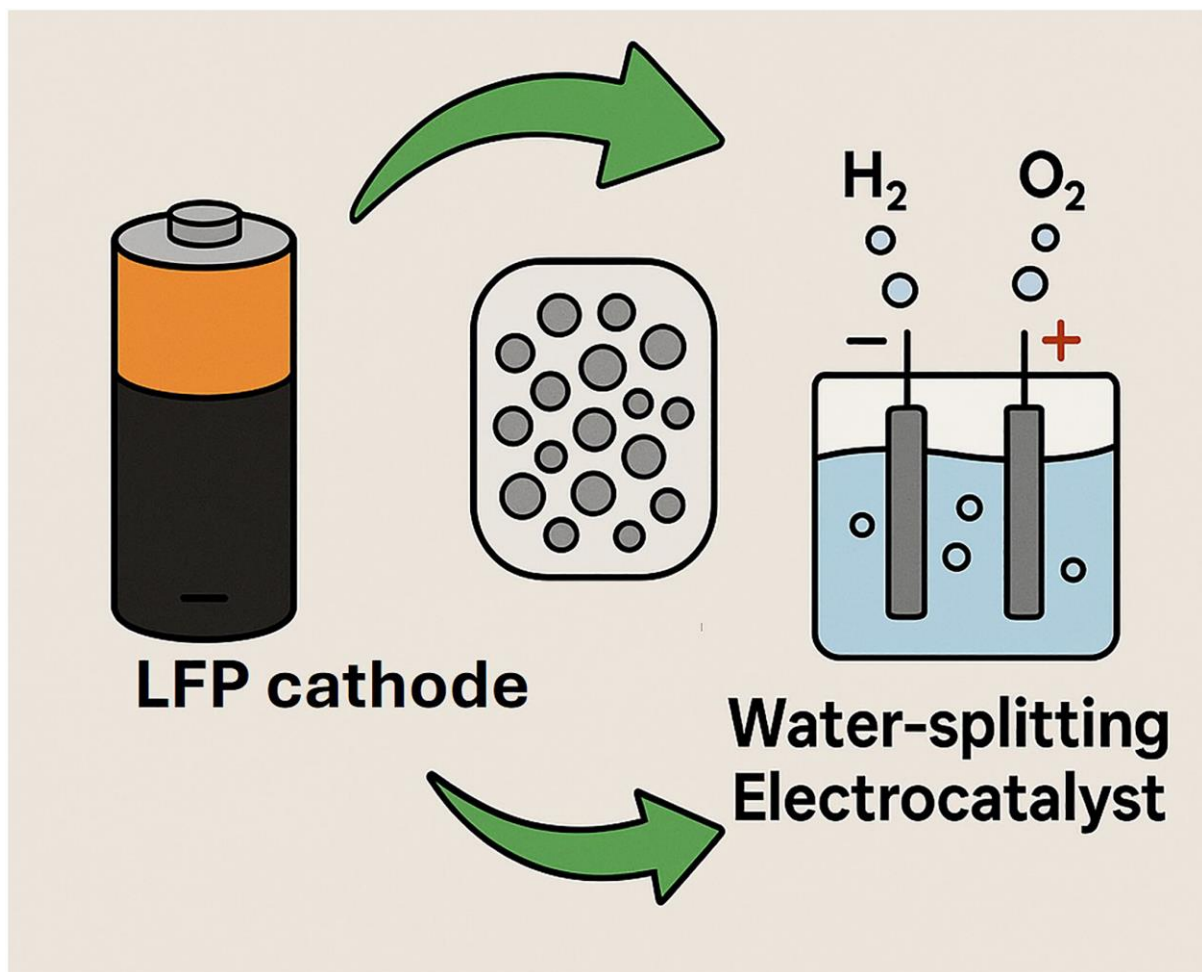
## References

- (1) Jiang, Q.; Chen, N.; Liu, D.; Wang, S.; Zhang, H. Efficient Plasma-Enhanced Method for Layered  $\text{LiNi}_{1/3}\text{Co}_{1/3}\text{Mn}_{1/3}\text{O}_2$  cathodes with Sulfur Atom-Scale Modification for Superior-Performance Li-Ion Batteries. *Nanoscale* 2016, **8**, 11234–11240.
- (2) Chu, Y.; Mu, Y.; Zou, L.; Wu, F.; Yang, L.; Feng, Y.; Zeng, L. Oxygen Release in Ni-rich Layered Cathode for Lithium-ion Batteries: Mechanisms and Mitigating Strategies. *ChemElectroChem* 2024, **11**, 00653.
- (3) Dose, W. M.; Li, W.; Temprano, I.; O’Keefe, C. A.; Mehdi, B. L.; De Volder, M. F. L.; Grey, C. P. Onset Potential for Electrolyte Oxidation and Ni-Rich Cathode Degradation in Lithium-Ion Batteries. *ACS Energy Lett.* 2022, **7** (10), 3524–3530.
- (4) Wei, Q.; Wu, Y.; Li, S.; Chen, R.; Ding, J.; Zhang, C. Spent Lithium Ion Battery (LIB) Recycle from Electric Vehicles: A Mini-Review. *Sci. Total Environ.* 2023, **866**, 161380.
- (5) Latini, D.; Vaccari, M.; Lagnoni, M.; Orefice, M.; Mathieu, F.; Huisman, J.; Tognotti, L.; Bertei, A. A Comprehensive Review and Classification of Unit Operations with Assessment of Outputs Quality in Lithium-Ion Battery Recycling. *J. Power Sources* 2022, **546**, 231979.
- (6) Yu, L.; Bai, Y.; Polzin, B.; Belharouak, I. Unlocking Value Recycling Scrap from Li-Ion Battery Manufacturing: Challenges Outlook, *J. Power Sources* 2024, **593**, 233955.
- (7) Fleischmann, J.; Hanicke, M.; Horetsky, E.; Ibrahim, D.; Jautelat, S.; Linder, M. & van de Rijt. *Battery 2030: Resilient, sustainable, circular*. McKinsey & Company 2023, **16**.
- (8) Castillo, S. Advances in the Recovering of Spent Lithium Battery Compounds. *J. Power Sources* 2002, **112**, 247–254.
- (9) Xu, J.; Thomas, H. R.; Francis, R. W.; Lum, K. R.; Wang, J.; Liang, B. A Review of Processes and Technologies for the Recycling of Lithium-Ion Secondary Batteries. *J. Power Sources* 2008, **177**, 512–527.
- (10) Saleem, H.; Khosravi, M.; Maroufi, S.; Sahajwalla, V.; O’Mullane, A. P. Repurposing Metal Containing Wastes and Mass-Produced Materials as Electrocatalysts for Water Electrolysis. *Sustain. Energy Fuels* 2022, **6**, 4829–4844.
- (11) Chen, N.; Qi, J.; Du, X.; Wang, Y.; Zhang, W.; Wang, Y.; Lu, Y.; Wang, S. Recycled  $\text{LiCoO}_2$  in Spent Lithium-Ion Battery as an Oxygen Evolution Electrocatalyst. *RSC Adv.* 2016, **6**, 103541–103545.
- (12) Kaur, A.; Alarco, J.; Mullane, A. P. O. Investigating the Potential Use of Ni-Mn-Co (NMC) Battery Materials as Electrocatalysts for Electrochemical Water Splitting. *ChemPhysChem* 2024, **25**, e202400124.
- (13) Sultana, U. K.; Fernando, J. F. S.; O’Mullane, A. P. Transformation of Stainless Steel 316 into a Bifunctional Water Splitting Electrocatalyst Tolerant to Polarity Switching. *Sustain. Mater. Technol.* 2020, **25**, e00177.
- (14) Babar, P.; Lokhande, A.; Karade, V.; Pawar, B.; Gang, M. G.; Pawar, S.; Kim, J. H. Towards Highly Efficient and Low-Cost Oxygen Evolution Reaction Electrocatalysts: An Effective Method of Electronic Waste Management by Utilizing Waste Cu Cable Wires. *J. Colloid Interface Sci.* 2019, **537**, 43–49.

- (15) Sivanantham, A.; Ganesan, P.; Shanmugam, S. Hierarchical NiCo<sub>2</sub>S<sub>4</sub> Nanowire Arrays Supported on Ni Foam: An Efficient and Durable Bifunctional Electrocatalyst for Oxygen and Hydrogen Evolution Reactions. *Adv. Funct. Mater.* 2016, **26**, 4661–4672.
- (16) Salem, K. E.; Saleh, A. A.; Khedr, G. E.; Shaheen, B. S.; Allam, N. K. Unveiling the Optimal Interfacial Synergy of Plasma-Modulated Trimetallic Mn-Ni-Co Phosphides: Tailoring Deposition Ratio for Complementary Water Splitting. *Energy Environ. Mater.* 2022, **6**, e12324.
- (17) Arian, R.; Zardkhoshouei, A. M.; Hosseiny Davarani, S. S. Rational Construction of Core-Shell Ni-Mn-Co-S@Co(OH)<sub>2</sub> Nanoarrays toward High-Performance Hybrid Supercapacitors. *ChemElectroChem* 2020, **7**, 2816–2825.
- (18) Chinnadurai, D.; Rajendiran, R.; Li, O. L.; Prabakar, K. Mn-Co Bimetallic Phosphate on Electrodeposited PANI Nanowires with Composition Modulated Structural Morphology for Efficient Electrocatalytic Water Splitting. *Appl. Catal. B* 2021, **292**, 120202.
- (19) Cao, H.; Xie, Y.; Wang, H.; Xiao, F.; Wu, A.; Li, L.; Xu, Z.; Xiong, N.; Pan, K. Flower-like CoP Microballs Assembled with (002) Facet Nanowires via Precursor Route: Efficient Electrocatalysts for Hydrogen and Oxygen Evolution. *Electrochim. Acta* 2018, **259**, 830–840.
- (20) Sultana, U. K.; Riches, J. D.; O’Mullane, A. P. Gold Doping in a Layered Co-Ni Hydroxide System via Galvanic Replacement for Overall Electrochemical Water Splitting. *Adv. Funct. Mater.* 2018, **28**, 1804361.
- (21) Lu, B.; Zang, J.; Li, W.; Li, J.; Zou, Q.; Zhou, Y.; Wang, Y. Co-Doped Ni<sub>x</sub>Py Loading on Co<sub>3</sub>O<sub>4</sub> Embedded in Ni Foam as a Hierarchically Porous Self-Supported Electrode for Overall Water Splitting. *Chem. Eng. J.* 2021, **422**, 130062.
- (22) Dhakal, P. P.; Pan, U. N.; Paudel, D. R.; Kandel, M. R.; Kim, N. H.; Lee, J. H. Cobalt–Manganese Sulfide Hybridized Fe-Doped 1T-Vanadium Disulfide 3D-Hierarchical Core-Shell Nanorods for Extreme Low Potential Overall Water-Splitting. *Mater. Today Nano* 2022, **20**, 100272.

## Chapter 7

### Using Recovered Lithium Iron Phosphate Battery Material as an Electrocatalyst for the Oxygen Evolution Reaction



The following paper has been published in a peer reviewed journal based in this chapter.

**Arshdeep Kaur**, Hongxia Wang, Umair Gulzar, Colm O'Dwyer and Anthony P. O'Mullane, "Using Recovered Lithium Iron Phosphate Battery Material as an Electrocatalyst for the Oxygen Evolution Reaction", **CleanMat**, 1-13, 2025.

[doi.org/10.1002/clem.70005](https://doi.org/10.1002/clem.70005)

The authors listed below have certified that:

1. They meet the criteria for authorship and that they have participated in the conception, execution, or interpretation, of at least that part of the publication in their field of expertise;
2. They take public responsibility for their part of the publication, except for the responsible author who accepts overall responsibility for the publication;
3. There are no other authors of the publication according to these criteria;
4. Potential conflicts of interest have been disclosed to (a) granting bodies, (b) the editor or publisher of journals or other publications, and (c) the head of the responsible academic unit, and
5. They agree to the use of the publication in the student's thesis and its publication on the QUT's ePrints site consistent with any limitations set by publisher requirements.

<b>Contribution</b>	<b>Statement of Contribution</b>
Arshdeep Kaur	Conceptualisation, methodology, investigation, data curation, writing – original draft.
Hongxia Wang	Methodology, resources, supervision, writing – review & editing
Umair Gulzar	Methodology, resources, writing – review & editing.
Colm O'Dwyer <sup>3</sup>	Methodology, resources, writing – review & editing.
Anthony O'Mullane	Conceptualisation, methodology, resources, supervision, funding acquisition, writing – review & editing.

**Background:** Previous chapter examined whether NMC recovered from cycled batteries would impact water-splitting performance and concluded that increase in number of battery cycles decreases OER performance. To further examine the nature of cycled materials this chapter provides insights on LFP-based materials recovered from waste Li-ion batteries, including LiFePO<sub>4</sub> film electrodes, LiFePO<sub>4</sub> powder, and materials extracted from cycled batteries, and assessed for their electrochemical performance in water splitting

## 7.1 Abstract

The rapid emergence of Li ion batteries to satisfy ever increasing energy demands will result in a future waste problem at their end of life. Li ion batteries that use lithium iron phosphate (LFP) as a cathode material are becoming more widespread with increasing market share. Therefore, there will be significant volumes of this type of battery waste in the future. In this work we propose to recover LFP from spent LFP based Li ion batteries and demonstrate their usefulness as electrocatalysts for the oxygen evolution reaction which is critical to electrochemical water splitting and the production of green hydrogen. We show that recovered LFP once immobilised onto a Ni substrate reconstructs into a mixed Fe/Ni oxide surface layer which is highly active for the OER. Promisingly LFP recovered from a battery that was cycled multiple times showed excellent electrocatalytic performance. This resulted in an electrocatalyst with a low Tafel slope of 58 mV dec<sup>-1</sup>, overpotential values of 250 and 310 mV to reach 10 and 100 mA cm<sup>-2</sup>, respectively and 24 h stability at over 200 mA cm<sup>-2</sup>. This outcome provides potential motivation for recyclers to isolate LFP from spent Li ion batteries for use in water electrolysis.

## 7.2 Introduction

Preserving our environment and establishing a global renewable energy system is one of the most crucial challenges of our society. Rising carbon dioxide emissions with resultant climate change is now manifesting as localised environmental threats where extreme weather is becoming more common. As a result, there is a significant drive to reduce our dependence on fossil fuels by moving towards renewable energy sources like solar, wind etc.<sup>1, 2, 3, 4</sup>. However, even though solar and wind are abundant energy sources they are intermittent and when combined with ever increasing energy demands, energy storage is required in the absence of sun and wind<sup>5</sup>.

As an energy carrier, hydrogen is considered as a promising fuel for a sustainable energy future as it has the capacity to replace fossil fuels due to its clean/green by-product after utilisation and high gravimetric energy density (142MJ/kg) compared to other fuels<sup>6</sup>. However, the deployment of hydrogen-based infrastructure and realisation of a hydrogen society needs certain advancements particularly in generating hydrogen through water electrolysis<sup>7</sup>. This process involves electrochemical conversion of water into H<sub>2</sub> and O<sub>2</sub> using effective electrocatalysts at the cathode and anode respectively,<sup>7, 8, 9, 10</sup> which can be powered by renewable electricity.

For the two half reactions, the hydrogen evolution reaction (HER) and the oxygen evolution reaction (OER), the latter is slower and more sluggish in nature due to slower kinetics which requires the transfer of 4 electrons which impacts the overall process and ultimately hydrogen production<sup>11, 12, 13, 14, 15</sup>. Although many commercial electrocatalyst are noble-metal based metal oxides like RuO<sub>2</sub> and IrO<sub>2</sub>, their limited availability and high cost limits there extensive use on large scales<sup>6, 16</sup>. Thus, there is an urgent demand to discover outstanding OER electrocatalysts that are active, cost-effective with high durability<sup>17</sup>.

In recent years, significant interest has developed in exploring various cost effective non-noble metal catalysts for the OER. In particular, oxides of first row transition metals have garnered significant attention, which is due to their abundant availability, durability and high catalytic performance. For instance Co based oxides,<sup>18, 16, 12</sup> layer double hydroxides (LDH) (Ni, Fe, Co, Mn LDH)<sup>19</sup>, Fe-doped nickel-based (oxy)- hydroxides (NiFe-O<sub>x</sub>H<sub>y</sub>) show fast kinetics for the OER<sup>11</sup>. Additionally, precursor materials such as phosphate-based materials have demonstrated good activity. For example, Co based phosphates<sup>20, 21, 22</sup> Ni-based phosphate (Ni : Pi Fe) show low overpotentials compared to non-phosphate material<sup>6</sup>. Lui *et. al.*, demonstrated that electrochemical tuning of olivine-type lithium transition-metal phosphates LiMPO<sub>4</sub> (M= Fe, Mn, Co, Ni) show promising OER performance<sup>15</sup>. Similarly, Wu *et. al.*, synthesized Fe doped LiCoPO<sub>4</sub> for enhanced OER activity<sup>18</sup>. In recent studies, earth abundant iron phosphate demonstrated favourable results for OER catalytic activity where Cui et al. demonstrated that Ni incorporated into LiFePO<sub>4</sub> shows promising activity<sup>23</sup>. Generally, in these studies these materials act as precursors to the active form which transitions into a metal oxyhydroxide (MOOH) species during the OER.

Furthermore, in the pace to curb CO<sub>2</sub> emissions from the electricity generation and transportation sectors, there has been a dramatic increase in battery production<sup>24</sup>. This rising

use of batteries will inevitably lead to a considerable amount of electronic waste when battery powered devices have reached their end-of-life<sup>25</sup>. Furthermore, the demand of critical metals to produce new batteries and disposal polices of waste batteries have led to a rise in environmental and financial concerns where there is a probability that concentrated valuable metals will be disposed of without effective metal recovery processes<sup>26</sup>. Also, if not handled correctly, battery waste is detrimental to both human health and the environment<sup>27</sup>. Additionally, to drive the shift towards low-carbon technologies to address the climate change and reserve valuable resources the economy needs to shift from a linear approach of Make → Use → Dispose to a circular approach of Make → Use → Reuse → Recycle. This will minimise the use of primary resources and repurpose them for various applications<sup>28, 29</sup>.

A general battery module is structured as a cathode (positive electrode), anode (negative electrode), and an electrolyte, as is the case for a Lithium-Ion-Battery (LIB). Therefore, the composition of materials in a LIB consists of 31% active cathode material, 22% anode, 17% copper, 15% electrolyte solution, 8% aluminium, 4% carbon black and binder and 3% separators. The cathode materials in particular usually consist of precious metals that exhibit desirable electrochemical properties<sup>30, 31</sup>. Our previous research showed that the current collector from a waste Ni metal hydride battery<sup>32</sup> and cathode materials NMC 811 and NMC622 from waste LIB's could be used as electrocatalysts for the OER<sup>33</sup>. Indeed, this is an emerging area of interest to add value to battery recycling<sup>34, 35, 36, 37, 38</sup>. Given the effectiveness of Fe-Ni based oxides for the OER under alkaline conditions<sup>39, 40, 41, 42, 43, 44</sup> we investigate lithium iron phosphate ( $\text{LiFePO}_4$ ) cathode materials to determine their potential effectiveness as OER catalysts. Herein, various LFP based materials from waste Li-ion batteries such as LiFePO<sub>4</sub>-film electrodes, LiFePO<sub>4</sub>-powder and material recovered from cycled batteries are compared with respect to their electrochemical properties for water splitting. It was found that LFP supported on Ni foam restructures into a highly active form that can be utilized as an electrocatalyst for the OER and that the effect of battery cycling did not significantly impact performance. This suggests that LFP cathode materials recovered from Li based batteries can be repurposed and is an effective approach to recycle e-waste.

### 7.3 Results and Discussion

Initially powders of commercial iron phosphate (FP) and lithium iron phosphate (LFP) from Sigma Aldrich were sonicated in water and then immersed onto NF substrates to test the applicability of these materials for the oxygen evolution reaction. Figure 7.1(a) shows linear

sweep voltammograms (LSVs) recorded at 0.1 mV s<sup>-1</sup> at FP-NF and LFP-NF electrodes in 1 M KOH. For both samples (with equal mass) the OER current is significantly higher than the NF substrate electrode. The potential required to pass a current density of 100 mA cm<sup>-2</sup> for NF-LFP and NF-FP was 1.55 and 1.60 V, respectively. The improved performance of the LFP material compared to FP suggests that the presence of Li may be beneficial for the OER. Therefore, with this data it provided confidence that the recovery of LFP from the cathode of a Li ion battery could be a viable route to synthesising effective OER electrocatalysts.

Therefore, a commercial LFP battery electrode was investigated for its OER activity. The electrode consisted of a LFP film on an 18 mm diameter Al foil substrate from CUSTOMCELLS®. The film was removed from the Al substrate via simple immersion in a 1 M KOH solution after which it was collected and washed. A specific amount of the isolated film was then dispersed via sonication in a Nafion solution and (NF is immersed in solution) and NF substrate is used for electrochemical studies (full details are provided in the Experimental section). This pristine LFP-NF sample also showed enhanced activity compared to the NF substrate (Figure 7.1b) which is the same behaviour as seen for the powdered LFP sample (Figure 7.1a). Then the OER activity of LFP that was recovered from a cycled battery was investigated for batteries that were initially conditioned and then subjected to 5 and 100 cycles at a rate of 1 C which are denoted as samples NF-LFP(CV5) and NF-LFP(CV100), respectively.

The LSV data indicates that upon increasing the number of battery cycles the OER activity marginally increases where potentials of 1.56 and 1.57 V were required to pass 100 mA cm<sup>-2</sup> for NF-LFP(CV5) and NF-LFP(CV100), respectively. The Tafel slopes recorded for these samples were 56, 89 and 97 mV dec<sup>-1</sup> for NF-LFP (CV100), NF-LFP and NF-LFP (CV5), respectively indicating improved kinetics for the more extensively cycled battery (Figure 7.1c).

The samples stability for the OER was tested using chronoamperometry for 24 h at a potential of 1.7 V (Figure 7.1d). As expected from the LSV data the trend in current density passed was NF < LFP-NF < LFP-NF(CV5) ≤ NF-LFP(CV100). For both LFP-NF(CV5) and NF-LFP(CV100) the decay in OER is less pronounced compared to pristine LFP-NF and NF electrodes. This is consistent with the work of Guo *et. al.*, who investigated phosphate-based water splitting electrocatalysts and reported 30 h stability tests and chemical stability for (Co<sub>0.5</sub>Ni<sub>0.5</sub>)(PO<sub>4</sub>)<sub>2</sub>/Ni based catalysts for the OER<sup>23</sup>.

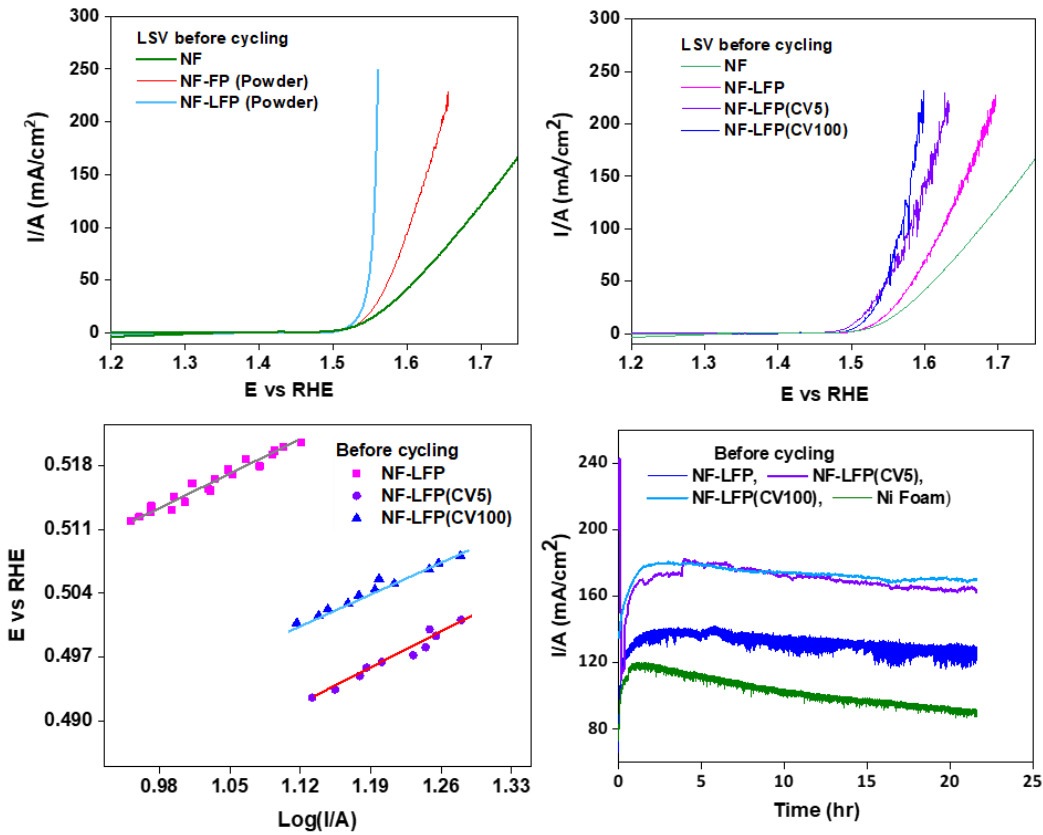


**Figure 7.1:** LSVs recorded at 0.1 mV s<sup>-1</sup> at (a, b) NF substrate, NF-FP, NF-LFP (Powder), NF-LFP, NF-LFP(CV5), NF-LFP(CV100) and (c) Tafel plots obtained for NF-LFP(CV5), NF-LFP(CV100), NF-LFP electrodes before cycling d) Chronoamperometric experiments conducted at 1.7 V for 24 h in 1 M KOH for NF substrate, NF-LFP(CV5), NF-LFP(CV100).

To determine if surface area is playing a role in increased activity double layer capacitance measurements were used to determine the electrochemical surface area (ECSA) of the electrodes (Figure S1). Values of 0.65, 0.31, 0.35 and 0.65 cm<sup>2</sup> were calculated for NF-LFP, NF-LFP(CV5) and NF-LFP(CV100), respectively indicating that the increased activity of the battery cycled LFP is not attributable to increased surface area and therefore their inherent specific activity is higher than the pristine LFP material.

The samples were then tested for their stability to repetitive OER to accelerate the degradation process and were subjected to 2000 cycles up to a potential value of 1.9 V (Figure 7.2a). This process not only includes the OER but also the oxidation and reduction of the electrocatalyst as seen by the redox process at ca. 1.5 V before the onset of the OER. From this data it can be seen that the LFP that had been used in the battery maintains higher performance compared to the pristine LFP material. It should be noted that the LFP (CV100) data is

overlapping the NF-LFP (CV5) data for the 2000 cycles. Tafel plots were then constructed using data from slow scan rate LSV curves ( $0.1 \text{ mV s}^{-1}$ ) and are shown in Figure 7.2(b) with Tafel slope values of  $47$  and  $58 \text{ mV dec}^{-1}$  for NF-LFP (CV5) and NF-LFP (CV100), respectively which are lower than the values seen for the samples that were not subjected to 2000 OER cycles. These values are comparable to previous studies on Ni-LiFePO<sub>4</sub> with a reported value of  $45 \text{ mV dec}^{-1}$ <sup>35</sup> and Ni/Ni Mn Co O (N/NMCO) electrodes prepared from spent LIB's with a Tafel slope value of  $47 \text{ mV dec}^{-1}$ <sup>45</sup>.

These samples were also tested under continuous electrolysis conditions for  $24 \text{ h}$  at  $1.7 \text{ V}$  (Figure 7.2c). For NF and LFP-NF the 2000 OER cycles did not significantly affect their performance when compared to Figure 1d. However, there is now a marked difference in OER activity for the NF LFP(CV5) sample which shows much higher current densities of  $> 200 \text{ mA cm}^{-2}$  compared to the other samples and is reasonably stable over a  $24 \text{ h}$  electrolysis period. Therefore, the effect of repetitive cycling has had a significant impact on the LFP material that had been subjected to more extensive battery cycling conditions. The ECSA of NF-LFP, NF-LFP(CV5), NF-LFP(CV100) however increased in all cases after 2000 cycles of the OER up to  $2.83$ ,  $2.75$  and  $2.71 \text{ cm}^2$ , respectively (Figure S1). Therefore, the marked increase in activity of NF-LFP(CV5) can be attributed to increased surface area and accessibility to active sites on the electrode surface. The electrochemical data associated with all samples in this study is summarised in Table 7.1.

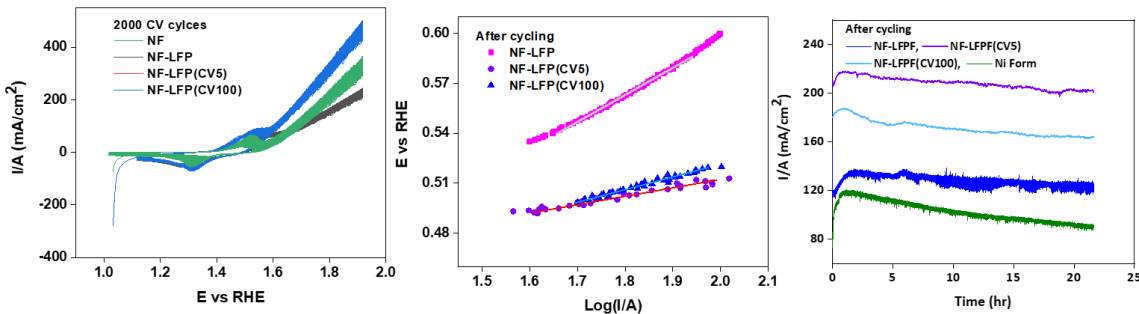


**Figure 7.2:** (a) Cyclic voltammograms recorded at  $100 \text{ mV sec}^{-1}$  for NF, NF-LFP(CV5), NF-LFP(CV100), NF-LFP electrodes in  $1 \text{ M KOH}$  for 2000 cycle at  $1.0$  to  $1.9 \text{ V}$ , (b) Tafel plots obtained for NF-LFP(CV5), NF-LFP(CV100), NF-LFP electrodes after cycling and (c) Chronoamperometric experiments conducted at  $1.7 \text{ V}$  for  $24 \text{ h}$  in  $1 \text{ M KOH}$  for NF substrate, NF-LFP(CV5), NF-LFP(CV100), NF-LFP electrodes after repetitive OER potential cycling.

**Table 7.1:** Electrochemical data for LFP materials used in this study.

Samples	Overpotential $\eta_{100}$ (mV)				Tafel (mV dec <sup>-1</sup> )		ECSA (cm <sup>2</sup> )	
	Before		After		Before	After	Before	After
	$\eta_{10}$	$\eta_{100}$	$\eta_{10}$	$\eta_{100}$	-	-	-	-
NF	310	450	350	470	103	180	0.09	1.70
NF-LFP	300	400	270	390	89	132	0.65	2.83
NF-LFP(CV5)	270	350	250	300	97	47	0.31	2.75
NF-LFP(CV100)	280	330	250	310	56	58	0.35	2.71
NF-LFP (Powder)	290	320	260	370	26	128	0.195	2.99
NF-FP	300	370	290	470	66	150	0.26	2.55

Previous studies on transition metal phosphite materials <sup>19</sup> reported good OER activity and predicted an increase in the oxidation states of Ni, Fe and PO<sup>-</sup> ions. This usually leads to the formation of new surface intermediates like of O, OH and OOH compounds that decreases the activation energy for the OER reaction and enhances the kinetics of the reaction. In addition, the presence Ni/Fe/PO<sub>4</sub> at the surface can lead to the formation of phosphate, phosphite and hypophosphite ions that can result in higher OER activity <sup>32</sup>. Moreover, there are many previous studies reporting that the presence of Fe suppresses higher Ni oxidation states and enhances overall OER activity of the electrode <sup>36</sup>. Additionally, the presence of Fe in a Ni based electrode like Ni foam enhances OER activity by forming layered double hydroxide phases in NiOOH<sup>46</sup>, which increases the number of catalytic active sites, enabling the edges, corners and defect sites of NiOOH to become the most active sites for the OER<sup>47</sup>. Furthermore, the presence of Fe<sup>+3</sup> prevents over oxidation of Ni sites which is believed to be an essential step in reducing the activation energy barrier of the OER reaction. The suppression of the over oxidation of Ni<sup>2+</sup> surface species is seen in Figure S2 where for NF the anodic peak grows and shifts anodically by 60 mV after 2000 cycles compared to NF-LFP which shows a suppressed and broader oxidation peak that does not grow in magnitude and only shifts by 30 mV. This is consistent with previous studies on Fe/Ni oxide systems used for the OER <sup>48, 49, 50, 51</sup>. From this cyclic voltammetric data it indicates that there is a significant change in the surface properties of the electrocatalyst and it is postulated that a mixed Fe/Ni oxide material is formed on the NF surface during electrochemical oxidation where Fe from the LFP is

incorporated into the oxidised NF surface layer. Therefore, the electrodes were characterised to determine this effect as well as the potential influence of lithium and phosphate species on the OER performance. Scanning electron microscopy images of a pristine LFP electrode is shown in Figure 7.3a indicating a well packed homogeneous layer of LFP particles.

Transmission electron microscopy images of these particles (from the sonicated solution) are shown in Figure 7S3 which demonstrates that the particles are crystalline with lattice fringe spacings of 0.22 nm corresponding to the (111) plane of  $\text{Fe}_2\text{P}$ <sup>52,53</sup> for LFP and 0.36 nm is attributed to the (111) plane of P- $\text{Fe}_2\text{O}_3$ -LFPs. SEM images of LFP(CV5) and LFP(CV100) electrodes recovered from cycled batteries are shown in Figure 7.3 (a). The images indicate increasing particle size upon cycling the battery which was reflected in the ECSA values which showed a decrease in surface area for the recovered LFP materials (Table 1). EDS mapping of the NF-LFP(CV100) sample is also included showing the homogeneous distribution of Fe, P and O across the NF substrate. TEM images of recovered LFP(CV5) and LFP(CV100) particles are shown in Figure S4 and S5 respectively. For LFP(CV5) the lattice fringe spacing of 0.22 nm corresponding to the (111) plane of  $\text{Fe}_2\text{P}$  is still evident whereas for LFP(CV100) lattice fringe spacings of 0.39 nm representing the (210) plane of orthorhombic  $\text{LiFePO}_4$ <sup>54</sup> and 0.47 nm representing the (003) plane of  $\text{Fe}_3\text{O}_4$ <sup>55</sup> were observed. This indicates that the battery cycling process subtly alters the composition of the LFP particles and also results in more aggregated particles as seen from the TEM images.

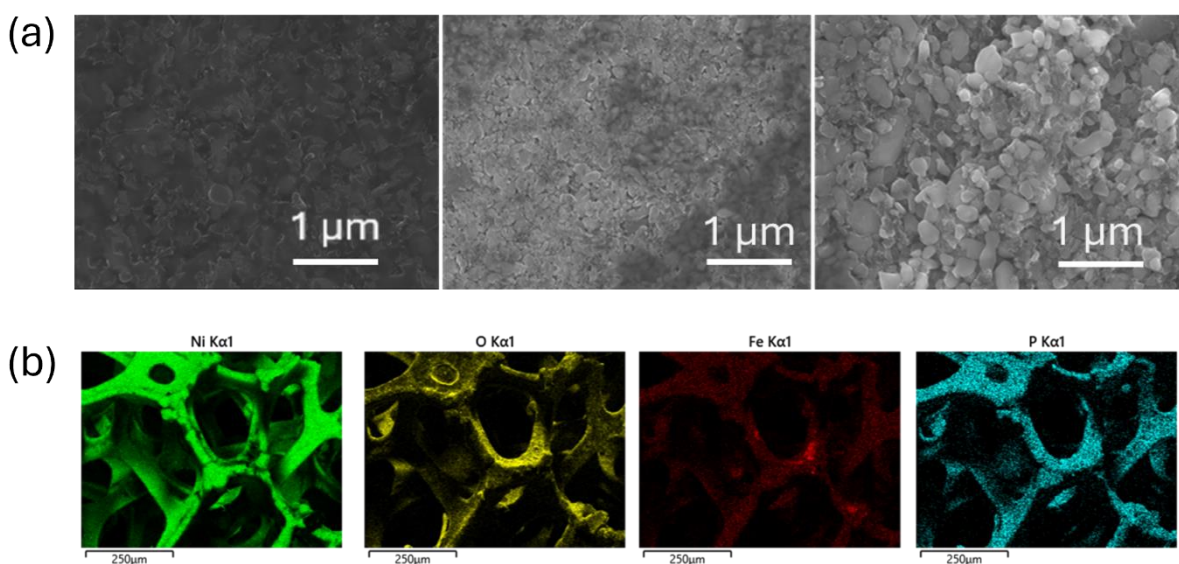


**Figure 7.3:** (a) SEM images of pristine LFP, LFP(CV5) and LFP(CV100) electrodes, and (b) EDS map of NF-LFP(CV100).

From the data in Figure 7.2 it indicates that repetitive OER cycling for 2000 cycles activates the NF-LFP electrodes that were used in battery cycling and improves the OER performance (Figure 7.2c). TEM analysis of LFP(CV5) particles that were sonicated off the NF support after 2000 cycles of the OER are shown in Figure 7.4. Both samples show agglomerated small particles with the emergence of a distinct lattice fringe spacing at 0.23 nm which corresponds to the presence of NiFe layered double hydroxide type materials<sup>45</sup>. No other crystalline phases could be identified for the LFP(CV100) sample and the SAED patterns recorded for both samples showed a distinct decrease in crystallinity for LFP(CV100) compared to LFP(CV5) via the absence of distinct rings and spots in the selected area electron diffraction (SAED) pattern (Figure 4d). For the LFP(CV5) material in particular, the generation of an amorphous material containing distinct crystallites may be a factor in the improved activity as there are now several reports on the importance of amorphous/crystalline interfaces for improving both the activity and stability of OER electrocatalysts<sup>56, 57, 58, 59</sup>. For LFP(CV100) the sample is much more amorphous as seen in the SAED pattern and therefore may be less active due to fewer amorphous/crystalline interfacial regions in the sample.

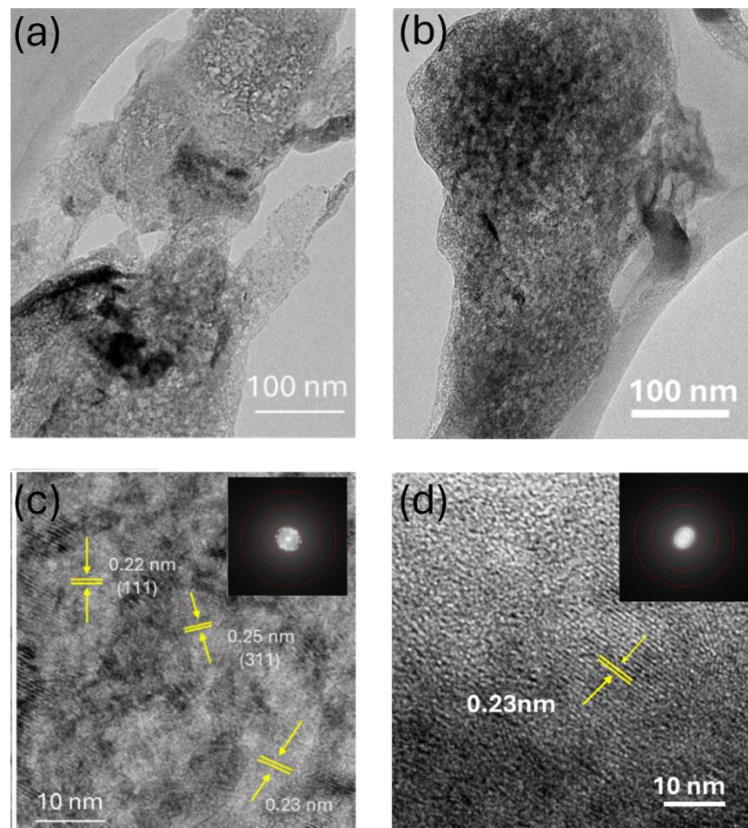


**Figure 7.4:** TEM images of (a, c) NF-LFP(CV5) and (b, d) NF-LFP(CV100) after 2000 OER cycles.

The potential formation of Fe/Ni oxide species due to the OER was further confirmed by TEM-EDS analysis shown in Figure 7.5. LFP(CV5) particles before the OER showed the presence of Fe, P and O distributed homogeneously through the particles. After the OER when the particles were removed from the NF substrate there is a clear presence of Ni, Fe, P and O indicating the incorporation of Ni into the LFP particles during repetitive OER cycling. The distribution of Ni, O and P is relatively homogeneous while there are some localised areas of increased concentration of Fe. Therefore restructuring of the catalysts surface during the OER is quite extensive and results in the formation of a new material at the electrode surface which will be the active form for the OER.

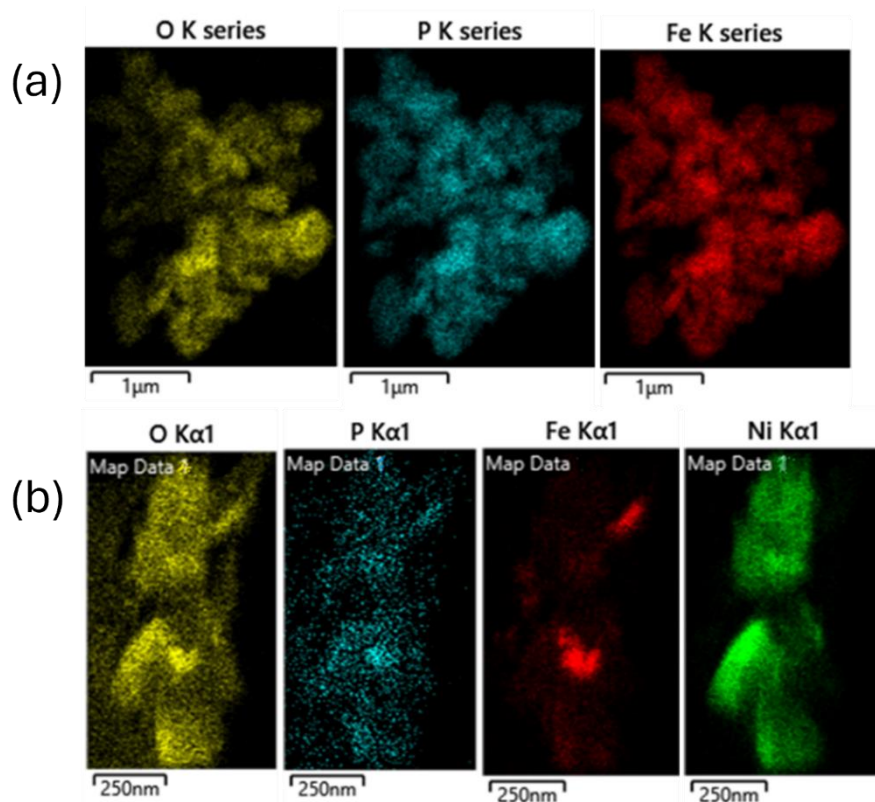


**Figure 7.5.** TEM-EDS mapping of (a) LFP(CV5) particles before the OER and (b) after 2000 OER cycles.

To identify the surface species on the electrodes, X-ray photoelectron spectroscopy (XPS) was undertaken both before and after OER potential cycling for particles removed from the NF substrate. The Ni 2p spectra in Figure 7.6 indicate that for LFP, LFP(CV5) and LFP(CV100) particles that Ni is incorporated into the particles in each instance, however the intensity of the signal for LFP(CV100) is much higher than the other samples with distinct satellite peaks at 877 and 880.0 eV indicating the presence of NiO or Ni(OH)<sub>2</sub><sup>60</sup>.

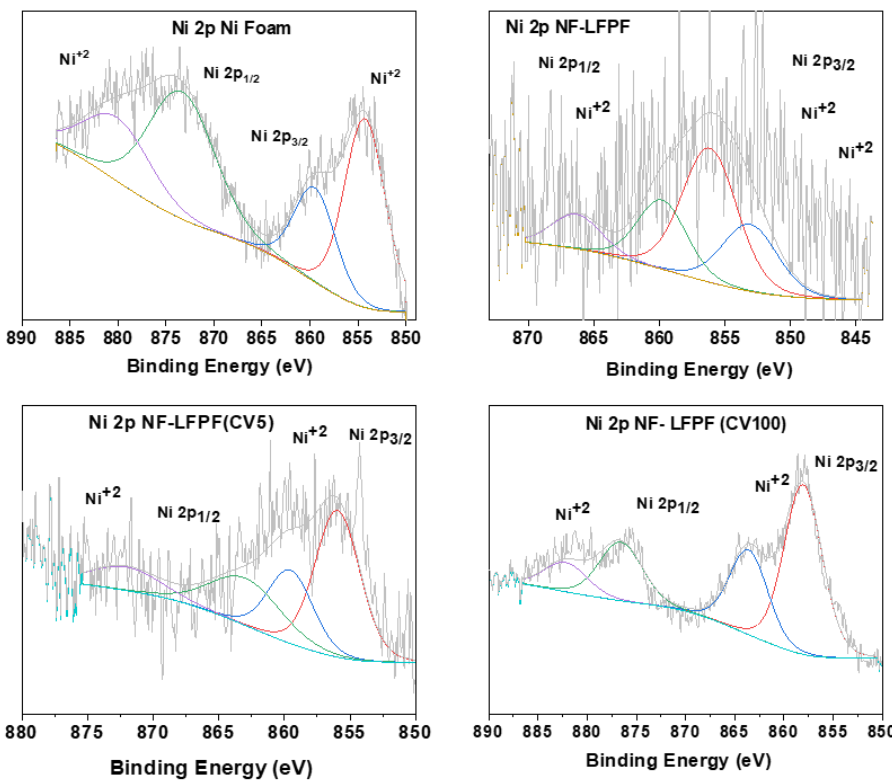


**Figure 7.6:** Ni 2p core level spectra for NF-LFP, LFP(CV5) and LFP(CV100) samples removed from the NF support after the OER.

The Fe 2p XPS spectra were recorded for all samples before and after the OER and shown in Figure 7.7. For the LFP sample the data is consistent with the presence of  $\text{Fe}^{+2}$  in  $\text{LiFePO}_4$ . For LFP(CV5) peaks at 718 and 730.3 eV emerge corresponding to the  $\text{Fe}^{+3}$  oxidation state<sup>61</sup> which are also evident for LFP(CV100) indicating that battery cycling results in some oxidation of LFP. After the OER, the signal intensity for Fe 2p reduces for the LFP sample while for LFP(CV100) and LFP(CV5) Fe is in the  $\text{Fe}^{2+}$  and  $\text{Fe}^{3+}$  states (potentially  $\text{FeOOH}$ ) and the peak at 718.0 eV indicates an Fe-Ni species<sup>62</sup>.

The P 1s XPS spectra for the samples indicate the presence of P-O and  $\text{PO}_3^-$  groups in all samples before the OER, however after the OER phosphorous is lost from the LFP and LFP(CV5) samples which is typical for transition metal phosphate materials<sup>63</sup> but is retained in the LFP(CV100) sample with peaks at 135.5 and 133.53 eV attributed to formation of  $\text{H}_3\text{PO}_4$  and Ni-P-O bonds, respectively<sup>13</sup>. Recently Sugawara *et al* reported the stability of P in Ni based phosphates during the OER in the form of  $\text{Ni}_3(\text{PO}_4)_2$  and indicates that the same type of stabilisation of the P element may be occurring here for sample LFP(CV100).

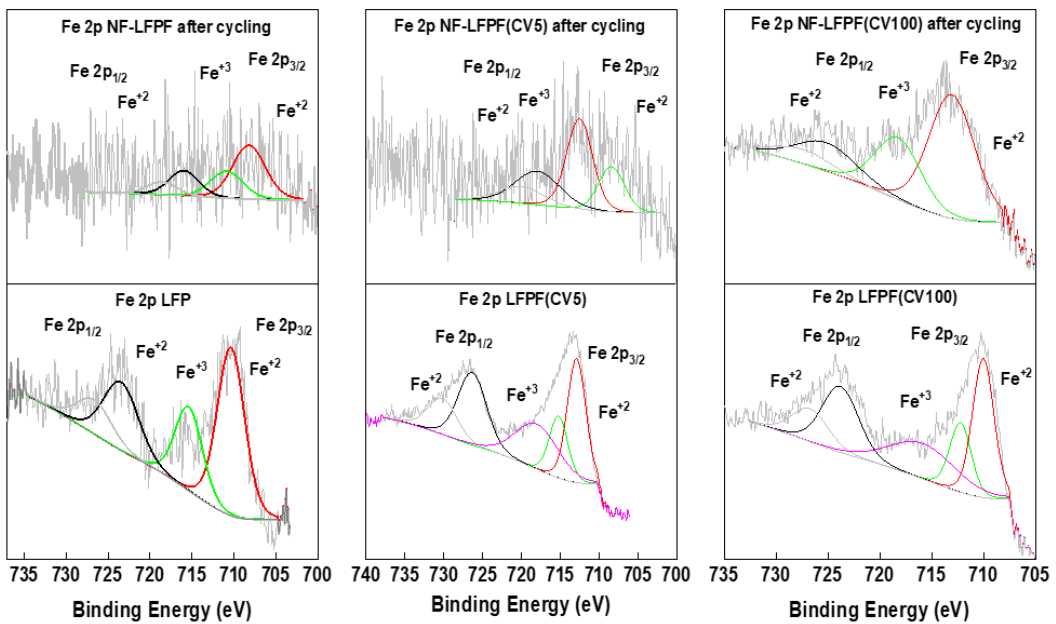


**Figure 7.7:** Fe 2p core level spectra for NF-LFP, LFP(CV5) and LFP(CV100) samples removed from the NF support both before and after the OER.

The O 1s spectra for LFP, LFP(CV5) and LFP(CV100) are consistent with the presence of phosphate groups on the surface (P-O) as well as some hydroxide species due to surface oxidation. After the OER there is a clear increase in the amount of M-OH species on the electrode surface which is most prominent in the LFP(CV100) sample. Finally the presence of Li was investigated and confirmed for each sample (Figure S6) before the OER. After the OER Li leached from the LFP and LFP(CV5) samples but was retained in the LFP(CV100) sample. A full description of all peak positions for each element is included in the supporting information.

From the TEM and XPS data the surface of the NF-LFP electrodes reconstruct quite significantly after the OER. In all cases the presence of a mixed Fe/Ni hydroxide and oxyhydroxide species are formed indicating that Ni migrates from the surface of the NF into the overlying LFP particle during potential cycling. These types of materials are known for their excellent OER activity which is also the case here as they outperform the NF substrate quite significantly in terms of current density and stability.

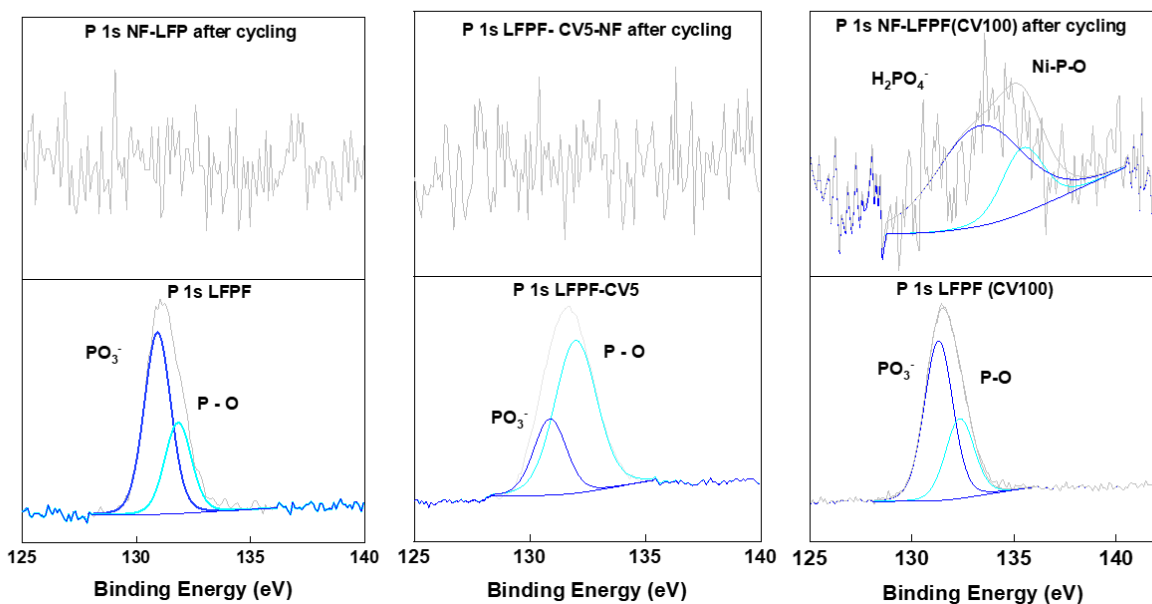


**Figure 7.8:** P 1s core level spectra for NF-LFP, LFP(CV5) and LFP(CV100) samples removed from the NF support both before and after the OER.

The best performing material was the LFP electrode that was cycled in a battery for 5 cycles. Although the initial LSV data was comparable to the battery cycled 100 times (Figure 1b) the LFP(CV5) material performed much better after extensive OER cycling and maintained good current densities of over  $200 \text{ mA cm}^{-2}$  for 24 h (Figure 7.2c).

Interestingly, XPS analysis revealed that the LFP(CV100) sample was the only sample to retain P and Li at the surface. The presence of these elements within the Ni/Fe hydroxide layer may impact on the activity of the material. Previous reports have shown that the presence of P-O species can promote electron transfer between the active metal centre and the oxygen adsorbate, thereby enhancing electrocatalytic activity<sup>64</sup>, however that is not the case here as LFP(CV5) is the most active material for the OER. Recent work on a  $\text{NiFe}_2\text{O}_4\text{-Vo-P}$  material where Vo are oxygen vacancies and P is the dopant revealed that filling P atoms into the material effectively modulates the electronic structure of the material and stabilizes the oxygen vacancies, which can increase cycling stability<sup>65</sup>. However, that same study reported that too much P filling had a detrimental effect on the OER and should be optimised. This may contribute to the lower activity of the LFP(CV100) sample as P species are still evident at the surface after the OER. For the LFP(CV5) sample without surface P Tafel slope of  $58 \text{ mV dec}^{-1}$  and overpotential value of 250 mV (after OER cycling for 2000 cycles) was measured which

provides confidence that a recycled material from a used battery has the potential to be used as an effective OER electrocatalyst with comparable activity to a specifically designed material.

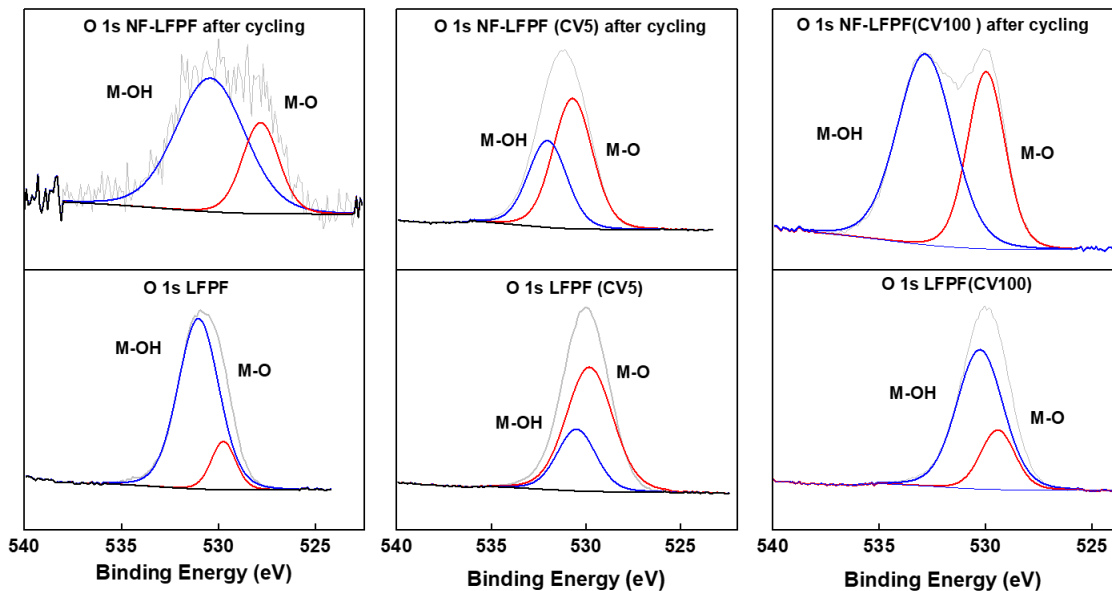


**Figure 7.9:** O 1s core level spectra for NF-LFPF, LFP(CV5) and LFP(CV100) samples removed from the NF support both before and after the OER.

Recently Suntivich *et al* reported that the presence of small cations such as  $\text{Li}^+$  in the electrolyte inhibits the electrocatalytic activity of metal oxide materials for the OER<sup>66</sup>. They indicated that the presence of cations can modify the energy of the OER intermediates, which are negatively charged and therefore are susceptible to electrostatic modification by the cations. Therefore, for sample LFP(CV100) which has Li species in the reconstructed surface layer may inhibit the formation of favourable intermediates during the course of the OER. For sample LFP(CV5) there appears to be no Li species in the reconstructed layer and therefore this effect does not occur which may lead to the increased activity.

#### 7.4 Conclusion

We have demonstrated that  $\text{LiFePO}_4$  cathode materials are potential electrocatalysts for the OER under alkaline conditions once they are immobilised on a Ni support and conditioned to form an active surface layer that incorporates Fe, Ni, O, P and Li. Performing the OER results in reconstruction of the NF electrode and incorporation of Ni into the LFP particles. The resultant material is a far more effective electrocatalyst for the OER compared to the NF substrate. For LFP cathodes recovered from cycled Li ion batteries at 1 C for 5 and 100 cycles a difference in OER activity was found where the less extensively cycled material was found

to be more active and stable after 2000 OER cycles. A low Tafel slope of 58 mV dec<sup>-1</sup>, overpotential values of 250 and 310 mV to reach 10 and 100 mA cm<sup>-2</sup>, respectively and 24 h stability at over 200 mA cm<sup>-2</sup> indicates a promising material for use in water electrolysis. The lower activity for the more extensively cycled battery material is attributed to the presence of P and Li species that are retained in the electrocatalyst. It is postulated that overfilling with P detrimentally effects the electronic activity while Li deactivates the Fe/Ni hydroxide layer via electrostatic interactions with negatively charged OER intermediates. However, even with this effect the LFP recovered from the more extensively cycled battery is still a far more effective electrocatalyst than pure NF. This study indicates that recovering LFP cathode materials from spent Li ion batteries may be viable and offers motivation to recycle these types of batteries in the future.

## 7.5 Experimental

### Materials

Potassium hydroxide (KOH 99.99% purity) and absolute ethanol and Nickel Foam (NF) were purchased from Sigma Adrich. Milli-Q water with resistivity of 18.2 MΩ.cm was used for the preparation of electrolyte solutions and washing purposes. (1×1.5 cm<sup>2</sup>) was first cleaned with 3 M HCl in order to remove surface oxides and then further sonicated in acetone, ethanol and deionised water for 30 min each followed by overnight drying at 60 degrees. 1 mg equivalent LFP in the form of film was prepared by taking of its aluminium layer by dipping 1M KOH solution for 2-5 seconds. Measuring the predecided amount of film and dissolve in Nafion (100 μL) and ethanol/water solvent in a 1:1. The mixture was stirred followed by 60 min sonication to disperse it. Around 300 μL of ink was then used for immersing the LFP material on the nickel foam. The prepared electrode was dried at 60 degrees overnight and then stored in an oven at room temperature.

### Electrochemical experiments

Electrochemical measurements were performed by using Biologic VSP workstation operated by EC -lab software (version 11.34) in a three-electrode cell. A leakless Ag/AgCl purchased from (eDAQ Pty Ltd) and a high purity graphite rod (1 mm diameter, Johnson Matthey Ultra “F” purity grade) were used as reference and counter electrode respectively. However, working electrode were prepared as mentioned in the method previously discussed. The working electrodes were washed with Milli-Q water after electrochemical tests to remove any electrolyte solution from the surface and dried at room temperature for further characterisation. All measurements were conducted in 1 M KOH electrolyte solution. The following equation

was used to convert the recorded potential to the RHE scale for all electrochemical measurements:

$$E_{RHE} = E_{Ag/AgCl} + (0.059 \times pH) + 0.197 V$$

while the overpotential ( $\eta$ ) for the OER was calculated using the formula  $\eta = E_{RHE} - 1.23 V$ . The current density was normalised to the geometric surface area of the electrode.

## Characterisation

The morphology of the samples was analysed by scanning electron microscopy (SEM) and energy dispersive spectroscopy (EDS) using a JEOL 7001F electron microscope at an operating voltage of 5 kV and 15 kV, respectively. X-ray photoelectron spectroscopy (XPS) data was collected using an Omicron Multiclan Lab Ultra-High Vacuum Scanning Tunnelling Microscope (UHV-STM) where a 125 mm hemispherical electron energy analyser was incorporated. XPS measurements were performed using non-monochromatic Mg K $\alpha$  (1253.6 eV) X-ray source (DAR 400, Omicron Nanotechnology), and the incident angle was 65° to the sample surface. The analyser pass energy of 50 eV with steps of 0.5 eV and the dwell time was 200 ms. High-resolution scans with a narrow region for Ni 2p, Fe 2p, P 1s, Li 1s, C 1 s and O 1 s were taken at 20 eV pass energy, 0.2 eV steps and with a 200 ms dwell time. Besides a wide scan of low binding energy region was performed from 250 eV to 0 eV swept at high resolution. The base pressure in the analysis chamber was  $1.0 \times 10^{-9}$  Torr and the pressure was  $1.0 \times 10^{-8}$  Torr during the measurement. Powder XRD patterns were collected using a Rigaku SmartLab diffractometer. HRTEM, SAED, and STEM-EDS measurements were performed using a JEOL 2100 TEM instrument operating at an accelerating voltage of 200 kV. The JEOL 2100 machine was equipped with a high-sensitivity OXFORD 80 mm<sup>2</sup> silicon drift X-ray detector for accurate elemental analysis and JEOL BF/DF detectors for STEM imaging.

## 7.6 Acknowledgements

AOM acknowledges funding from the Australian Research Council (DP180102869). The authors acknowledge the instrumentation and technical support of the QUT Central Analytical Research Facility (CARF) and scholarship support through the QUT/Max Planck Institute of Colloids and Interfaces Joint Laboratory on Nanocatalysis for Sustainable Chemistry

## References

- [1] Z.W. She, J. Kibsgaard, C.F. Dickens, I. Chorkendorff, J.K. Nørskov, T.F. Jaramillo, Combining theory and experiment in electrocatalysis: Insights into materials design, *Science* 355 (2017). <https://doi.org/10.1126/science.aad4998>.
- [2] S. Chu, A. Majumdar, Opportunities and challenges for a sustainable energy future, *Nature* 488 (2012) 294–303.
- [3] N.S. Lewis, D.G. Nocera, Powering the planet: chemical challenges in solar energy utilization, *Proc. Natl. Acad. Sci. U. S. A.* 103 (2006) 15729–15735.
- [4] J.A. Turner, Sustainable Hydrogen Production, *Science* 305 (2004).
- [5] P. Du, R. Eisenberg, Catalysts made of earth-abundant elements (Co, Ni, Fe) for water splitting: Recent progress and future challenges, *Energy Environ. Sci.* 5 (2012) 6012–6021.
- [6] R. Guo, X. Lai, J. Huang, X. Du, Y. Yan, Y. Sun, G. Zou, J. Xiong, Phosphate-Based Electrocatalysts for Water Splitting: Recent Progress, *ChemElectroChem* 5 (2018) 3822–3834.
- [7] C.C.L. McCrory, S. Jung, J.C. Peters, T.F. Jaramillo, Benchmarking heterogeneous electrocatalysts for the oxygen evolution reaction, *Journal of the American Chemical Society* 135 (2013) 16977–16987.
- [8] V.R. Stamenkovic, D. Strmcnik, P.P. Lopes, N.M. Markovic, Energy and fuels from electrochemical interfaces, *Nature Materials* 16 (2016) 57–69.
- [9] J. Suntivich, K.J. May, H.A. Gasteiger, J.B. Goodenough, Y. Shao-Horn, A Perovskite Oxide Optimized for Oxygen Evolution Catalysis from Molecular Orbital Principles, *Science* 334 (2011).
- [10] I. Roger, M.A. Shipman, M.D. Symes, Earth-abundant catalysts for electrochemical and photoelectrochemical water splitting, (2017). <https://doi.org/10.1038/s41570-016-0003>.
- [11] X. Meng, J. Han, L. Lu, G. Qiu, Z.L. Wang, C. Sun, Fe<sup>2+</sup>-Doped Layered Double (Ni, Fe) Hydroxides as Efficient Electrocatalysts for Water Splitting and Self-Powered Electrochemical Systems, *Small* 15 (2019) 1–10.
- [12] J. Huang, Y. Sun, Y. Zhang, G. Zou, C. Yan, S. Cong, T. Lei, X. Dai, J. Guo, R. Lu, Y. Li, J. Xiong, A New Member of Electrocatalysts Based on Nickel Metaphosphate Nanocrystals for Efficient Water Oxidation, *Advanced Materials* 30 (2018). <https://doi.org/10.1002/adma.201705045>.
- [13] X. Wu, Y. Zhao, T. Xing, P. Zhang, F. Li, H. Lee, F. Li, L. Sun, Hierarchically Structured FeNiOxHy Electrocatalyst Formed by In Situ Transformation of Metal Phosphate for Efficient Oxygen Evolution Reaction, *ChemSusChem* 11 (2018) 1761–1767.
- [14] Z. Lu, H. Wang, D. Kong, K. Yan, P.C. Hsu, G. Zheng, H. Yao, Z. Liang, X. Sun, Y. Cui, Electrochemical tuning of layered lithium transition metal oxides for improvement of oxygen evolution reaction, *Nature Communications* 5 (2014) 1–7.

- [15] Y. Liu, H. Wang, D. Lin, C. Liu, P.C. Hsu, W. Liu, W. Chen, Y. Cui, Electrochemical tuning of olivine-type lithium transition-metal phosphates as efficient water oxidation catalysts, *Energy and Environmental Science* 8 (2015) 1719–1724.
- [16] T. Wu, S. Sun, J. Song, S. Xi, Y. Du, B. Chen, W.A. Sasangka, H. Liao, C.L. Gan, G.G. Scherer, L. Zeng, H. Wang, H. Li, A. Grimaud, Z.J. Xu, Iron-facilitated dynamic active-site generation on spinel CoAl<sub>2</sub>O<sub>4</sub> with self-termination of surface reconstruction for water oxidation, *Nature Catalysis* 2 (2019) 763–772.
- [17] D. Wang, Y. Xu, X. Guo, Z. Fu, Z. Yang, W. Sun, Nickel foam as conductive substrate enhanced low-crystallinity two-dimensional iron hydrogen phosphate for oxygen evolution reaction, *Journal of Alloys and Compounds* 870 (2021) 159472.
- [18] X. Wu, Y. Lin, Y. Ji, D. Zhou, Z. Liu, X. Sun, Insights into the Enhanced Catalytic Activity of Fe-Doped LiCoPO<sub>4</sub> for the Oxygen Evolution Reaction, *ACS Applied Energy Materials* 3 (2020) 2959–2965.
- [19] M. Luo, Z. Cai, C. Wang, Y. Bi, L. Qian, Y. Hao, L. Li, Y. Kuang, Y. Li, X. Lei, Z. Huo, W. Liu, H. Wang, X. Sun, X. Duan, Phosphorus oxoanion-intercalated layered double hydroxides for high-performance oxygen evolution, *Nano Research* 10 (2017) 1732–1739.
- [20] G.M. Carroll, D.K. Zhong, D.R. Gamelin, Mechanistic insights into solar water oxidation by cobalt-phosphate-modified  $\alpha$ -Fe<sub>2</sub>O<sub>3</sub> photoanodes, *Energy Environ. Sci.* 8 (2015) 577–584.
- [21] M.W. Kanan, D.G. Nocera, In situ formation of an oxygen-evolving catalyst in neutral water containing phosphate and Co<sup>2+</sup>, *Science* 321 (2008) 1072–1075.
- [22] S. Cobo, J. Heidkamp, P.-A. Jacques, J. Fize, V. Fourmond, L. Guetaz, B. Jousselme, V. Ivanova, H. Dau, S. Palacin, M. Fontecave, V. Artero, A Janus cobalt-based catalytic material for electro-splitting of water, *Nat. Mater.* 11 (2012) 802–807.
- [23] B. Cui, C. Liu, J. Zhang, J. Lu, S. Liu, F. Chen, W. Zhou, G. Qian, Z. Wang, Y. Deng, Y. Chen, W. Hu, Waste to wealth: Defect-rich Ni-incorporated spent LiFePO<sub>4</sub> for efficient oxygen evolution reaction, *Science China Materials* 64 (2021) 2710–2718.
- [24] Global emissions, Center for Climate and Energy Solutions (2022).  
<https://www.c2es.org/content/international-emissions/> (accessed October 21, 2024).
- [25] World Energy Outlook 2020, IEA (n.d.). <https://www.iea.org/reports/world-energy-outlook-2020> (accessed October 21, 2024).
- [26] C. Status, G. Analysis, I. Perspectives, Australian landscape for lithium-ion battery recycling and reuse in 2020, (n.d.).
- [27] T. Zhao, W. Li, M. Traversy, Y. Choi, A. Ghahreman, Z. Zhao, C. Zhang, W. Zhao, Y. Song, A review on the recycling of spent lithium iron phosphate batteries, *Journal of Environmental Management* 351 (2024) 119670.

- [28] G. Harper, R. Sommerville, E. Kendrick, L. Driscoll, P. Slater, R. Stolkin, A. Walton, P. Christensen, O. Heidrich, S. Lambert, A. Abbott, K. Ryder, L. Gaines, P. Anderson, Recycling lithium-ion batteries from electric vehicles, *Nature* 575 (2019) 75–86.
- [29] The circular economy in detail, (n.d.). <https://www.ellenmacarthurfoundation.org/the-circular-economy-in-detail-deep-dive> (accessed October 21, 2024).
- [30] M. Jacoby, It's time to get serious about recycling lithium-ion batteries, *Chemical & Engineering News* (20190715). <https://cen.acs.org/materials/energy-storage/time-serious-recycling-lithium/97/i28> (accessed October 21, 2024).
- [31] Bloomberg, (n.d.). <https://www.bloomberg.com/graphics/2017-lithium-battery-future/> (accessed October 21, 2024).
- [32] A. Kaur, M. Khosravi, A.P. O'Mullane, Repurposing the current collector of a car battery module into a bifunctional electrode for overall electrochemical water splitting, *Sustain. Energy Fuels* 7 (2023) 2486–2494.
- [33] A. Kaur, J. Alarco, A.P.O. Mullane, Investigating the potential use of Ni-Mn-co (NMC) battery materials as electrocatalysts for electrochemical water splitting, *Chemphyschem* 25 (2024) e202400124.
- [34] H. Saleem, M. Khosravi, S. Maroufi, V. Sahajwalla, A.P. O'Mullane, Repurposing metal containing wastes and mass-produced materials as electrocatalysts for water electrolysis, *Sustain. Energy Fuels* 6 (2022) 4829–4844.
- [35] Z. Wang, M. Li, B. Fu, W. Cao, X. Bo, Recycling cobalt from spent lithium-ion batteries for designing the novel cobalt nitride followers: Towards efficient overall water splitting and advanced zinc-air batteries, *J. Colloid Interface Sci.* 662 (2024) 218–230.
- [36] Kamlesh, Z. Zaidi, M. Mudgal, A.K. Srivastava, A. Singh, Recycled steel from waste dead nickel–metal hydride (Ni–MH) batteries as efficient bifunctional electrodes for water splitting: Ideal way from waste to energy, *ACS Appl. Energy Mater.* 6 (2023) 10610–10627.
- [37] Recycling Cobalt Spent Lithium-Ion Batteries Design Two-Dimensional Porous CoOx/CoNx Nanosheets Full Water Splitting Nonenzymatic Glucose Detection, n.d.
- [38] S. Natarajan, K. Krishnamoorthy, A. Sathyaseelan, V.K. Mariappan, P. Pazhamalai, S. Manoharan, S.-J. Kim, A new route for the recycling of spent lithium-ion batteries towards advanced energy storage, conversion, and harvesting systems, *Nano Energy* 101 (2022) 107595.
- [39] D. Tyndall, M.J. Craig, L. Gannon, C. McGuinness, N. McEvoy, A. Roy, M. García-Melchor, M.P. Browne, V. Nicolosi, Demonstrating the source of inherent instability in NiFe LDH-based OER electrocatalysts, *J. Mater. Chem. A Mater. Energy Sustain.* 11 (2023) 4067–4077.
- [40] D.K. Sarfo, J. Crawford, J.D. Riches, A.P. O'Mullane, Confining the electrodeposition of FeCoNi oxide within a Nafion layer for the fabrication of stable oxygen evolution electrocatalysts, *Chem Catal.* 3 (2023) 100750.

- [41] X. Chen, J. Liu, T. Yuan, Z. Zhang, C. Song, S. Yang, X. Gao, N. Wang, L. Cui, Recent advances in earth-abundant first-row transition metal (Fe, Co and Ni)-based electrocatalysts for the oxygen evolution reaction, *Energy Mater* 2 (2022) 28.
- [42] D. Friebel, M.W. Louie, M. Bajdich, K.E. Sanwald, Y. Cai, A.M. Wise, M.J. Cheng, D. Sokaras, T.C. Weng, R. Alonso-Mori, R.C. Davis, J.R. Bargar, J.K. Nørskov, A. Nilsson, A.T. Bell, Identification of highly active Fe sites in (Ni,Fe)OOH for electrocatalytic water splitting, *J. Am. Chem. Soc.* 137 (2015) 1305–1313.
- [43] Surface Interrogation Scanning Electrochemical Microscopy Ni<sub>1-x</sub>Fe<sub>x</sub>OOH ( $0 < x < 0.27$ ) Oxygen Evolving Catalyst: Kinetics “fast” Iron Sites, n.d.
- [44] M.W. Louie, A.T. Bell, An investigation of thin-film Ni-Fe oxide catalysts for the electrochemical evolution of oxygen, *J. Am. Chem. Soc.* 135 (2013) 12329–12337.
- [45] X. Zheng, X. Zhao, J. Lu, J. Li, Z. Miao, W. Xu, Y. Deng, A.L. Rogach, Regeneration of spent cathodes of Li-ion batteries into multifunctional electrodes for overall water splitting and rechargeable Zn-air batteries by ultrafast carbothermal shock, *Science China Materials* 65 (2022) 2393–2400.
- [46] S. Klaus, Y. Cai, M.W. Louie, L. Trotochaud, A.T. Bell, Effects of Fe electrolyte impurities on Ni(OH)<sub>2</sub>/NiOOH structure and oxygen evolution activity, *J. Phys. Chem. C Nanomater. Interfaces* 119 (2015) 7243–7254.
- [47] M.B. Stevens, C.D.M. Trang, L.J. Enman, J. Deng, S.W. Boettcher, Reactive Fe-sites in Ni/Fe (oxy)hydroxide are responsible for exceptional oxygen electrocatalysis activity, *J. Am. Chem. Soc.* 139 (2017) 11361–11364.
- [48] M. Görlin, J. Ferreira de Araújo, H. Schmies, D. Bernsmeier, S. Dresp, M. Gliech, Z. Jusys, P. Chernev, R. Krahnert, H. Dau, P. Strasser, Tracking catalyst redox states and reaction dynamics in Ni-Fe oxyhydroxide oxygen evolution reaction electrocatalysts: The role of catalyst support and electrolyte pH, *J. Am. Chem. Soc.* 139 (2017) 2070–2082.
- [49] S. Anantharaj, S. Kundu, S. Noda, “The Fe Effect”: A review unveiling the critical roles of Fe in enhancing OER activity of Ni and Co based catalysts, *Nano Energy* 80 (2021) 105514.
- [50] M. Görlin, P. Chernev, J. Ferreira de Araújo, T. Reier, S. Dresp, B. Paul, R. Krähnert, H. Dau, P. Strasser, Oxygen evolution reaction dynamics, faradaic charge efficiency, and the active metal redox states of Ni-Fe oxide water splitting electrocatalysts, *J. Am. Chem. Soc.* 138 (2016) 5603–5614.
- [51] M.A. Sayeed, A.P. O’Mullane, Electrocatalytic water oxidation at amorphous trimetallic oxides based on FeCoNiO:X, *RSC Adv.* 7 (2017) 43083–43089.
- [52] Y. Luo, P. Wang, G. Zhang, S. Wu, Z. Chen, H. Ranganathan, S. Sun, Z. Shi, Mn-doped nickel – iron phosphide heterointerface nanoflowers for efficient alkaline freshwater / seawater splitting at high current densities, *Chem. Eng. J.* 454 (2023) 140061.

- [53] S.Y. Lim, J.H. Lee, S. Kim, J. Shin, W. Choi, K.Y. Chung, D.S. Jung, J.W. Choi, Lattice Water for the Enhanced Performance of Amorphous Iron Phosphate in Sodium-Ion Batteries, *ACS Energy Letters* 2 (2017) 998–1004.
- [54] S. Sarkar, S. Mitra, Carbon Coated Submicron sized-LiFePO<sub>4</sub> : Improved High Rate Performance Lithium Battery Cathode, *Energy Procedia* 54 (2014) 718–724.
- [55] N. Co, O. Mn, Effect of - FePO<sub>4</sub> coating on structure and electrochemical performance, (2023) 171–182.
- [56] Investigating Influence Amorphous/Crystalline Interfaces Stability IrO<sub>2</sub> Oxygen Evolution Reaction Acidic Electrolyte, n.d.
- [57] Y. Zhang, F. Gao, D. Wang, Z. Li, X. Wang, C. Wang, K. Zhang, Y. Du, Amorphous/crystalline heterostructure transition-metal-based catalysts for high-performance water splitting, *Coord. Chem. Rev.* 475 (2023) 214916.
- [58] L. Li, H. Sun, X. Xu, M. Humayun, X. Ao, M.F. Yuen, X. Xue, Y. Wu, Y. Yang, C. Wang, Engineering amorphous/crystalline rod-like core-shell electrocatalysts for overall water splitting, *ACS Appl. Mater. Interfaces* 14 (2022) 50783–50793.
- [59] A.P. O'Mullane, Creating active interfaces as a strategy to improve electrochemical water splitting reactions, *JPhys Energy* 2 (2020). <https://doi.org/10.1088/2515-7655/ab8c5f>.
- [60] S.-J. Huang, A. Muneeb, P. Sabhapathy, K.S. Bayikadi, T. Murtaza, K. Raju, L.-C. Chen, K.-H. Chen, R. Sankar, Two-dimensional layered NiLiP<sub>2</sub>S<sub>6</sub> crystals as an efficient bifunctional electrocatalyst for overall water splitting, *Catalysts* 11 (2021) 786.
- [61] L.I. Barbosa, A. Caballero, MIL-100 (Fe) MOF as an emerging sulfur-host cathode for ultra long-cycle Metal-Sulfur batteries, 608 (2024). <https://doi.org/10.1016/j.jpowsour.2024.234613>.
- [62] M. Abu Sayeed, G.J. Millar, A.P. O'Mullane, Harnessing Native Iron Ore as an Efficient Electrocatalyst for Overall Water Splitting, *ChemElectroChem* 6 (2019) 3667–3673.
- [63] Y. Zhang, J. Wu, B. Guo, H. Huo, S. Niu, S. Li, P. Xu, Recent advances of transition-metal metaphosphates for efficient electrocatalytic water splitting, *Carbon Energy* (2023). <https://doi.org/10.1002/cey.2.375>.
- [64] Y. Lu, C. Li, Y. Zhang, X. Cao, G. Xie, M. Wang, D. Peng, K. Huang, B. Zhang, T. Wang, W. Junsheng, Y. Huang, Engineering of cation and anion vacancies in Co<sub>3</sub>O<sub>4</sub> thin nanosheets by laser irradiation for more advancement of oxygen evolution reaction, *Nano Energy* 83 (2021) 105800.
- [65] W. Yang, Y. Bai, L. Peng, M. Qu, K. Sun, Enhanced oxygen evolution performance of iron-nickel oxide catalyst through dual-defect engineering, *J. Colloid Interface Sci.* 648 (2023) 701–708.
- [66] Influence Cation Oxygen Reduction Evolution Activities Oxide Surfaces in Alkaline Electrolyte, n.d.

- [67] M.T.M. Koper, Thermodynamic theory of multi-electron transfer reactions : Implications for electrocatalysis, *Journal of Electroanalytical Chemistry* 660 (2011) 254–260.
- [68] O. van der Heijden, J.J.J. Eggebeen, H. Trzesniowski, N. Deka, R. Golnak, J. Xiao, M. van Rijn, R.V. Mom, M.T.M. Koper, Li<sup>+</sup> cations activate NiFeOOH for oxygen evolution in sodium and potassium hydroxide, *Angew. Chem. Int. Ed Engl.* 63 (2024) e202318692.

# **Chapter 8**

---

## **Conclusions and future scope of work**

This thesis serves as a significant illustration of the effective utilization of electronic waste, in particularly batteries, as a valuable source of essential metals such as Ni, Fe, Mn, Co and P. Upon recovery, these metals can play a crucial role as electrocatalysts for hydrogen evolution reaction (HER) and oxygen evolution reaction (OER) in water splitting for hydrogen production, while also having potential for other electrocatalytic reactions such as CO<sub>2</sub> conversion into valuable products.

Therefore, electrochemical studies were performed on potential waste materials that could be obtained from lithium-ion batteries, particularly cathode materials. Initially Fe/Ni mesh current collectors recovered from a Toyota prius NiMH battery module was observed for its electrocatalytic activity, and it was found that it efficiently promotes both the Hydrogen Evolution Reaction (HER) and Oxygen Evolution Reaction (OER) and can be regarded as a potential bifunctional electrocatalyst for water splitting (Chapter 4). The Fe/Ni mesh current collector was examined for OER/HER performance before and after 2000 full water splitting cycles. It is revealed that recovered electrode has stable OER currents up to 300 mA cm<sup>-2</sup> and for HER of 150 mA cm<sup>-2</sup>. The Tafel slopes for both OER and HER shows lower values after 2000 cycling than NF (Nickel Foam) control sample of equal geometric area. The presence of Fe in the FNC electrode was found to be favourable towards the activity of the electrode with Fe-NiOOH species formed on the surface. Fe is additionally, presumed to suppress the extensive oxidation of Ni species that results in higher OER activity. Moreover, Fe is present in its Fe<sup>+3</sup> oxidation state as detected by XPS analysis acts as an active site in Ni-Fe oxide system results in increase in OER performance. Furthermore, the presence of Ni<sup>0</sup> (metallic form) is also detected that is believed to enhance electron transfer by increasing the conductivity of electrode. For HER cathodic corrosion exists but still enhanced activity is observed for FNC electrode over NF. The most prominent observation is stability of the electrode observed under 2h periods of electrolysis while subjected to rapid shutdown of 10 mints after each 2h period. A steady current passed over entire 24 h period that indicates the tolerance of electrode towards harsh conditions stating its applicability where electrolyzers are integrated with intermittent sources of energy.

The use of MnCo<sub>2</sub>O<sub>4</sub> type materials as OER electrocatalysts have been previously identified and could be reused in water electrolyzers replacing noble metal oxides like IrO<sub>2</sub> and RuO<sup>66</sup>. Therefore, cathode materials like Nickel, Manganese and Cobalt (NMC) oxides were explored as potential electrocatalysts in Chapter 5. Given the various compositions of NMC used in batteries an electrochemical analysis was performed between the most commonly used NMC 622 and NMC 811 battery materials as well the NF control. It is concluded that NMC electrodes are not suitable for the HER and exhibits similar current densities to commercial NF. It is also observed that during the electrochemical process the presence of Mn and Co as secondary metals effects the redox behaviour of Ni based oxides in of the surface of the electrode. Therefore, the broadening of oxidation response resulting in higher current densities is observed compared to unmodified NF electrode. Additionally, the redox process prior to OER keeps on increasing in magnitude with repetitive cycling (2000CV) and shifts towards more positive potentials indicating a change in the surface area of electrode. Thus, it is concluded that OER process introduce some surface sites in the form of metal oxides that lowers the activation energy of OER reactions.

Additionally, Tafel values obtained are lower than those previously reported for ternary metal oxides of this type. Amongst NMC 622, NMC 811 and NF, NMC 622 stands out to show the best OER activity. However, ECSA studies present lower surface area of the electrode as compared to NMC 811 representing a significant increase in the intrinsic activity of the electrode. This is possibly due to higher content of Mn and Co content in NMC 622 as compared to NMC 811. According to TEM/EDS analysis there is leaching of Mn and Co content after potential cycling (1 to 1.9V for 2000 cycles) which is more prominent in NMC 622. There is slight decrease in the performance of the electrodes after 2000 CV cycles, which illustrates a promising use as anodes in electrolyzers subjected to fluctuations in input voltage.

The next chapter (Chapter 6) then focused on whether NMC recovered from cycled batteries would influence the performance of water splitting reactions and how it would compare to NMC materials examined in Chapter 5. Given that NMC622 was identified as the superior material from Chapter 5, this material was investigated after recovery from cycled batteries.

All recovered materials from batteries cycled to different extents exhibit high current densities of up to 450 mA cm<sup>-2</sup> while the potential required to reach a current density of 100 mA cm<sup>-2</sup> was 1.62 V for uncycled which is the lowest value compared to other electrodes.

Additionally, chronoamperometric experiments under constant voltage present a highest current density of  $170 \text{ mA cm}^{-2}$ . The significant observation is that the OER activity gradually declines from the unprocessed cycled sample to the one subjected to 200 battery cycles, suggesting that battery cycling adversely affects the electrocatalytic performance of NMC for the OER. This was explained by SEM analysis which shows a high degree of agglomerated particles while cracks are found on the micron scale. Thus, cycling causes agglomeration of active sites, thereby lowering electrocatalytic performance. Furthermore, XPS data reveals no prominent difference observed between unprocessed sample and the sample cycled 200 times but confirms high species of M-OH amount for 200 battery cycles electrode. Thus, increasing the number of battery cycles decreases the OER performance and history of battery impacts its further use as an electrocatalyst.

Lithium iron phosphate is the emerging cathode material that is being commercially used in Li ion batteries. Therefore, in this research a similar set of work was conducted by analysing different LFP-based materials sourced from discarded Li-ion batteries, including LiFePO<sub>4</sub> film electrodes, LiFePO<sub>4</sub> powder, and materials recovered from cycled batteries immobilised on a NF support were evaluated for their electrochemical performance in water splitting (Chapter 7). The chapter demonstrates LiFePO<sub>4</sub> cathode materials are best suited for OER reactions when they are in contact with Ni available from nickel foam acting as a substrate. These electrodes are observed to reconstruct themselves forming Fe/Ni hydroxide and oxyhydroxide species that are more active for OER reactions. Commercial LPF sample electrode (NF-LFP) was tested against LFP that was recovered from a cycled battery initially conditioned and cycled for 5 to 100 cycles represented as NF-LFP(CV5) and NF-LFP(CV100). The electrochemical analyses were conducted before 2000 CV cycling revealed lower overpotential values of 1.56, 1.57 and 1.62 to pass  $100 \text{ mA cm}^{-2}$  for NF-LFP(CV5), NF-LFP(CV100) and NF-LFP respectively. After potential cycling of 2000 cycles it was concluded the electrodes from cycled materials efficiently maintained high performance than pristine electrode with lower Tafel values of 47 and 58 mV dec<sup>-1</sup> for NF-LFP (CV5) and NF-LFP (CV100), respectively. The most significant analysis was observed for the NF LFP(CV5) sample which shows much higher current densities of  $> 200 \text{ mA cm}^{-2}$  compared to the other samples. SEM revealed well packed homogeneous layer of LFP particles and SEM-EDS mapping of NF-CV(100) showed homogeneous distribution of Fe, P and O across the NF substrate. TEM analysis revealed the presence of NiFe layered double hydroxide after 2000 cycles. A decrease in crystallinity and increase in amorphous state also occurs for LFP(CV100)

compared to LFP (CV5). Therefore, the presence of amorphous/crystalline regions could be the reason behind increased activity of LFP(CV5) electrode. XPS revealed that the LFP(CV100) sample was the only sample to retain P and Li at the surface after 2000 cycles. This may contribute to lower activity of LFP(CV100) for OER as presence of P can also lead to lower activities as also reported in literature<sup>202</sup>. Similarly, the presence of Li<sup>+</sup> in the electrolyte also reduces OER efficiency. Thus, for sample LFP(CV5) with no Li species in the reconstructed layer may lead to the increased activity.

Therefore, the study provides details on recovered LFP cathode materials from spent Li-ion battery is sustainable and present an opportunity to repurpose the materials as efficient OER catalysts.

The data from both Chapters 6 and 7 on different cathode materials provided the same general outcome in that more extensive battery cycling results in slightly worse electrocatalytic performance for the OER. Cycling in a battery causes significant impacts on the morphology and chemistry of the particles which is not beneficial for electrocatalysis as seen for the NMC622 and LFP case studies. However, it should be noted that in all cases the activity was still higher than the control NF samples, indicating that recovery of these materials from waste Li ion batteries is still a potentially viable option for this application. For example, recovered LFP battery material LFP CV(100) after 2000 cycles has lower Tafel slope of 58 mV dec<sup>-1</sup> and overpotential value of 310 required to pass 100 mA cm<sup>-2</sup> current as compared to NF with Tafel value 128 mV dec<sup>-1</sup> and overpotential of 390mV for 100 mA cm<sup>-2</sup> current.

## Future scope of work

Materials from the waste of batteries were analysed for the purpose of green hydrogen production by water splitting process. While performing HER analysis of Fe/Ni current collector from Toyota prius NiMH battery, the electrode could be further analysed for any kind of corrosion processes that have occurred on the surface and could affect performance of the electrode. Additionally, the electrode can be tested as bifunctional electrocatalyst in electrolyzers that face voltage fluctuations. Similarly other waste materials from batteries like Al foils and Cu foils could be tested for their applicability towards water splitting reactions.

With the emergence of studies towards recycled batteries waste used as electrocatalysts for water splitting reactions the NMC cathode materials from Li-ion batteries is promising. This work further provides an opportunity to explore various formulations of Li-ions batteries

like different ratios of NMC like NMC 111, NMC 532 etc. To observe the impact of various ratios of distribution of Ni, Mn, Co would further streamline the best approach to recycle waste from batteries dependent on batteries manufactures. This is a significant work in curbing future issues related to E-waste management.

Another area of interest that can transform the approach to manage challenges related to repurpose battery waste is to understand the relation between cycled batteries that are cycled for various number of cycles and impact of cycling on electrocatalytic performance for water splitting. Here, increased number of cycles decreased electrocatalytic activity. Therefore, an opportunity to discover better efficient recovery processes to produce isolated particles with more active sites should be worked as a part of future scope in this area.

It was observed that cycled LFP material-based electrodes showed efficient electrocatalytic performance than commercially available pristine LFP. But LFP cathodes recovered from cycled Li ion batteries at 1 C for 5 and 100 cycles, a variation in OER activity was observed where the less cycled material was more active and stable after 2000 OER cycles. The reason behind these results were high amounts of P and Li detected in 100 cycles sample that blocks the active sites of the materials as compared to 5 cycles LFP sample. This observation needs to be further studied to truly understand the role of P and Li in evaluating the catalytic activity of spent LFP cathodes from Li-ion batteries.

Therefore, NMC and LFP based electrodes can be tested as anode in alkaline electrolyzers as they possess the tendency to be cost effective anode materials in comparison with Iridium and Platinum based anode materials in electrolyzers.

Another significant challenge is what impact mixed history batteries have on electrocatalysis as each battery will have its own unique use profile. Is large scale recovery of NMC622 for instance which have been exposed to different profiles still work as an overall effective OER electrocatalyst? How much batch-to-batch variation might occur, or would the recovered materials need to be homogenised further via mechanical methods? However, if the physically recovered materials can be used rather than having to employ leaching processes that can be time consuming, costing and potentially environmentally harmful then it may be a viable option for e-waste recyclers to consider to value add to their process.

## References

- (1) Ummul, K.; Joseph, F. S.; Fernando, A. P. Transformation Stainless Steel 316 Bifunctional Water Splitting Electrocatalyst Tolerant Polarity Switching”. *Sustainable Materials Technologies* **2020**, 25.
- (2) Daily, R.; Padrón, Z.; Sameh, M.; Osman, R. Recycling Electronic Waste: Prospects Green Catalysts Design”. *Current Opinion Green Sustainable Chemistry* 25.
- (3) Farzana, R.; Sayeed, M. A.; Joseph, J.; Ostrikov, K.; O’Mullane, A. P.; Sahajwalla, V. Manganese Oxide Derived from a Spent Zn–C Battery as a Catalyst for the Oxygen Evolution Reaction. *ChemElectroChem* **2020**, 7 (9), 2073–2080.
- (4) Weia, S.; Jia, Z.; Miaoa, Z.; Shichang, J.; Ting, L.; Keith, Y.; Lic, W.; Dinggen, Y.; Xu, J. Reuse Ni-Co-Mn Oxides from Spent Li-Ion Batteries Prepare Bifunctional Air Electrodes”. *Resources, Conservation & Recycling* **2018**, 129, 135–142.
- (5) Natarajan, S.; Anantharaj, S.; Tayade, R. J.; Bajaj, H. C.; Kundu, S. Recovered Spinel MnCo<sub>2</sub>O<sub>4</sub> from Spent Lithium-Ion Batteries for Enhanced Electrocatalytic Oxygen Evolution in Alkaline Medium. *Dalton Trans.* **2017**, 46 (41), 14382–14392.
- (6) Vasanth, R.; Jothi, R.; Bose, H.; Rajan, C.; Jung, S. C. Harvesting Electronic Waste Development Highly Efficient Eco-Design Electrodes Electrocatalytic Water Splitting”. *Adv. Energy Mater* **2018**, 8.
- (7) Meng, J.; Liu, F.; Yan, Z.; Cheng, F.; Li, F. Spent Alkaline Battery-Derived Manganese Oxides Efficient Oxygen Electrocatalysts Zn-Air Batteries”. *Inorg. Chem. Front* **2018**, 5.
- (8) Farzana, R.; Rajarao, R.; Pravas, R.; Behera, K. Zinc Oxide Nanoparticles from Waste Zn-C Battery via Thermal Route: Characterization Properties”. *Nanomaterials* **2018**, 8.
- (9) Lv, W.; Wang, Z.; Cao, H.; Sun, Y.; Zhang, Y.; Sun, Z. A Critical Review and Analysis on the Recycling of Spent Lithium-Ion Batteries. *ACS Sustainable Chemistry and Engineering*. American Chemical Society February 2018, pp 1504–1521. <https://doi.org/10.1021/acssuschemeng.7b03811>.
- (10) King, S.; Boxall, N. J. Lithium Battery Recycling in Australia: Defining the Status and Identifying Opportunities for the Development of a New Industry. *J. Clean. Prod.* **2019**, 215, 1279–1287.
- (11) Yang, W.; Bai, Y.; Peng, L.; Qu, M.; Sun, K. Enhanced Oxygen Evolution Performance of Iron-Nickel Oxide Catalyst through Dual-Defect Engineering. *J. Colloid Interface Sci.* **2023**, 648, 701–708.

## **Appendix 1: Peer reviewed Journal Articles and Conference Proceedings**

---

1. Arshdeep Kaur, Jose Alarco and Anthony P. O'Mullane, "Investigating the potential use of Ni-Mn-Co (NMC) battery materials as electrocatalysts for electrochemical water splitting", ChemPhyChem, Accepted Article, 2024.  
<https://doi.org/10.1002/cphc.202400124>.
2. Arshdeep Kaur, Monireh Khosravi and Anthony P. O'Mullane, "Repurposing the current collector of a car battery module into a bifunctional electrode for overall electrochemical water splitting", Sustainable Energy & Fuels, 7, 2486-2494, 2023.  
DOI: <https://doi.org/10.1039/D3SE00232B>.
3. Arshdeep Kaur, Hongxia Wang, Colm O'Dwyer and Anthony P. O'Mullane, "Using Recovered Lithium Iron Phosphate Battery Material as an Electrocatalyst for the Oxygen Evolution Reaction", CleanMat, 1-13, 2025.  
[doi.org/10.1002/clem.70005](https://doi.org/10.1002/clem.70005)

## **Conference Proceedings**

1. Arshdeep Kaur & Anthony O'Mullane, Reusing LFP battery cathode materials for water splitting reactions, 24th Australasian Electrochemistry Symposium, La Trobe University, Melbourne, 4-5 December 2024, Australia.
2. Arshdeep Kaur & Anthony O'Mullane, Recovery materials from energy devices for electrocatalytic, Poster Presentation, 35<sup>th</sup> Tropical ISE Meeting, Gold Coast, 8-10<sup>th</sup> May 2023, Australia.
3. Arshdeep Kaur & Anthony O'Mullane, Recovery materials from energy devices for electrocatalytic applications, 23<sup>rd</sup> Australasian Electrochemistry Symposium, Gold Coast, Oral Presentation, 7<sup>th</sup> May 2023, Australia.

## Appendix 2: Supplementary information (Chapter 4)



**Figure 4 S1.** Digital image of recovered FNC electrode from battery module.

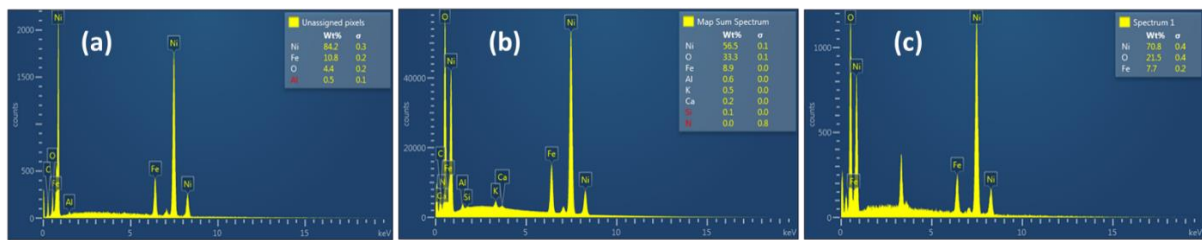


**Figure 4 S2.** EDX spectra of NFC electrode (a) recovered from battery, (b) after 2000 cycles of OER and (c) after 2000 cycles of HER.

**Table 4 S1:** Properties of various electrocatalysts

Electrocatalyst	Overpotential (mV) to reach 10 mAc <sup>-2</sup>	Tafel slope (mVdec <sup>-1</sup> )	Electrolyte	Reference
Ni Foam	217	130 (HER)	1M KOH	Hu <i>et. al.</i> , 2019 <sup>1</sup>
Ni Foam	337	97 (OER)	1M KOH	Hu <i>et. al.</i> , 2019 <sup>1</sup>
Stainless steel	420	233 (HER)	1M KOH	Hu <i>et. al.</i> , 2019 <sup>1</sup>
Stainless steel	277	51 (OER)	1M KOH	Hu <i>et. al.</i> , 2019 <sup>1</sup>
Stainless steel foil	361	57 (OER)	1M KOH	Lie <i>et. al.</i> , 2017 <sup>2</sup>
Ni-Fe LDH	260	274 (HER)	1M KOH	Chen <i>et. al.</i> , 2021 <sup>3</sup>
Ni-Fe LDH	330	51.44 (OER)	1M KOH	Chen et al., 2021 <sup>3</sup>
Ni-Fe-O	209	161 (HER)	1M KOH	Chen <i>et. al.</i> , 2021 <sup>3</sup>
Ni-Fe-O	360	61.59 (OER)	1M KOH	Chen et al., 2021 <sup>3</sup>
Ni-Fe-OP	209	161 (HER)	1M KOH	Chen <i>et. al.</i> , 2021 <sup>3</sup>
Ni-Fe-OP	310	43.10 (OER)	1M KOH	Chen <i>et. al.</i> , 2021 <sup>3</sup>

NiFeLDH/Cu(OH) <sub>2</sub> /Cu	275 to reach (20 mAcm <sup>-2</sup> )	83 (OER)	I M KOH	Babar <i>et. al.</i> , 2019 <sup>4</sup>
In situ growth of Fe (Ni)OOH on Stainless Steel	300	34 (OER)	I M KOH	Tang <i>et. al</i> , 2017 <sup>5</sup>
316L Stainless Steel	370	30 (OER)	I M KOH	Yu <i>et. al.</i> , 2016 <sup>6</sup>
Cathodised Stainless Steel Mesh	275	70 (OER)	I M KOH	Zhang et.al., 2020 <sup>7</sup>
Stainless Steel Mesh with interacted Ni(Fe)O <sub>x</sub> H <sub>4</sub> nanosheets	310 to reach (20 mAcm <sup>-2</sup> )	37 (OER)	I M KOH	Zhang <i>et. al.</i> , 2018 <sup>8</sup>
304 Stainless Steel	323	51 (OER)	I M KOH	Wu <i>et. al.</i> , 2021 <sup>9</sup>
Pentlandites: Fe <sub>8</sub> Ni S <sub>8</sub>	493	75 (OER)	I M KOH	Amin <i>et. al.</i> , 2021 <sup>10</sup>
Ni-Fe-P/SSAT Ni-Fe-P coating on anodically treated stainless steel.	323	43, 88 (OER)	I M KOH	Cartagena et, al., 2022 <sup>11</sup>
Ni-FeP/SS (Ni-FeP on polished stainless steel.)	341	48, 184 (OER)	I M KOH	Cartagena et, al., 2022 <sup>11</sup>
Ni-FeP/SSAT Ni-Fe-P coating on anodically treated stainless steel.	327	93 (HER)	I M KOH	Cartagena et, al., 2022 <sup>11</sup>
Ni-FeP/SS (Ni-FeP on polished stainless steel)	363	119 (HER)	I M KOH	Cartagena et, al., 2022 <sup>11</sup>

## References

1. X. Hu, X. Tian, Y. W. Lin and Z. Wang, *RSC Advances*, 2019, **9**, 31563-31571.
2. X. Liu, B. You and Y. Sun, *ACS Sustainable Chemistry and Engineering*, 2017, **5**, 4778-4784.
3. J. Chen, Z. Guo, Y. Luo, M. Cai, Y. Gong, S. Sun, Z. Li and C. J. Mao, *ACS Sustainable Chemistry and Engineering*, 2021, **9**, 9436-9443.
4. P. Babar, A. Lokhande, V. Karade, B. Pawar, M. G. Gang, S. Pawar and J. H. Kim, *Journal of Colloid and Interface Science*, 2019, **537**, 43-49.
5. D. Tang, O. Mabayoje, Y. Lai, Y. Liu and C. Mullins, Buddie, *ChemistrySelect*, 2017, **2**, 2230-2234.
6. F. Yu, F. Li and L. Sun, *International Journal of Hydrogen Energy*, 2016, **41**, 5230-5233.
7. G.-R. Zhang, L.-L. Shen, P. Schmatz, K. Krois and B. J. M. Etzold, *Journal of Energy Chemistry*, 2020, **49**, 153-160.
8. Q. Zhang, H. Zhong, F. Meng, D. Bao, X. Zhang and X. Wei, *Nano Research*, 2018, **11**, 1294-1300.
9. F. Wu, Z. Yao, K. Huang, B. Zhang, J. Xia, Z. Chen and J. Wu, *Journal of Materials Research and Technology*, 2021, **15**, 6721-6725.
10. H. M. A. Amin, M. Attia, D. Tetzlaff and U. P. Apfel, *ChemElectroChem*, 2021, **8**, 3863-3874.
11. S. Cartagena, F. E. Bedoya-Lora and J. A. Calderón, *Journal of The Electrochemical Society*, 2022, **169**.

### Appendix 3: Supplementary information (Chapter 5)

**Table 5 S1.** Various NMC type catalyst materials used for the OER identifying the catalyst substrate, overpotential required to pass  $10 \text{ mA cm}^{-2}$  ( $\eta_{10}$ ) and onset values.

Catalyst material	Substrate used	Overpotential ( $\eta_{10}$ ) mV	Tafel slope (mV dec $^{-1}$ )	Reference
NiCo <sub>2</sub> S <sub>4</sub> nanowire arrays	Ni Foam	260	40.1	1
NiCo <sub>2</sub> O <sub>4</sub> /NF	No Foam	330	66.9	1
Ni <sub>3</sub> S <sub>2</sub> /NF	Ni Foam	300	51	1
NiCoP/NF	Ni Foam	280	87	1
NiCo-OH/NF	Ni Foam	201	91	2
Ni <sub>2</sub> P/NF	Ni Foam	93	85	2
MNC-P/NF	Ni Foam	350	85	3
MNC-OH/NF	Ni Foam	-	114	3
Ni <sub>x</sub> Co <sub>y</sub> Mn <sub>z</sub> O <sub>4</sub>	Ni Foam	-	79-97 (before cycling)	3
Ni <sub>x</sub> Co <sub>y</sub> Mn <sub>z</sub> O <sub>4</sub> from KIT-6 silica calcined at 300°C	Ni Foam	400	79-84 (after cycling)	3
NiCoMnO <sub>4</sub> nanoparticles	Nitrogen-doped graphene	392	128	4
NiCoMnO <sub>4</sub>	Nitrogen-MWCNT	-	-	4,5
Ni <sub>x</sub> Co <sub>y</sub> Mn <sub>z</sub> O <sub>4</sub> from KIT-6 silica calcined at 300°C	Ni Foam	400	-	3
Nickel-cobalt-manganese spinel oxide nanoparticles	Glassy carbon	180	68 (before cycling)	6
Co-doped Ni-Mn LDH nanoplates	Glassy carbon	310	59	7
Mn <sub>1</sub> -Ni <sub>1</sub> -Co <sub>1</sub> -P-(O)	Nickel foam	289	85	8
Ni-Co-Mn oxalates (ball milled to oxides)	Glassy carbon	367	43.8	9
Mn-NiCoP nanopins arrays	Ni foam	266 (100 mA cm $^{-2}$ )	53	10

1.5Mn-NiCo hydroxide nanosheets with carbon nanotubes	Ni foam	239	92.1	11
---	---------	-----	------	----

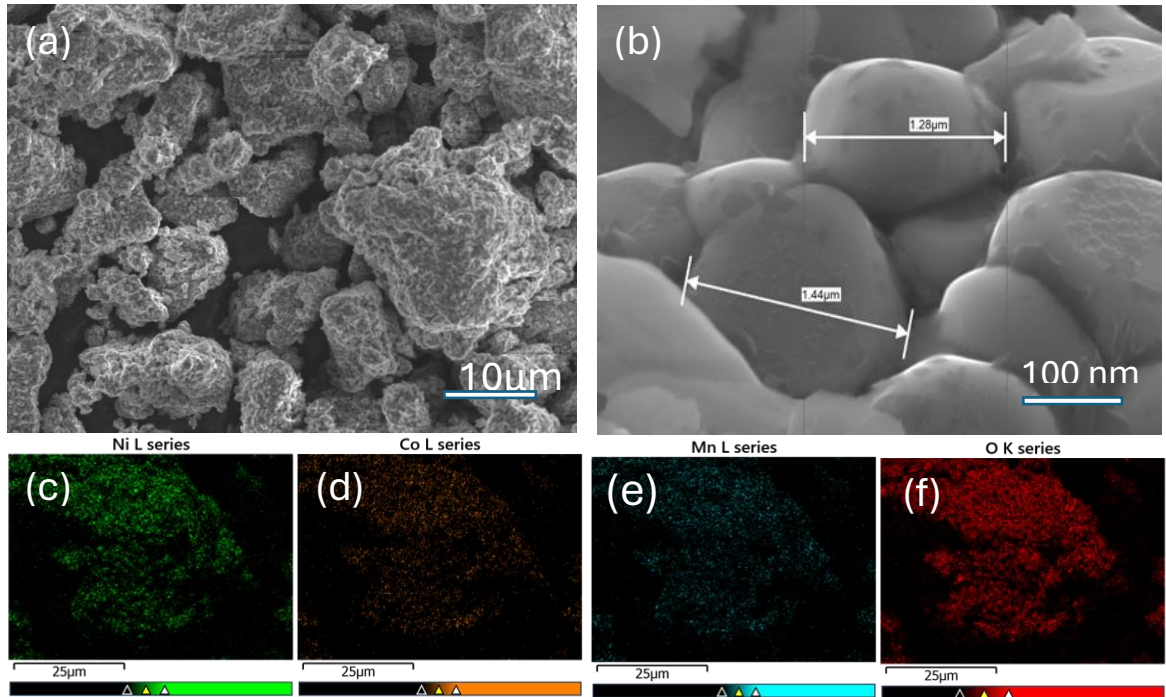


**Figure 5 S1.** SEM image and EDS mapping (Ni, Mn, Co and O elements) of NMC 622.

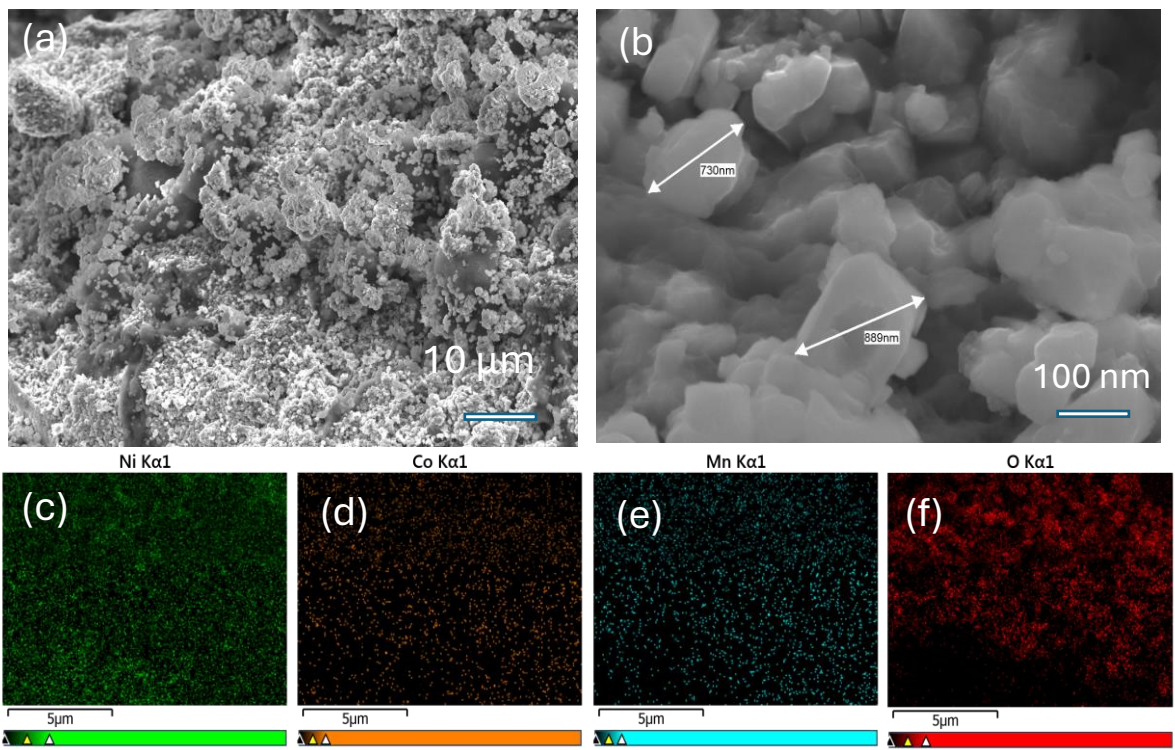


**Figure 5 S2.** EDS mapping (Ni, Mn, Co and O elements) of NMC 811 before cycling.

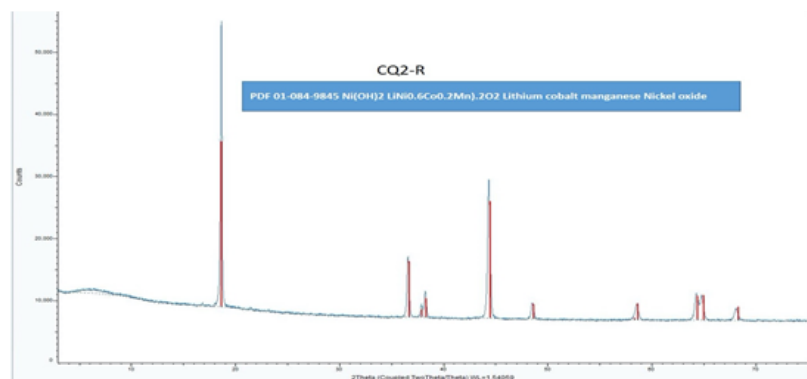
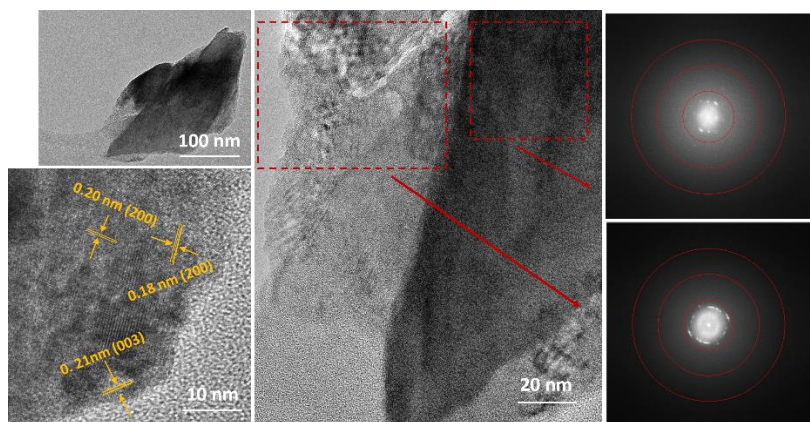


**Figure 5 S3.** TEM images, SAED pattern and XRD pattern of NMC 622.

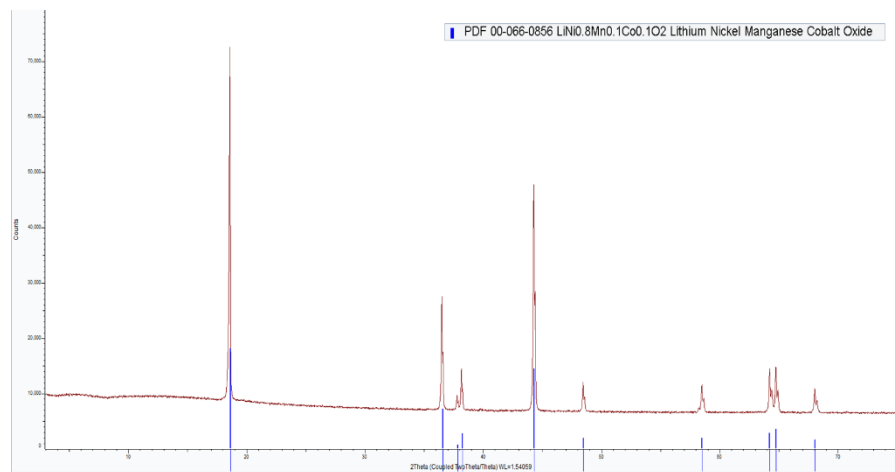
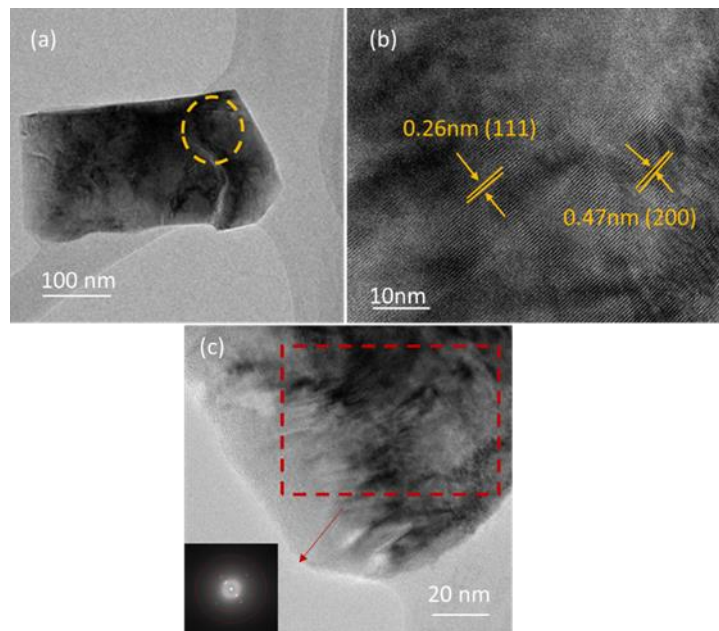


**Figure 5 S4:** TEM images, SAED pattern and XRD pattern of NMC 811

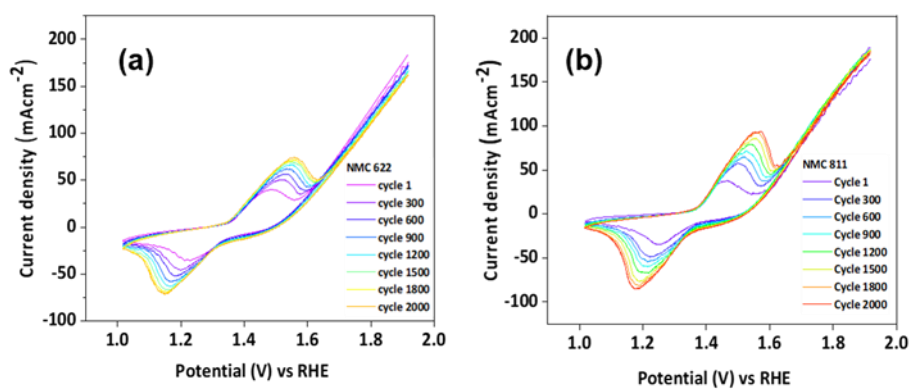


**Figure 5 S5.** Cyclic voltammograms recorded for NMC 622-NF and NMC 811-NF at 100 mVsec<sup>-1</sup> for 2000 cycles.

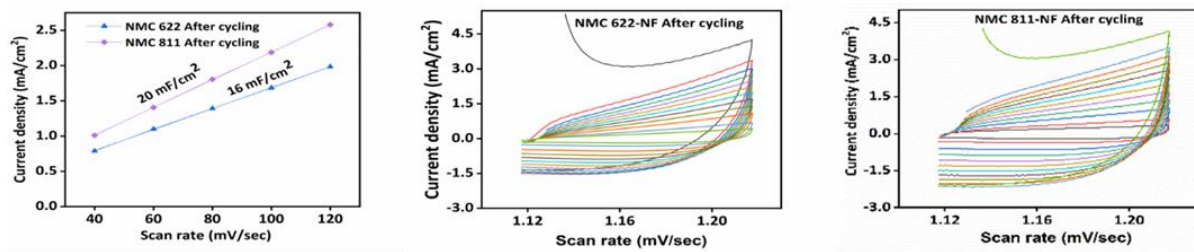


**Figure 5 S6.** Current density V sweep rate from data obtained from cyclic voltammetric experiments recorded at different sweep rates for NMC 622-NF and NMC 811-NF electrodes in 1 M KOH after repetitive cycling for 2000 cycles.

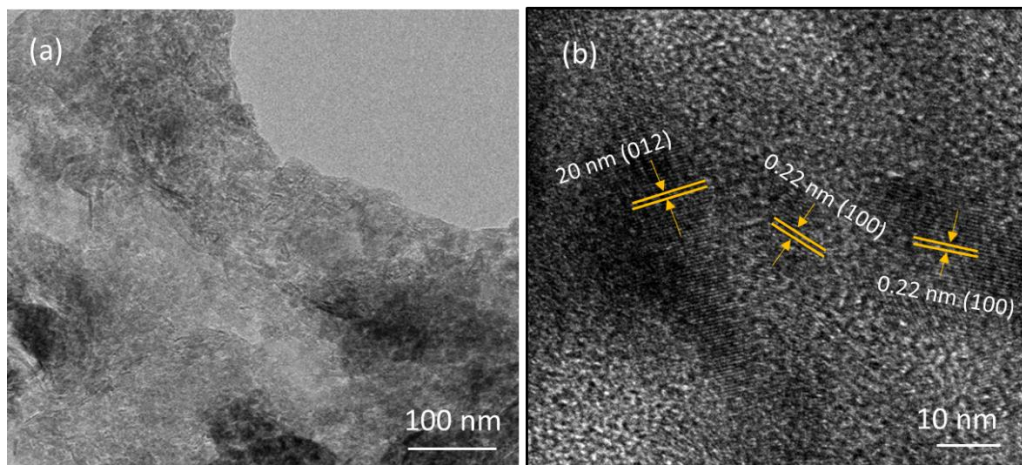


**Figure 5 S7.** TEM images of NMC 622 after cycling.

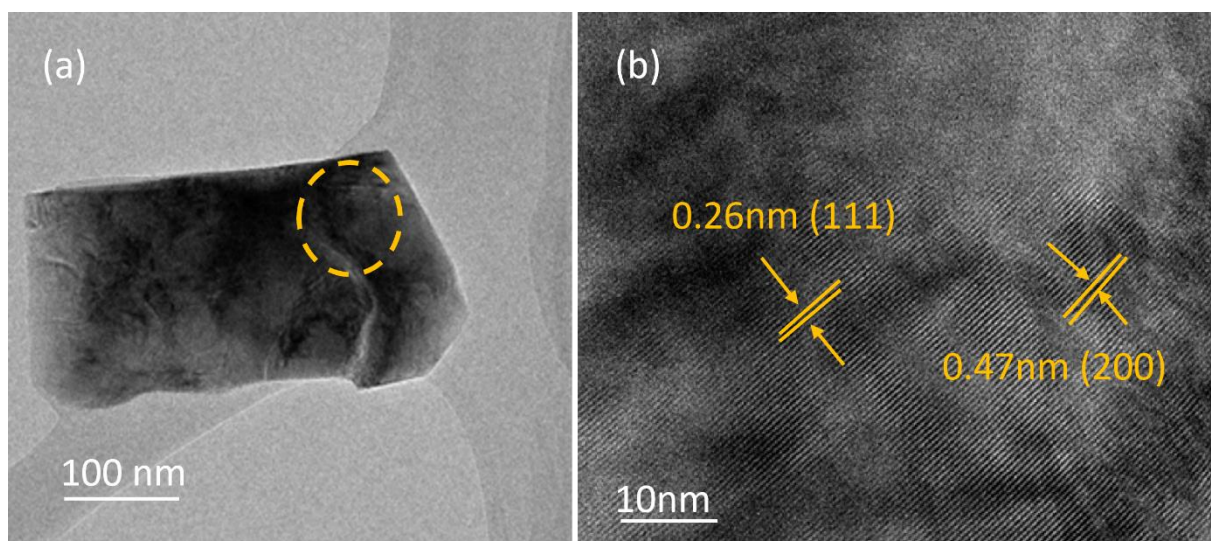


**Figure 5 S8.** TEM images of NMC 811 after cycling.

## References

1. Sivanantham, A., Ganesan, P., and Shanmugam, S. (2016). Hierarchical NiCo<sub>2</sub>S<sub>4</sub> Nanowire Arrays Supported on Ni Foam: An Efficient and Durable Bifunctional Electrocatalyst for Oxygen and Hydrogen Evolution Reactions. *Adv. Funct. Mater.* 26, 4661-4672. 10.1002/adfm.201600566.
2. Liang, H., Gandi, A.N., Anjum, D.H., Wang, X., Schwingenschlögl, U., and Alshareef, H.N. (2016). Plasma-Assisted Synthesis of NiCoP for Efficient Overall Water Splitting. *Nano Lett.* 16, 7718-7725. 10.1021/acs.nanolett.6b03803.
3. Priamushko, T., Guillet-Nicolas, R., Yu, M., Doyle, M., Weidenthaler, C., Tuysüz, H., and Kleitz, F. (2020). Nanocast Mixed Ni-Co-Mn Oxides with Controlled Surface and Pore Structure for Electrochemical Oxygen Evolution Reaction. *ACS Applied Energy Materials* 3, 5597-5609. 10.1021/acsaem.0c00544.
4. Pendashteh, A., Palma, J., Anderson, M., and Marcilla, R. (2017). NiCoMnO<sub>4</sub> nanoparticles on N-doped graphene: Highly efficient bifunctional electrocatalyst for oxygen reduction/evolution reactions. *Appl. Cat. B* 201, 241-252. 10.1016/j.apcatb.2016.08.044.
5. Afshin Pendashteha, Jesus Palmaa, Anderson, M., and Marcillaa, R. (2017). NiCoMnO<sub>4</sub>nanoparticles on N-doped graphene: Highly efficientbifunctional electrocatalyst for oxygen reduction/evolution reactions. *Appl. Cat. B* 201, 241- 252.
6. Sivakumar, P., Subramanian, P., Maiyalagan, T., Gedanken, A., and Schechter, A. (2019). Ternary nickel–cobalt–manganese spinel oxide nanoparticles as heterogeneous electrocatalysts for oxygen evolution and oxygen reduction reaction. *Mater. Chem. Phys.* 229, 190-196. 10.1016/j.matchemphys.2019.03.017.
7. Wang, Y., Liu, X., Zhang, N., Qiu, G., and Ma, R. (2018). Cobalt-doped Ni–Mn layered double hydroxide nanoplates as high-performance electrocatalyst for oxygen evolution reaction. *Applied Clay Science* 165, 277-283. <https://doi.org/10.1016/j.clay.2018.07.036>.
8. Salem, K.E., Saleh, A.A., Khedr, G.E., Shaheen, B.S., and Allam, N.K. (2023). Unveiling the Optimal Interfacial Synergy of Plasma-Modulated Trimetallic Mn-Ni-Co Phosphides: Tailoring Deposition Ratio for Complementary Water Splitting. *Energy and Environmental Materials* 6, e12324. <https://doi.org/10.1002/eem2.12324>.
9. Balqis, F., Irmawati, Y., Geng, D., Nugroho, F.A.A., and Sumboja, A. (2023). Nanostructured Ball-Milled Ni–Co–Mn Oxides from Spent Li-Ion Batteries as Electrocatalysts for Oxygen Evolution Reaction. *ACS Applied Nano Materials*. 10.1021/acsanm.3c02092.
10. Ma, G., Ye, J., Qin, M., Sun, T., Tan, W., Fan, Z., Huang, L., and Xin, X. (2023). Mn-doped NiCoP nanopin arrays as high-performance bifunctional electrocatalysts for sustainable hydrogen production via overall water splitting. *Nano Energy* 115, 108679. <https://doi.org/10.1016/j.nanoen.2023.108679>.
11. Wu, K., Cao, C., Li, K., Lyu, C., Cheng, J., Li, H., Hu, P., Wu, J., Lau, W.-M., Zhu, X., et al. (2023). Regulating electronic structure by Mn doping for nickel cobalt hydroxide nanosheets/carbon nanotube to promote oxygen evolution reaction and oxidation of urea and hydrazine. *Chemical Engineering Journal* 452, 139527. <https://doi.org/10.1016/j.cej.2022.139527>.

## Appendix 4: Supplementary information (Chapter 7)

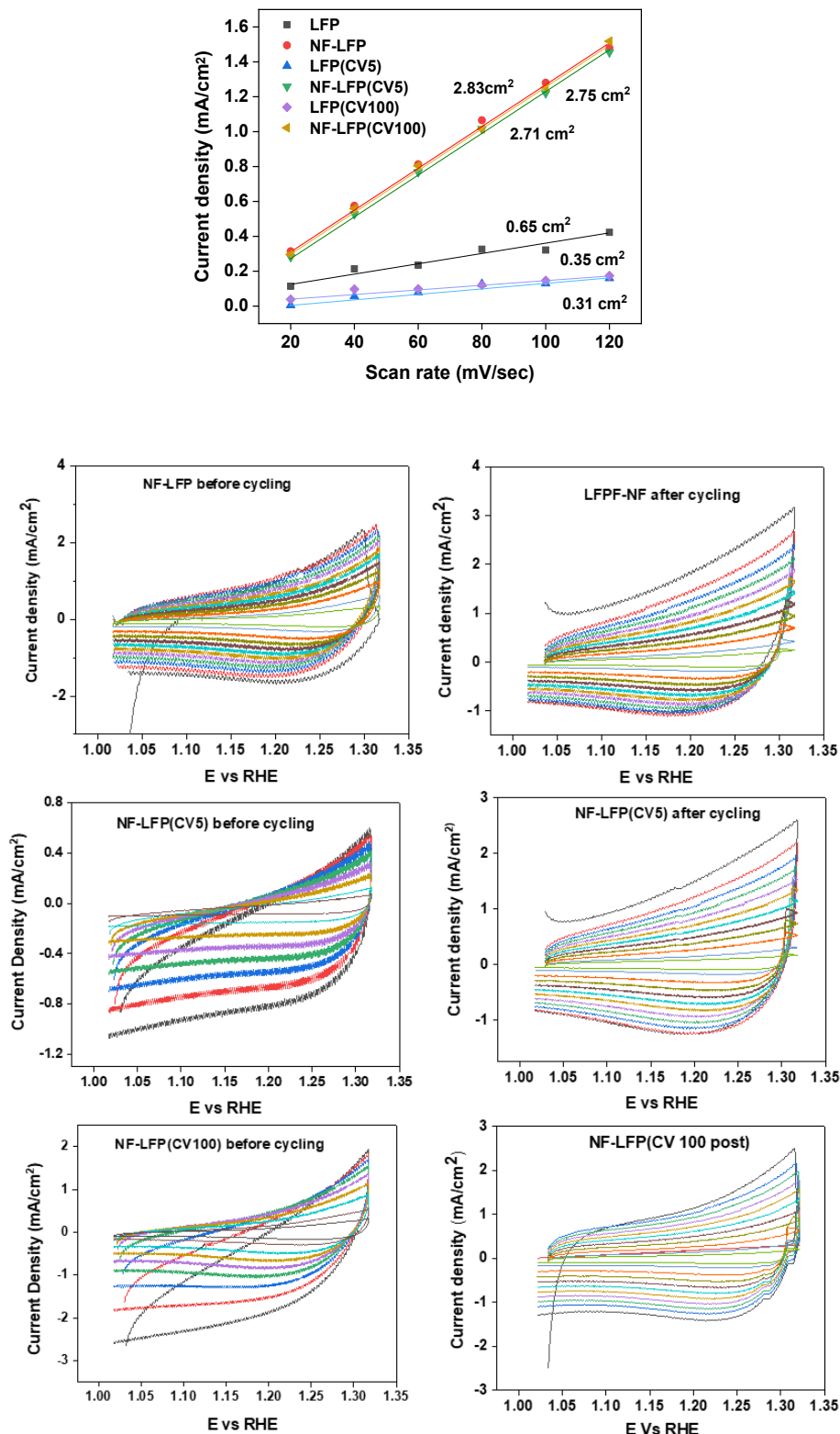


**Figure 7 S1:** Current density Vs sweep rate from data obtained from cyclic voltammetric experiments recorded at different sweep rates for NF-LFP(CV5), NF-LFP(CV100), NF-LFP in 1 M KOH before after repetitive cycling.

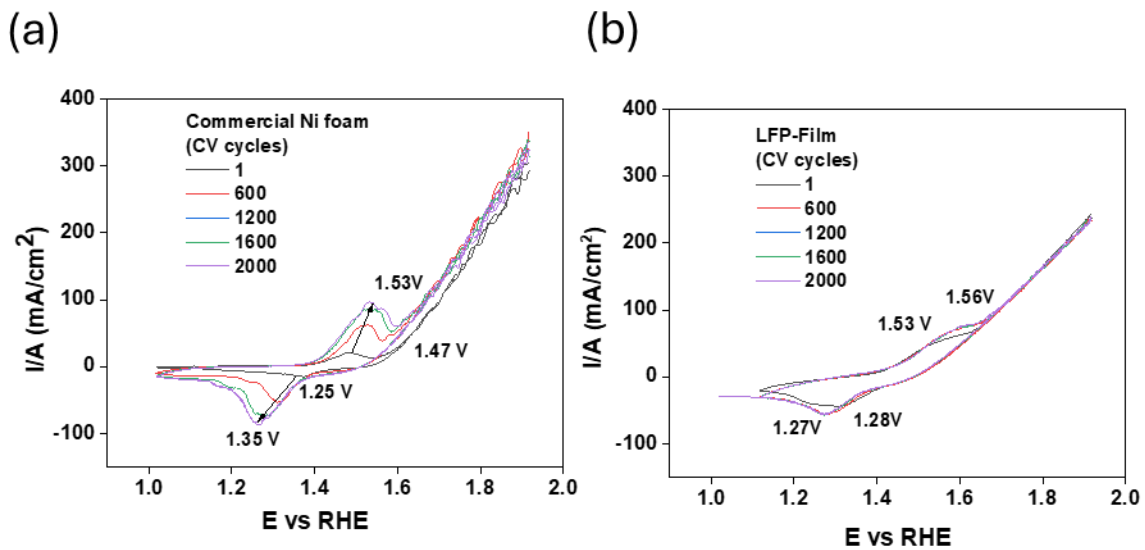


**Figure 7 S2:** Cyclic voltammograms recorded at  $100 \text{ mV sec}^{-1}$  for NF and NF-LFP for 2000 cycles, 1.0 to 1.9 V) in 1 M KOH.

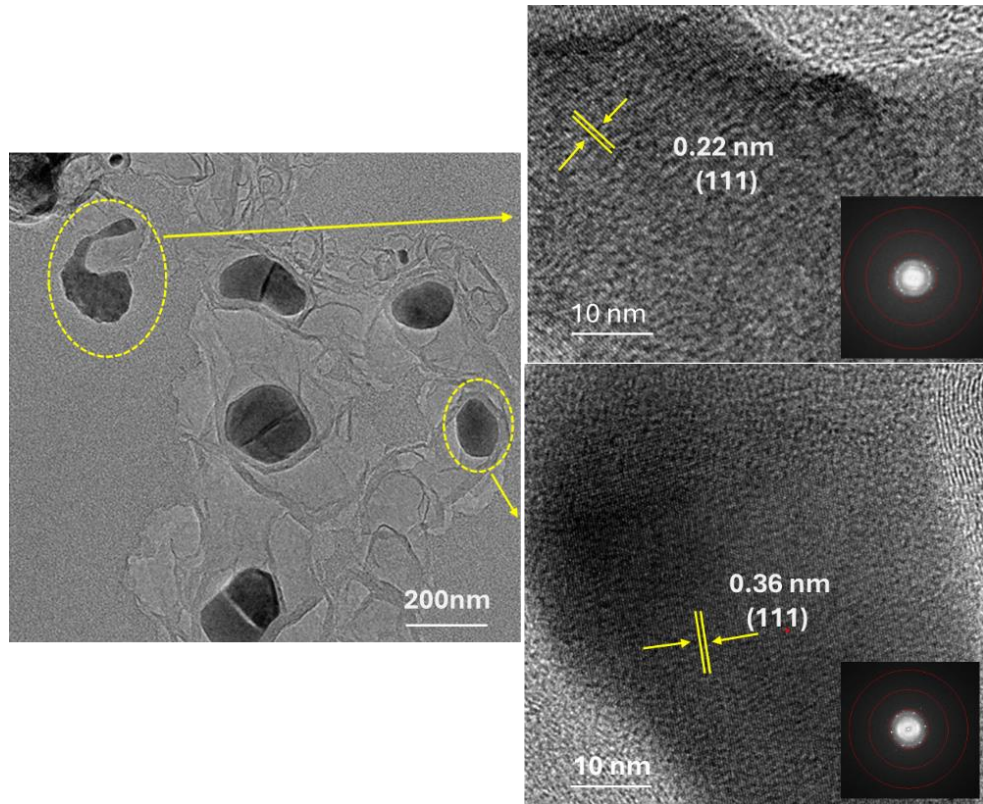


**Figure 7 S3:** TEM images of pristine LFP particles

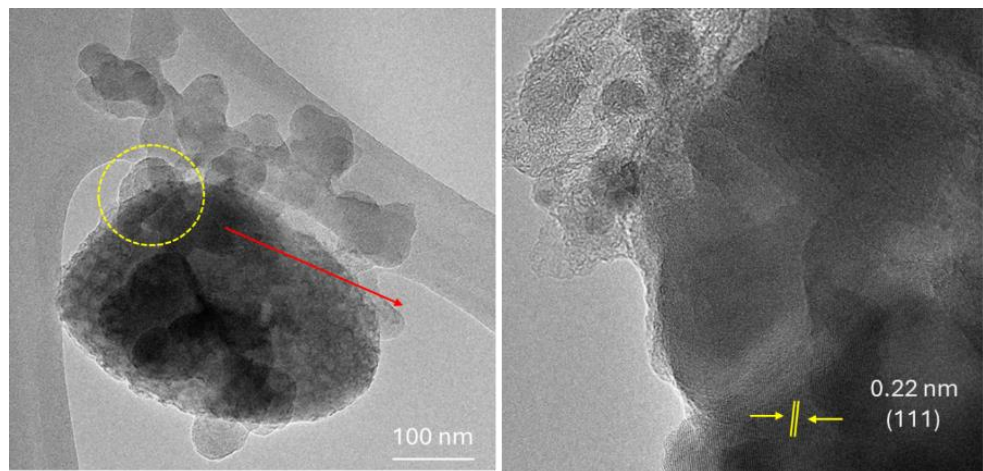


**Figure 7 S4:** TEM images of LFP CV5 particles

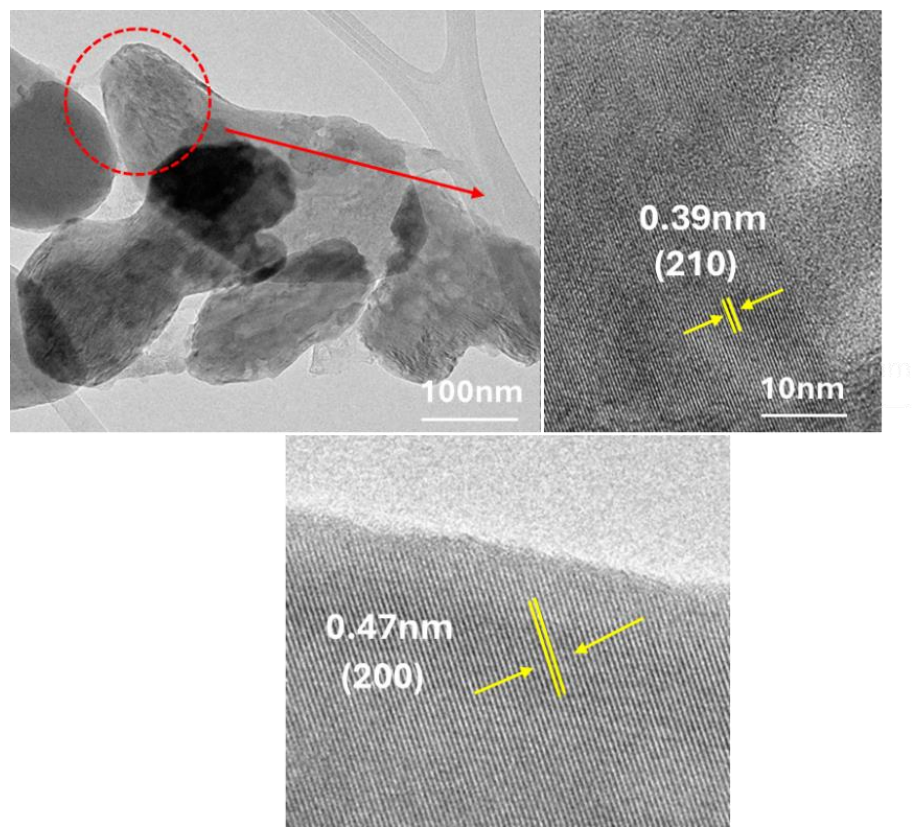


**Figure 7 S5:** TEM images of LFP CV100 particles

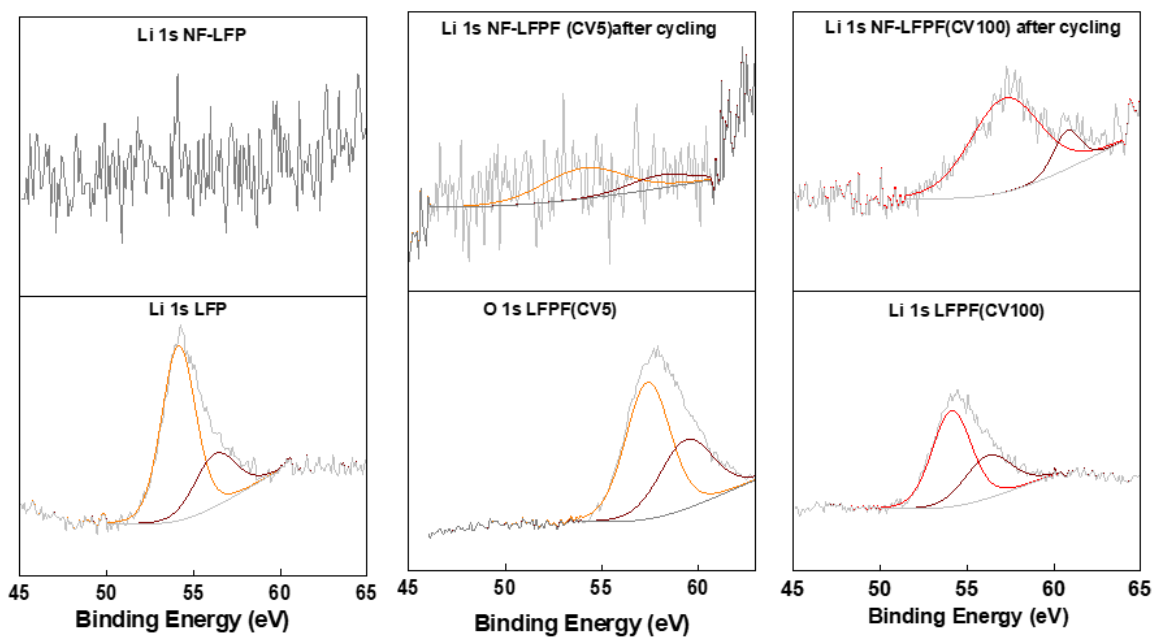


**Figure 7 S6:** Li 1s core level spectra for LFP, LFP(CV5) and LFP(CV100) samples removed from the NF support both before and after the OER.

### XPS Analysis

To observe the oxidation state and the elemental composition of the transition metals on the surface of the electrocatalysts XPS is performed <sup>205</sup>.

#### Fe LFP

The high resolution Fe 2p spectrum for LFP sample pre cycling showed peaks around 710.5 (Fe<sup>+2</sup> 2p<sub>3/2</sub>)<sup>204</sup> and 724.1 eV (Fe<sup>+2</sup> 2p<sub>1/2</sub>)<sup>123</sup> with satellite peaks at 715.1 (Fe<sup>+2</sup> 2p<sub>3/2</sub>)<sup>205</sup> and 726.3 eV (Fe<sup>+2</sup> 2p<sub>1/2</sub>)<sup>123</sup> that shows the presence of Fe<sup>+2</sup> in LiFePO<sub>4</sub>.

However, NF-LFP post cycling high resolution spectrum denotes peaks around binding energy 708.2 eV and 711.1 related to (Fe<sup>+2</sup> 2p<sub>3/2</sub>)<sup>205</sup> and peaks around 716.1eV appears after interaction of Fe-Ni with possible representation of presence of Fe<sup>+3</sup> oxidation state with satellite peak at 718 eV <sup>135</sup>.

## **Fe CV5**

The Fe2p spectrum analysis for LFP(CV5) pre cycling sample presented peaks around B.E. 712.9 eV <sup>164</sup> and satellite peak at 715 eV belongs to Fe<sup>+2</sup> 2p<sub>3/2</sub><sup>164</sup> and, with peaks at 718 and 730.3 eV as satellite peaks corresponding to Fe<sup>+3</sup> oxidation state <sup>166</sup>.

Additionally, the high-resolution spectra of NF-LFP(CV5) post cycling sample confirmed peaks at binding energy 708.3 and 712.2 eV <sup>204</sup>, <sup>164</sup> for Fe 2p<sub>3/2</sub> represents Fe<sup>+2</sup> and satellite peak at 718 eV usually occurs for Fe<sup>+3</sup> oxidation <sup>164</sup>, thus is possible indication of presence of Fe<sup>+3</sup> valance state of Fe and with presence of satellite peak at 720.5 eV belongs to Fe 2p<sub>1/2</sub><sup>135</sup>.

## **Fe CV100**

The core level Fe2p spectra for LFP (CV 100) pre cycling sample represents peaks around B.E at 710.5 eV <sup>123</sup>, [44] and 712.2 eV <sup>164</sup> for Fe<sup>+2</sup> belongs to Fe<sup>+3</sup> and Fe<sup>+2</sup> oxidation states, with satellite peak at 716.1 eV for Fe 2p<sub>3/2</sub><sup>135</sup>. Binding energy at 724.4 eV <sup>123</sup>, <sup>164</sup>, <sup>206</sup> with satellite peak at 726.4 eV for Fe 2p<sub>1/2</sub><sup>123</sup>, <sup>197</sup>.

Whereas, the high resolution Fe2p spectrum for NF-LFP-(CV 100) post cycling sample states peaks at 713.1 eV [19] and satellite peak at 718.1eV for Fe 2p<sub>3/2</sub> [48] is present due to presence of Fe<sup>+3</sup> valance states. Peaks at B.E. 725.3 eV also represents Fe<sup>+3</sup> oxidation state and satellite peak at 728.4 eV for Fe 2p<sub>1/2</sub><sup>123</sup>, <sup>64</sup>. The presence of peak around 718 eV shows the interaction of Ni-Fe in the electrode [48].

## **Phosphorus-LFPF**

The high-resolution spectra of P 1s (for pre cycling sample) confirmed the presence of peaks at 130.9 confirms possible interaction of Phosphorus with other elements <sup>78</sup>, 131.8 eV present interaction pf P-O bonds stating PO<sub>4</sub><sup>-</sup> group presence, however for LFP-NF electrode there was no phosphorus spectra observed [19].

There was no phosphorus peaks observed for post cycling sample.

### **Phosphorus-LFPF-CV5**

High resolution spectra of P 1s for LFPF(CV 5) pre cycling sample shows presence of peaks around B.E. 135.6 and 134.5 eV that usually occurs for H<sub>3</sub> PO<sub>4</sub> formation and similarly merged peaks of phosphorus was observe in the sample with electrode preparation [12].

There was no phosphorus peaks observed for post cycling sample.

### **Phosphorus LFP-CV100**

However, for **LFP(CV100)** peaks are observed at 132.3 and 131.3 eV represents P-O bonding and for **NF-LFP (CV100) electrode prepared (post cycling sample)** showed peaks at 135.5 and 133.53 eV which shows formation of H<sub>3</sub>PO<sub>4</sub> and Ni-P-O bonds respectively, and B.E at 133 eV also shows existence of formation of phosphate ion (PO<sub>4</sub><sup>3-</sup>, H<sub>2</sub>PO<sub>4</sub>) [12], <sup>164</sup>.

### **O-LFPF Pre**

Regarding high resolution 1 Os spectra of the peak at 529.7 eV is attributed to PO<sub>4</sub><sup>-</sup> and 531. 1 to hydroxyl groups [19], <sup>123</sup>.

Whereas peaks for **LFPF-NF post** at 530.9 eV corresponds to metal hydroxy groups and peaks at 527.7 to OH groups <sup>164</sup>.

### **O-LFP-CV100**

Regarding O 1S spectra peaks at **Pre** 530.4 belongs to oxygen atoms of hydroxyl groups <sup>164</sup>, 531.7 eV shows presence of phosphates or hydroxyl groups <sup>207</sup> for **Post CV** sample peak around 530.4 and 532.9 eV shows hydroxy groups as well as adsorbed water molecules <sup>123</sup>.

### **O-LFP-CV100**

Similar, set of peaks are observed for O-CV-100 **for pre** cycling 530.7, 532.6 corresponds to H<sub>2</sub>PO<sup>4</sup> and PO<sub>3</sub><sup>-</sup> and **post cycling** 533.2, 531.8 eV could be attributed to P-O-Ni or Ni-OH <sup>207</sup>.

## **Ni-LFP**

The Ni2p core level spectrum with binding state of high energy Ni 2p<sub>3/2</sub> and low energy Ni 2p<sub>1/2</sub>.

Peak at 854 eV belongs to oxidation states of Ni 2p<sub>3/2</sub> with satellite peaks at 858.2 eV<sup>208</sup> confirms presence of Ni<sup>+2</sup> state and peaks at 864 eV is attributed to Ni<sup>+2</sup> oxidation state of Ni 2p<sub>1/2</sub> with satellite peak at 870 eV<sup>67,153</sup>.

## **Ni-CV5-LFP**

Peaks at binding energy 856.3 and 864 eV corresponds to Ni<sup>+2</sup> oxidation state<sup>78,67,123</sup> and satellite peaks at 860.2, 872.3 corresponds to Ni 2p<sub>3/2</sub> and Ni 2p<sub>1/2</sub> [52],<sup>78</sup> respectively.

## **Ni-CV100-LFP**

Peaks at binding energy 857.7 are related to Ni<sup>+2</sup> and Ni-P<sup>85</sup> and 864 eV<sup>67</sup> to Ni<sup>+2</sup> predicting the presence of NiO and Ni(OH)<sub>2</sub> with two satellite peaks at 877 and 880.0 eV<sup>197</sup>.

## **Ni Foam**

Peaks at 854.4 and 873.5 belongs to Ni<sup>+2</sup> oxidation state with satellite peaks at 860 eV and 880 eV of Ni2p<sub>3/2</sub> and Ni 2p<sub>1/2</sub>, respectively [52], [57],<sup>197</sup>.